Synthesis and Development of Diagnostic Tools for Medical Imaging

Schaarup-Jensen, Henrik

Publication date:
2017

Document Version
Publisher's PDF, also known as Version of record

Synthesis and Development of Diagnostic Tools for Medical Imaging

PhD thesis

Henrik Schaarup-Jensen

Kgs. Lyngby 2017

Department of Chemistry
Technical University of Denmark

Abstract

The need for novel diagnostic tools in medical imaging is increasing since they can improve the positive therapeutic outcome as well as patient compliance. In this thesis different diagnostic tools were developed within an interdisciplinary project, whereas the main work reported in this thesis was the synthesis of different materials.

The first project introduces the development of injectable fiducial markers within the field of image-guided radiotherapy. Fiducial markers for computed tomography (CT)-imaging are today needed in order to correlate the positioning of the tumor to provide a more precise and improved radiation, as tumors rarely display a fixed position during radiotherapy. A fiducial marker based on encapsulated gold nanoparticles within the gelation matrix of sucrose acetate isobutyrate (SAIB) was developed and tested *in vivo*. The scientific objective was to provide sufficient surface engineering of the gold nanoparticles that will allow full dispersion of AuNPs within the hydrophobic environment of the SAIB matrix. As stabilizing coating-materials PEG, PNIPAM polymers and a dithiolane SAIB derivative were tested.

The unique gelation properties of the SAIB matrix led to the second project of injectable fiducial tissue markers for surgical guidance of non-palpable tumors and brachytherapy. As radioactive tracer, radioiodinated SAIB-derivatives were developed based on the regioselective *ipso*-iodination of aryl-TMS moieties. Radioiodination was conducted under carrier free conditions in high radiochemical yields by $Tl(OOCCF_3)_3$ and **[**^{125}**]**NaI. The application of the radiolabeled ^{125}I-SAIB derivative was tested *in vivo* as a tissue marker for surgical guidance and evaluated in terms of dosimetry.

The third project involved the synthesis of iodide-based contrast agents designed for remote loading of liposomes. Long circulating contrast agents for blood pool imaging by CT-imaging are of interest due to the current limitations of short retention times and the considerable amounts needed to achieve a proper contrast. A small library of contrast agents designed for remote loading of liposomes was synthesized. Remote loading of one candidate was successful; however, the proper contrast level was not sufficient to be visible by CT-imaging.

Another diagnostic tool for blood pool imaging is DOTA-modified pluronic/cyclodextrin (CD)-based polyrotaxanes (PRs). With the previously reported chelation of Gd and the prolonged retention time of Gd-chelated Pluronic/CD PRs, the aim was to extend the use of DOTA-modified Pluronic/CD-based PRs as positron emitting agents by chelation of ^{64}Cu. Pluronic/CD-based PRs grafted with DOTA was synthesized in the fourth project. The last project deals with the site-specific radioiodination of peptides and proteins. To achieve a conclusive outcome in radioimmunoassays as well as retaining a high binding affinity of receptor binging peptides, the regioselective radioiodination is crucial. Therefore, a TMS-substituted tyrosine was synthesized via the Negishi coupling to test

if regioselective iodination could be obtained. The tyrosine derivative was used in the synthesis of dipeptides of phenylalanine, tyrosine and tryptophan respectively in order to evaluate the selectivity towards the *ipso*-substitution of the TMS in the iodination reaction. First proof-of-concept experiments using aryl-TMS as placeholder in the site-specific iodination of peptides and proteins have been demonstrated.

Resumé

Behovet for nye redskaber inden for medicinsk billedbaseret diagnosticering har igennem de sidste år været tiltagende grundet ønsket om at forbedre de terapeutiske resultater samt patienternes tryghed under behandlingen. Denne afhandlingen beskriver tilblivelsen af flere forskellige nye billedbaserede diagnosticerings metoder, som alle er udviklet i et interdisciplinært projekt kaldt Nanoguide. Hovedvægten i rapporteringen ligger på syntesebeskrivelsen af de forskellige materialer, der indgår i disse metoder.

Det første projekt beskriver udviklingen af en injicerbar markør inden for billede-guidet radioterapi. Der er i dag et behov for markører der er synlig via CT billeddannelse og som kan indsættes i tumorer som et reference punkt til en mere præcis og forbedret strålebehandling under et radioterapi forløb. Dette er med formål at tilvejebringe at positioneringen af tumorer varierer under et radioterapi forløb. En markør baseret på sterisk stabiliseret guld nanopartikler (AuNPs) formuleret i en geleringsmatrix bestående af sucrose acetate isobutyrat (SAIB) blev udviklet og testet *in vivo*. Den videnskabelig udfordring var at overfladestabilisere AuNPs hvormed fuld blandbarhed i SAIB matricen kunne opnås. De stabiliserende overfladematerialer der blev anvendt var polymerer af PEG og PNIPAM samt et SAIB derivat der blev syntetiseret fra sucrose over fire trin.

De unikke geleringsegenskaber af SAIB matricen førte ligeledes til udviklingen af en injicerbar vævsmarkør til kirurgisk vejledning af ikke mærkbare tumorer inden for brystcancer samt brachyterapi. Som del af denne vævsmarkør blev et ^{125}I mærket SAIB derivat syntetiseret ud fra et TMS baseret SAIB forgangsmateriale via en regioselektiv *ipso*-substitutering. Ioderingen blev gennemført uden brug af ikke-radioaktiv Jod i et høj radiokemisk udbytte ved brug af $Tl(OOCCF_3)_3$ og **[^{125}I]**NaI. Det ^{125}I mærket SAIB derivat blev formuleret og testet *in vivo* for at undersøge egnetheden som vævs markør inden for kirurgisk vejledning. Dosimetri blev ligeledes beregnet for brug i patienter.
Det tredje projekt involverede syntesen af jod-baserede kontraststoffer konstrueret til at undergå loading af liposomer ved brug af en gradient. Langtids cirkulerende kontraststoffer til billeddannelse af det kardiovaskulære system er interessante på grund af de nuværende begrænsninger i form af kort opholdstider og de betragtelige mængder af konstraststof nødvendig for at kunne opnå en tilstrækkelig konstrast af det cardiovaskulære system. Et mindre bibliotek af kontraststoffer blev syntetiseret der er i stand til at kan loades i liposomer ved brug af en gradient. Gradient medieret loading af liposomer var succesfuldt for en af de syntetiserede kandidater. Desværre viste studiet at mængden af kontraststof ikke var tilstrækkelig til at opnå en tilfredsstillende konstrast der var synbar via CT-billeddannelse.

Et andet diagnostisk værktøj til visualisering af det cardiovaskulære system er DOTA-

modificerede pluronic/cyclodextrin-baseret polyrotaxaner (PRs). Med den tidligere rapporterede chelering af Gd og den forlængede retentionstid i blodet for Gd-chelaterede Pluronic/CD PRs, var målet at udvide brugen af DOTA-modificerede Pluronic / CD-baserede PRs til at chelere positron emitterende isotoper som ^{64}Cu. DOTA modificerede Pluronic/CD-baserede PRs blev syntetiseret i dette projekt.

Det sidste projekt beskæftiger sig med den regiospecifikke radioiodinering af peptider og proteiner. For at opnå et konkluderbart og præcist radioimmunassay samt at fastholde en høj affinitet for receptor bindende peptider efter radiomærkning, regioselektiv radioiodinering er altafgørende. Derfor blev et TMS-substitueret tyrosin derivat syntetiseret via Negishi-koblingen for at teste, om der kunne opnås regioselektiv iodinering af peptider og proteiner. Tyrosin-derivatet blev anvendt i syntesen af dipeptiderne af phenylalanin, tyrosin og tryptophan for at evaluere selektiviteten for *ipso*-iodineringen af TMS-gruppen i iodineringsreaktionen. De første beviser på at aryl-TMS kan anvendes i regioselektive iodineringer af peptider og proteiner blev demonstreret.

Preface

The work presented in this PhD thesis is the result of three years of research conducted from March 2013 to May 2016 at Center of Nanomedicine and Theranostics, Department of Chemistry at the Technical University of Denmark. The Danish Council for Strategic Research (Nanoguide, application no. 0603-00442B) and the Department of Chemistry gratefully the PhD project. The work was conducted under the supervision of Prof. Mads H. Clausen as main supervisor and Prof. Thomas L. Andresen as co-supervisor.

A three months external stay was conducted in the group of David H. Thompson at the Department of Chemistry, Purdue University, Indianapolis, USA.

Appended to this thesis is the scientific paper including results presented in chapter **??**. The paper was published during the PhD study.

Injectable Colloidal Gold for Use in Intrafactional 2D Image-Guided Radiation Therapy. Rasmus. I. Jølck, Jonas S. Rydhög, Anders N. Christensen, Anders E. Hansen, Linda M. Bruun, Henrik Schaarup-Jensen, Asger Stevner von Wenck, Betina Børresen, Annemarie T. Kristensen, Mads H. Clausen, Andreas Kjær, Knut Conradsen, Rasmus Larsen, Per Munck af Rosenschöld Thomas L. Andresen. *Adv. Healthcare Mater.* **2015**, 4, 856-863. *included as appendix.*

Publications based on results presented in remaining chapters are currently on-going.

Acknowledgements

There are numerous people that have contributed and being involved in the projects I have been involved in during my PhD.

First and foremost, I would sincerely like to thank Prof. Mads. H. Clausen for accepting me as a Ph.D. student in his group and allowing me the opportunity to develop as a person. I can not put into words what a learning experience this has been to me. I started as a rookie to end up as being a promising researcher. I am grateful for such an extraordinary guidance and useful discussions. It has been a privilege. I would likewise like to thank Prof. Thomas L. Andresen for his visionary ideas; your approach to solve scientific problems is a true inspiration. All collaborators of the Nanoguide project are gratefully acknowledged for their work and contributions in order to realize the projects. It has been a true learning experience dealing with scientific problems of high complexity in a context beyond the field of organic chemistry. Part of the Nanoguide project I would especially like to thank Dr. Rasmus I. Jølck, Dr. Anders E. Hansen, *Associate* Prof. Jonas R. Henriksen, Gokce Engudar, Linda M. Bruun, Dr. Andreas I. Jensen and *Associate* Prof. Henrik H. El-Ali.

I would also like to thank former and present members of the Mads H. Clausen group as well as colleagues of DTU Chemistry for a good company. Especially I would like to thank Dr. Beatrice Bonora, I could not have wished for a better lab-mate and friend. I would also like to thank Dr. Peter Hammershøj for the daily supervision and useful discussions. Jorge Peiro, you will always remain as my Real Madrid nemesis but your positive attitude and friendship mean a lot to me. I would like to commend Dr. Casper Hoeck for useful NMR discussions and second-opinions. For synthetic discussions, I am thankful to especially Kim T. Mortensen, Dr. Thomas Flagstad and Dr. Lasse B. Olsen. The late night hard-working company of Christine Kinneart and Kim T. Mortensen was truly appreciated.

I would like to express my deepest gratitude to Prof. David H. Thompson for my external stay. Thank you for your guidance and encouragement. As a person, you are a true inspiration. I would especially like to thank Dr. Seok-Hee Hyun for hosting me during my stay together with the rest of the group of Prof. David H. Thompson especially Bradley Loren, Vivek Badvaik and Christopher Collins for an extraordinary friendship and company. I would like to thank the financial support of Frants Allings Legat and Oticon Fonden during my external stay at Purdue University.
The finalization of this thesis was not possible without the tedious and extraordinary proof-readings of Dr. Irene Boos and Dr. Shahid I. Awan. I would like to declare a personally and profound acknowledgement to Irene Boos for sparing, useful discussions and helping out the last months of this thesis.

Finally, I would like to thank my family for you encouragement, and support throughout

this thesis, without you, this would not be possible. You are my solid ground. Especially, I would like to thank my mom and dad, This thesis is to you, I owe you everything.

Table of contents

Synthesis of Nanoparticle-based Fiducial Markers for Image-Guided Radiotherapy

1

1.1 Image-guided radiotherapy

External beam radiotherapy (EB-RT) remains today as one of the most promising and used treatments for cancer [1]. It is reported that approximately 50% of all cancer patients undergo radiotherapy treatment [1]. Likewise, it is estimated that usage of radiation therapy is cost-efficient and constitutes only 5% of the total cost of cancer treatment [1].
The technical term tumor control used in EB-RT treatment is stated to be proportional to the dose of radiation delivered to the tumor [2]. This is described via the linear-quadratic model presented in Brenner *et al.*, correlating the therapeutic radiation dose to cell/tumor viability [3]. The main reason that limits the of dose to malignant tissue, is the increased risk of harming or damaging nearby vital organs or surrounding healthy tissue [2]. This emphasize that the current issue within EB-RT is related to the current standards of precision of high radiation doses to a defined target.

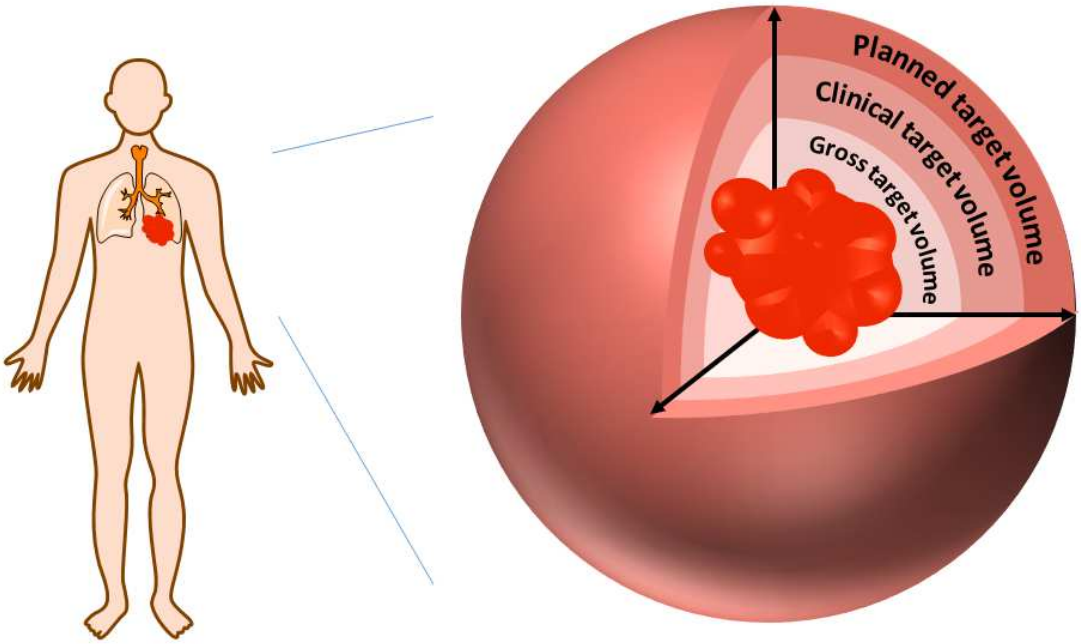

Figure 1.1: Schematic representation of the different kinds of target volume.

As a common procedure in the planning of EB-RT, a gross target volume (GTV) is

outlined corresponding to the tumor volume (Figure 1.1). GTV plus the surrounding area within the risk of microscopy spread in total constitute the clinical target volume (CTV) [2]. To compensate for daily positioning errors and internal motion of organs, an additional technical margin is added to CTV to afford the total planned target volume (PTV) [2], confer Figure 1.1. The technical margin is inferred as tumors rarely display a fixed position during radiation treatment. Tumor motion is clearly illustrated in the example shown below (Figure 1.2).

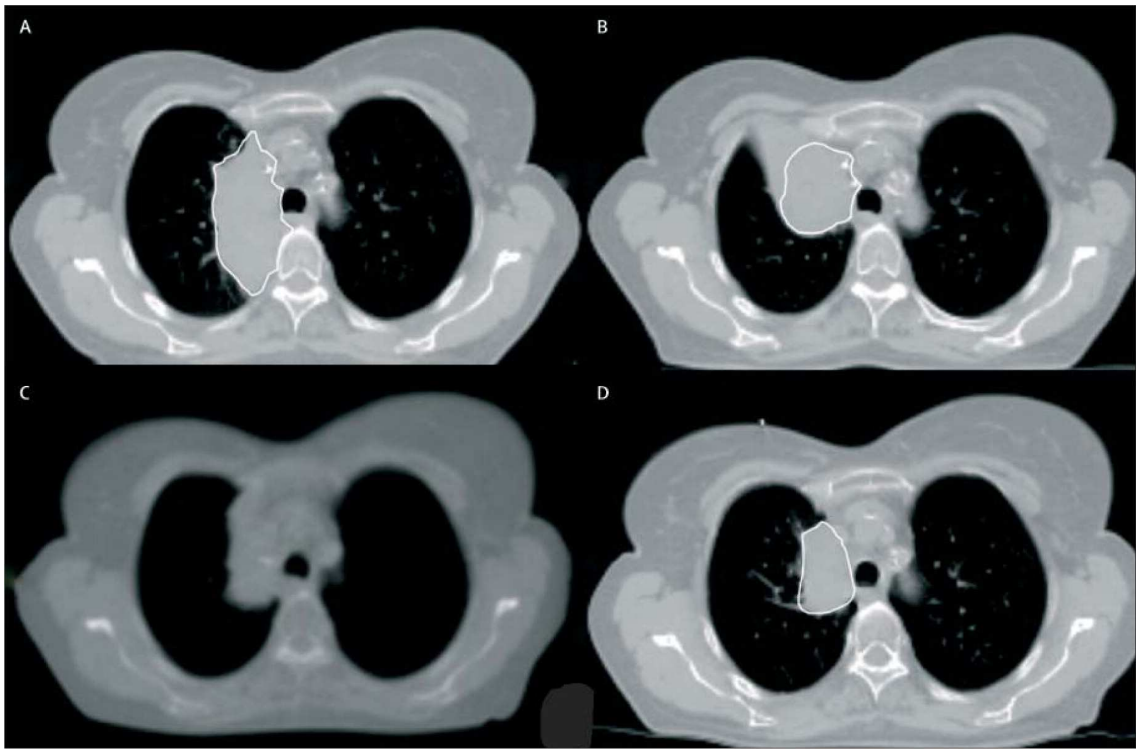

Figure 1.2: CT images showing a change in volume and position of adenocarcinoma of the right lung during radiotherapy. The white line indicates the gross tumor volume (GTV) (white line missing for image c). a) Delineation of gross target volume from the original planning CT scan. b) CT scan conducted after 24 days. c) megavoltage CT scan conducted after 60 days. d) kilovoltage scan conducted after 67 days [4].

The dynamic of the irradiation process is balanced by the clinical evaluation of gaining tumor control - also referred to as tumor control probability (TCP) - versus the risk of complicating normal healthy tissue known as the normal tissue complication probability (NTCP) [2].

To illustrate the impact of the addition of margins to assure full irradiation of a target, consider spherical tumor with a diameter of 4 cm. With an additional 3 mm standard deviation in order to assure full coverage (derived from systematic and random deviation) leads to a 6 cm diameter volume to be irradiated which roughly corresponds to three times the volume of the initial tumor [5]. Alternatively, a reduction of 1.5 mm in safety margin of a 5.0 cm spherical tumor reduce the irradiated volume including healthy tissue from 316 cm^3 to 48 cm^3. To further underline the difficulties ensuring tumor control within EB-RT,

the minimum radiation dose should ideally be homogenously distributed throughout the PTV [5]. This is not the case in many situations as the distribution of dose is heterogeneous and as a consequence, the PTV has to be increased [5]. As described by Jaffray *et al.* – "If all regions of a tumor are considered to be equal in their radiation response, the dose that determines tumor control is the minimum dose to the tumor" [5].

Improved accuracy and precision of radiotherapy are required to enhance tumor control []. Therefore, in order to improve and specify the therapeutic radiation dose to the tumor, the strategy is to provide a conformal dose distribution, corresponding to the target volume. Conformal dose distribution in accordance to the target volume is achieved by advanced computerized planning systems [4]. Among initiatives to decrease the PTV, the implementation of frequent imaging during treatment, referred to as image-guided radiotherapy (IGRT) has been developed. IGRT provides knowledge of the exact tumor position and elucidates the dynamic behavior of organ motions and tumors during radiotherapy [2]. The main contribution of IGRT is usually in repositionings if gross misalignments are observed due to unpredictable tumor or organ motion [4]. In addition, IGRT has enabled the implementation of intensity modulated radiotherapy (IMRT). In IMRT, the intensity of the radiation dose is modulated (a non-uniform dose) to conform more precisely throughout the PTV. This is in accordance to the prerequisite for IMRT of high control of geometric uncertainties as a steep decline between target delineation and healthy tissue is required [4]. This enables potential dose escalation to the tumor without irradiation of nearby tissues [2]. Being able to customize and adapt the dose more directly towards the treated volume imply a higher acceptance of risk as high conformal radiation doses will lead to control of tumor and lowering the possibility to damaging healthy tissue, NTCP [5]. The toxicity of radiotherapy can be obtained, as fewer fractionations are needed to achieve therapeutic effect. As an example, front-line radiotherapy using conformal radiotherapy and IMRT, has facilitated high-dose conformal radiotherapy of unresectable tumors in liver cancer which previously was not suitable for radiotherapy [4]. Image guidance is usually referred to as either online or offline. Online, images are recorded before each fractions of radiation doses to assess simple positioning corrections. In the case of offline image guidance, images are recorded after several fractions without intervention by which statistical derivations are computed to check for systematic geometric errors. Online image guidance has proven to reduce the number of geometric errors and to be more accurate when the surrounding tissue is vital or high dose radiation is given in one or few fractions [4]. Adjusting the radiation to the specific situation provide adaptive radiotherapy [4].

1.2 Use of radiopaque fiducial markers in IGRT

In those cases of cancers where the anatomical tumor position cannot be accurately identified or correlated to anatomical reference points, like parts of the skeleton, radiopaque fiducials markers are inserted in or nearby the tumor [4]. A radiopaque fiducial marker is defined as a material possessing radioopacity which makes it possible to use as a reference point [4]. Inserting these markers in tumors improves the contrast and tumor localization and allows for fluoroscopic real-time tumor tracking. This has proven to increase the accuracy of treatment for moving tumors [6–8]. The radiopaque fiducial

markers used today are typical solid metal-based implants of gold seeds with rather large physical dimensions, typically in the range of 1 mm x 5 mm (diameter x length) [6]. Gold fiducial markers have been implemented in the location of tumors within prostate, lung, liver, pancreatic, and paraspinal cancers [4]. Internal markers have proven to be a necessity for accurate tumor correlation in gated radiotherapy used in lung cancer and have been shown to provide a tumor correlation than external/superficial markers [7,9,10] . Moreover, the implantation procedure requires complicated insertion procedures typically via percutaneous insertion using 18 G needles. Especially in the case of fiducial marker insertion in lung tumors, this can lead to complications in form of pneumothorax (33-68% of the cases) [11–13]. Bleeding is likewise also reported [11–13]. Besides these adverse effects, solid markers also have a tendency to migrate from their original position [13, 14].

1.3 Problem statement

In order to enhance the precision of radiotherapy towards a defined target volume and the use of fiducial markers to enhance contrast and correlation of tumors, it was envisioned within the Nanoguide project, that a nanoparticle-based liquid fiducial radiopaque marker for CT/fluoroscopy could be developed for IGRT. A nanoparticle based fiducial marker should encompass an improved quality of image-guided radiotherapy by providing better tumor coverage, including better tumor correlation and online tracking. The intended outcome should hopefully be a more favorable conformation of the radiation dose and improved intensity modulated radiotherapy leading to better tumor control. In the more advanced setups like gated radiotherapy (in lung cancers) or if the tumor is inaccessible, where the radiation dose has to conform tightly with the PTV, it was envisioned that the design would improve irradiation compared to the current fiducial markers. Consequently, a new nanoparticle-based liquid fiducial radiopaque marker will provide a safer and convenient insertion and meet higher patient compliance.

1.4 Design and theoretical deliberations

As mentioned above, considerable complications belong to insertion procedures of fiducial markers particularly within lung cancers. The nanoparticle-based fiducial marker could overcome this problem and be compatible with CT imaging modalities. The design was based on the intention of developing a liquid radiopaque fiducial marker that will possess sol-gel properties similar to the lower critical solution temperature (LCST) properties of many polymeric systems and proteins.The sol-gel property will ensure that the marker will gel up upon injection. Liquefaction of the fiducial marker will entail percutaneously insertions (injections) using hyper- and thin hypodermic needles within the range of 25 G needles.This will reduce the dimensions of the the current standards of 18 gauge needles used today for percutaneous insertions, thus affording improved usability in clinical routines and patient compliance. As contrast property (radioopacity), it was reasoned that use of gold nanoparticles (AuNPs) could be sufficiently suspended within a proper sol-gel system. The premise will be based on the AuNPs being sterically stabilized towards aggregation and leakage of AuNPs from the gel-system will be kept at a minimum. AuNPs have likewise been proven stable during irradiation with X-rays [15].

1.5 Contrast properties of AuNPs

In order to develop a proper contrast agent for computed tomography (CT), heavy atoms that possess high X-ray attenuation and contribute with a high mass fraction of the contrast agents have to be located at the desired targets [16]. The most common heavy atoms used today in contrast agents are mainly based on gold or iodine. Gold possess higher X-ray attenuation than iodine (at 100 KeV: Au - 5.16 cm^2 g^{-1}, I - 1.97 cm^2 g^{-1}, soft tissue - 0.169 cm^2 g^{-1}, bone - 0.186 cm^2 g^{-1}) [17]. In accordance to Lambert Beer's law, attenuation is most efficiently achieved by a material with high absorption coefficient or by increasing the thickness of the material [18]. As gold is a more dense material than iodine X-ray attenuation is higher [18]. This difference was illustrated in the comparison of PEGylated AuNPs and the iodine-based Ultravist contrast agent (iopromide). PEGylated AuNPs with a size of 30 nm and at a concentration of 33 mg AuNPs mL^{-1} provided a contrast of 838 Hounsfield Units (HU), as opposed to Ultravist, where a concentration of 407 mg mL^{-1} Auravist is needed to afford the same contrast level. Per weight iodine (mg I mL^{-1}), this would correspond to 189 mg I mL^{-1} which gives a ratio of 5.6 higher of contrast of AuNPs compared to iodine in this particular case [19]. The study also confirmed that biocompability and non-toxicity of PEGylated AuNPs [19]. The was further substantiated in the study of Hainfeld *et al.*, where AuNPs provided longer cardiovascular circulation times than the corresponding Omnipaque (Iohexol). In addition, The AuNPs was not taken up by the liver or spleen but cleared renally. Intravenous injection likewise indicated a biphasic clearance profile and the LD_{50} for mice was reported to be 3.2 g Au kg^{-1} [17].

1.6 Sucrose acetate isobutyrate

Almost a decade ago, an attractive gelling system was published based on the sucrose acetate isobutyrate (SAIB) for the sustained release of risperidone [20]. SAIB is a fully esterified derivative of sucrose. The esters are mixed acetyl - and isobutyryl esters in a ratio of six isobutyryl - to two acetyl groups. The acetate groups are positioned at the primary positions while the remaining primary - and secondary hydroxy-groups are isobutyrylated. The main isomer **1.1a** of SAIB has the 6-OH and 6'-OH positions acetylated (Figure 1.3). The isomers **1.1b** and **1.1c** differ in the acetylation pattern of the primary hydroxy groups.

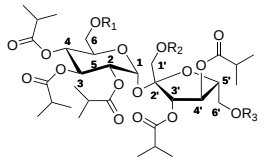

1.1a R_1 = Ac, R_2 = *i*-Pr(C=O)-, R_3 = Ac
1.1b R_1 = *i*-Pr(C=O)-, R_2 = Ac, R_3 = Ac
1.1c R_1 = Ac, R_2 = Ac, R_3 = *i*-Pr(C=O)-

Figure 1.3: The general structure of sucrose acetate isobutyrate.

Due to the mixture of regioisomers with regards to the positioning of the acetates, SAIB is provided as a highly viscous liquid with a reported viscosity of 100.000 Pa·s [20]. Dilution of SAIB with common solvents like EtOH or NMP in the range of 15-35%, change the viscosity drastically into a Newtonian liquid with a viscosity in the range of 50-200 Pa·s, which makes it suitable for percutaneous injections through hypodermic needles [20].
In vitro release studies indicate that EtOH is the best solvent - together with poly(lactic

acid) (PLA) as excipient - to mediate a sustained release of risperidone, as the burst release is kept at a minimum [20]. The sustained flux of risperidone is characterized by the modulated release described by Higuchi diffusion mass-transfer equations [20, 21]. An interesting property of the EtOH diluted SAIB mixtures is the change observed upon hydration conditions (submersion to a hydrophilic environment). Under these conditions, an efflux of EtOH occurs, by which the corresponding hardening of a SAIB-based gel-like implant occur, leaving a water insoluble, amorphous gel-like implant of high viscosity [6]. The process occurs by the non-solvent induced phase separation (NIPS), a term usually applied within membrane preparation. It refers to the behavior of a three-component system: 1) A polymer material (in this case SAIB) that does not dissolve in a hydration media (non-solvent), 2) a non-solvent providing hydration also referred to coagulation bath, and 3) a solvent excipient (in this case EtOH) which acts as solvent for polymer material solution and is partly or fully miscible in the non-solvent hydration media [20,22]. Upon immersion in the coagulation bath (non-solvent), exchange of the non-solvent and the solvent excipient occurs. This result in an efflux of the solvent excipient (EtOH) from the polymer solution towards the non-solvent (hydration media) and a corresponding hydration of the polymer (SAIB) affording a membrane-like settling according to the immiscibility of the non-solvent and the polymer [20, 22]. As the *in situ* settling is not occurring immediately, a burst release from gel system is observed and the hardening process is seen as a development over time (Figure 1.4) [20] .

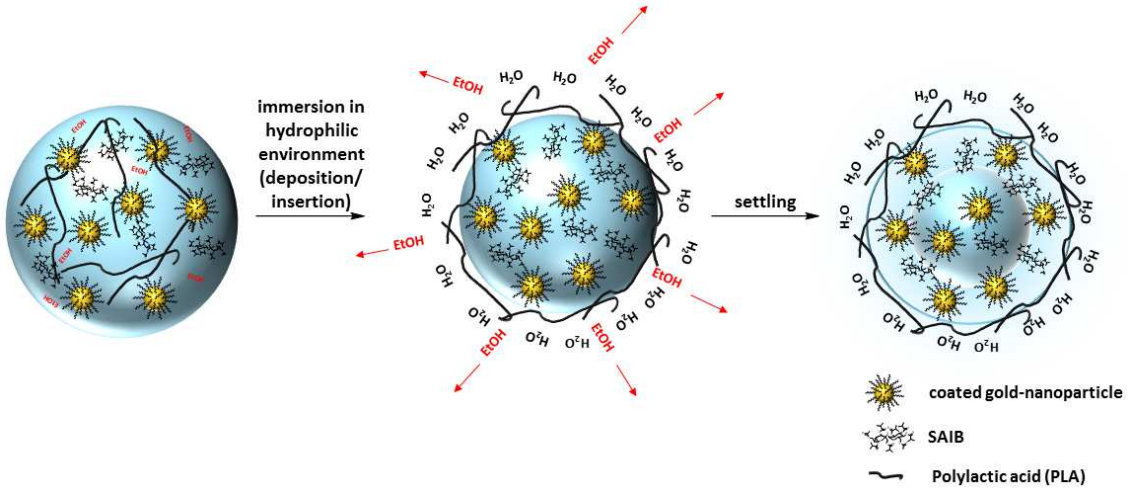

Figure 1.4: Schematic representation of the non-solvent induced phase separation of the SAIB formulation. From left: the SAIB formulation (with EtOH) as a viscous liquid. Upon hydration, an efflux of EtOH is taking place (middle figure). The figure to the right illustrates the settling process of the SAIB-deposit. The settling process is taking hours illustrated by the graduate change in color.

Based on the inferred findings of the gelation-properties of SAIB and the contrast properties of AuNPs, it was envisioned that combining AuNPs with the *in situ* gelation of SAIB could constitute the liquid radiopaque fiducial marker. The underlying challenge would be to ensure compatibility between the SAIB matrix and AuNPs that will ensure the stabilization and encapsulation of AuNPs within the hydrophobic environment of the

SAIB gel.

1.7 The first generation - SAIB-AuNPs based liquid fiducial radiopaque marker

As presented in Joelck *et al.*, the first generation of an injectable fiducial marker was developed by other members of the Nanoguide-project [6]. The AuNPs were synthesized according to the Turkewich/Frens method using a seeding protocol where tetrachloroauric acid ($HAuCl_4$) is reduced by sodium citrate as a mild reducing agent [23, 24]. The size of the AuNPs was controlled by the addition of $HAuCl_4$. The synthesized AuNPs were subsequently changed from being electrostatically stabilized by citrate to be sterically stabilized by PEGylation by ligand exchange using a MeO-PEG_{5000}-SH polymer with the thiol as anchoring group (Scheme 1.1).

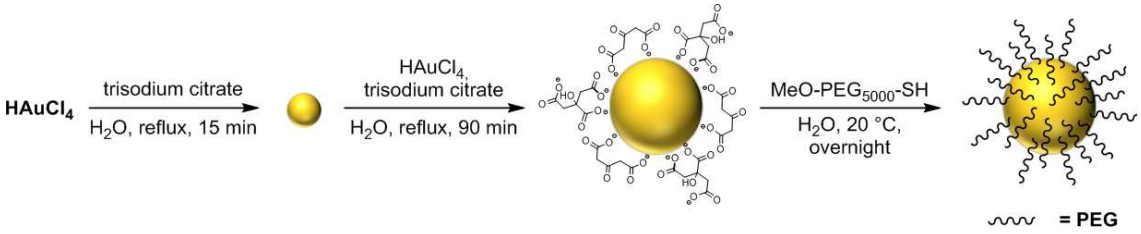

Scheme 1.1: AuNP synthesis and sterically stabilization using MeO-PEG_{5000}-SH.

Size distribution and ζ-potential by DLS measurements were analyzed together with surface characterization by UV-VIS. The characterization of the AuNPs is depicted in Figure 1.5 (ζ-potential not shown). UV-VIS spectroscopy confirmed that the surface plasmon resonance (SPR) property was intact upon the steric stabilization of the synthesized AuNPs. The hydrodynamic diameter increased likewise in accordance with the introduction of polymer coating. In order to tune the proper contrast to the intended level, the contrast in HU was correlated to the concentration of AuNPs.

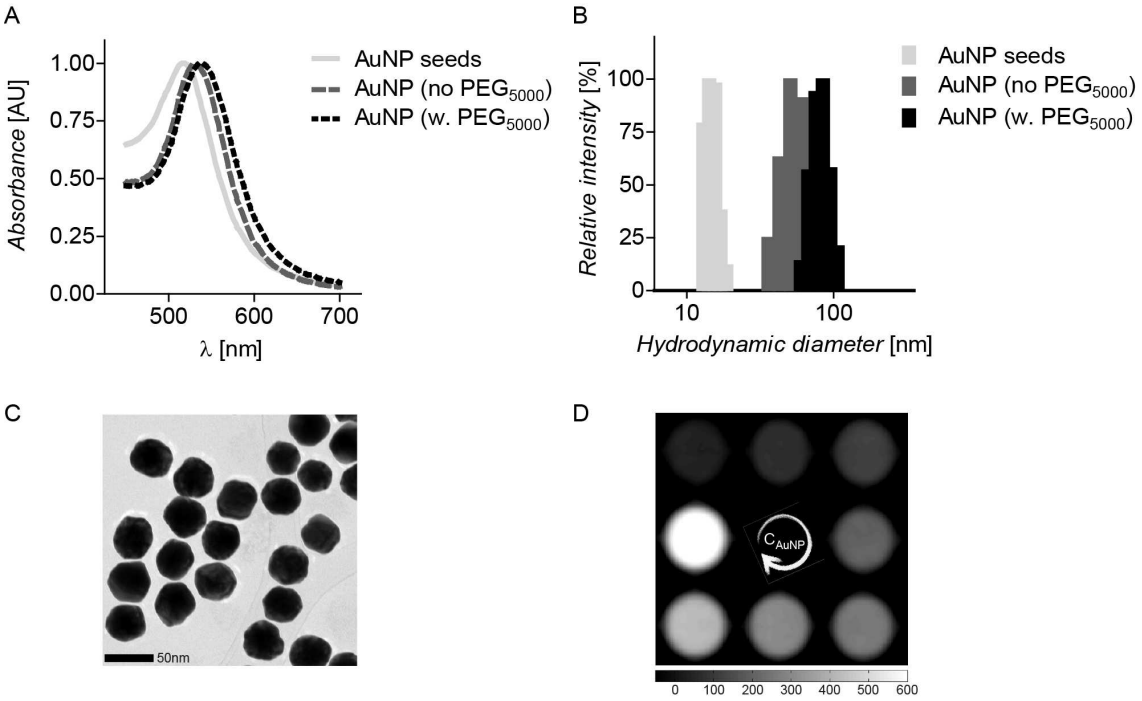

Figure 1.5: Characterization of synthesized AuNPs. a) UV-Vis spectrum showing the surface plasmon resonance effect. b) DLS measurements of synthesized AuNPs. c) TEM imaging of the quasi-spherical morphology of the synthesized PEGylated AuNPs. d) Calibration of AuNPs concentration versus CT-contrast in Hounsfield Units (HU). Upper Left corner and proceeding clockwise; MQ-H_2O, 1.0, 2.5, 5.0, 7.5, 10.0, 15.0, 20.0 mg AuNP mL^{-1}. [6]

In order to achieve a proper contrast level, 10 mg AuNPs mL^{-1} was chosen for the *in vivo* experiments. Advantageously, the sterically stabilized AuNPs could be re-dispersed in other solvents by centrifugation of the AuNPs and decantation of the aqueous solution. Final compositions of AuNPs and SAIB formulation were chosen to be 10 mg AuNPs mL^{-1} of either SAIB/EtOH (80:20 vol%) formulation or SAIB/EtOH/PLA (75:20:5 vol%) formulation which were tested *in vitro* and *in vivo*.

The *in vitro* burst release analysis of AuNPs is depicted in Figure 1.6.

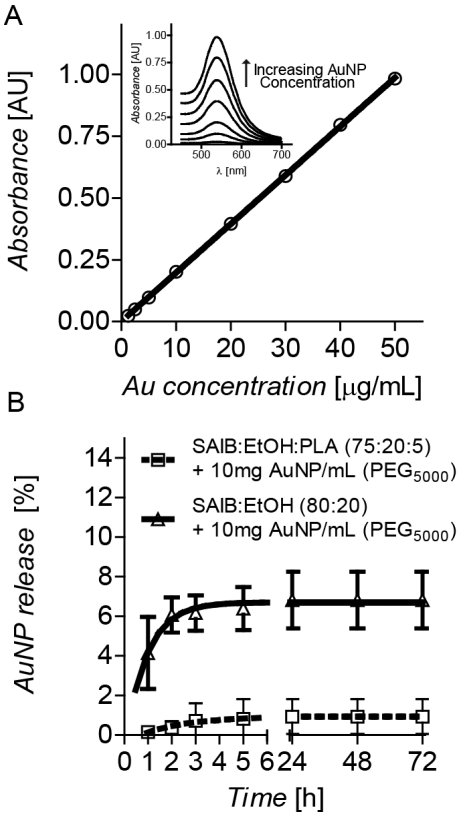

Figure 1.6: *In vitro* burst release analysis. a) Standard curve of PEGylated AuNPs in PBS-buffer. b) *In vitro* release of PEGylated AuNPs in PBS-buffer [6].

In vitro studies indicated a quite significant burst release of AuNPs in the range of 6% from the SAIB/EtOH deposit formulation [6]. The burst release seemed to be controlled in the other deposit formulation of SAIB/EtOH/PLA (75:20:5 vol%), which was explained by the presence of 5% PLA as part of the formulation. Accordingly to the sustained release study of risperidone using the SAIB deposit, it was proposed that the addition of PLA forms a diffusional membrane at the outer rim of gel. Upon contact with release media, the PLA polymer undergoes precipitation as the solvent composition changes in the interface between the gel and release media [20]. This is further substantiated by Fick's law of diffusion, as increasing the thickness dx of the membrane will have the effect of lowering the flux. The decrease in flux is likely also due to the alteration in the partition coefficient of the AuNPs in the PLA-layer.

The maximum loading of AuNPs within the SAIB/EtOH/PLA (75:20:5 vol%) formulation was found to be 30 mg AuNPs mL^{-1}. This was obtainable but led to a drastic burst release in the range of 20%, which could be lowered by changing the amount of EtOH [6]. The *in vivo* performance of the 10 mg AuNPs mL^{-1} SAIB/EtOH/PLA (75:20:5 vol%) formulation was analyzed by the subcutaneous injection in mice using thin 25 G needles. The deposit was visible on micro-CT and afforded a contrast enhancement of 200 HU. The average contrast level decreased 24% over 12 weeks post-injection. Homogeneity analysis revealed in-homogeneities within the gel as AuNPs accumulated at the rim of the gel-deposit [6],

as illustrated in the recorded CT-images (Figure 1.7).

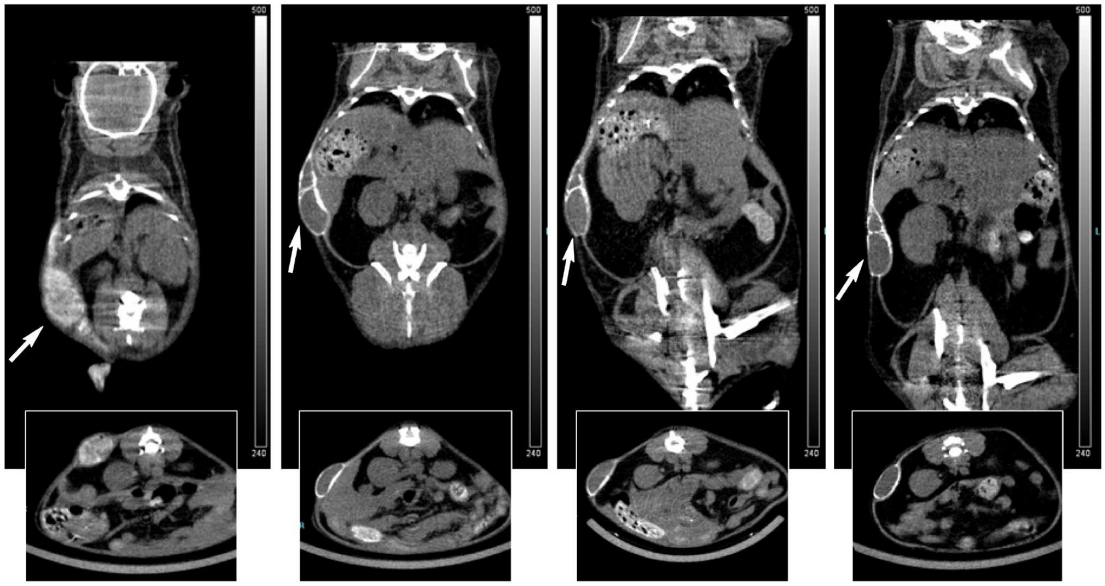

Figure 1.7: Coronal CT slides displaying the stability of the nanogel in size and shape. The images from the left to right are same mouse recorded after post-injection at 0.5 h, 3 weeks, 6 weeks and 12 weeks. Arrow is indicating the gel deposit. Notice how the contrast develop from being evenly distributed to be found at the rim of gel. [6].

This led to a follow-up optimizing study, with the intention to improve the stabilization of AuNPs within the SAIB formulation and likewise to increase the contrast level from 200 HU units, which is borderline for 2D X-ray visualization. From the above-mentioned findings, it was inferred that the steric stabilization of AuNPs was the underlying issue leading to the heterogeneity of the first generation of SAIB based injectable fiducial marker. The choice of the PEG-coating as steric stabilization of the AuNPs could be expected to be too hydrophilic compared to the hydrophobic environment of the SAIB formulation. Increasing the hydrophobicity of the coating agent could potentially enhance the stability of the AuNPs. Therefore two new strategies were tested based on the chemisorption of a newly developed SAIB derivative derived with a dithiolane moiety as anchoring group and chemisorption of thiol terminated poly(*N*-isopropyl acrylamide) polymers (PNIPAM-SH_{3500}).

1.8 The chemistry of sucrose

Background information of the most common trends of protecting group manipulation, reactivity and functionalization of sucrose is highlighted in this section in order to develop SAIB-based derivatives for AuNP functionalization that will ensure steric stabilization in the hydrophobic environment of the SAIB gel. The following sections are mainly based on the literature of Jarosz *et al.* and Queneau *et al.* [**?**, 25]

1.8.1 Sucrose

Sucrose is a naturally occurring disaccharide consisting of β-D-fructofuranosyl-(2→1)-α-D-glucopyranoside. It is a non-reducing sugar as both reducing ends of the glucopyranoside and fructofuranosyl units are bonded to each other. Thus, the hemiacetal chemistry of the anomeric center is replaced by the bis-acetalization chemistry of the glycosidic linkage [**?**]. The glycosidic linkage of sucrose is stable in basic environment but labile under acidic conditions [25]. Beside the glycosidic linkage, sucrose possesses three primary hydroxy groups and five secondary hydroxy groups. All hydroxy groups show similar reactivity, but differentiation of the primary and secondary hydroxy groups is achievable using bulky reagents. The secondary hydroxy groups can furthermore be differentiated but not without difficulties [25].

Sucrose possess interesting conformations as shown in Figure 1.8. In the solid state, two hydrogen bonds exist; one in-between the 6'-OH and the pyranosidic *endo*cyclic oxygen while the second hydrogen bonding occur between 2-OH and 1'-OH (**1.2a**) [**?**, 25]. Upon solvation, only the hydrogen bonding between the 2-OH and 3'-OH or 1'-OH are occurring, **1.2b** and **1.2c** respectively. This hydrogen bonding together with the neopentyl reactivity of 1'-OH underpin the less accessibility and reactivity compared to 6-OH and 6'-OH.

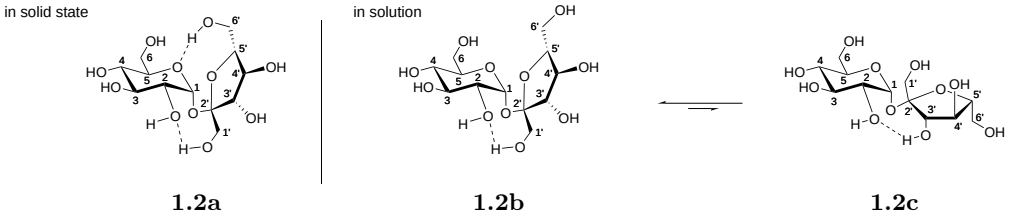

Figure 1.8: Structural conformations of sucrose. The conformation of **1.2a** shows the two hydrogen bonding present in the solid state. **1.2b** and **1.2c** show the equilibrium states of the two types of hydrogen bonding present in solution [26]

The most acidic hydroxy-groups of sucrose have been estimated to be those nearest the glycosidic linkage, thus 2-OH, 1'-OH and 3'-OH [**?**]. This property has been used to regioselectively modify the 2-OH position of unprotected sucrose e.g. by using benzyl bromide and NaH in DMF yielding 2-*O*-benzyl-sucrose as the main species [**?**]. A common strategy to allow regioselective modification of sucrose at the primary positions is to protect the primary hydroxy group(s) of interest - using a bulky protecting group - followed by orthogonal protection of the remaining hydroxy-groups. Subsequent deprotection of the primary position(s) afford the hydroxy-group(s) of interest available for modification [25]. In terms of the use of ester-type protection groups at the secondary/remaining positions, the deprotection of the bulky protecting group at the primary position(s) can lead to acyl-migration of the neighboring acyl group. Migration is usually facilitated by acidic or basic conditions, which is usually a requirement for the deprotection of the bulky protecting groups of silylating agents or trityl moieties.

1.8.2 Ether modification of sucrose

The bulky protecting groups used to differentiate between the primary and the secondary hydroxy groups are usually *tert*-butyldiphenylsilyl (TBDPS) or triphenylmethyl (Trt). The reactivity of the primary hydroxy-groups differentiates, based upon the different reagents used. The overall order of reactivity observed is usually 6-OH>6'-OH>1'-OH. 1'-OH is less reactive due to its accessibility and neopentyl-like reactivity. The reaction pattern of unprotected sucrose **1.3** towards bulky protecting groups are illustrated in Scheme 1.2. Regarding tritylation, excess use of TrtCl (3.6 equiv.) in basic conditions at elevated temperature afford the 6,1',6'-tri-*O*-trityl-sucrose **1.4** as the main derivative. Carrying out the same reaction using similar equivalents at room temperature afford beside **1.4**, 6,6'-di-*O*-tritylsucrose **1.5**. Lowering the amount of TrtCl to 2.0 equiv. provide a mixture of mono-tritylated sucrose, 6-*O*-trityl-sucrose **1.6** and 6'-*O*-trityl-sucrose **1.7**. Lowering the amount of TrtCl to 1.2 equiv, afford the same mixture of monotritylated sucrose derivatives in lower yields [25].

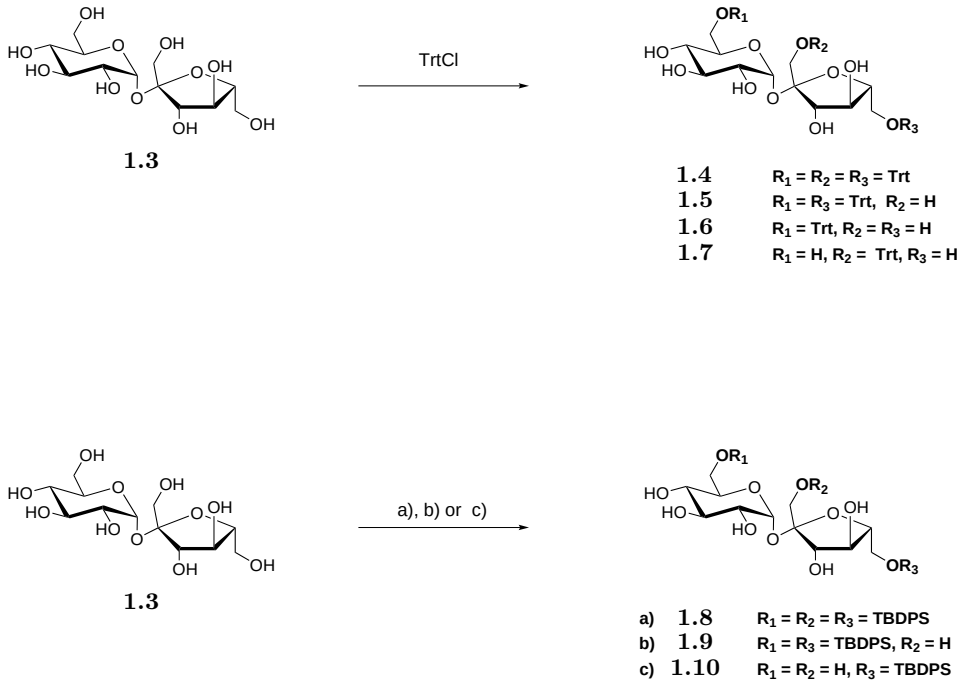

Scheme 1.2: The reaction pattern of sucrose **1.3** using TrtCl and TBDPSCl [25, 27]

Application of the bulky silyl group of TBDPS enables improved selectivity between the primary hydroxy groups of sucrose. Reactions performed using a 1.1 equiv. of TBDPSCl in pyridine and 4-dimethylamino-pyridine (DMAP) at room temperature provide the 6'-*O*-TBDPS-sucrose **1.10** as the main species together with the formation of 6,6'-di-*O*-

TBDPS-sucrose **1.9** in trace amounts [25, 27]. Using TBDPS as the bulky protecting group inverts the reactivity towards the regioisomer of the 6'-OH position compared to the use of Trt. Providing excess amount of TBDPSCl (4.6 equiv.) at elevated temperature show similar reactivity and afford the fully 6,1',6'-tri-*O*-TBDPS-sucrose **1.8** while lowering to 3.0 equiv. affording a 1:3 ratio of **1.9** and **1.8** [25].
Studies using 2,3,3',4,4'-penta-*O*-benzylsucrose **1.11** as model substrate have shown that the primary hydroxy groups can be further discriminated through additional protecting-group manipulations (scheme Figure 1.9) [25].

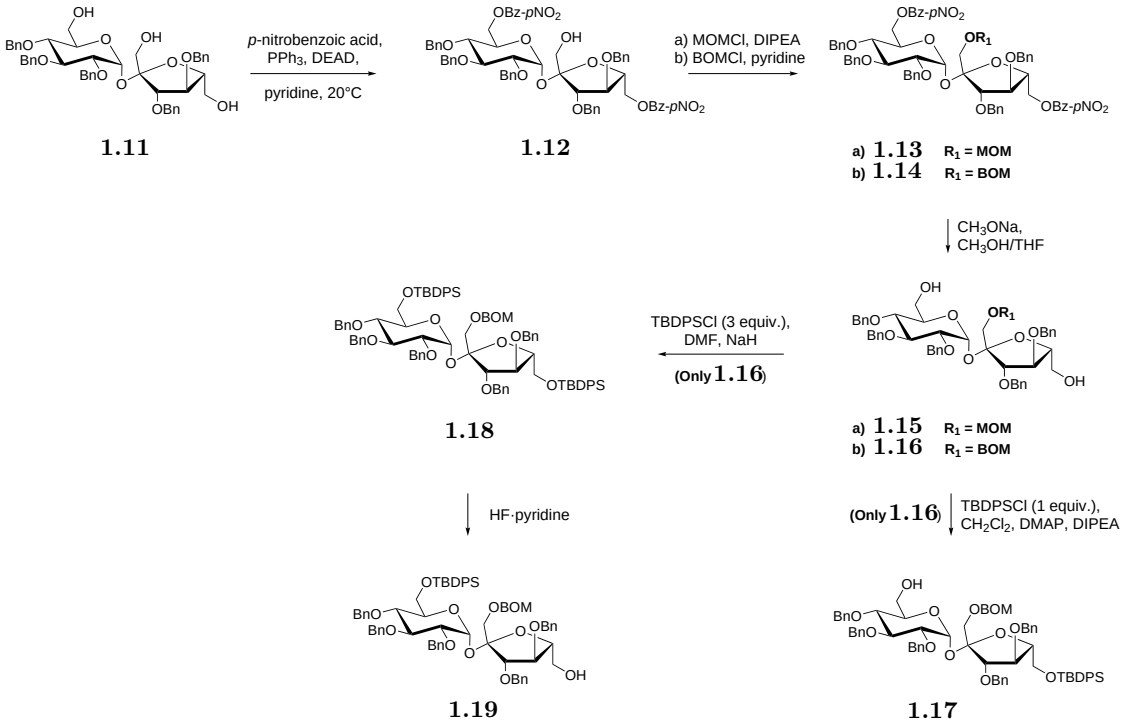

Figure 1.9: Further discrimination of the primary hydroxy groups starting from **1.11** [25].

Employing Mitsunobu conditions using *p*-nitrobenzoic acid as the nucleophile, afford 6,6'-diester of **1.12** which subsequently can lead to regioselective protection of the 1'-OH position affording **1.13** or **1.14** using MOM or BOM as protecting group, respectively. The 6,6'-diol of **1.15** or **1.16** can subsequently be re-established using Zempleén conditions. Further discriminations between the 6-OH and 6'-OH can be made, because TBDPS-protection (1 equiv.) will block the 6-OH position available (**1.17**), in line with the reactivity described previously. The 6'-OH position can be achieved by fully di-TBDPS protection of **1.18** followed by subsequent regioselective mono-desilylation using 1 equiv. of HF·pyridine liberating the 6'-OH position (**1.19**) available for further modification [25].

1.8.3 Ester modifications of sucrose

Applying Mitsunobu conditions have also been exerted to perform ester-linkages of different carboxylic acids. Mitsunobu-conditions on native sucrose **1.3** yielded the 6-*O*-acyl-sucrose using a slight excess of a fatty acid derivative, whereas two equiv. provide the 6,6'-di-*O*-acyl-sucrose [25]. In terms of ester protections of the primary hydroxy-groups, the

common pivaloylation, benzoylation and acetylation have been conducted on sucrose [25]. Pivaloylation showed similar trend of reactivity on the primary hydroxy-groups as mentioned in section 1.8.2, while benzoylation mainly occur on 6-OH compared to 1'-OH and 6'-OH. Regioselective acetylation of primary hydroxy groups has been conducted using either kinetic conditions to afford 6-*O*-acetylsucrose while using DABCO and 3-acyl-5-methyl-1,3,4-thiadiazole-2(3H)-thiones afford the regioisomeric 6'-*O*-acyl-sucrose [25].

1.8.4 Acetalization of sucrose

Sucrose **1.3** undergoes isopropylidene acetalization with the diols of 4-OH and 6-OH and furthermore at the 1'-OH and 2-OH. As acid is required for the acetalization, the choice of acid has proven to be a key factor for the outcome of the acetalization. Using mineral acids and acetone led to decomposition of sucrose while organic acids like *p*-toluenesulfonic acid and 2-methoxypropene in slight excess provides the 4,6-*O*-isopropylidene-sucrose in decent yield. Formation of the corresponding benzylidene acetal is likewise reported but in low yield. The benzylidene acetal offers the possibility of regioselective ring-opening of the acetal that would provide either 4-*O* or 6-*O* functionalized derivatives of sucrose [25].

Stannylene-acetals are well known in carbohydrate chemistry and are widely used. Using $(n\text{-Bu})_2\text{SnO}$ with native sucrose afford the dimer of 4,6-*O*-stannyleneacetal-sucrose **1.20** (Scheme 1.3) [25, 28].

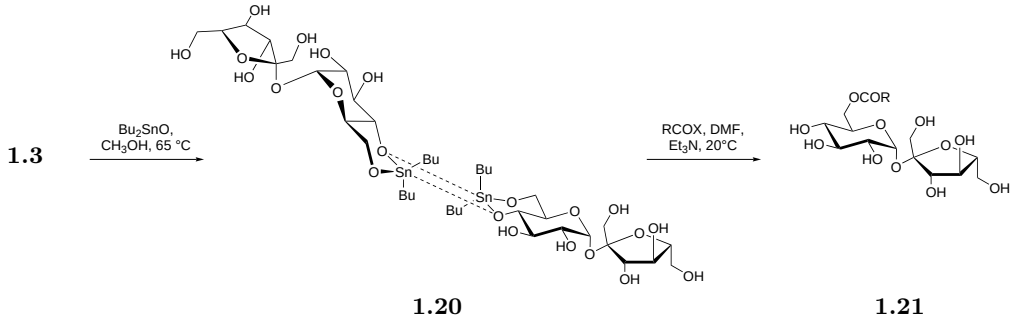

1.20 **1.21**

Scheme 1.3: Stannylene acetylation of sucrose [28].

The formation of this acetal increases the nucleophilicity of 6-*O* position which in the presence of electrophilic agents undergo regioselective nucleophilic substitution affording the 6-*O*-acyl-sucrose **1.21** [25, 29]. Likewise, the formation of 5-membered cyclic stannylene acetals have been reported on the **1.4**. Stannylene acetal formation occurred between the trans-diol of 3'-OH and 4'-OH of **1.4**. Depending on the solvent applied, mesylation or triflation at the 3'-OH or 4'-OH position of **1.4** was achievable, respectively [30].

Another convenient transformation used on sucrose **1.3** is the Appel reaction converting the primary positions of 6-OH and 6'-OH into the corresponding dihalo derivatives of sucrose using standard conditions of tetrahalomethane (chloro or bromo) and triphenylphosphine (PPh_3) [25].

A wide range of enzymes have also been employed to afford sucrose derivatives.

Peracetylated sucrose **1.22** can be regioselectively deacetylated liberating the given hydroxy group of interest for further modifications. An overview of the different enzymes and their deacetylation position is illustrated in figure Scheme 1.4 [25].

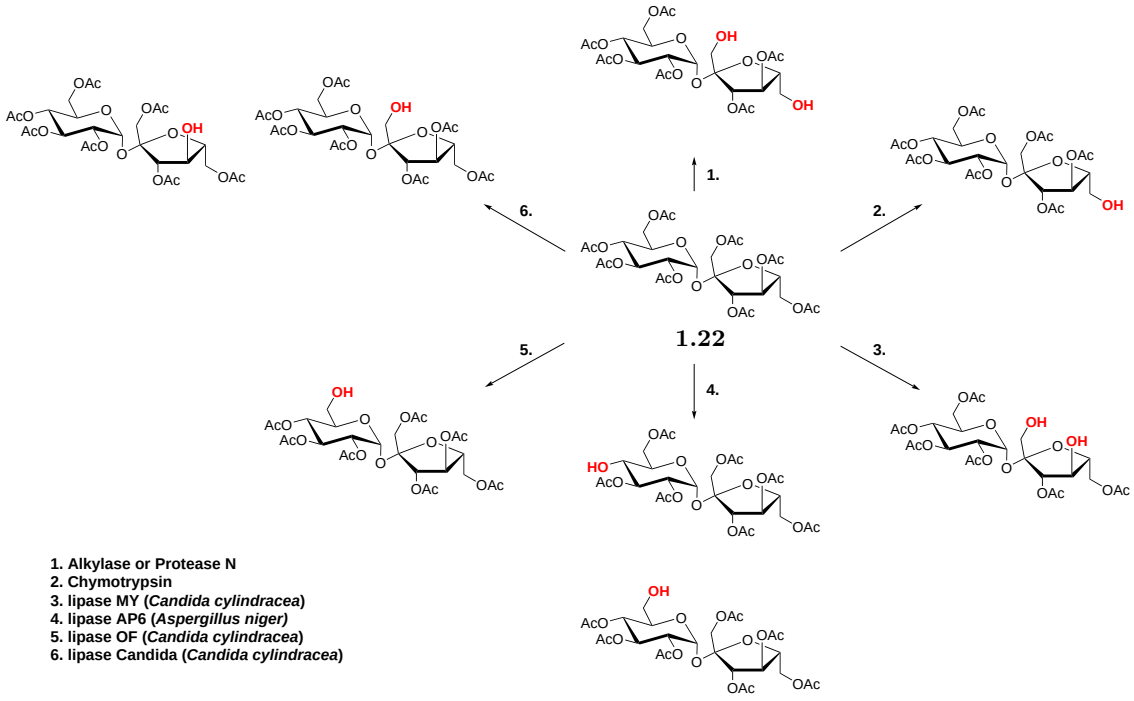

Scheme 1.4: Different options of using enzymes to achieve regioselective deacetylation of peracetylated sucrose **1.22** [25].

1.9 Design of the dithiolane-functionalized SAIB derivative

The design of a SAIB-based ligand for AuNP functionalization was based upon the "like dissolves like principle". Being as similar as possible in structure to SAIB **1.28** - could potentially encompass enhanced stability within the SAIB formulation. In a retrosynthetic perspective, such a ligand could be achieved in few steps, in accordance with the synthetic trends and strategies of sucrose described in section 1.8. Several studies have shown that the dithiolane group provide enhanced stability in AuNP functionalization when compared to thiol conjugation [31–33]. Since the lipoic acid is commercially available, and thiols commonly tend to form disulfides it was decided to use lipoic acid as anchoring group. Having the butyl linker in-between the dithiolane group and the carboxylic acid will act as a spacer.

Functionalization of AuNps with carbohydrates have been reported previously within the field of Au glyconanoparticles. Glyconanoparticles have been used within the area of carbohydrate research to gain knowledge about how carbohydrates are involved in signaling and carbobydrate-based interactions in cellular functioning []. The carbohydrate based ligands developed within this field are of unprotected sugars, which was expected not be compatible with the hydrophobic environment of SAIB **1.28**.

1.10 The synthesis of dithiolane functionalized SAIB derivative

The dithiolane functionalized SAIB derivative was synthesized in four steps starting from sucrose **1.3** (Scheme 1.5).

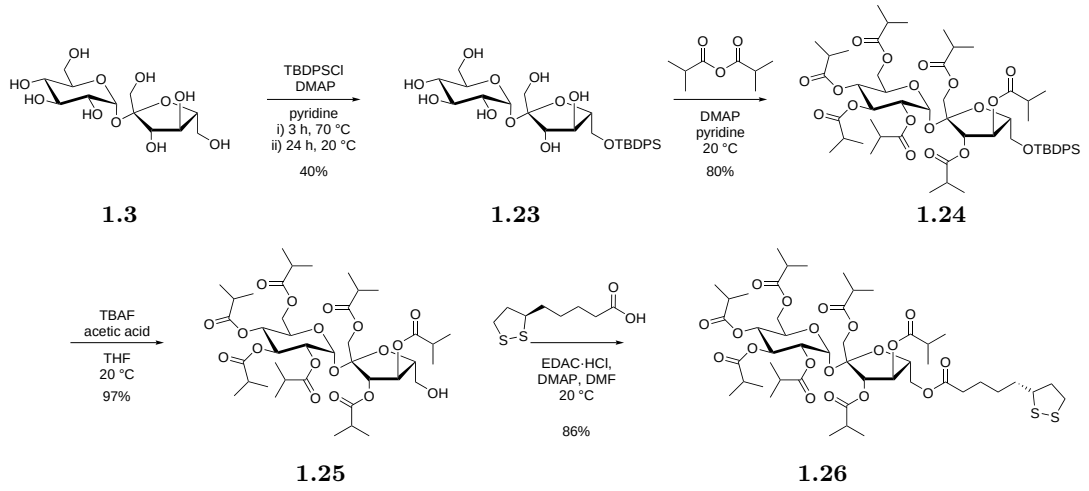

Scheme 1.5: Overall scheme for the synthesis of **1.26** [6].

Regioselective *tert*-butyldiphenylsilyl (TBDPS) protection of sucrose afforded the 6'-TBDPS-*O*-sucrose **1.23** using 1.2 equiv. TBDPSCl in pyridine. The mono silylated sucrose **1.23** was subsequently isobutyrylated at the remaining positions using isobutyric anhydride and DMAP conducted in pyridine affording the 6'-*O*-TBDPS-hepta-isobutyryl sucrose **1.24** in 80% yield. The position of the TBDPS of **1.3** was verified by 2D-NMR experiments of **1.24** and was in accordance with literature [25, 27]. The isobutyrylation of **1.24** was confirmed to be fully isobutyrylated by the presence of seven carbonyl ester carbon resonances in ^{13}C NMR together with HMBC correlations to the backbone of sucrose.

The TBDPS group was attempted removed using 1.2 equiv. of tetra-*N*-butylammonium fluoride (TBAF) in THF. These conditions were apparently too harsh in terms of basicity as - besides the deprotection of the TBDPS **1.25** - this also led to the de-isobutyrylation at the 4'-OH position affording the diol **1.27** (Scheme 1.6).

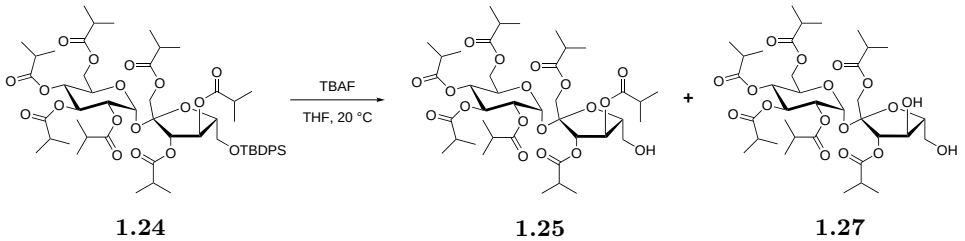

Scheme 1.6: Deprotection of **1.24** using TBAF.

With the isolation of this side-product **1.27** could indicate that migration occurred to the neighboring 6'-OH position upon silyl-deprotection followed by subsequent hydrolysis. In order to control and keep the migration to a minimum, the deprotection was optimized by adding acetic acid in slight excess (1.5 equiv.) compared to TBAF (1.2 equiv). This gave the desilylated product **1.25** in almost quantitative yield (97%), as shown in the Scheme 1.5. The dithiolane moiety was introduced by the formation of the activated ester using *N*-dimethylaminopropyl-*N'*-ethyl carbodiimide HCl (EDC·HCl) and DMAP. The esterification afforded the dithiolane derivative **1.26** in 86% yield.

1.11 Surface functionalization of AuNP

Citrate reduced and stabilized AuNPs with a size of 40 nm were surface functionalized with PEG_{5000}-SH or $PNIPAM_{3500}$-SH or **1.26** in aqueous solution overnight at 20 °C (Scheme 1.7).

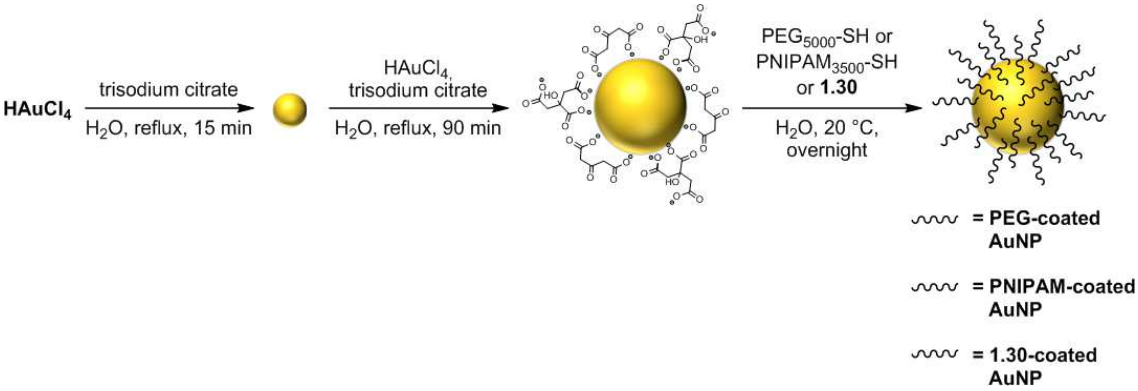

Scheme 1.7: Synthesis and coating of AuNPs [9].

From the recorded UV-VIS spectrums, SPR was consistent upon ligand exchange for PEG_{5000}-SH and $PNIPAM_{3500}$-SH as a slightly red-shift was observed in accordance with surface functionalization. Unfortunately, the surface functionalization with **1.26** was unsuccessful as the UV-VIS spectrum indicated broadening of the λ_{max}, which usually is a strong indication of aggregation. The aggregation was further substantiated by the measured hydrodynamic diameter of 100 nm and a polydispersity of 0.6 indicating a drastic increment in size and particle distribution usually associated with aggregation. The ζ-potential also confirmed that the chemisorption of **1.26** was unsuccessful as the ζ-potential value was in the same range of the citrate reduced AuNPs. It was expected that the ζ-potential would decrease in comparison to the ζ-potential of the citrate reduced AuNPs since **1.26** would provide a neutral coating. This tendency was observed for the successful coating using PEG-SH_{5000} and PNIPAM-SH_{3500} respectively (Figure 1.10).

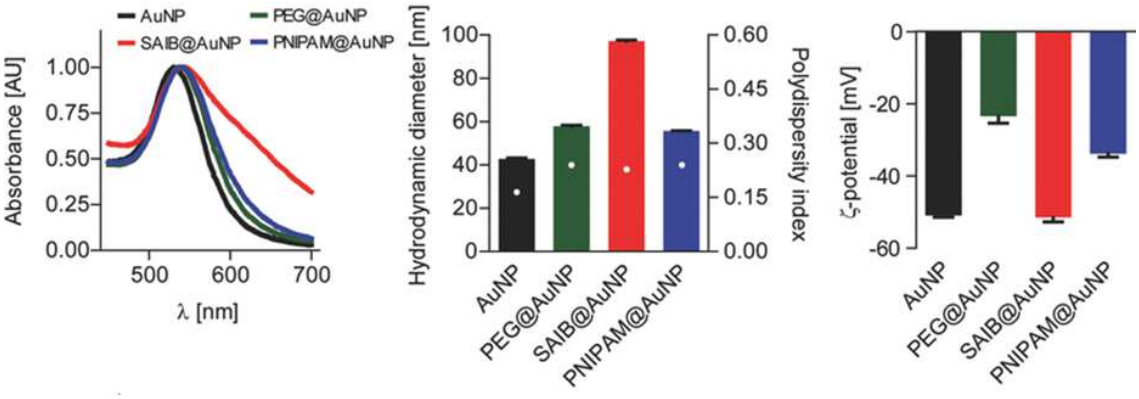

Figure 1.10: AuNPs characterization. SAIB@AuNP corresponds to **1.26**@AuNP. From left to right. UV-VIS spectrum displaying the SPR effect. DLS analysis showing the hydrodynamic diameter and ζ-potential respectively. [9].

1.12 Discussion and future perspectives

The surface functionalization of AuNPs using **1.26** could be questioned as the coating of **1.26** leads to aggregation. It could also be questioned whether **1.26** is able to exchange with citrate upon the reduction of AuNPs? Or that the packing density of **1.26** has been too low to provide a sufficient surface coverage to inhibit the Van der Waal interactions and thereby induce instability and aggregation of the AuNPs. This supports the measured ζ-potential and aggregation. The poor surface coverage could be due to the fact that the multiple ester moieties have a coordinating effect that could interact with the AuNP surface and thus result into a horizontal interaction instead of the intended anchoring of the dithiolane group leading to the monolayer assembly (Figure 1.11).

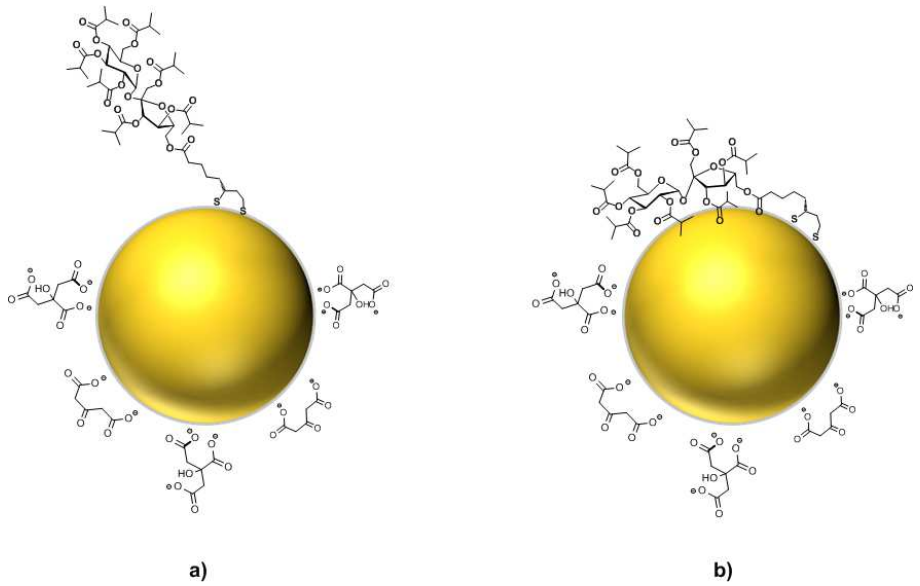

Figure 1.11: Schematic representation of types of interaction between AuNPs and **1.26**. a)Schematic representation of the intended mono-layer assembly of **1.26** using the dithiolane as anchoring group. b) Schematic representation illustrates horizontal interaction of **1.26** via carbonyl groups.

As stated, the chemisorption/ligand exchange was conducted in aqueous solution which was a sufficient solvent for the polymeric coatings of PEG_{5000}-SH and $PNIPAM_{3500}$-SH. The choice of performing the coating of AuNPs with **1.26** in aqueous solution was expected to be insufficient in regards to the solubility **1.26** in aqueous solution.
Phase transfer of citrate reduced and stabilized AuNPs to chloroform have been reported in the literature [33]. This method encompasses the use of cetrimonium bromide (CTAB) as a surfactant and the use of a highly hydrophobic dithiolane functionalized oleyl based ligand [33]. Phase transfer has been reported for AuNPs for sizes in the range between 5-70 nm. Retro-perspectively, optimization by use of a phase transfer agent in order to transfer the as-synthesized AuNPs to an organic solvent, could potentially overcome the solvent limitation of **1.26**, by which AuNPs functionalization potentially could be achieved.

In the study of Hurst *et al.* [34], the assembly of DNA onto the surface of AuNPs was analyzed as quantitation method. Likewise, it was analyzed how the assembly of DNA fragments can be improved by the presence of NaCl. The study also emphasized the importance of the length of the linker between the anchoring alkanethiol and the DNA fragment, and how this influenced the loading onto the AuNPs. The PEG spacer seemed to lead to a higher loading compared to the nucleotide-base based spacers of A_{10} and T_{10}, which could be argued to be reasoned that the bulky DNA moiety is moved further away from the particle surface by which the sterically crowding and interstrand repulsion is minimized [34].

Hill *et al* highlighted how the size and curvature of AuNPs influence surface characteristics in terms of surface coverage of AuNPs [35]. As an indirect measure of the spatial

conformation of the ligands, the deflection angle (Figure 1.12) can be used as an indirect measure of spatial space in-between ligands [35]. A bigger surface will intuitively host a larger amount of ligands. But consequently, the corresponding curvature will be less steep by which smaller deflection angles will be derived for bigger surfaces meaning that the anchoring ligands are within close proximity by which steric hindrance and repulsion can be dominating factors for the overall stability of the assembly. Higher deflection angles are related to smaller particles due to a steep curvature by which the spatial configuration is more spacious (Figure 1.13) [35].

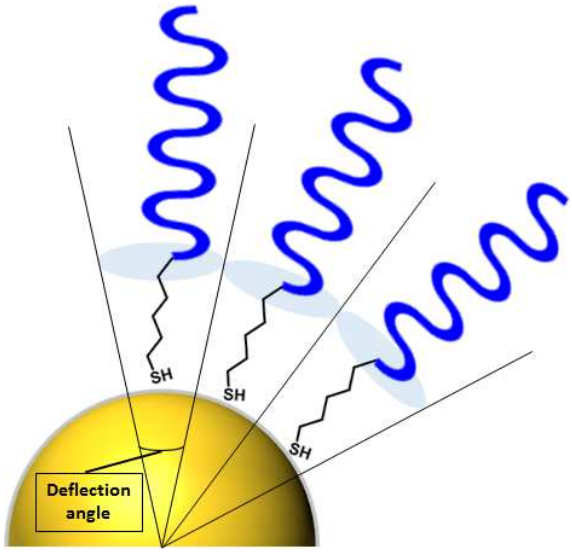

Figure 1.12: Schematic representation of the deflection angle [35].

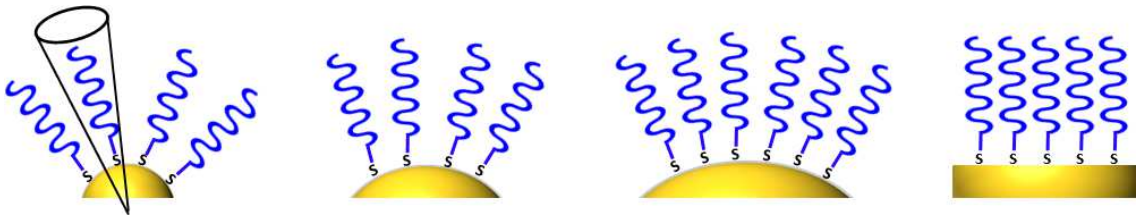

Figure 1.13: Schematic representation showing how the deflection angle varies with the surface curvature of the AuNP [36].

These ideas and theoretical deliberations could indicate the following conclusions regarding the design of **1.26**. A monolayer of **1.26** on AuNPs could supposedly be afforded, so forth a proper deflection angle is provided and the only interaction of **1.26** is via the dithiolane anchoring group and not by the SAIB moiety. A proper deflection angle would most likely be needed to assure less steric repulsion in-between the spacious inter-stranded SAIB moieties of **1.26**. Surface coverage of AuNPs with **1.26** using smaller sizes of AuNPs (higher deflection angles) would have been interesting, as this should lead to increased inter-distant space. Use of smaller sized AuNPs would risk compromising the overall contrast properties, as a higher loading of AuNPs within the SAIB formulation most likely would be needed. However, it has been reported that smaller AuNPs possess

higher X-ray attenuation [37, 38]. The use of higher concentration of AuNPs could be limited by the cytotoxicity of AuNPs at increased concentrations [15, 37].

Introducing a longer spacer between the dithiolane anchoring group and the SAIB moiety of **1.26** would afford that the SAIB moiety would have been moved further away from the AuNPs surface. This could potentially increase the spatial surroundings leading to less steric hindrance. It was decided not to continue optimizing the functionalization of AuNPs using **1.26**.

1.13 PNIPAM and PEG coated AuNPs in SAIB formulation

30 mg mL^{-1} PEG_{5000}-SH or $PNIPAM_{3500}$-SH coated AuNPs in SAIB/EtOH/PLA (75:20:5 vol%) were tested *in vitro* in MQ-H_2O at 37 °C. A significant burst release was observed of the PEG coated AuNPs while no burst release of the PNIPAM coated AuNPs was observed. The enhanced stability of PNIPAM coated AuNPs and high loading is assumed to be due to the fact that PNIPAM is more hydrophobic, but this could also be explained by the hydrogen bonding of the amide [9]. The SAIB/EtOH/PLA formulation containing the PNIPAM coated AuNPs was likewise tested *in vivo* by subcutaneous injection (using 25 G needles) in immunocompetent NMRI-mice at the upper left flank. The visualization of the injected gel is illustrated in Figure 1.14. A mean contrast in the range of 1200 HU was achieved using the PNIPAM AuNPs and the deposit was clearly visible for duration of 8 weeks using a micro-CT. The mean contrast level decreased to a level of approximately 800 HU over 8 weeks as illustrated in figure Figure 1.15. Overall, the level of contrast makes the gel suitable for 2D X-ray visualization [9].

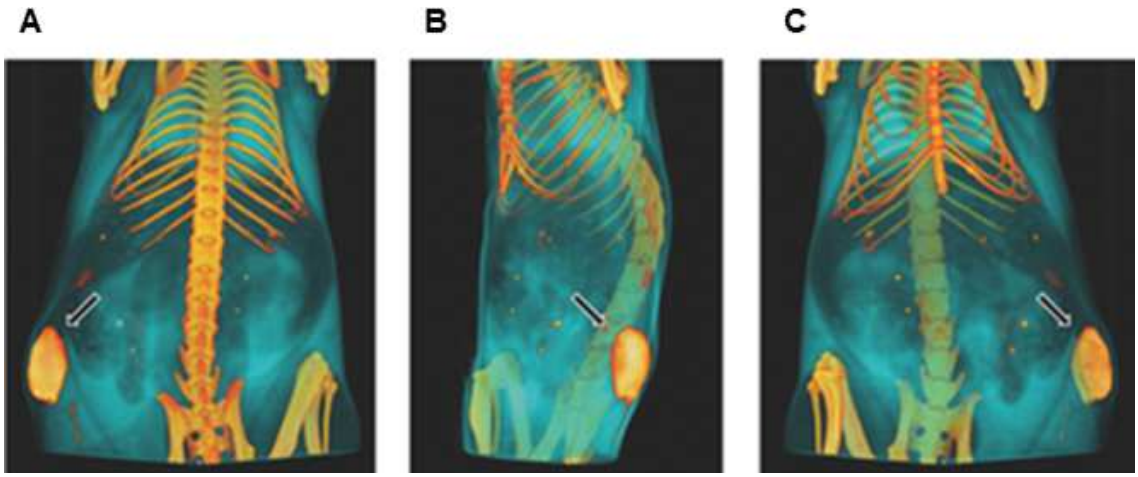

Figure 1.14: Schematic 3D reconstruction from micro-CT images of mouse. The SAIB deposit (SAIB/EtOH/PLA (75:20:5 vol%) + 30 mg PNIPAM coated AuNPs mL^{-1}) is clearly seen from different angles with similar contrast levels as the skeleton. The SAIB deposit was injected subcutaneously at the upper left flank [9].

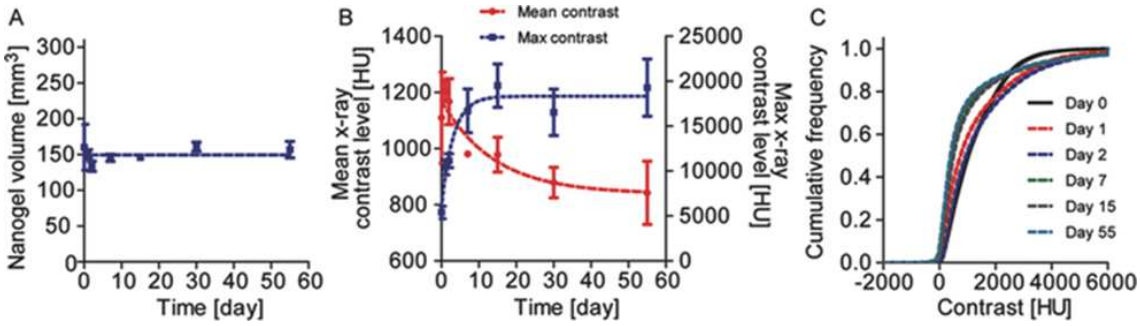

Figure 1.15: *In vivo* characteristics of SAIB formulation percutaneously inserted at the upper left flank. a) Volume of SAIB deposit followed over 8 weeks. b) Mean and maximum contrast level the SAIB deposit over 8 weeks. c) Accumulated histogram of SAIB deposit accounting for each pixel from a representative mouse over a period of 30 days [9].

Inhomogeneity was indicated in line with that the mean contrast decreased over time, which indicates instability over time. The instability was concluded to be caused by gradually aggregation of the PNIPAM coated AuNPs as previously reported for the PEG-coated AuNPs. This was further substantiated as small regions of high contrast were observed at low contrast level indicating a high local concentration of aggregated AuNPs. Due to the fact that the contrast level of SAIB formulation containing the PNIPAM coated AuNP is far above the resolutions used in clinical imaging systems by which the inhomogeneity is addressed, this inhomogeneity will not be visible within the current clinical systems used today.
In order to assure proof of concept and quality assure certain *in vivo* parameters like interstitial fluid pressure (IFP)[1] and migration ability, that are not addressed by subcutaneous injections, the SAIB formulation was injected into a male dog diagnosed intratumorally in a mast cell tumor [9].
The intratumorally injection of the radiopaque fiducial SAIB marker was tested in image-guided radiotherapy practice in order to direct the delivery of radiation doses according to the position [9]. The recorded images are illustrated in figure Figure 1.16

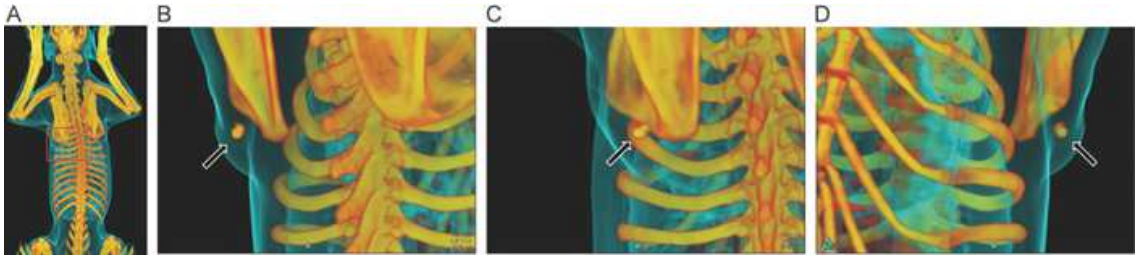

Figure 1.16: Schematic 3D reconstruction from micro-CT images of canine patient injected with the SAIB formulation (SAIB/EtOH/PLA (75:20:5 vol%) + 30 mg PNIPAM coated AuNPs mL^{-1}). The deposit was injected intratumorally into an intermediate-grade mast cell tumor. a) Full-body scan of canine, b-d) Visualization of SAIB deposit viewed from different angles [9].

[1]IFP may influence the intratumoral injectablity.

From the recorded images during this radiotherapy treatment, it was concluded that the SAIB formulation remained persistent in volume and retained the same position as the tumor indicating no migration despite the canine induced mechanical stress upon the gel formulation. The gel showed same morphology during four fractions of 6 Gy indicating that the gel seemed unaffected by the radiation.

1.14 Conclusion

Two liquid radiopaque fiducial markers were developed based on the SAIB gelation matrix and AuNPs. The coating of the AuNPs was decisive for the overall stability within the SAIB formulation. Higher AuNPs concentration and improved stability were obtainable using the $PNIPAM_{3500}$-SH compared to the PEG_{5000}-SH. Coating using **1.26** was unsuccessful. The fiducial marker was easily injected in mice and a male dog with a solid mast tumor using 25 gauge hypodermic needles. The contrast level of the developed fiducial marker was approximately 1200 HU with a decrease to a level of 800 HU over 8 weeks according to the *in vivo* studies. The inhomogeneity of the gel was concluded to be due to aggregation of AuNPs.

1.15 Iodine based SAIB derivative for IGRT

Contrary to the AuNPs based SAIB formulation developed in chapter 1, it was decided within the Nanoguide-project to see if the level of contrast and homogeneity could be enhanced by developing an iodine-based contrast derivative. Iodide derivatives are widely used as CT-agents due to the attractive X-ray attenuation coefficients [].
A common trend for the iodine-based contrast agents used today is the use of the 2,4,6-triiodoaryl moiety. This is used, because it introduces three iodide atoms with relatively stable carbon-iodide bonds. Examples where this core structure have been used are iohexol **1.29**, diatrizoic acid **1.30**, iopromide **1.31** and metrizamide **1.32** among many others. Iodide based contrast agents are further highlighted in chapter 3.

1.15.1 BioXmark

In the Nanoguide project it was decided that a triiodophenol SAIB derivative (TIP-SAIB) could be synthesized from the similar synthetic strategy, outlined in section 1.8, used in the synthesis of **1.26**. TIP-SAIB **1.33** was synthesized by other project partners (Scheme 1.8). The diol **1.34** could be obtained by TBDPS protection of sucrose **1.3** affording **1.9**, followed by isobutyrylation to **1.35** and TBDPS-deprotection affording **1.34**. This was conducted in a 51% yield over three steps. The 2-(2,4,6-triiodophenoxy)-acetic acid **1.36** was made from the reaction of 2,4,6-triiodophenol **1.37** and *tert*-butyl 2-bromoacetate followed by acidic hydrolysis of the *tert*-butyl ester affording the acid **1.36** in 85% over two steps. Conjugation to the SAIB diol **1.34** was mediated through standard ester coupling by activation of **1.36** using EDC·HCl and DMAP providing **1.33** in 83% yield.

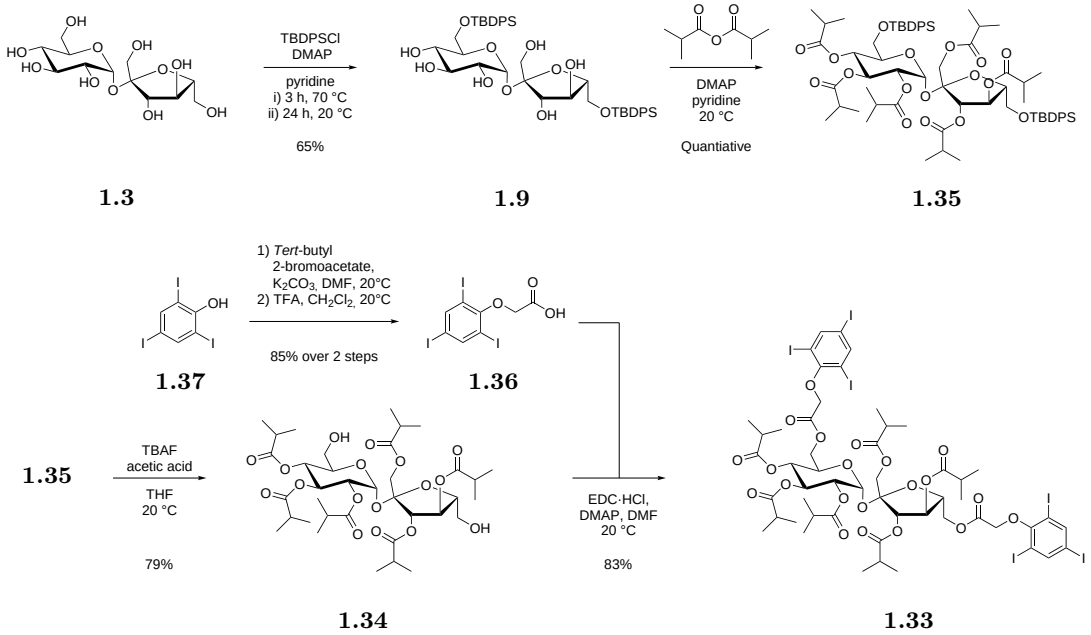

Scheme 1.8: The scheme for the synthesis of **1.33** [39].

1.15.2 BioXmark as fiducial marker in lung cancer

The visibility of TIP-SAIB **1.33** was determined and compared to the current standard of solid markers used in clinics [40]. Four different concentrations were tested, where the highest concentration of the BioXmark formulation showed comparable radiopacity to the standards used today. The quality of CT-images was improved, since less CT-artifacts were reported. The artifacts from BioXmark was though more pronounced accordingly to the difference in physical size [40].
The *in vivo* stability of BioXmark was tested during radiotherapy as a liquid fiducial marker for locally advanced non small cell lung cancer in patients. The formulation of **1.33** was readily inserted using 25G hypodermic needles. Variations of the BioXmark deposit diverging from the gross target volume (GTV) was evaluated during inter-fractional radiotherapy. The BioXmark deposit displayed a mean contrast of 991 ± 219 HU. The volume of the BioXmark deposit decreased to a level of 24% relative to the initial deposit. The relative deviation in distance (3D vector) between the GTV and BioXmark deposit was reported to be -1.5±2.3 mm. The clarification of these characteristics are further elaborated in [40, 41].

Injectable fiducials for pre-operative localization of tumors in breast cancer

2

With the increasing quality of mammographic imaging and the introduction of screenings, non-palpable tumors in breast cancer are detected to a much higher degree and in an earlier stage [42–44]. Almost one fourth of all breast lesions today are detected as non-palpable [45]. With the identification of the non-palpable tumors in the early stages and the use of neoadjuvant systemic therapy, breast conserving treatments like lumpectomy have become an attractive option compared to mastectomy [42]. Combined lumpectomy and external radiotherapy as treatment, elaborated in the context of long-term survival, shows similar survival rates when compared to mastectomy [46]. Despite this attractive future prospective of survival rates, the number of recurrences in lumpectomy are reported higher than in mastectomy [46]. This drawback is related to the complexity of the excision procedure of non-palpable tumors, which is highly dependent on accurate target delineation (prelocalization) needed for surgical guidance [42, 43]. This has highlighted the need for improved pre-operative image-guided localization for surgical guidance, in order to lower the number of resections and recurrence rates [42, 47]. The underlying main criteria to improve the quality of lumpectomy will be that the specimen is excised at the interface between healthy and malignant tissue with an additional margin to provide a negative margin [44]. A positive margin is defined as tumor tissue present at the boundary-site (colored with ink) by the Society of Surgical Oncology and American Society for Radiation Oncology (SSO-ASTRO) [46]. Adequate margins are therefore added from the site of the positive margin in order to remove tissue with chance of microscopic spread of cancer [**?**]. This requisite of a negative margin is emphasized since recurrences of malignant tissue is related to positive margins [46]. The margins reported in many cases are in-sufficient, as margins today are reported positive in up to 50% of the cases [44]. The outcome of the lumpectomy rely to a great extent on the pre-operative image guided localization which is conducted as surgical guidance so the surgeon will locate the non-palpable lesion for excision. The pre-operative image guided localization is conducted in accordance to the preceding mammographic images [44].

The current technologies used in clinical routines today for preoperative localization are wire-guided localization (WGL), radioactive occult lesion localization (ROLL) and radioactive seed localization (RSL).

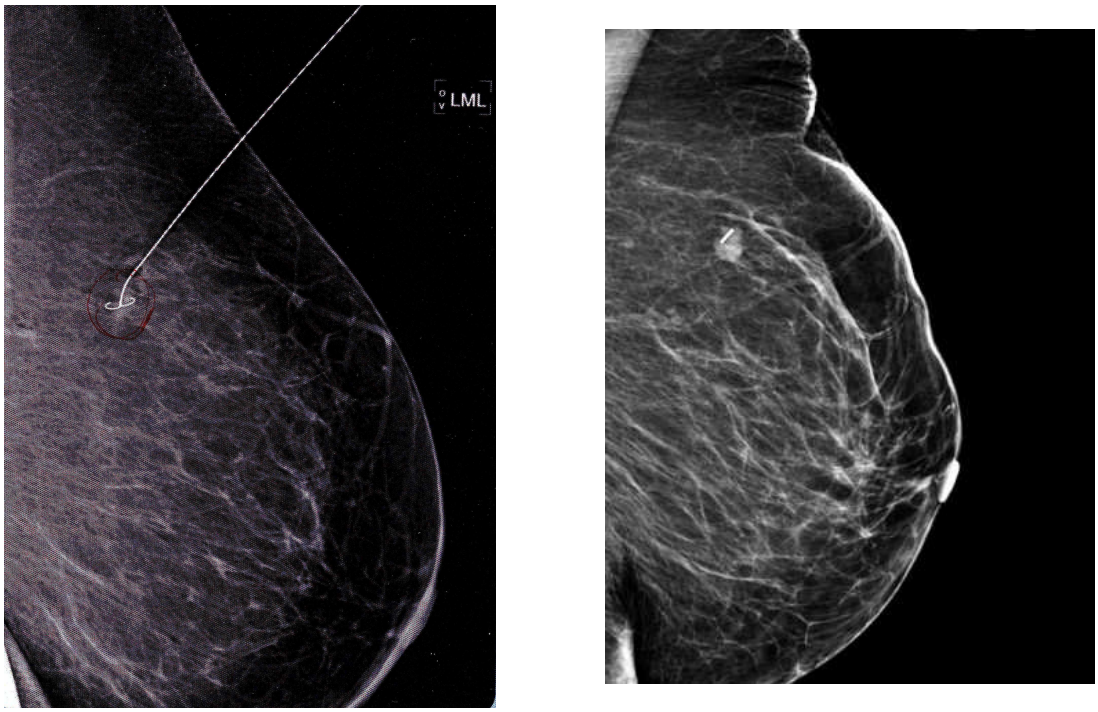

Figure 2.2: Mammographic image confirming the insertion of the pre-operative localization using a radioactive seed [48].

WGL has been the gold standard for many years and encompasses a hooked wire, which is inserted in the breast with the terminal point of the hooked wire pointing towards the tumor localization (Figure 2.1) [44]. WGL was introduced by Dodd *et al.* [49]. WGL have, beside the high rate of positive margins (13-58%) a number of other limitations [42, 43]. The overall procedure of WGL requires first of all the localization of the tumor followed by the insertion of the wire, which is conducted by a radiologist. The surgical removal is then conducted subsequently by the surgeon accordingly to the pre-localization performed by the radiologist . Logistically, this usually turns out to be problematic, as the surgery is not carried out immediately after the WGL. This can cause a number of difficulties e.g. the inserted wire have to be maintained in the correct position until surgery [44, 47, 50]. Additionally, the WGL conducted by the radiologist may not be in accordance with the preferred incision point of the surgeon to achieve the best cosmetic outcome. Other issues encountered are wire misplacement or transection of the wire [50]. In terms of patient compliance, WGL is perceived as unpleasant, painful and in some cases traumatic to patients [42, 44]. The high rate of reported positive margins and the above-mentioned drawbacks of using WGL has led to the search of alternative methods like ROLL and RSL with the hope of potentially reducing the number of positive margins [43].

ROLL was first reported by Luini *et al.* at the European Institute of Oncology (Figure 2.3) [51, 52]. The technology uses ^{99m}Tc labeled colloidal albumin particles, which are injected intratumorally. The pre-operative localization is confirmed from the corresponding gamma-probe trace of the gamma-emitting ^{99m}Tc. ROLL has been reported to be easier to perform by the radiologist and surgeons with less severe pain to patients [44]. ^{99m}Tc labeled colloidal albumin particles are also used in the standard procedure of sentinel lymph node (SLN) mapping and the corresponding biopsy (Figure 2.4).

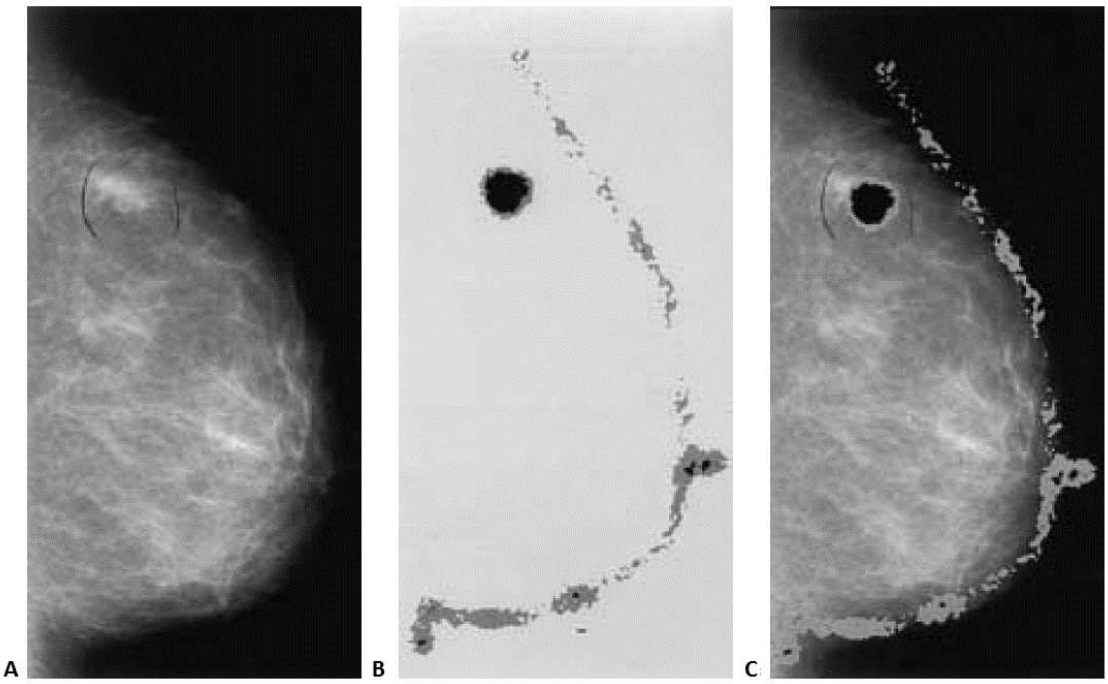

Figure 2.3: Imaging using ROLL, a) Preceding mammographic imaging, b) Lateral scintigraphic imaging upon injection of ^{99m}Tc and c) overlay of images a and b [52].

ROLL uses the same source of identification as in SLN mapping, which have been stated to be advantageous or disadvantageous depending on the study [54].

One advantage of ROLL would be that surgeons are already experienced in using ^{99m}Tc for the SLN mapping, and biopsy, moreover only one type of injection is needed. A major drawback of ROLL is that the insertion of ^{99m}Tc cannot be post-confirmed by mammographic imaging (ROLL is visible using scintigraphic imaging) as opposed to RSL where the seed is clearly visible (described below) [43].

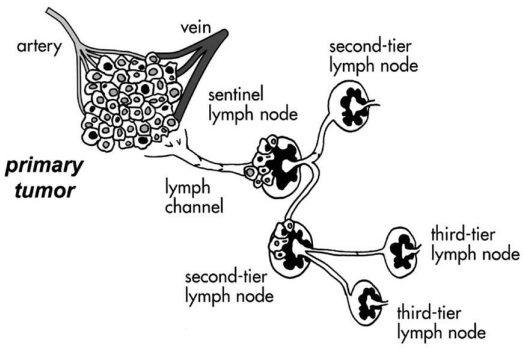

Figure 2.4: schematic representation of the sentinel lymph node [53]

Another limitation of ROLL as a reference point of radioactivity is the diffusive behavior of ^{99m}Tc labeled colloidal albumin particles into the surrounding tumor tissue from the insertion point [42, 44]. This is a consequence of the ability of the small-sized ^{99m}Tc labeled albumin particles to penetrate into the surrounding tissue by diffusion [43]. Due to the diffusive tendency healthy tissue might be recognized as tumor tissue by which unnecessary tissue is excised during the lumpectomy.

The half-life of ^{99m}Tc (6 h) makes the time-frame for surgery short from the time of injection [47, 50]. Intratumoral injections are additionally not preferable according to the absence of lymphatic system within the tumor and the high intratumorally pressure. [54, 55]. Intratumorally injections is confined by the high interstitial fluid pressure in tumors, making injections difficult [9].

In RSL, a radioactive seed coated with radioactive iodide ^{125}I (typical dimensions 0.8 x 4.5 mm) is used with an activity ranging from 3.7 to 10.7 MBq [56]. The seed is percutaneously implanted using 18 G needles in the non-palpable lesion (Figure 2.5) [44, 56]. RSL was first presented by Gray *et al.* [57]. The position of the specimen for excision is given by the gamma probe signal intensity (Figure 2.5) [50].

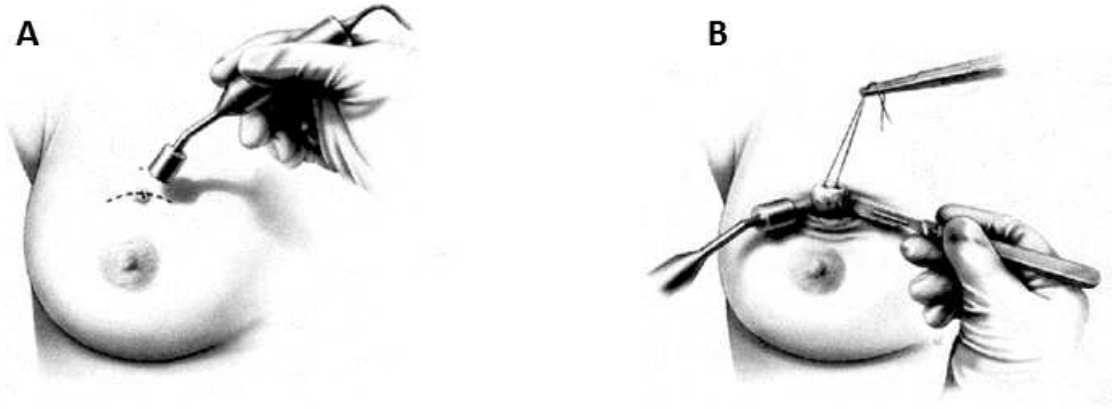

Figure 2.5: Schematic illustration of a) the detection of the radioactive seed by a gamma probe and b) the guided lumpectomy using guidance from the radioactive seed [58]

RSL have been attractive logistically owing to the half-life of ^{125}I (60 days). This enables the opportunity that the radioactive seed can be inserted up to 5 days before surgery, which provides flexibility in surgery planning [50, 59]. Advantageously, the seed can be post-confirmed upon insertion by mammographic imaging [43]. RSL in combination with SLN mapping render possible a dual trace system where both sources are gamma-emitting. They are differentiable as the emission energies are different (^{125}I, 30 KeV, ^{99m}Tc 140 KeV). The study of Pouw *et al.* illustrated the combinatorial use of ^{125}I coated seeds together with the ^{99m}Tc labeled particles [45, 48]. This study indicated that the use of high activity ^{99m}Tc (100 MBq, corresponding to a one-day protocol by which the patient proceeds directly to surgery) can lead to considerable emission energies that will be detectable within the detection window of the ^{125}I emissions due to Compton scattering. A potential limitation of RSL have been concerned migration of the inserted seed. Though, it has been reported that clinically seed migration has been observed in less than 1% of the patients [43, 50]. As RSL is a rather new methodology compared to WGL, it is still within the process of implementation which require training and handling of radioactive material as well as safe disposal.

Overall clinically, when comparing the different technologies in terms of clinical performances, ROLL and RSL have been reported to lower the rate of positive margins and resections in randomized studies [42,47]. In the study of Gray *et al.*, the number of patients in need of additional resections was reported lower for RSL than for WGL [57]. Most studies indicate no significant difference (in margins) on the number of positive margins between WGL and RSL or ROLL though [44, 46, 47, 60, 61]. No significant differences in

terms of positive margins and re-excisions were found when comparing ROLL to RSL [43]. It has been stated in several studies that using radioactive tracers as reference for the localization facilitates reorientation and real-time feedback for the surgeon in regards of localization [**?**, 56]. This allow for a better assurance that the entire lesion is removed as intended [**?**].
In terms of patient compliance and logistics, RSL have been superior compared to WGL and ROLL [43]. In a study regarding patient compliance, less severe pain and improved convenience were deduced by patients treated with RSL compared with patients treated with WGL [60].

2.0.3 Problem statement

Taking the unique gelation properties of the SAIB formulation into account (section 1.6), the potential application as a tissue marker for surgical guidance of non-palpable lesions in breast cancer was devised. The aim of this project was therefore to develop a liquid radioactive fiducial tissue marker - based on SAIB - that will function as a radioactive seed and will be injectable using hypodermic needles.
To develop a radioactive fiducial tissue marker for surgical guidance of non-palpable tumors in breast cancer, a radioactive source have to be associated with the tissue marker. As radioactive source, it was decided to develop a radioiodinated SAIB derivative that will provide the radioactive point source. Deriving a SAIB precursor for radioiodination will offer that all attractive isotopes of iodide can be used like the positron emitting isotope ^{124}I ($\tau_{1/2}$ = 4.2 days) - enabling e.g. CT/PET imaging in combination with the developed TIP-SAIB **1.33** derivative - or the gamma-emitting isotopes of ^{123}I ($\tau_{1/2}$ = 13.2 h) or ^{125}I ($\tau_{1/2}$ = 60 days), or the beta-emitting isotope ^{131}I ($\tau_{1/2}$ = 8 days). Additionally, the radioactivity of the developed tissue marker can be custom-made to the given application as this is given by the concentration of the radiolabeled SAIB derivative.
It was decided that the developed radioactive fiducial tissue marker should be based on TIP-SAIB **1.33** reasoned its unique contrast properties and its use as injectable radiopaque fiducial marker within IGRT of lung cancer patients [40, 41]. The use of **1.33** will benefit visualization by CT imaging as well as biodegradability and biocompatibility and easy percutaneous insertion using hypodermic needles. Combining **1.33** with a radioiodinated SAIB derivative will render the novel injectable seed which will be applicable as a tissue marker for surgical guidance of non-palpable tumors.

Such a radioactive fiducial tissue marker could potentially also find use within the field of brachytherapy (BT) as similar seeds used in RSL are employed in BT for therapeutic treatment in various type of cancers mainly prostate and cervix cancer [].

2.1 Design and theoretical deliberations

Building on the already established experience of synthesizing SAIB derivatives, it was envisioned that the radiolabeled SAIB derivative of interest can be synthesized in accordance to the synthetic strategies highlighted in section 1.8. As described in the introduction, the ^{125}I isotope is attractive due to its half-life (60 days). The limitation of

using radioactive isotopes of iodide, is the issue regarding up-take of iodide in the thyroid gland. Considerable uptake in thyroid gland of radioactive iodide is a potential adverse side effect. The extent of uptake will have to be evaluated. The requirement would therefore be a long term stable iodinated SAIB derivative that will not undergo deiodination. As a placeholder and directing group for regioselective iodinations, activated trimethylsilyl (TMS) aryl moieties have been used in multiple studies [62]. This is further elucidated in following section 2.2.

2.2 The β-cationic effect of trimethylsilanes in electrophilic substitutions

The following section describe the *ipso*-substitution of trimethylsilyl (TMS) aryl moieties and the β-cationic effect. The following section is based on the review of Chan [63].

Silanes is usually referred to as super - or a big proton []. It is considered as a hard electrophile that forms strong bonds with hard nucleophiles (flouride, oxygen, chloride) []. The C-Si bond is considered more polarized than the C-H bond [63].
Aryl-TMS moieties are known to undergo electrophilic aromatic *ipso*-substitution (Scheme 2.1).

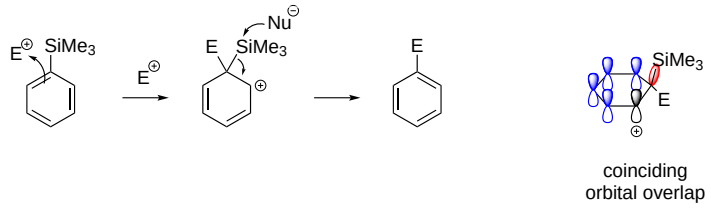

Scheme 2.1: The electrophilic aromatic *ipso*-substitution of aryl-TMS. Scheme adapted from [64].

Beside the intended *ipso*-substitution of the TMS group, the competing substitution of hydrogen in accordance to the substitution pattern (activated vs de-activated) of the given aryl-TMS is a possibility [**?**]. The reason *ipso*-substitution is typically favored can be explained by the stabilized carbocation formed, as depicted in Scheme 2.1. The electrophilic addition to the *ipso*-carbon takes place so the orientation of the formed empty p-orbital in the β-position is in alignment with the C-Si σ-binding orbital. This coinciding overlap of the empty p-orbital and C-Si σ-binding orbital induces an inductive effective to the bonding electrons of C-Si σ-bond, which leave the C-Si bond weakened. The electrophilicty of $(CH_3)_3Si$- is likewise increased and makes it prone to nucleophilic attack. This is known as the β-cation stabilizing effect. This electrophilic aromatic substitution is completed as the TMS group is eliminated in the presence of weak nucleophile by which the aromaticity is regained. The electrophilic aromatic *ipso*-substitution is more prone to undergo reaction in activated arene systems.
It should be mentioned that another β-cation can be formed which would correspond to the β-cation when electrophilic substitution occurs in the *meta*-position in regard to aryl silane (*meta*-directing, Scheme 2.2).

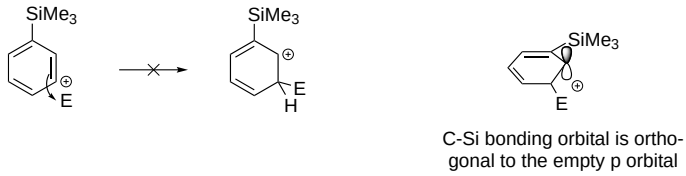

Scheme 2.2: The non *meta*-directing effect of aryl-TMS. Scheme adapted from [64].

In this case, the C-Si bond remains sp^2 hybridized and thereby in the plane of the aromatic system and perpendicular to the empty p orbital. In this case, no overlap is possible which explains why aryl silanes are not *meta*-directing. The β-cationic effect is also observed in case of vinylic, allylic and alkynylic TMS compounds.

2.3 Synthesis of SAIB-based precursor for radioiodination

.

As the prototype to establish proof of concept, it was inferred that the SAIB precursor for radioiodinations could be obtained from the intermediate **1.25**, used in section 1.10, and 2-(*p*-TMS-phenoxy)-acetic acid **2.1** (Scheme 2.3).

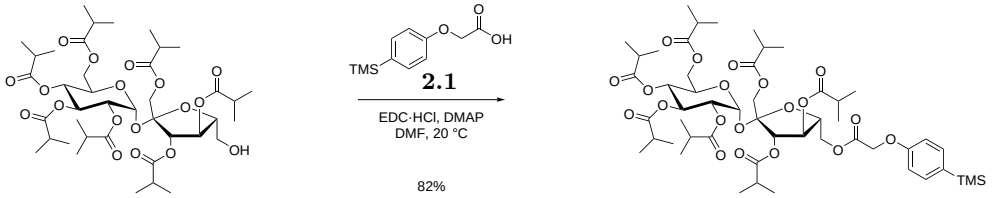

1.25 **2.2**

Scheme 2.3: The scheme for the synthesis of precursor **2.2**.

2-(*p*-TMS-phenoxy)acetic acid **2.1** was obtained in three steps starting from *p*-bromophenol **2.3** (Scheme 2.4).

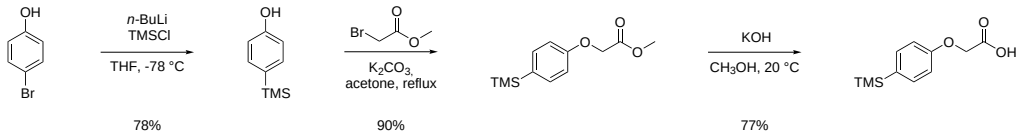

2.3 **2.4** **2.5** **2.1**

Scheme 2.4: The scheme for the synthesis of 2-(*p*-TMS-phenoxy)acetic acid **2.1**.

Metal-halogen exchange of the bromide of **2.3** using *n*-BuLi followed by addition of TMSCl afforded *p*-TMS-phenol **2.4** in 78% yield. The phenol was *O*-alkylated using methyl bromoacetate and K_2CO_3 giving **2.5** in 90% yield. The methyl ester of **2.5** was subsequently

hydrolyzed under basic conditions using KOH in CH_3OH. The potassium carboxylate was carefully neutralized using dilute HCl to avoid protodesilylation. This afforded the acid **2.1** in 70% yield. Standard ester coupling using EDC·HCl and DMAP gave the TMS derived SAIB derivative **2.2** in 82% yield.

Different iodination conditions were tested on **2.5** as a model system. The iodinations conditions applied were: 1) thallation using $Tl(OOCCF_3)_3$ followed by NaI ligand exchange, 2) iodine monochloride (ICl), 3) *N*-iodosuccinimde (NIS) together with trimethylsilyl trifluoromethanesulfonate (TMSOTf) and 4) chloramine T oxidation of NaI. The iodination conditions and corresponding results are shown in Table 2.1.

Table 2.1: Iodinations of **2.5**.

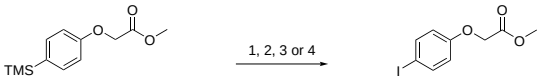

2.5 **2.6**

Entry	Reagents	Solvent	Temperature	Yield
1	$Tl(OOCCF_3)_3$, NaI	TFA/CH_3CN (3:7 v/v)	20 °C	90%[1]
2	ICl	CH_2Cl_2	0 °C	77%[2]
3	NIS, TMSOTf	CH_2Cl_2	20 °C	82%[2]
4	Chloramine T, NaI	DMF	20 °C	70%[2]

[1] Yield estimated by ^{1}H-NMR.
[2] Isolated by dry column vacuum chromatography.

Thallation followed by ligand exchange with NaI yielded the iodinated product **2.6** as a crude with a purity of >90%. As a reference reaction to the other iodination methods and to assure the reactivity of **2.5**, the direct source of the iodonium ion was applied by the use of ICl to **2.5** and gave the iodinated product **2.6** in good yield (77%). Iodination conducted using NIS and TMSOTf likewise afforded the iodinated product **2.6** in an isolated yield of 82%. Chloramine T oxidation of NaI yielded the iodinated product **2.6** in decent yield (70%).

As all iodination conditions tested gave promising yields, **2.2** was subjected to the same conditions (Table 2.2).
All iodination reactions tested beside the CAT oxidation of NaI provided the iodinated SAIB derivative **2.7**, in good isolated yields (Scheme 2.5). As CAT generates ICl *in situ* and due to the fact the iodination occurred upon treatment with ICl, this could indicate that the oxidation did not take place as planned.

Table 2.2: Iodinations of **2.2**.

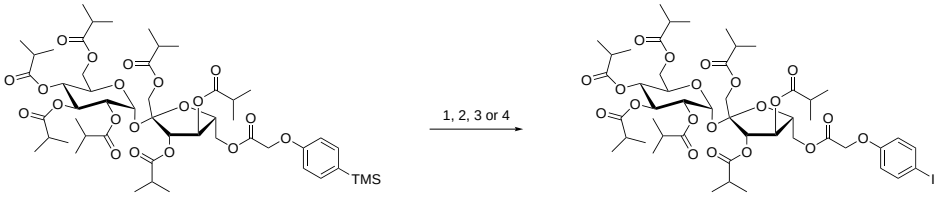

2.2 **2.7**

Entry	Reagents	Solvent	Temperature	Yield[1]
1	$Tl(OOCCF_3)_3$, NaI	TFA/CH_3CN (3:7 v/v)	20 °C	97%
2	ICl	CH_2Cl_2	0 °C	93%
3	NIS, TMSOTf	CH_2Cl_2	20 °C	81%
4	Chloramine T, NaI	DMF	20 °C	-

[1] Isolated by dry column vacuum chromatography.

2.4 Radioiodination of SAIB precursor

From the preliminary iodinations performed, it was decided to perform the radioiodination of **2.2** using $Tl(OOCCF_3)_3$ followed by ligand exchange with NaI (Scheme 2.5). The radioiodination was conducted by other project members of the Nanoguide project.

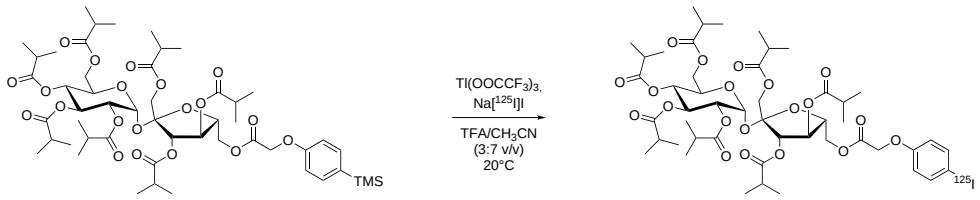

2.2 **[^{125}I]- 2.7**

Scheme 2.5: The radioiodination of **2.2** using $Tl(OOCCF_3)_3$.

The choice of $Tl(OOCCF_3)_3$ as iodination reagent was, despite the toxicity, owed to the mild conditions of the thallation and the experience within the group of Mads Clausen using $Tl(OOCCF_3)_3$ [62]. Moreover, since the commercially available source of radioactive iodine is NaI, it can be directly used with the thallated intermediate without any preceding transformations and proceeds under carrier free conditions. The iodination was designed to ensure no thallated intermediates would be part of the radioiodinated product **[^{125}I]-2.7**. The radioactive iodide was therefore first allowed to react with the thallated intermediate before excess of non-radioactive iodine was added. Surprisingly,

it was observed that 90% of the radioactivity was incorporated in the SAIB derivative **[^{125}I]-2.7** within a reaction time of 15 min, before addition of non-radioactive NaI. According to the study of Mckillop *et al.* and the previous experience with iodinations by thallation in the group, this was at first thought a bit surprising as the iodide is believed to enter the reaction in two equivalents upon the formation of aryl-Tl(OOCCF$_3$)$_2$ to prompt the ligand exchange [62, 65]. Subsequently, the 'reductive elimination like' reaction yields the aryl iodide together with Tl(I)-I. In accordance with this reaction pattern, the maximum radiochemical yield is 50%, which is not in agreement with the observed >90% yield. Mckillop *et al.* also reported the observation when using the iodide in trace amount or < 1 equiv. Under these conditions the aryl iodide was also found in nearly quantitative yields. It was proposed by McKillop *et al.*, that the unstable aryl-Tl(III)-I-(OOCCF$_3$) intermediate is formed leading to the aryl-iodide together with Tl(I)-(OOCCF$_3$). Following addition of non-radioactive NaI and SEP-PAK cartridge purification, **[^{125}I]-2.7** was isolated in a radiochemical yield of 83%. All fractions from the SEP-PAK cartridge purification was analyzed by ICP-EOS measurements. No traces of thallium was found in the fractions of **[^{125}I]-2.7**. All thallium used (>98%) in the radiolabeling was pre-eluted using aq. diethylenetriaminepentaacetic acid (DTPA) prior to the elution of **[^{125}I]-2.7**.

2.4.1 *In vivo* performance of [^{125}I]-2.7

The combined formulation of **[^{125}I]-2.7** and **1.33** was tested *in vivo* using an NMRI-mice model. This study was conducted by other project partners of the Nanoguide-project. A deposit of the gel-like implant, corresponding to a 50 μL percutaneous injection (27 G hypodermic needles) was inserted in the right flank of the NMRI-mice. CT images of the gel-like implant was recorded at 1, 24 and 168 h respectively, and the ^{125}I-biodistribution analysis was obtained by well-counting of the deposit as well of the tissues/organs of interest. From the recorded CT-images recorded afer 1 h, 24 h, and 168 h respectively, the implant is clearly visible displaying a contrast level >1500 HU (Figure 2.6).

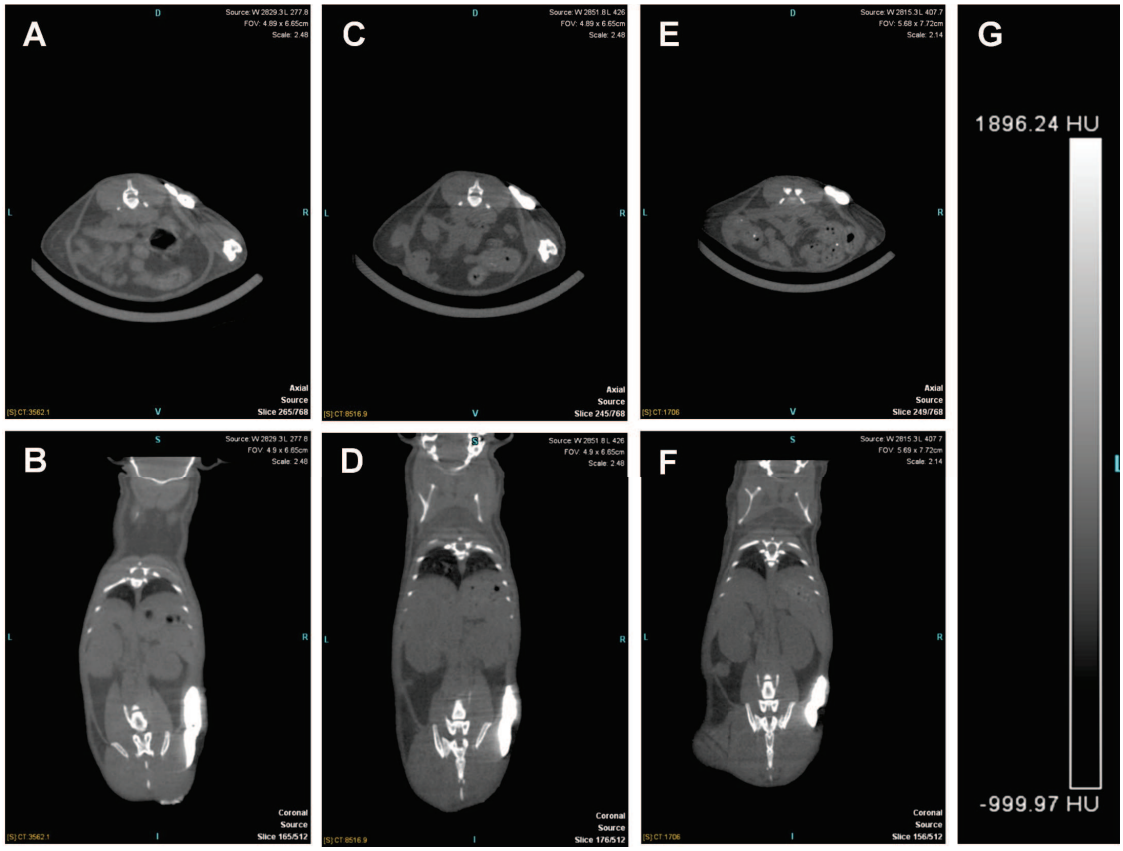

Figure 2.6: CT images recorded after 1 h (A and B), 24 h (C and D) and 168 h (E and F) respectively of the combined formulation of **[^{125}I]-2.7** and **1.33** percutaneously injected in NMRI mice. The CT images was recorded from two different angles, axial (A, C and E) and coronal (B, D and F). The scale bar in G indicates contrast in hounsfield units (HU).

Beside the expected reduction in volume of the gel-like implant, which was in accordance to previously observed experiments when using **1.33** in SAIB, the volume of the implant remained stable within the time-frame analyzed of 168 h (Figure 2.7).

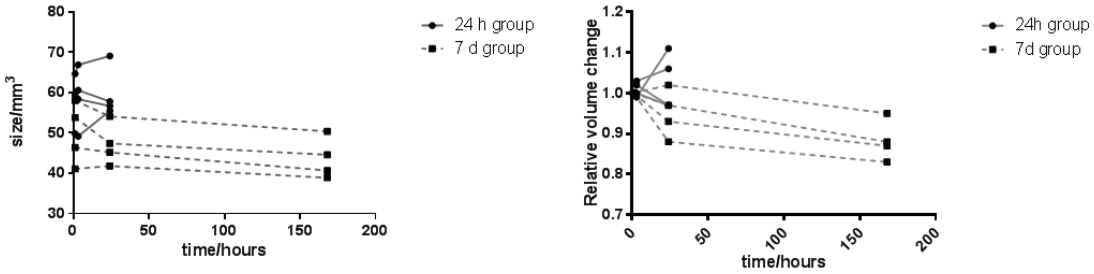

Figure 2.7: Volume changes over time.

The ^{125}I-seeds used in clinic today consist of a ^{125}I-coated silver wire which is encapsulated within a titanium shell []. This type of system is considered as a closed radioactive

source [58]. Since **[^{125}I]-2.7** can be considered as an open radioactive source by which accumulation in other tissue could occur e.g. the thyroid gland, the accumulation of ^{125}I in vital organs and tissue was evaluated. Well-counting of the different tissues/organs as well as the gel-implant elucidated the extent of the ^{125}I-biodistribution (Figure 2.8).

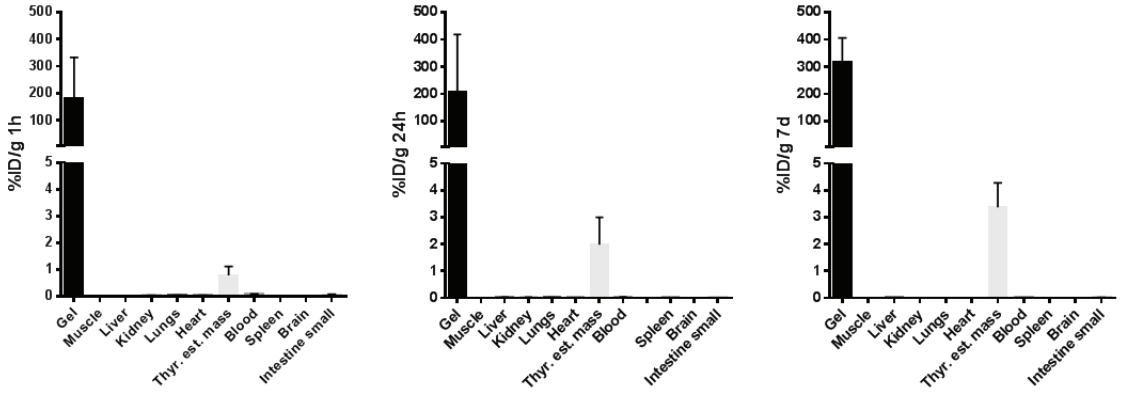

Figure 2.8: Biodistribution of ^{125}I in organs and tissues of interest measured by well-counting (not decay corrected). The activities were measured at 1 h, 24 h and 168 h respectively. The measured activities are standardized as % of injected dose per gram tissue/organ (%ID/g) at the ordinate.

As observed in Figure 2.8, the activity remained within the gel-implant. As expected, the only significant uptake of ^{125}I-activity was seen in the thyroid-gland. An increment from 1% ID·g^{-1} after 1 h to a final level of 3.5% ID·g^{-1} after 7 days was observed. For the other tissues/organs analyzed, insignificant activities less than $7{\cdot}10^4$ CPM[1]·g^{-1} (compared to gel deposit of $2{\cdot}10^8$ CPM·g^{-1}) was observed after 24 h (data not shown). These activity levels decreased to trace levels ($< 1{\cdot}10^5$ CPM·g^{-1}) after 168 h. This could indicate that the radioactivity in theses tissues either gets cleared from the body or explains the increased accumulation in the thyroid gland.

To ensure the suitability of the developed tissue marker for surgical guidance in breast cancer patients, a dosimetric extrapolation was calculated for human patients, based on the observed bio-distribution found in mice. The dosimetric calculation was based on the cumulative absorbed dose from the gel its self (as a point source) plus the absorbed dose as a result of the biodistribution after 7 days. The model and other assumptions for the calculated dosimetry are further elaborated in the attached draft. The weighted effective dose (mSv·MBq) for the different tissues/organs are found in Table 2.3
From the above-listed weighted effective dose in Table 2.3 estimated for human patients, the combined formulation of **[^{125}I]-2.7** and **1.33** seems as a promising candidate as a novel tissue marker for surgical guidance in breast cancer.

[1]CPM: Counts Per Minute

Table 2.3: The weighted absorbed dose for the organs/tissues of interest and the effective dose in mSv·MBq^{-1}.

Tissue/Organ	Weighted effective dose (mSv·MBq^{-1})
Gel-Implant	$5.91 \cdot 10^{-1}$
Thyroid	$4.15 \cdot 10^{-2}$
Brain	$4.58 \cdot 10^{-6}$
Lungs	$1.07 \cdot 10^{-2}$
Heart	$4.88 \cdot 10^{-3}$
Liver	$5.35 \cdot 10^{-4}$
Spleen	$8.70 \cdot 10^{-5}$
Kidneys	$1.42 \cdot 10^{-5}$
Intestine	$4.78 \cdot 10^{-6}$
Muscle	$1.00 \cdot 10^{-4}$
Effective dose Equivalent (EDE)	1.84
Effective dose	$6.56 \cdot 10^{-1}$

2.5 TMS-BioXmark

Based on the convincing results of **1.33** as radiopaque fiducial marker for IGRT together with the promising results of **[^{125}I]-2.7** formulated in the TIP-SAIB formulation, it was desirable to develop a TMS derivative of **1.33** that upon radioiodination will be identical to **1.33**. As BioXmark has been authorized for clinical use as a medical device by the Danish Health Authority, the ^{125}I-labeled BioXmark **[^{125}I]-1.33** could add-on application within the field of surgical guidance and brachytherapy. It would likewise enable biodistribution and stability studies of **1.33**.

The challenging moiety to construct synthetically, would be the core structure of diiodo-TMS-phenol. The positioning of the TMS, whether it would be positioned in the *ortho* or *para*-position was thought at this stage not to be decisive for the outcome of the radioiodination. The synthetic challenge would be to introduce TMS without compromising the already installed iodides. Having the *p*-TMS-phenol building block **2.4**, used in the development of **[^{125}I]-2.7**, it was considered that the iodides could be installed by regioselective electrophilic aromatic iodination or *ortho*-lithiation.
In the case of *ortho*-lithiation, a directing group would have to be introduced to **2.4** as

a handle that upon the installation of the iodides in the *ortho*-positions is readily removed.

2.5.1 Electrophilic aromatic iodination

Electrophilic aromatic bromination of the activated *m*-TMS-anisole and *m*-TMS-phenol have been reported to take place in the corresponding *para* or *ortho*-positions with preservation of the TMS-group [63, 66].
For the electrophilic aromatic iodination of **2.4**, it was devised that with the formation of the corresponding phenoxide of **2.4**, the nucleophilicity of the *ortho*-positions could be improved and thereby circumvent the competing *ipso*-substitution of the TMS-moiety. Treatment of **2.4** with KOH and NIS and TMSOTf in a mixture of CH_3CN and H_2O led to a mixture of mono, di and tri-iodinations including *ipso*-substitution, thus without preservation of the TMS-group. Deprotonation by NaH in THF followed by iodination using NIS and TMSOTf was likewise tested but without any signs of selective *ortho*-iodinations. From these experiments, it was inferred that the combinatorial effect of having the TMS in in the activated *para*-position was too strong to allow regioselective *ortho*-iodination.

2.5.2 Directed *ortho* metalation of *p*-TMS-phenol

One common way to add functional groups to an aromatic system is by *ortho*-lithiation also known as directed ortho metalation. Aromatic hetero-atom-containing functional groups allow directed metalation adjacent to the aromatic functional group (*ortho*-position). The overall *ortho*-lithiation reaction constitute first bringing the lithiating species into proximity, by complexation, followed by deprotonation [67].
Some of the most common groups showing directing ability in directed ortho metalation is the methyl, methoxymethyl (MOM) and benzyloxymethyl (BOM) ethers of the corresponding phenol. Since the removal of the methyl or MOM require harsh acidic conditions (refluxing acid), these conditions could lead to protodesilylation. Clayden ranked the directing group ability of certain functional groups (Figure 2.9) [67].

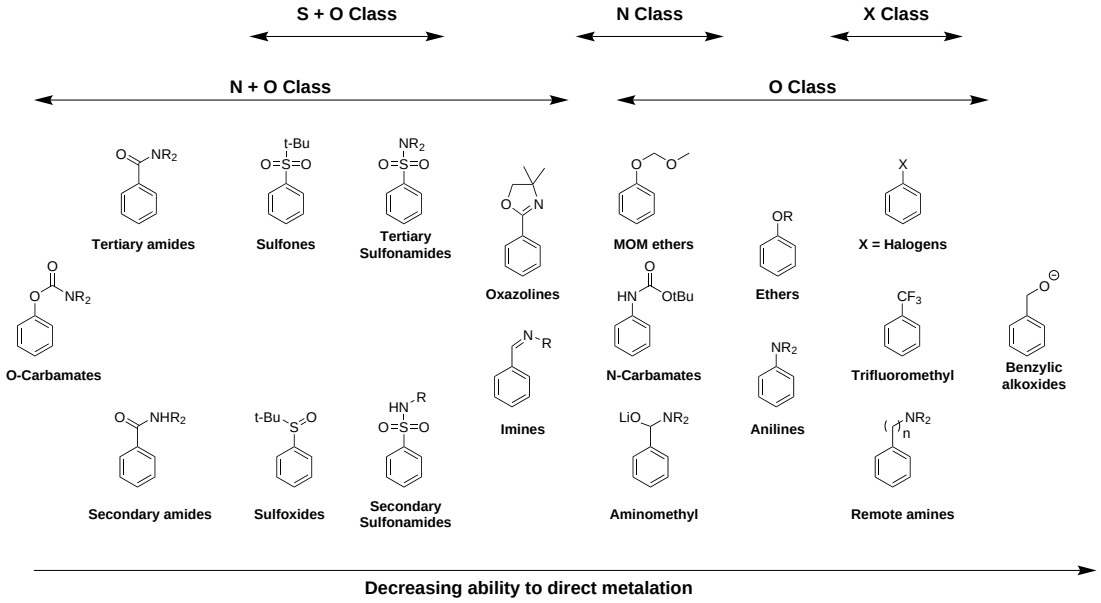

Figure 2.9: Ranking of the directing group ability of some most common directing groups. Figure is adapted from [67].

Among these directing groups, the group of Snieckus has shown the installation of a variety of functional groups using the diethyl carbamoyl group as a directing metalation group (DMG) [68, 69]. The cleavage of the diethylcarbamate has likewise been reported by Snieckus to be mild either through reduction using Schwartz's reagent or $LiAlH_4$ or basic hydrolysis using refluxing NaOH/aq. CH_3OH [69, 70].
In an attempt to introduce the iodides by this way, **2.4** was transformed into the corresponding diethyl carbamate **2.8**. This was done in accordance to literature procedures using diethylcarbamoyl chloride and NaH in THF in >90% yield (Scheme 2.6) [71].

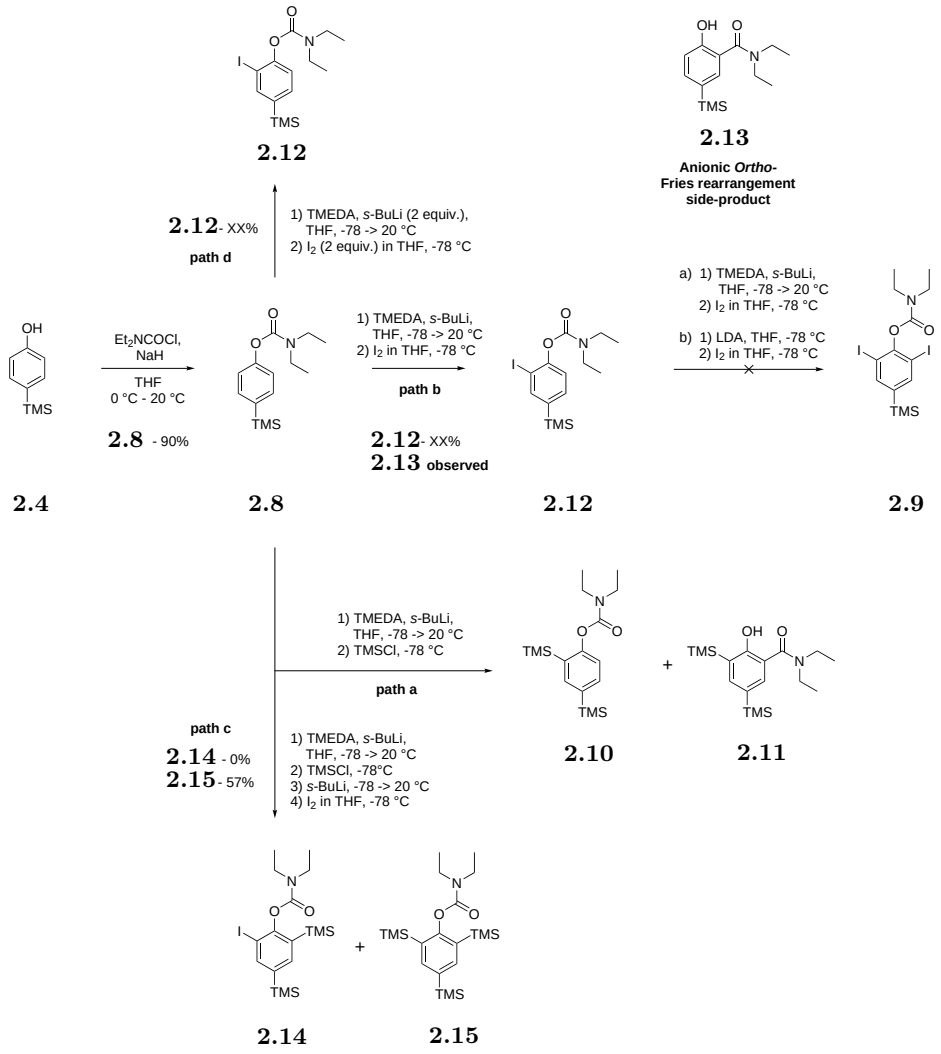

Scheme 2.6: Scheme showing different attempts of ortholithiations.

Different *ortho*-lithiation strategies were attempted in order to try to afford the 2,6-diiodo-4-TMS-phenyl-(diethyl)-carbamate **2.9**. Firstly, it was ensured that the lithiation conditions would enable *ortho*-lithiation according to literature [68]. Providing a slight excess of *s*-BuLi at -78 °C to a pre-cooled solution of tetra-methylethylenediamine (TMEDA) and **2.8** followed by treatment of TMSCl gave, beside residues of **2.8**, isomers of the intended TMS-substituted derivative according to LC-MS analysis (path a). It was hypothesized that the two isomers were the product **2.10** and **2.11** (the anionic *ortho*-Fries-rearranged isomer), respectively. Changing the electrophile to I_2 in THF could indicate whether the iodide could be introduced without *ipso*-substituting the TMS in the *para*-position (path b). Same lithiation-conditions was applied, beside that the I_2 in THF was added upon the *ortho*-lithiation. The *ortho*-iodinated product **2.12** was observed together with considerable formation of the anionic *ortho*-Fries rearranged isomer **2.13** and residues of starting material **2.8** (Scheme 2.6). The starting material of **2.8** and *ortho*-iodinated product **2.12** were hardly separable by chromatography, unless full conversion of **2.8**. The *ortho*-lithiated product of **2.12** was isolated in a decent yield. Noticeable, traces of what to be believed as **2.9** was observed according to LC-MS analysis.

These experiments indicated that the reaction temperature and the stoichiometric amounts of *s*-BuLi were important to control in order to achieve the intended substituted product in a clean fashion. Elevation of temperature (to room temperature) is likewise reported to promote the formation of the [1-3] acyl migration of the diethylcarbamoyl-group [69].

Following these one-step lithiations, it was attempted to perform sequential one-pot *ortho*-lithiations, as it was reported in study of Reed *et al.*, the sequential insertion of first a TMS followed by iodide in the other *ortho*-position [68]. This would yield the 2-iodo-4,6-di-TMS-phenyl diethylcarbamate **2.14** which potentially would be of value, as only one TMS would be needed to be regio-selectively substituted by iodide, prospectively (Scheme 2.6). To a cooled solution of **2.8** and TMEDA, the order of addition was: 1) *s*-BuLi, 2) TMSCl, 3) *s*-BuLi and 4) I_2 in THF (path c), in accordance to the original procedure. Surprisingly this afforded the 2,4,6-tri-TMS-phenyl diethylcarbamate **2.15** as the only species, isolated in 57% yield. The formation of **2.15** raised the questioning about the stoichiometric amounts of *s*-BuLi and TMSCl added. The addition of I_2 in THF was discontinued as the reaction mixture turned yellow upon addition of the first droplets of I_2. Since the iodide was not introduced, this could suggest that the TMS was installed at both *ortho*-positions – as a result of either the sequential addition of *s*-BuLi, or due to the di-lithiated anion was formed directly during the first addition of *s*-BuLi. In context of the bulky behavior of the diethylcarbamoyl group, it could be questioned whether the DMG group enhances the complex induced proximity effect of the second *ortho*-position, due to steric effects of the firstly introduced TMS, making the second lithiation more prone to occur during the addition of the second equivalent of *s*-BuLi. The introduction of the second TMS-group is under the assumption that TMSCl is present during the second addition of *s*-BuLi - before the addition of I_2 in THF.

Sequential one-pot *ortho*-iodinations were also performed on **2.8** with the repeating addition of *s*-BuLi and I_2 in THF (Scheme 2.6). This afforded only 2-iodo-4-TMS-phenyl diethylcarbamate **2.12**. The observation of the mono-iodinated product **2.12**, after two sequential iodinations, could indicate that the directed metal-halogen exchange occurred of the already installed iodide from the first lithiation. This was further investigated by monitoring the *ortho*-lithiation of **2.12** by quenching the lithiated intermediate of **2.12** using D_2O as the electrophile. As there was no sign of the deuterium introduced in the second *ortho*-position of **2.12**, the deuterium experiment indicated, that the iodide of **2.12** more likely undergoes directed metal-halogen exchange. It was therefore tried to promote a kinetic deprotonation using a steric base that will not be prone to undergo metal-halogen exchange (from path b). Treatment of **2.12** with lithium diisopropylamide (LDA) in THF at -78 °C followed by addition of I_2 in THF showed no formation of **2.9** (Scheme 2.6).
As a final attempt it was tried to apply 2 equiv. of *s*-BuLi to **2.8** to see whether the dianionic species could be formed followed by the addition of 2 equiv. of I_2 in THF (path d, Scheme 2.6). This experiment only led to formation of **2.12** in a more clean fashion.

Hoppe *et al.* presented the use of an isopropyl carbamoyl directing group as an alternative to diethylcarbamoyl moiety [72]. The isopropyl carbamoyl group should be easier to cleave

after use according to conditions reported in [73]. In addition, Hoppe likewise reported the mono magnesium-iodide exchange of the 2,6-diiodophenyl isopropylcarbamate using *i*-PrMgCl [73]. Based on these findings, it was considered that the mono magnesium iodine exchange could be conducted on the substrate 2,4,6-triiodophenyl isopropylcarbamate **2.17** affording the 2,4-diiodo-6-TMS-phenyl isopropylcarbamate **2.16**. The corresponding isopropyl carbamate **2.17** was therefore constructed from the isopropyl isocyanate and 2,4,6-triiodophenol **1.37** in quantiative yields (Scheme 2.7).

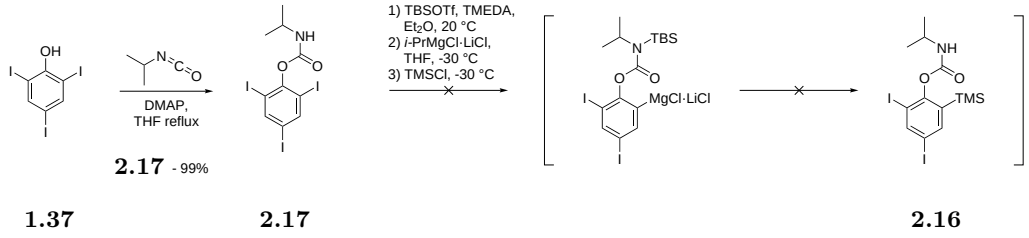

Scheme 2.7: Selective magnesium-iodine exchange attempted on **2.17**.

Pretreatment with TBSOTf of **2.17** was conducted for the *in situ* *N*-TBS protection of the isopropyl carbamate hydrogen. *i*-PrMgCl·LiCl was added at -30 °C followed by addition of TMSCl after 30 min. Unfortunately there was no signs of the TMS insertion. It was at first believed, that the use of *i*-PrMgCl·LiCl (turbo Grignard [74]) would be compatible within directed *ortho*-lithiations. By second thought, the use of *i*-PrMgCl·LiCl could be questioned in terms of the outcome of the reaction, as the LiCl could compete in terms of coordination with the DMG of **2.16**.

The strategy was then changed from trying to introduce the iodides on the aryl TMS, to introducing the TMS-group having the iodides already set e.g. from phenol **1.37**. The group of Hiyama reported the Pd-catalyzed insertion of TMS using 2-(diphenylphosphaneyl)phenol **2.18** as ligand and hexamethyldisilane (TMS-TMS) as TMS source, respectively [75]. Within the scope of this reaction, the presence of ester moieties as well as di- and tri-brominated arenes - as non-participating group - were tested compatible to the reaction conditions. The Pd-catalyzed TMS insertion was therefore conducted on the methyl and *tert*-butyl esters of **1.37**. The methyl ester **2.19** and *tert*-butyl ester **2.20** was conducted by *O*-alkylation using K_2CO_3 and the methyl or *tert*-butyl bromoacetate, respectively (Scheme 2.8).

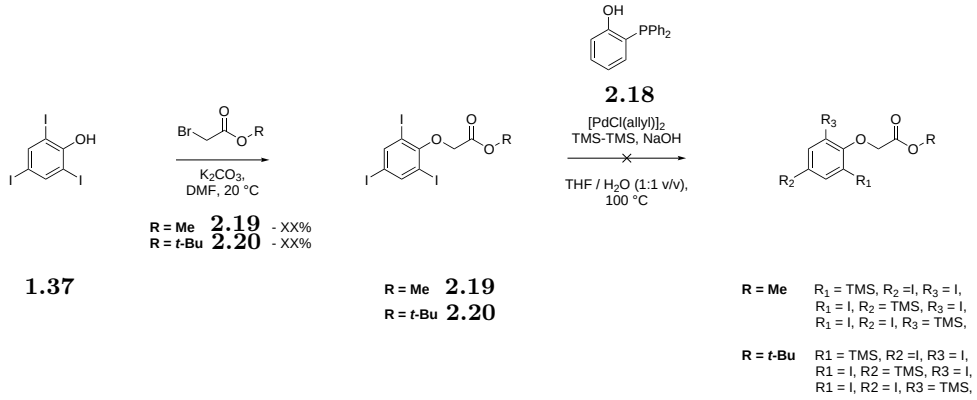

Scheme 2.8: Selective magnesium-iodine exchange attempted on **2.32**.

This gave **2.19** and **2.20** in excellent yields, respectively. The Pd-catalyzed insertion of the TMS was not observed in **2.19** and **2.20** using the conditions reported in Hiyama *et al.* (Scheme 2.8). On the other hand, hydrolysis of the ester **2.19** was observed due to the basic conditions.

Metal-halogen exchange was then attempted, to see if the TMS-group could be introduced by exchanging with an already fixed iodide of 2,4,6-triiodophenol or derivatives hereof. Metal-halogen exchange was carried out using varying equivalents and types (n or s) of BuLi and i-PrMgCl·LiCl. Metal-halogen exchange of **1.37** only led to de-iodinations. In order to simplify the metal-halogen exchange of **1.37**, it was inferred that a bulky protecting group introduced at the oxygen position of **1.37** could aid steric hindrance and screen of the iodides in the *ortho*-positions hopefully leading to regioselective metal-halogen exchange in the *para*-position. Phenol **1.37** was transformed into the TBPDS ether **2.21** using TBDPSCl, and imidazole as base. The reaction was performed in DMF and afforded **2.21** in 65% yield. Metal halogen exchange was then performed using 1 or 2 equiv. of n-BuLi (Scheme 2.9). LC-MS analysis indicated the formation of an apolar species that was not ionizable. ^{1}H-NMR of the crude reaction mixture indicated of what to be a TMS resonance in the area of 0.5-(-0.5)ppm. The crude mixture was therefore attempted purified by chromatography but due to the very apolar character of the components and instability on silica gel, isolation of what to be the expected TMS substituted **2.22** was unsuccessful. Different conditions were therefore applied in order to deprotect what was expected to be the TMS-substituted di-iodophenyl-TBDPS-ether **2.22**. In order not to compromise the installed TMS-group, traditional fluoride based deprotection could be challenging in terms of selectivity, as this type of deprotection show poor selectivity []. Therefore, alternative milder conditions would have to be applied. Wang *et al.* reported the deprotection of aryl silyl-ethers using LiOAc in a mixture of DMF and H_2O [76]. Another attractive removal of aryl silyl ethers was developed by the group of Kim *et al.* using DBU in CH_3CN/H_2O [77].

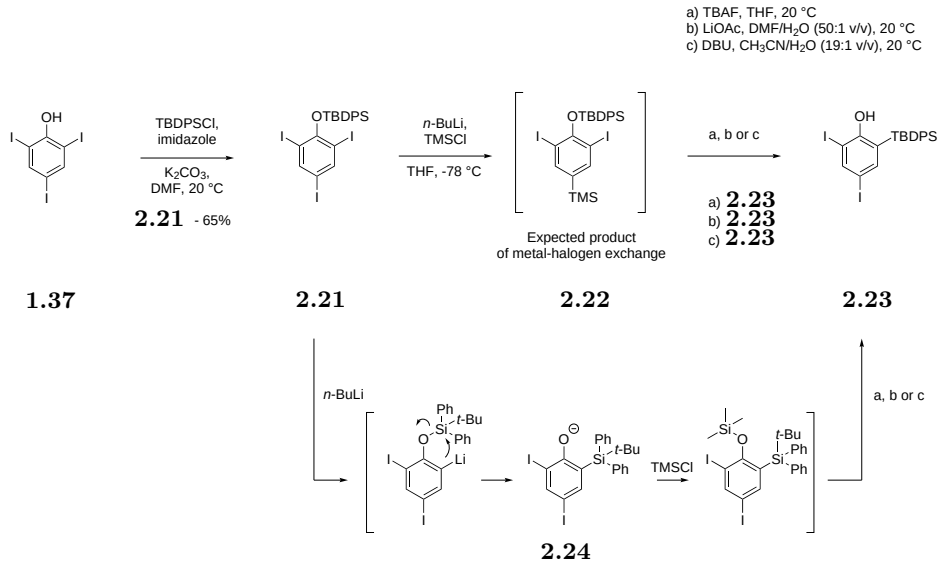

Scheme 2.9: Synthesis and metal halogen exchange of **2.21**.

As a control, TBAF deprotection was attempted (Scheme 2.9). Treatment gave one main species, which did not correspond to the intended product according to LC-MS analysis. The following LiOAc and DBU deprotection showed the same tendency in reaction profile with one main species (**??**). This compound was isolated and NMR analysis did not indicate any sign of a TMS-group in the of compound. On the other hand, the TBDPS was still present and the phenolic hydroxy-group was also confirmed. Further 2D-NMR analysis revealed that this side-product surprisingly was 2-TBDPS-4,6-diiodophenol **2.23** in accordance with the observed m/z by LC-MS analysis. With the isolation of **2.23**, this could indicate, that **2.21**, upon addition of *n*-BuLi, led to metal-halogen exchange in the *ortho*-position followed by reverse Brook-rearrangement. Upon the addition of TMSCl the rearranged lithium 4,6-diiodo-2-TBDPS-phenoxide **2.24** gets re-protected as the TMS phenyl ether. The liability of the aryl TMS ethers explains the suspicious behavior of **2.24** during the isolation as well as during the applied deprotection conditions with immediate reaction.

As recently published, and inspired from the experiments above, it was reasoned that the TMS-group could be introduced via the reverse Brook- rearrangement by the formation of 2,4,6-triiodophenyl TMS ether **2.25** followed by lithiation in the *ortho*-position of **2.25** [78]. As a simplified model system to gain experience, the reverse Brook-rearrangement was conducted on 2-iodo-phenol using *n*-BuLi and TMSCl. The reverse Brook-rearrangement of 2-iodo-phenol was feasible in promising yield according to LC-MS analysis. Based on this procedure, reverse Brook-rearrangement was carried out on **1.37**. The phenol **1.37** was first protected using TMSCl and Et_3N in THF. Upon workup of the TMS-protection, crude ^{1}H-NMR confirmed the formation of the phenyl TMS ether of **2.25** (Figure 2.10).

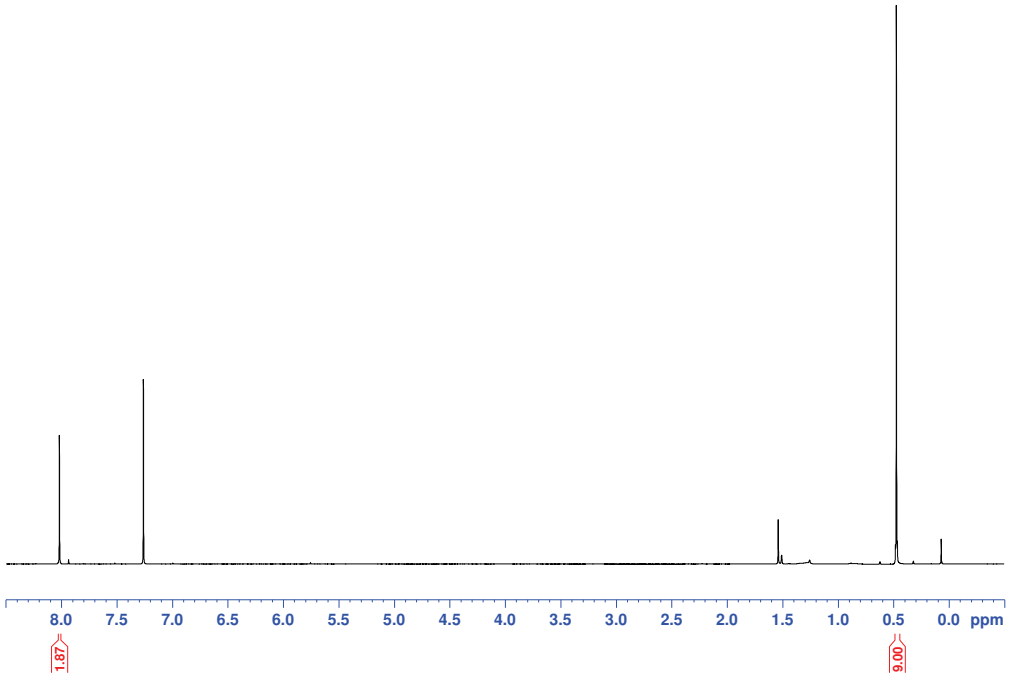

Figure 2.10: ^{1}H-NMR of the crude **2.25**.

To our satisfaction, subjecting the crude **2.25** to *s*-BuLi at -78 °C yielded the rearranged product **2.26** in 72% yield (Scheme 2.10).

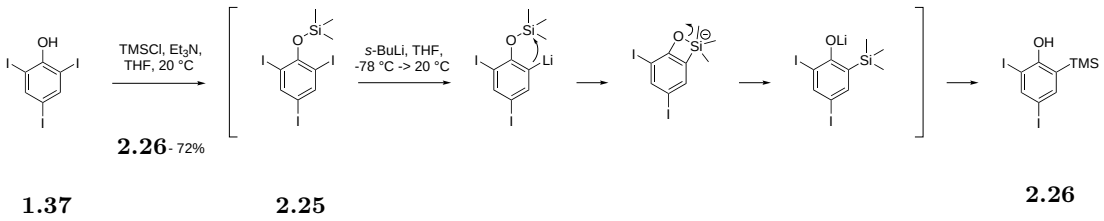

Scheme 2.10: Scheme for the synthesis of **2.26**.

2,4-Diiodo-6-TMS-phenol **2.26** was then *O*-alkylated using methyl bromoacetate and K_2CO_3 in refluxing acetone. This afforded the methyl ester **2.27** in 96% yield (Scheme 2.11). It was believed that ester hydrolysis should be fairly convenient using KOH in CH_3OH. Due to low solubility of **2.27** in CH_3OH, hydrolysis was conducted in a mixture of CH_3OH and THF. The product isolated from hydrolysis was unfortunately the proto-desilylated product **2.28** in 81% yield. This was either attributed to be due to the basic conditions or the acidification during workup that led to the protodesilylation. Concurrently to this project, the methyl ester of **2.29** (section 5.10) had to be hydrolyzed. It was reported that the methyl ester of **2.29** could be transformed to the corresponding

acid using aq. Na_2CO_3 in CH_3CN [79]. These conditions were applied to **2.27** followed by drop-wise acidification during workup, which yielded the corresponding acid **2.30** in 90% yield (Scheme 2.11).

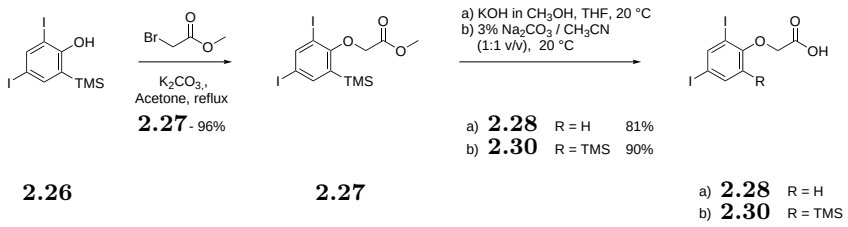

Scheme 2.11: Scheme for the synthesis of **2.30**.

The assembly of the TMS-precursor of BioXmark **2.31** was constructed using standard ester coupling of **1.34** and **2.30** mediated by EDC·HCl and DMAP (Scheme 2.12). The 6,6'-diol **1.34** was kindly afforded by NCK A/S, the company appointed for the scale-up synthesis of **1.33**. Previous attempts of TBDPS-protection afforded crude mixtures of 6,6'-diol and 1',6'-diol. Therefore, in order to assure that the final labeled version of BioXmark would be identical with non-labeled BioXmark, the diol **1.34** provided by NCK A/S was used. This afforded the TMS derived BioXmark precursor **2.31** for radioiodination in 83% yield.

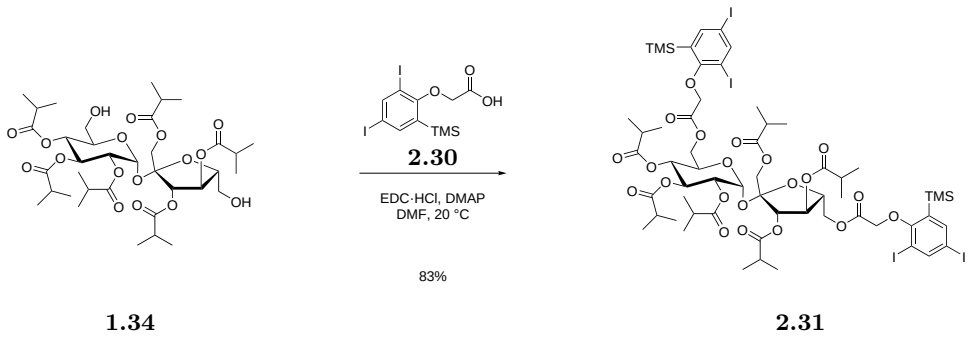

Scheme 2.12: Scheme for the synthesis of **2.31**.

2.5.3 Iodination of TMS-BioXmark precursor 2.31

Iodinations of **2.31** using $Tl(OOCCF_3)_3$ and NaI did not proceed as expected. Iodination was only observed in trace levels. By monitoring the reaction by LC-MS analysis, an unknown side product with an observed m/z of 1664 was formed during the thallation, prior to the addition of NaI. Optimization of the thallation reaction was attempted. The temperature was raised from 20 °C to 37 °C and the stoichiometric amounts of $Tl(OOCCF_3)_3$ (10 equiv.) and NaI (20 equiv.) were increased[2]. Prolonged reaction time were conducted. Changing these parameters had the only affect of increasing the

[2]Standard conditions developed in the group of Mads Clausen are $Tl(OOCCF_3)_3$ (2 equiv.) and NaI (4 equiv.) in TFA/CH_3CN (3:7 v/v) at 20 °C.

formation of the side-product with the observed m/z of 1664 in almost quantiative amount. LC-MS analysis indicated even that the side product was formed almost quantitatively prior to the ligand exchange with NaI. Moreover, the side-product remained unaffected upon the addition of NaI. This unexpected side-product could indicate that thallation of the 2-(2,4-diiodo-6-TMS-phenoxy)acetyl moiety is more prone to undergo this unknown side-reaction than substituting the TMS as intended. The reactivity/nucleophilicity, due to the mesomeric/inductive effect of the two iodides already present of the 2-(2,4-diiodo-6-TMS-phenoxy)acetyl moiety, could question the nucleophlicity of the aryl-TMS.
To assure that **2.31** could undergo electrophilic aromatic iodination, **2.31** was subjected to ICl as the direct source of the iodonium ion (**??**). LC-MS analysis indicated after 18 h the formation of the mono-iodnated intermediate **2.32** and the di-iodinated product **2.33** of **2.34** (**??**). Further optimization is needed to assure full iodination of **2.31**. Additionally **[^{125}I]-1.33** formulated in **1.33** would have to be tested *in vivo*.

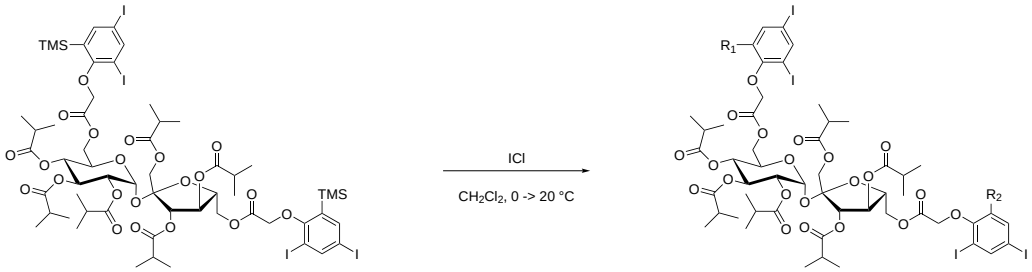

2.31

2.32 R_1 = TMS, R_2 = I
R_1 = I, R_2 = TMS

2.33 R_1 = I, R_2 = I

(b) Iodination of **2.31** using ICl.

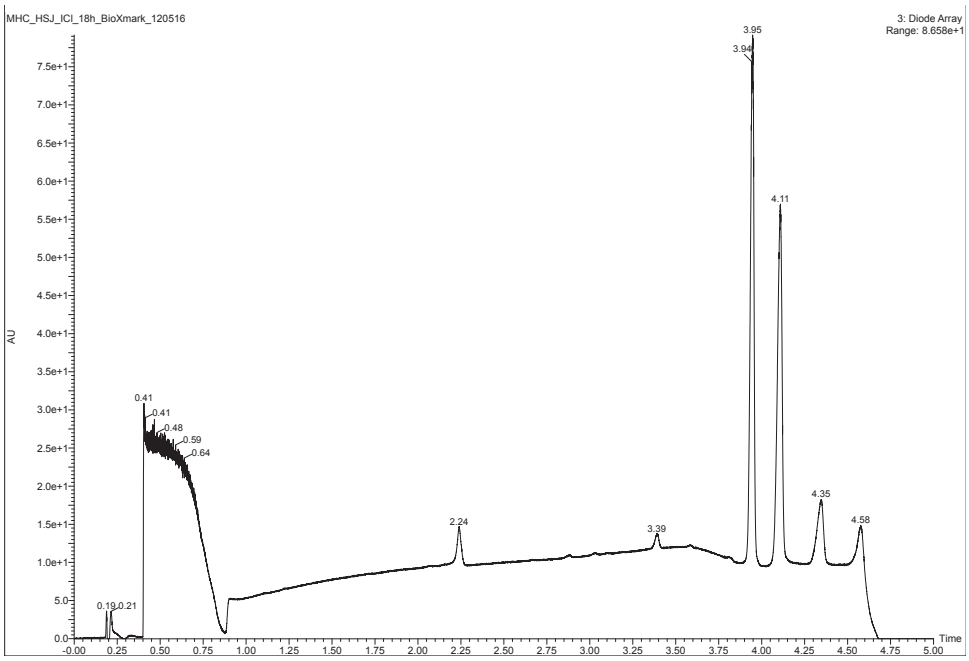

(d) UV-chromatogram of the iodination of **1.33** using ICl after 18 h of reaction. The peak eluting at 3.95 min has a m/z of 1808.65 corresponding to the $[M+Na]^+$ adduct of **2.33**. The peak eluting at 4.11 min has a m/z of 1754.88 corresponding to the $[M+Na]^+$ adduct of **2.32**. The peak eluting at 4.35 min has a m/z of 1701.18 corresponding to the $[M+Na]^+$ adduct of **2.34**.

Figure 2.11: Reaction scheme & LC-MS analysis of the iodination of **2.31** using ICl in CH_2Cl_2.

2.6 Conclusion

A radioactive fiducial tissue marker for surgical guidance has been developed based on the fiducial marker of **1.33** and the synthesis of **[^{125}I]-2.7**. Radiolabeling of **2.2** using $Tl(OOCCF_3)_3$ and NaI gave **[^{125}I]-2.7** in high radiochemical yield (83%) with a radiochemical purity of 95% under carrier free conditions. The corresponding gel implant of the formulation containing **1.33** and **[^{125}I]-2.7** was deposited *in vivo* in the right flank of NMRI mice. The implant remained stable during the seven days of investigation. The

biodistribution study of **[^{125}I]-2.7** indicated only limited uptake in the thyroid gland to a level of 3.5% ID·g^{-1} The dosimetry analysis indicated overall that the vital organs and tissue would not be affected by the radiation dose corresponding to the uptake in the respective organs/tissue. A SAIB-based precursor **2.31** for radio-iodination, that upon radio-iodination will be identical with **1.33**, was developed. Iodination via thallation of **2.31** was unsuccessful, though iodination using ICl seemed to be successful. The iodination of **2.31** and its *in vivo* performance are currently under investigation.

Synthesis of Contrast Agents for Active Loading in Liposomes 3

3.1 Contrast agent for blood pool imaging

X-ray computed tomography (CT) imaging is regarded as a non-invasive imaging technology which *inter alia* led to the award of the Nobel Prize in 1979 to G. Hounsfield and A. McCormack [80]. The use of CT imaging in angiography or blood pool imaging can help visualize various cardiovascular diseases including discovery of tumors in early stages and how tumors respond during therapy [81]. This is further substantiated as the process of angiogenesis is related to tumor growth [81]. Blood pool imaging likewise aid delineation of abnormalities e.g. thrombi or atherosclerotic lesions [81].

The blood pool remains a challenge to clearly visualize using the CT modality, as the X-ray attenuation of soft tissues are not sufficiently distinctive in order to achieve a proper contrast [80]. With the different mass X-ray attenuations of e.g. bone and soft tissue, a distinctive contrast is achievable [**?**]. Soft tissues like fat and muscle, or organs and tumor, with similar densities is not clearly separable by CT-imaging [**?**]. This has induced the use/need of contrast agents to delineate soft tissues and the cardiovascular system to enhance the contrast of anatomic compartments [80]. The common contrast agents used in CT imaging today should - beside possessing high X-ray attenuation (radioopacity) - be compatible with the serum of blood plasma. Additionally, as highlighted by Hallouard *et al.*, the main challenges can be summed up to be: "to provide the highest contrast possible within the blood that will remain stable over time and allow for imaging, and when combined with either passive or active targeting will potentially accumulate at the site of interest" [80]. The use of iodinated contrast agents within cardiovascular CT-imaging, has been developed to aid proper contrast. One of the first examples reported was the use of the salt NaI [82]. The recently employed types of CT contrast agents within cardiovascular CT imaging are derivatives of 2,4,6-triiodo-benzoic acids and other arenes as the core-moiety. An overview of the iodinated contrast agents are depicted in Figure 3.1.

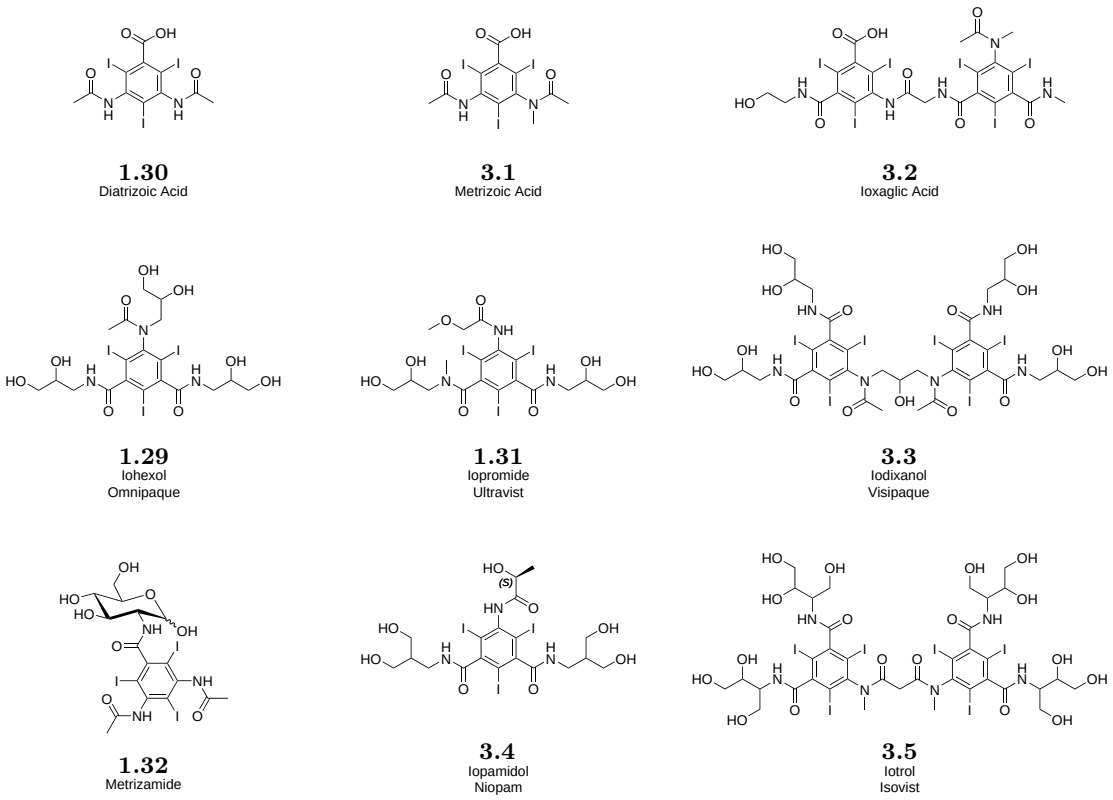

Figure 3.1: Examples of some of the most used iodinated contrast agents used in clinics today.

The primarily ionic character of the iodinated benzoic acid derivatives (diatrizoic and metrizoic acid, **1.30** and **3.1** respectively) ensures solubility in blood plasma but administration of these type of derivatives indicated that the ionic character was a limitation in terms of osmolality. These contrast agents have proved to be highly osmolar (diatrizoicate **1.30**: 1570 mOsm·kg^{-1}, ioxaglic acid **3.2**: 560 mOsm·kg^{-1} given at concentration of 300 mg I·L^{-1} [82]). In those cases where the osmolality of the contrast agent surpasses the osmolality of the blood plasma (300 mOsm·kg^{-1} [83]), a net flow of free/unbound water in plasma occurs to neutralize the concentration difference between the compartments. This can cause adverse side-effects as it can lead to an increase in blood viscosity, which can further lead to e.g. endothelial damage, hypervolaemia and etc. [82, 83]. Concentrations up to 1.5 M of diatrizoicate adducts (sodium or meglumine) have likewise been reported, having in mind the molality of 0.16 M of body fluids [82, 83].

This led to the improved developments of the non-ionic (monomeric as well as dimeric) iodide-based contrast agents like iohexol **1.29** (trade name: Omnipaque, GE Healthcare, USA), iopromide **1.31** (trade name: Ultravist, Bayer Healthcare, Germany) iodixanol **3.3** (trade name: Visipaque, Ge Healthcare, USA), metrizamide **1.32** and iopamidol **3.4** (trade name: Niopam, Bracco Diagnostics, Italy) (Figure 3.1) [84]. These contrast agents have displayed improved compatibility in terms of osmolality, as the osmolality have been reduced by approximately 50% [82]. The LD_{50} of the non-ionic contrast agents are likewise reported to be lower than the ionic-based contrast agents. Additionally, the pharmacoki-

netic parameters have been characterized and indicated a higher tolerance, limited plasma protein interactions and being inert to biotransformations [83]. As seen from Figure 3.1, a general trend in the structures is the poly-hydroxylyated side-chains of the tri-iodoaryl core structure which presumably assure sufficient solubility in the blood serum plasma.

Despite the improvement of lowering the osmolality by using non-ionic contrast agents, a general limitation of the both ionic and non-ionic contrast agents are the high viscosity due to the high concentrations administered. As an example, ionic monomeric contrast agent at concentration level of 370 mg I·mL^{-1} possess a density corresponding to 1.43 g·mL^{-1} [82]. Additionally, this class of iodinated contrast agents display lack of retention time within the blood pool as they are rapidly cleared *in vivo* by renal excretion [**?**]. This led to the use of formulations of contrast agents with prolonged retention time in the blood. Among the typical formulations for CT contrast agents are nanoparticle-based systems like nano-emulsions, polymeric nanoparticles or liposomes [80]. As the scope of this project was the development of contrast agents for active/mediated loading of liposomes, the following sections are focused on the liposomal formulation of CT contrast agents.

3.2 Liposomes

Liposomes are defined as being microscopic lipid vesicles possessing a bilayer structure [85]. The bilayer often consist of phospholipids that enclose an inner aqueous compartment (interior).
This assembly has been used as drug carrier for various hydrophilic and hydrophobic drugs that otherwise would cause severe side effects if administered without any drug delivery formulations [86]. Liposomes have even been assessed to be the closest drug delivery system to Paul Ehrlich's "magic bullet", when combined with targeting [85]. Liposomes can be designed to vary in size (20 nm - 1 μm) and lipid composition. Additionally, liposomes can be customized to contain either one bilayer (unilammellar) or several (multilamellar), thereby containing more than one aqueous compartment (Onion layer construct) [85, 86]. With the implementation of extrusion in the preparation of the liposomes, mono-disperse liposomes can be refined in size with a narrow vesichle-distribution [85]. Liposomes are classified by size and whether they are unilamellar or multilamellar. The most known types of liposomes are multilamellar vesichles (MLV, size range $>$0.5 μm), large unilamellar vesichles (LUV, size range $>$100 nm) and small unilamellar vesichles (SUV, size range 20-100 nm) according to [86].

Despite bio-compatibility, liposomes were discovered to be opsonized and cleared by the reticuloendothelial system [85]. The clearance was proved to be dependent of the size of the liposomes. Large multilamellar liposomes are rapidly removed while liposomes $<$ 100 nm are retained in the blood stream as they are more slowly taken up by the reticuloendothelial system. Further improvements in the circulation time was achieved by employing cholesterol as an additive, resulting in an increased rigidity of the bilayer by which opsonin-tagging will be kept to a minimum. Together with the use of steric sta-

bilization using mainly PEG-segments (also referred to as stealth formulation), an outer hydrophilic protective shield is formed that prevent disintegration by plasma proteins and opsonins (Figure 3.2). Particular, this development made liposomes long-circulating as macrophage uptake decreased significantly compared to liposomes without PEG on the surface [85]. With the discovery of what is known as the Enhanced Permeability and Retention effect (EPR effect) of liposomes, (Figure 3.3), enhanced accumulation in defective perforated vasuclature, typically found in inflamed and cancer tissues, was observed (normal vessels pore cut-off: 6-7 nm, subcutaneously tumor pore cut-off: 200 nm - 1.2 μm [80]). This has emphasized liposomes as one of the most potentially encapsulating drug carriers [85].

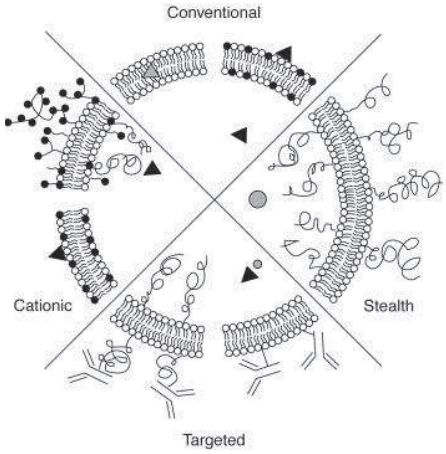

Figure 3.2: Schematic representation of liposomes and its different coatings [86].

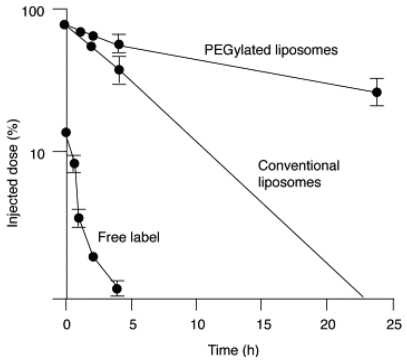

Figure 3.3: Blood circulation kinetics of different types of ^{67}Ga-labeled liposomes in rats [86].

3.3 Liposomal formulation of CT contrast agents

Liposomal formulation of contrast agents like LUVs and MLVs of diatrizoicate **1.30** and the corresponding labeled **[^{125}I]-1.30**, LUVs of metrizamide **1.32**, LUVs of iopromide **1.31**, and MLVs of radioiodinated iotrol **[^{125}I]-3.5** have been conducted previously [87–91]. The overall *in vivo* performance was likewise analyzed in the above-mentioned studies. Typically, the concentration of iodide was in the range between 25-110 mg·mL^{-1} [80]. As the size of liposomes used in these studies was constructed as rather large vesicles, the *in vivo* performance revealed mainly increased uptake and contrast enhancement in the reticuloendothelial system and the corresponding tissue (liver, spleen). Increment of contrast in the blood was also observed. Overall, the general tendency was a contrast enhancement in the range of 30-100 HU of various tissues. Prolonged circulation times were generally observed for all liposome formulation of contrast agents. The lipid composition seemed to influence the leakage behavior of the **[^{125}I]-1.30** [87].

Liposomal stealth formulations of iohexol **1.29** and iopromide **1.31** have likewise been reported with a narrow vesicle distribution (extrusion applied) [81, 92, 93]. The encapsulation efficiency reported for **1.31** was in the range of 40-45% [93]. In all the reported

liposomal formulation, the osmolality was not addressed.

The current limitation of liposomal formulation of contrast agents is stated to be the relative low concentration of mg I $\cdot mL^{-1}$ in the range of 70-80 mg I$\cdot mL^{-1}$ suspension [90]. The low concentration entails that a large volume of contrast agents has to be administered to enable a proper contrast enhancement. As deduced in the above mentioned examples as well as the study of liposomal formulation of iohexol **1.29**, up to 14 mL of the contrast formulation had to be injected in a rat (2.2 kg) corresponding to 14% of the blood plasma volume [81]. This could potentially lead to severe side effects since liposomal formulation of contrast agents usually possess a lower LD_{50} in rats and mice than the contrast agent itself. As example, the LD_{50} in rats measured for the non-formulated iopromide **1.31** is 11 g I$\cdot kg^{-1}$ while LD_{50} of the corresponding stealth liposomal formulation of **1.31** is 4.5 g I$\cdot kg^{-1}$ [80]. Administration of large amount of lipids may potentially lead to severe side effects []. The side-effect of lipid toxicity states that the concentration of contrast agent have to be increased. It has likewise been proposed that the proper iodide/lipid ratio should at least be in the range of 1:1 to be clinical applicable [94]. In the above-mentioned studies encapsulation efficiencies did not exceed 30-40% and to the knowledge of the authors, the contrast agents were encapsulated during the preparation of the liposomes (passive loading). Optimization of loading efficiencies has been looked into and inferred to be dependent on various parameters like contrast agent concentration, lipid composition, liposome concentration and manufacturing process like extrusion [80]. Likewise encapsulation of polar species and species with same charge as the head-group/surface of the bilayer (repulsive behavior) are stated to have lower encapsulation upon the hydration-process of the lipids [86].

3.4 Remote loading of active compounds in liposomes

Improvements especially within encapsulation methodologies of liposomes was first demonstrated by Nicols and Deamer, who showed that preparing liposomes in citrate buffer at pH 5 (establishing pH 5 in the water compartment) and subsequently changed the exterior solution to pH 8 provided a transmembrane gradient of three pH units [85,95]. This transmembrane gradient was used to mediate loading of catecholamines. The equilibrium and state of the pH-exchangeable amine will affect the permeability coefficient, which is defined as the ability to permeate and cross the bilayer of the membrane. Applying the intended amine in the range of the pka_H will afford the un-protonated amine, which can permeate through the bilayer and into the liposome. Upon permeation to the aqueous compartment, the amine will be protonated due to the pH 5 of the interior, by which the induced charge (protonation) affect the permeability coefficient of the amine. This renders the entrapment of the given amine/target compound (Figure 3.4).

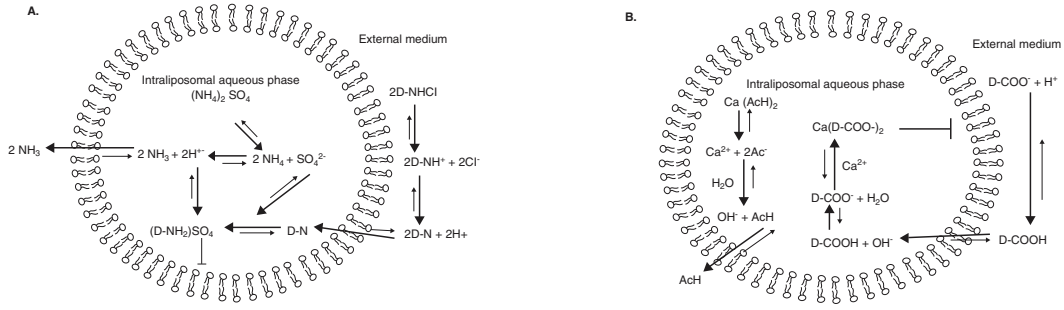

Figure 3.4: Schematic representation of the mechanism of loading. The illustration to the left accounts for amines while the illustration to the right accounts for loading of weak acids [85]

Usually, as the concentration of the amine in the aqueous inner compartment exceeds the solubility, this can cause precipitation of the amine salt of the corresponding conjugated base of the buffer used. As an example anthracycline citrate salts possess low solubility and are often reported to precipitate affording these coffee bean like liposomes (Figure 3.5) [85].

The state of the active species (solute or solid) can be dependent on the drug to lipid ratio w/w (D/L). At low ratios, the active species will usually be solubilized while at higher ratios, the active species is most likely found in a solid state [85]. D/L employed in a drug delivery context have found great use, due to the reason that liposomes possess the EPR effect. With the induced precipitation in the interior of the liposomes, leakage from liposomes is reduced and dose release is sustained, as the active species has to pass from solid state to solubilized form before permeating through the bilayer. This has lowered the leakage behavior of the active species from the inner compartment and emphasized why this state of CT contrast agent within the interior of the liposome is preferable.

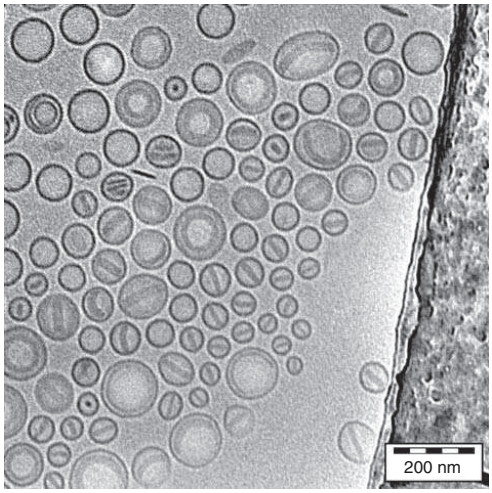

Figure 3.5: Cryo-TEM of precipitated idarubicin in liposomes [85].

This technology has among other things led to the first FDA approved liposomal formulation of doxorubicin (Doxil) []. Doxorubicin is one of the most known and used drugs in chemotherapy. Doxorubicin interfers with the DNA by which transcription and replication of DNA is stopped. Since Doxorubicin is non-specific towards any DNA, the use of Doxorubicin cause severe side-effects by affecting healthy cells during treatment. Using liposomes as a drug carrier, targeting towards cancer tissue can be applied due to the EPR effect with less side-effects. This class of drugs can be actively loaded with a D/L ratio of 0.3 with encapsulation efficiencies close to 100% in liposomes [85]. Beside using a buffer mediated pH gradient to achieve an inbalanced system for active loading, Haran *et al.*

employed $(NH_4)_2SO_4$ to generate what is referred to as a pH gradient. With the influx of the amine of interest and the corresponding protonation inside the aqueous compartment, neutral NH_3 is liberated and efflux of NH_3 through the bilayer takes place [85]. The group of Barenholz have further looked into determining multiple parameters that influence the mediated loading of liposomes [96]. The mediated loading of weak acids has likewise been demonstrated. A schematic representation of the mechanism of action for the mediated loading is depicted in Figure 3.4.

Beside the mediated loading of doxorubicin, Zhiageltsev *et al.* reported the mediated loading of the water insoluble drug docetaxel **3.6**. Docetaxel **3.6** was successfully loaded into liposomes with an encapsulation efficiency of 100% [85,97]. In order to achieve active loading, the prerequisite would be that the active specie possesses an amphiphilic nature as a function of pH. Therefore **3.6** was derivatized as a *N*-methyl periparazinyl butanoic acid derivative **3.7** (Scheme 3.1) with a weakly basic character, that enabled mediated loading with 100% encapsulation efficiencies in D/L up to 0.4 [97].

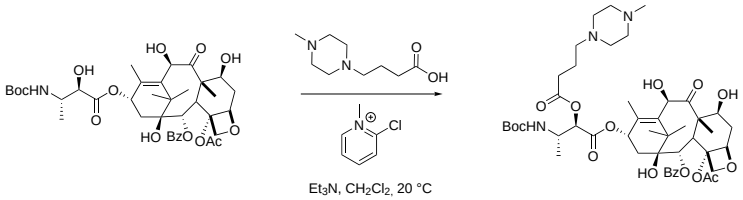

3.6
Water Insoluble

3.7

Scheme 3.1: *N*-methyl periparazinyl butanoic acid modification of docetaxel **3.6** that enabled mediated loading and led to 100% encapsulation efficiency [97].

3.5 Problem statement

Based on the above-mentioned concepts, the intention was to develop iodide based contrast agents for the application of CT blood pool imaging, which will facilitate mediated loading in liposomes. Providing higher loading efficiencies will potentially enable that a higher concentration of contrast can be achieved, which would lower the volume of contrast media needed to obtain a significant contrast. Liposomal formulation will likewise provide prolonged circulation time. The hydrophilic/hydrophobic balance of the contrast agent, together with the proper D/L ratio and salt combination are crucial parameters for the outcome of the mediated loading. These parameters will influence whether induced precipitation of the contrast agent in the aqueous interior of the liposome is feasible. The contrast property of the corresponding precipitates will be promising as the X-ray attenuation of solid compound will be high and the gradient towards the interior will be infinite from an equilibrium standpoint.

3.6 Design of contrast agents

In the development of contrast agents for mediated loading it would be necessary to introduce e.g. a weakly basic functional group that will be amphiphilic upon change in pH. According to the great success of using amine moieties in mediated loadings, the aim was to introduce amine functionalities to triiodoaryl-based contrast agents. In order to achieve highest contrast possible the final molecular weight of the derived contrast agent should be as low as possible by which the iodide mass contribution is as possible ($w_{iodide} \cdot w_{total}^{-1}$).

As proof of concept that mediated loading is achievable, two widely used contrast agents like iohexol **1.29** and diatrizoic acid **1.30** were chosen as starting points. As a rough and indicative measure to predict the polarity of the contrast agents, the calculated logP. Besides this, the intention was to show the flexibility and opportunity of providing building blocks of the 2,4,6-tri-iodophenol **1.37**. Using **1.37** as scaffold (Scheme 3.6), the phenol can be *O*-alkylated with a variety of functionalities. This will show the potential of how **1.37** can be transformed into novel contrast agents for CT imaging. To compensate for the hydrophobic nature of the triiodo-moiety of **1.37**, the transformation of **1.37** should be hydrophilic in order to provide a adequate aqueous solubility. From these building blocks, it was thought that a library of novel contrast agents could be prepared where hopefully the right candidate would induce precipitation upon loading.

3.7 Synthesis of iohexol derivative for mediated loading

Inspired by the synthesis of iohexol **1.29** from the corresponding 1-chloro-2,3-dihydroxypropane and 5-acetamido-*N*,*N*-bis(2,3-dihydroxypropyl)-2,4,6-triiodoisophtalamide **3.8**, it was inferred that the acetamide moiety of **3.8** could be functionalized in accordance to literature (Scheme 3.2) []. Treatment of the commercially available **3.8** with NaOH in 2-methoxyethanol selectively deprotonates the acetamide proton (estimated pKa = 11.5) and forms the corresponding sodium acetamidate that undergoes *N*-alkylation in the presence of a proper electrophile.

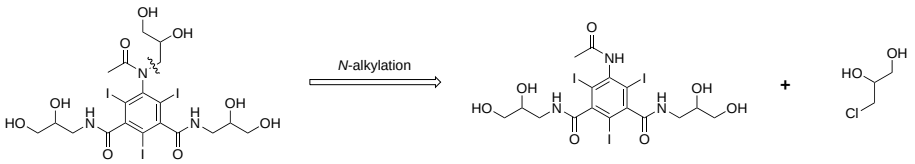

Scheme 3.2: Retrosynthetic analysis of iohexol **1.29** [].

Using 2-(Boc-amino)ethyl bromide as electrophile afforded the *N*-alkylated compound **3.9** (Scheme 3.3). Purification of **3.9** was conducted by dry column vacuum chromatography using H_2O/CH_3CN linear increments. The presence of the ethyl 2-(Boc amino) group was mainly confirmed by multiplicity-edited HSQC-NMR together with the presence of the *tert*-butyl resonance of the Boc-moiety. The following boc-deprotection was conducted

using TFA in CH_2Cl_2 affording the corresponding deprotected amine as a TFA salt **3.10**·TFA (Scheme 3.3).

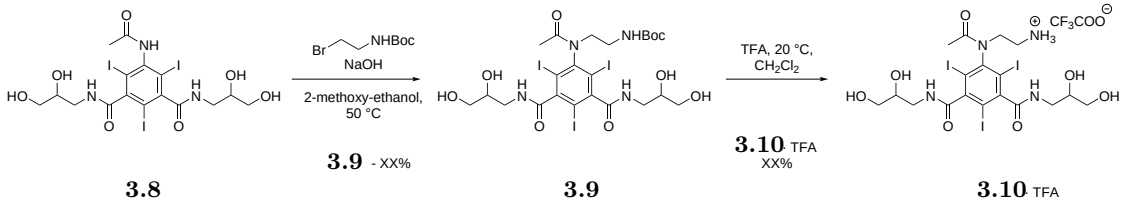

Scheme 3.3: Scheme for the amino functionalization of **3.8**.

It seemed that the overall yield was determined by the *N*-alkylation step. Further optimization attempts were conducted using CH_3ONa in CH_3OH as base and increasing the temperature to reflux. This did not led to any further improvements.

3.8 Synthesis of diatrizoic acid derivative for mediated loading

To derivatize diatrizoic acid **1.30**, the benzoic acid moiety was seen as a flexible handle that could undergo several transformations. Disappointingly, transformation of the corresponding activated ester of **1.30** using either EDC·HCl and DMAP, or 2-(3H-[1,2,3]triazolo[4,5-*b*]pyridinyl-1,1,3,3-tetramethylisouronium hexafluorophosphate (HATU) and 1-Hydroxybenzotriazole (HOBt) did not indicate any formation of the ethylenediamine product **3.11** nor the *N*-Boc ethylenediamine derivative **3.12**, respectively (Scheme 3.4).

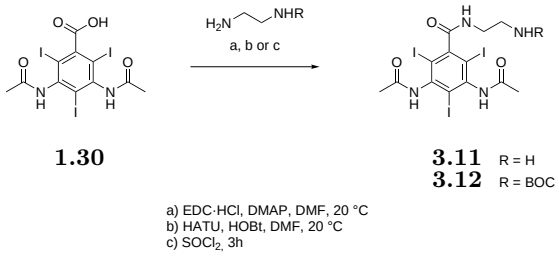

Scheme 3.4: Scheme for the amide bond functionalization of diatrizoic acid **1.30**.

Alternatively, it was decided to synthesize the acid chloride by refluxing in $SOCl_2$ for 3 h, despite the fact that the acid chloride of **1.30** has been reported to have low reactivity [98]. LC-MS analysis indicated the m/z corresponding to the sodium adduct of the acid chloride of **3.17**. Unfortunately, no conversion of the acid chloride to the corresponding *N*-Boc-ethylenediamine product was observed.

The strategy was then changed to use the carboxylic acid as a nucleophile. Generating the carboxylate could potentially generate the corresponding ester by nucleophilic substitution. Treatment of **1.30** with K_2CO_3 in DMF at 20 °C followed by the addition of

2-(Boc-amino)ethyl bromide did only afford traces of the corresponding ester **3.14** by LC-MS analysis. Cs_2CO_3 was applied instead which afforded the desired 2-(Boc-amino)ethyl ester **3.14** in more promising yields, though purification was unsuccessful. Alkylation using K_2CO_3 at elevated temperature (50 °C) in DMF overnight afforded the product **3.14** in acceptable yields (Scheme 3.5). Purification remained inconsistent as the product **3.14** precipitated when ethyl acetate extraction was attempted. Purification of the ester of **3.14** was possible using dry column vacuum chromatography. Boc-deprotection was conducted using standard conditions (TFA in CH_2Cl_2) affording the TFA salt of **3.15**·TFA in quantiative yields (Scheme 3.5). The similar synthesis afforded the *N,N*-dimethylethylamine derivative **3.16** from **1.30** and 2-bromo-*N,N*-dimethylethanamine, (Scheme 3.5).

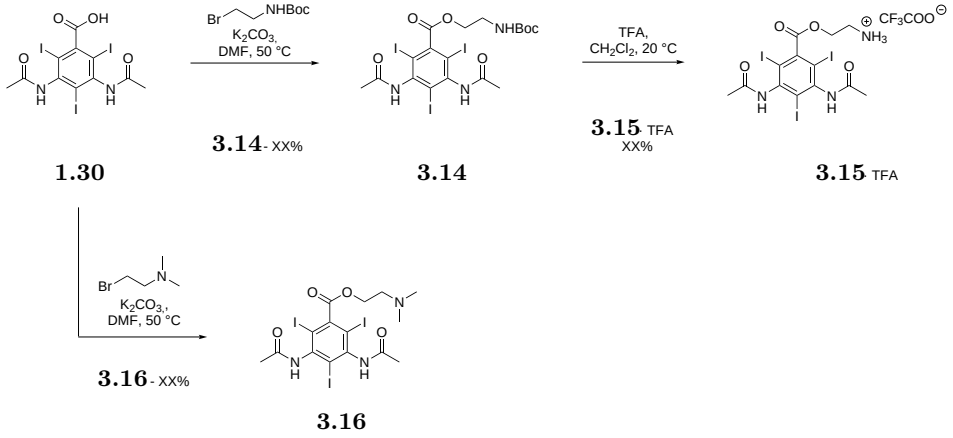

Scheme 3.5: Scheme for the amino functionalization of diatrizoic acid **1.30**.

3.9 Building blocks for development of new CT contrast agents

To display the potential scaffold of novel contrast agent, based on the core structure of 2,4,6-triiodophenol **1.37**, different building blocks were constructed. The choice of functional groups were chosen to show the chemical flexibility and the potential of providing different functionalities. Various building blocks were constructed by *O*-alkylation using K_2CO_3 in DMF at 20 °C. This afforded various building blocks with different functional groups (Scheme 3.6): 2-(2,4,6-triiodophenoxy)-ethanol **3.18**, 3-(2,4,6-triiodophenoxy)-propanol **3.19**, Boc-protected 2-(2,4,6-triiodophenoxy)-ethan-1-amine **3.20** and 2-(bromopropoxy)-1,3,5-triiodobenzene **3.21**. The corresponding *tert*-butyl and methyl 2-(2,4,6-triiodophenoxy)acetates **2.20** and **2.19** were likewise prepared in good yields.

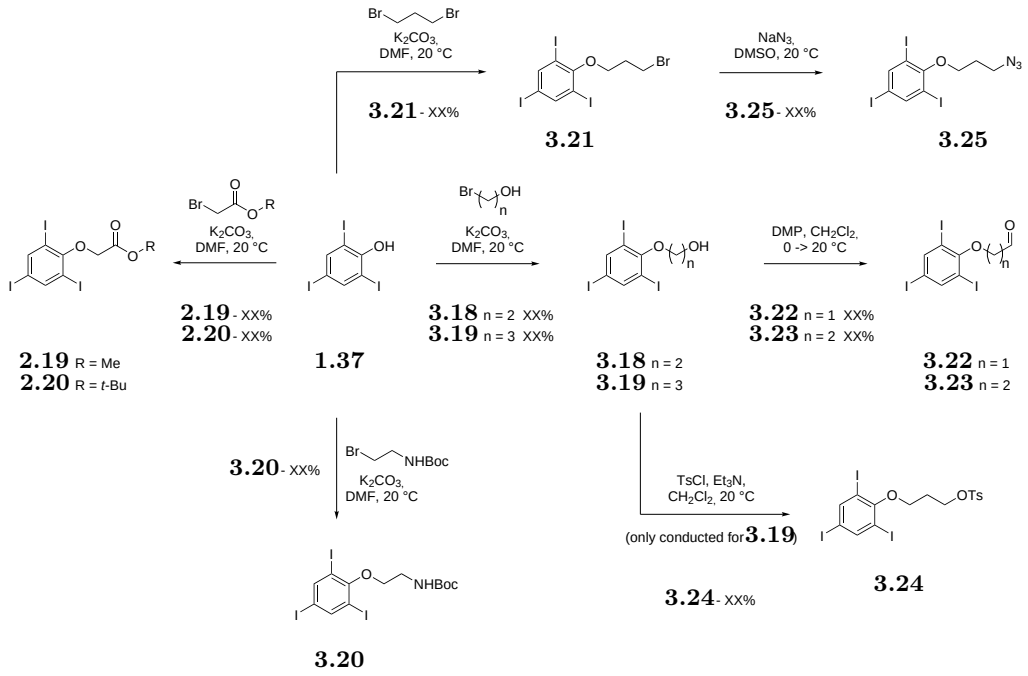

Scheme 3.6: Scheme for the scaffold of building blocks based on **1.37**.

The alcohols of **3.18** and **3.19** were converted to aldehydes **3.22** and **3.23** respectively by treatment with Dess Martin periodinane (DMP) in CH_2Cl_2 at 0 °C (Scheme 3.6). Moreover, **3.19** was transformed into the corresponding tosylate **3.24** using TsCl and Et_3N in CH_2Cl_2 (Scheme 3.6). The bromide **3.21** was treated with NaN_3 in DMSO at 20 °C to afford the azide **3.25** (Scheme 3.6). The synthesized building blocks were used in the following sections in the construct of new contrast agents.

3.10 Phosphoplipid based contrast agents

As an alternative, it was envisioned to implement CT contrast within the liposomic bilayer. This has previously been reported with the synthesis of diiodophosphatidylcholine lipid [99]. Instead of installing the iodide in the end of the fatty acid chain, modifying the head-group was attractive as the modified lipid would be available within one to two synthetic steps. From 1,2-dipalmitoyl-*sn*-glycero-3-phosphoetanolamine (DPPE, **3.26**) or 1,2-distearoyl-*sn*-glycero-3-phosphoetanolamine (DSPE, **3.27**), the corresponding head-group modified lipids were synthesized using **1.36**. The acid **1.36** was transformed into the *N*-hydroxysuccinimide activated ester **3.28** by use of *N,N'*-dicyclohexylcarbodiimide (DCC) and DMAP in ethyl acetate. The activated ester of **3.28** was directly subjected to **3.26** or **3.27** in DIPEA and $CHCl_3$ after aqueous work-up without any further purification. This afforded the head-group 2-(2,4,6-triiodophenoxy) acetamides of DPPE **3.29** and DSPE **3.30** (Scheme 3.7).

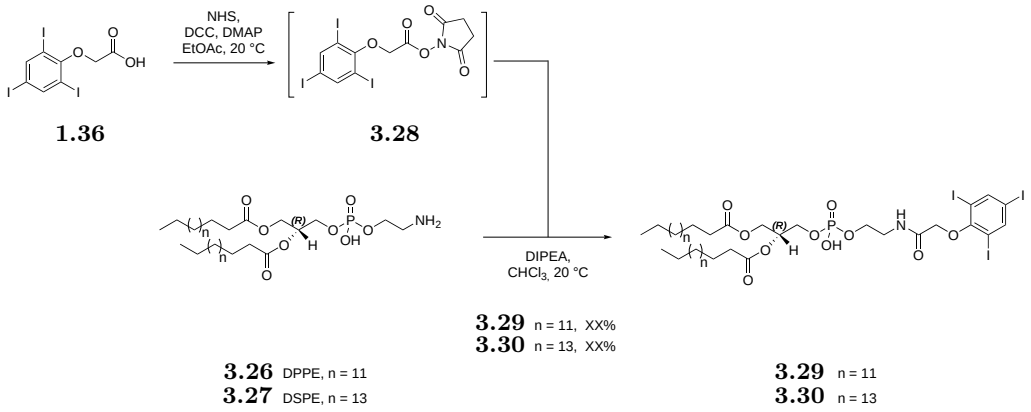

Scheme 3.7: Head-group modification of the phospholipids **3.26** and **3.27** using 2-(2,4,6-triiodophenoxy)acetic acid **1.36**.

3.11 Glucosamine based contrast agents

To compensate for the hydrophobic nature of the synthesized tri-iodophenoxy building blocks, the building blocks should be combined with hydrophilic counterparts to facilitate the proper permeability through the bilayer of the liposome. D-Glucosamine **3.31** was chosen for conjugation to the tri-iodophenoxy building blocks. Blocking the hemiacetal chemistry of the anomeric position by Fischer glycosylation followed by the installation of the 2,4,6-triiodophenoxy unit at the 2-amino position will leave the hydroxyl-groups of 3-OH, 4-OH and 6-OH available, which was thought as a handle for further modifications to control and customize the polarity of the synthesized contrast agents. In order to provide weak basic character for mediated loading the primary amine of glucosamine **3.31** could be converted into the secondary amine through reductive amination from the corresponding aldehyde building blocks of **3.22** and **3.23**. The secondary amine could likewise be achieved through nucleophilic substitution of the corresponding bromide of **3.21** or tosylate **3.24**, respectively. The amide could also be constructed from the **1.36** and glucosamine **3.31**.

According to literature, D-glucosamine hydrochloride **3.31**·HCl can be transformed into the methyl 2-deoxy-2-amino-D glucopyranoside hydrochloride **3.32**·HCl by peracetylation to give **3.33** followed by a Fischer glycosylation (Scheme 3.8) [100]. Peracetylation was conducted using acetic anhydride in pyridine at 20 °C. This gave the peracetylated product **3.33** (α/β = 20:1). The Fischer glycosylation of **3.33** was performed using refluxing 5% HCl in CH_3OH (Scheme 3.8). Prolonged reaction time was applied to make sure the acetamide was hydrolyzed. Concentration *in vacuo* afforded **3.32**·HCl in an α/β = 6:1 (Scheme 3.8). The ratio of α/β-isomers was concluded not to be decisive for the contrast properties nor the mediated loading properties, **3.32**·HCl was therefore used without further purifications.
The reductive amination was performed using **3.32**·HCl and the aldehyde **3.22** (Scheme 3.8). Compound **3.22** was chosen over **3.23** in order to avoid the potential side-reaction of β-elimination of the aldehyde **3.23**. Sodium triacetoxyborohydride ($NaBH(OAc)_3$) was

chosen as reducing agent over the corresponding sodium cyanoborohydride ($NaBH_3CN$) due to easier handling. The experimental procedure was conducted according to literature [101]. The hydrochloride salt of **3.32**·HCl was neutralized using Et_3N prior to the formation of the imine-intermediate. The reduction of the imine of **3.32** and **3.22** gave the *N*-alkylated **3.34** as the main species. The reductive aminated product **3.34** was isolated by dry column vacuum chromatography. The reductive amination was later on repeated and up-scaled. The upscaling was inconsistent as competing reduction of the aldehyde **3.22** to the corresponding alcohol **3.18** was observed. Therefore a disappointing yield was achieved. The observation of a low yield was believed to be due to the attempt of improving the yield by pre-mixing the amine of **3.32** and **3.22** in order to form the imine-intermediate prior to the addition of $NaBH(OAc)_3$. Since **3.34** only appeared in low yields, this could indicate that the imine-formation was formed inefficient.

The amide of **3.35** was obtained from the acid **1.36** and **3.32**·HCl, using EDC·HCl and DMAP (Scheme 3.8). Beside the intended product formation, a significant amount side-product of the migrated *N*-acylurea product of the activated ester was observed (according to LC-MS analysis). The presence of the *N*-acylurea side-product made purification by dry column vacuum chromatography difficult as similar retention factors of **3.35** and the side-product were observed. Applying an acidic wash (0.1 M HCl) during work-up, removed exclusively all of *N*-acylurea side-product by which isolation afforded the amidated product **3.35**.

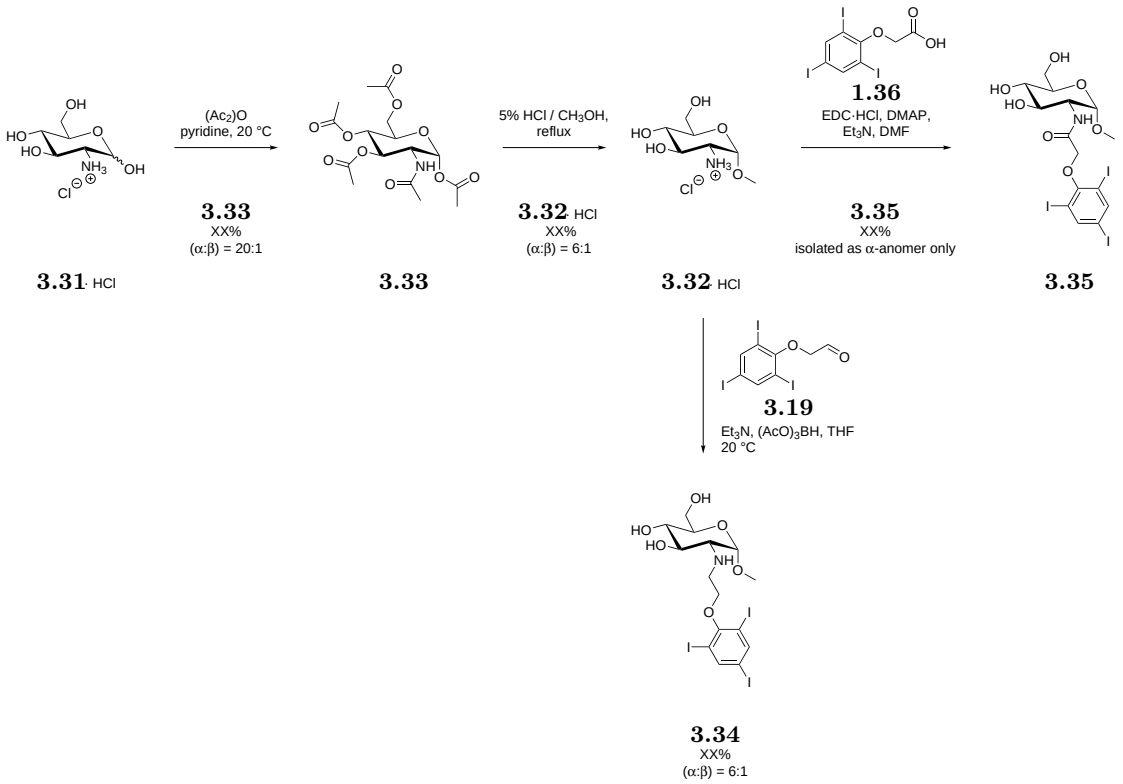

Scheme 3.8: Synthesis of glucosamine-derived CT-contrast agents **3.34** and **3.35**.

3.12 Mediated loading of contrast agents

Mediated liposome loading was demonstrated for contrast agents **3.10** and **3.15**. This was conducted by project partners of the Nanoguide-project. Liposomes with the lipid composition of HSPC/MPEG-2000-DSPE/cholesterol (3:1:1) (T_m = 55 °C, MW = 750 g·mol^{-1}) were prepared. 0.2 mol% of PE Lissammine Rhodamine B was added to the lipid composition in order to provide UV-Vis detection (λ_{max} = 560 nm). The lipid mixture was first lyophilized followed by rehydration using 120 mM $(NH_4)_2SO_4$ (pH 5.2) at 65 °C for 1 h. The size of the LMV liposomes was downsized and changed to LUVs by extrusion. Extrusion was conducted using 100 nm pore sized polycarbonate membrane and was repeated 21 times at 65 °C. This afforded LUVs with average size of 116 ± 0.29 nm with a narrow poly-distribution of PDI = 0.057.
The transmembrane $(NH_4)_2SO_4$ gradient was established by iso-osmotic dialysis against a 25 mM HEPES, 150 mM NaCl, pH 7.4 solution.The mediated loading was conducted at 65 °C. A solution of **3.10**·TFA or **3.15**·TFA in the given buffer with a D/L ratio = 0.1 were added to the liposome mixture. Encapsulation efficiencies of **3.10** did not exceed 10% while **3.15** was loaded to a level of 70% after 1 h at 65 °C. It was reasoned that the loading of **3.10** was insufficient due to the hydrophilic nature of **3.10**. No further optimization of the loading of **3.10** was pursued. The loading efficiency of **3.15** decreased over time, indicating a leaky behavior of **3.15** from the aqueous inner compartment. The reduction in loading over time was reasoned to be a consequence of the active loading being performed above the transition temperature (T_m) of the lipid-mixture constituting the bilayer of the liposomes.
Parameters like choice of external buffer solution, pH, mediated loading temperatures, size of liposome and D/L ratio were analyzed to optimize the loading of **3.15**.

3.13 Optimized loading using ammonium sulfate gradient

The loading temperature was analyzed at three different temperatures (40 °C , 55 °C or 65 °C) around the T_m of the lipid mixture using a pH 7.4 HEPES buffer. The highest loading was observed after 1 h at 65 °C corresponding to 72-73%. Similar loading efficiencies were seen after 24 h at 55 °C. The optimal D/L ratio were likewise found. Mediated loading of **3.15** using different D/L of 0.1 to 0.8 were analyzed. Using a D/L ratio of 0.1 yielded the best loading after 3 h.

The size of the liposomes were likewise analyzed. Two different sizes of 140 nm and 180 nm were tested. The highest loading was achieved using the 140 nm liposomes after 3 h while the same loading efficiency for the 180 nm liposomes was obtained after 20 h. Several buffers with different pH were tested for the mediated loading of **3.15**. The buffers and pH tested were 1) a 25 mM HEPES, 150 mM NaCl, pH 7.4 solution, 2) a 25 mM Tris, 150 mM NaCl, pH 8.1 solution, 3) a 25 mM MES, 150 mM NaCl solution and 4) a 25 mM PBS buffer, 150 mM NaCl, pH 7.0 solution. Beside the obtained loading using the HEPES buffer at pH 7.4, the best achievable mediated loading was achieved using the 25 mM PBS phosphate buffer, 150 mM NaCl. This afforded the encapsulated **3.15** liposomes (size 140 nm) with a 78% loading efficiency after 20 h according to UV-Vis measurements after spin column filtration. The measured osmolality of the liposome mixture was determined to

be 332 mOsm·kg^{-1}.

3.14 Mediated loading using citrate buffer gradient

Lipsomes based on the same lipid mixture as described above was used. Lyophilization and hydration using a 300 mM citrate buffer (pH 4, 576 mOsm·kg^{-1}) during heating at 65 °C for 1 h was performed. The size of the liposomes were increased as it was reasoned that the size of the liposome could be decisive for the mediated loading (bigger liposome, increased encapsulation efficiencies). Extrusion using 400 nm and 200 nm polycarbonate filters were used to afford LUV liposomes of 176±0.901 nm with a PDI = 0.071±0.032.
The gradient was established by adjusting the pH of the liposome mixture to pH 7.0 using 1 M Na_2CO_3. The contrast agent **3.15**·TFA was directly added to the mixture as a solid. The mediated loading was conducted at 55 °C for 3 h. This successfully afforded the loading of **3.15** with an encapsulation efficiency of 96% according to UV-Vis measurements. ICP measurements gave a loading efficiency of 91%.
With the promising loading efficiencies using the citrate buffer, the mediated loading was repeated in order to lower the osmolality of the liposome mixture for an *in vivo* study in mice, mainly to check whether the loaded **3.15** would provide a sufficient visible contrast. A 200 mM citrate buffer was used during the hydration affording the liposomes with a size of 169.7±2.4 nm and a PDI 0.063±0.021. The mediated loading was conducted by adjusting the pH using 1 M Na_2CO_3 solution. The final concentration of the loaded liposomes with a loading efficiency of 85%/73% (UV-Vis/ICP-MS) was determined to be 53 mM corresponding to a **3.15** concentration of 8.7 mg·mL^{-1} (5.01 mg I·mL^{-1}). The liposomes was further concentrated to a final iodine concentration of 10 mg I·mL^{-1}.

3.15 *In vivo* performance of mediated loaded liposomes

Liposome formulation of **3.15** was injected in the of NMRI mice from which CT scans was recorded. There was no visible contrast from the loaded liposomes.

3.16 Discussion and future perspectives

From the obtained mediated loadings and encapsulation efficiencies, it was clear that it would be difficult to achieve the previously reported concentrations of contrast agents by mediated loading. The current limitation to achieve the concentration corresponding to a sufficient contrast, is mainly proposed to be a consequence of the encapsulated amount of the buffer (citrate, $(NH_4)_2SO_4$ etc.). The amount of buffer encapsulated within the interior of the liposome after purification is estimated to be in range of 10% corresponding to a concentration of buffer in the range of 20-30 mol·L^{-1} solution liposome [102]. The concentration of buffer within the aqueous inner compartment would still correspond to the concentration used during the hydration-procedure (200-300 mM). Though, the concentration of buffer (20-30 mM) after purification puts the limit of the gradient and thus the extent of loading. An intuitive idea would be to increased the buffer-capacity of the buffer used. This will have the effect of providing a higher gradient implying that more material can be loaded. The limitation of increasing the buffer-capacity would be the corresponding increment in osmolality. A higher osmolality will lead to an increased

osmotic pressure across the membrane of the bilayer, by which in-stability of the liposomes is suspected to occur, due to uptake of solvent e.g. unbound water of the blood plasma leading to increased blood viscosity or even burst of the liposomes.

Another option would be to improve the size of the liposomes as an increased aqueous compartment would enable increased encapsulation of buffer during the hydration. Based on extensive experience, LUV liposomes are hardly reproducible in size [102]. In perspective: as the mediated loading have been applied to various drugs e.g. Doxorubicin where the therapeutic effect needed is low, mediated loading of contrast agents - where high concentrations are needed - is not suitable, unless precipitation inside the interior of the liposome is achievable.

Prospectively, it would therefore be of interest to conduct active loading of radioiodinated derivatives of **3.15** due to the sensitivity of radioactive compounds. This will likewise benefit the preparation method of liposomal formulations of radiolabeled contrast agents. According to the attractive isotopes of iodide and the EPR effect of liposomes, potentially novel liposomal contrast agents can be visualized by different imaging-modalities (SPECT and PET). This is at the moment being undertaking by project partners in the Nanoguide project.

3.17 Conclusion

Five new contrast agent (**3.10**, **3.15**, **3.16 3.34** and **3.35**) for CT imaging have been synthesized for mediated loading in liposomes. **3.10** and **3.15** were loaded in liposomes where **3.15** showed the most promising results. An encapsulation efficiency of 85% corresponding to a 5.01 mg I·mL^{-1} was achieved. The *in vivo* injection in a mouse model confirmed that this concentration was in-sufficient for obtaining contrast. It was concluded that the gradient established was not sufficient to loading the amount needed to achieve a proper CT contrast.

Cyclodextrin-pluoronic based polyrotaxanes for PET-imaging

4

An interesting supramolecular construct with application within nanomedicine and drug delivery is polyrotaxanes. Polyrotaxanes (PRs) are the term and collective name of the supramolecular construct of "threaded macrocyclics" onto an axle (usually a polymer). The intermediate assembly is referred to as the pseudorotaxanes where disassociation (de-threading) is still optional. The polyrotaxanes are formed when the pseudorotaxane is subsequently endcapped with a bulky endgroup with the intended purpose of trapping the macrocyclic threaded onto the polymer. When retained on the polymer, the macrocyclic possesses, at this state, only rotational and longitudinal motions until slippage of the macrocyclic occurs or detachment by either macrocyclic opening or the endcaps are liberated from the PRs. The driving force for the assembly is mainly based on non-covalent interaction. A schematic representation is shown in Figure 4.1.

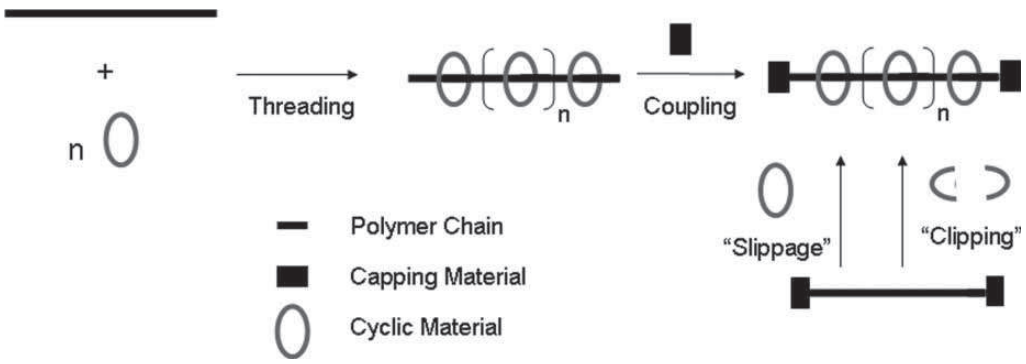

Figure 4.1: Schematic representation of the concept and synthesis of polyrotaxanes.

One example of a PR system is the cyclodextrin (CD)/pluoronic-based PRs. Pluoronic polymers are categorized as being the biocompatible and less toxic tri-block polymer of PEG-PPG-PEG. The pluoronic polymers vary in size as well as in the total ratio of the PEG and PPG segments. The most common pluoronic polymers are listed in Table 4.1. As seen from the table the size (1.9 – 12.5 kDa) of polymers as well as the hydrophilic/hydrophobic balance (HLB) vary for the different polymers. The HLB is defined as an empirical numerical scale, used today to rank polymers and surfactants by their polarity (higher the value, the more polar the polymer/surfactants will be) [].

Table 4.1: Table listing the different pluoronic polymers and the composition and properties.

Physicochemical characteristics of Pluronic block copolymers

Copolymer	mol.wt.	Average no. of EO units (x)[a]	Average no. of PO units (y)[a]	HLB[b]	Lot no.	CMC, %wt[c]
F88	11,400	207.27	39.31	28	WPAS-575B	0.28
F108	14,600	265.45	50.34	27	WPON-522C	0.032
F38	4,700	37.56	17.1	25	WPDR-504B	N.A.
F127	12,600	200.4	65.2	22	WPMN-581B	0.004
L35	1,900	21.59	16.38	19	WPMQ-592D	1
P85	4,600	52.27	39.66	16	WPOP-587A	0.03
L64	2,900	26.36	30.00	15	WPAQ-561B	0.14
P105	6,500	73.86	56.03	15	WPER-598D	0.004
L43	1,850	12.61	22.33	12	WPMS-508B	0.4
P103	4,950	33.75	59.74	9	WPWQ-557B	0.003
L81	2,750	6.25	42.67	2	WSOO-83457	0.0063
L101	3,800	8.64	58.97	1	WPHP-547B	0.0008
L121	4,400	10.00	68.28	1	WPAO-550B	0.0004

N.A., not applicable.
[a] The average numbers of EO and PO units were calculated using the average molecular weighs (mol.wt.) provided by the manufacturer.
[b] HLB of the copolymers were determined by the manufacturer.
[c] CMC values were determined previously using pyrene probe (Kozlov et al., 2000).

Cyclodextrins are defined as being cyclic oligosaccharides consisting of repeating α-1,4-D-glucopyranoside units (figure Figure 4.2). The most common CDs are α, β and γ CDs with a six, seven and eight glucopyranoside units, respectively []. The conformational structure of CDs are similar to a truncated cone by which the hydroxy-groups are oriented towards the exterior such that the interior is relatively hydrophobic similar to a mixture of EtOH and H_2O (Figure 4.2) []. The hydrophobic cavity allows for host guest inclusion complexes with small hydrophobic molecules or segments of polymers. Cyclodextrins have found several applications like drug delivery, solubility enhancement and mediated drug release [103, 104].

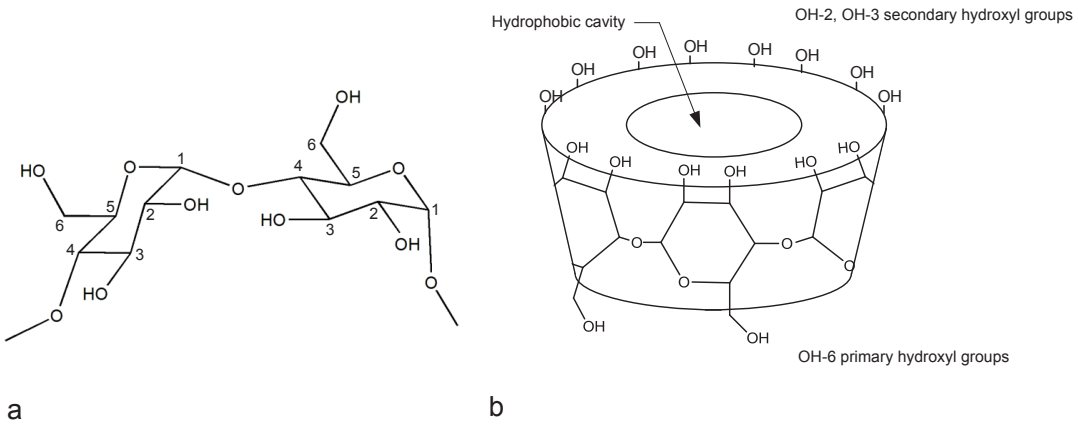

Figure 4.2: a) glycosidic linkage b) the conformational structure of CDs

The prerequisites for the rotaxanation reactions with CDs and pluoronic ploymers are among other parameters influenced by physical constraints. The cross-sectional area of the polymer must be of the proper dimension to induce a favorable inclusion complex with the CD. The solvent chosen for the rotaxanation must provide solubility but not be competitive in regard to the inclusion complex formation. The pluoronic polymer should be functional at the terminal ends for the endcapping reaction. Likewise, the endcapping

reaction has to be orthogonal/selective to the hydroxy-group chemistry of the CDs and be fast in order to capture as many CDs as possible. The review of Loethen *et al.* cover the common trends of choice of endcaps as well as the common post-modification options of threaded CDs [105].

4.1 Niemann Pick disease Type C

The group of Thompson as well as the Harada group are among the main frontiers within the field of CD/pluoronic PRs. CD/pluoronic PRs have found used with the Niemann Pick Type C (NPC) disease, drug delivery of gene therapy and contrast agents [].
The NPC disease is a not-tissue-specific genetic disorder owing to mutations in genes encoding for efflux proteins, which are located in the membranes as well as within the aqueous compartment of the late endosome/lysosome (LE/LY) [106, 107]. Normally, the role of these proteins is to control the regulation and efflux of un-esterified cholesterol. The deficiency of these proteins, due to mutations, leads to aberrant accumulation of un-esterified cholesterol, which is characterized as a lysosomal storage disease. The build-up of cholesterol in the lysosomes trigger a number of severe effects like lysosomal swelling, upregulation of genes controlling cholesterol synthesis, and low density lipoproteins uptake as well as neurological effects like demyelination of brain cell axons together with death of Purkinje cells [107] and release of cytokines in regard to macrophage activity [107]. These effects compiled lead to cell death with the symptoms taking shape as neurological, hepatic and/or pulmorary symptons that will become intensified over time [107]. At the severe stages, this can lead to dysarthria, hysphagia, ataxia as examples of neurological disorders caused by NPC [107].
In vivo studies have shown that CDs have been able to mobilize accumulated cholesterol from the late endosomes/lysosomes due to the inclusion complex ability of CDs [106]. The response of using 2-hydroxypropyl (HP)-β-CD is a normalization in intracellular levels of un-esterified cholesterol as well as down-regulation of the intrinsic cholesterol synthesis and activation of various related metabolic-genes [107]. Despite these promising signs of response using HP-β-CD, at this given point, mice studies have indicated that rather high doses in range of 4 g HP-β-CD·kg^{-1} body weight and even higher doses is expected to be needed as the clearance from the bloodstream is rapid in accordance to the water solubility and the relative low molecular weight of CDs [106]. Likewise, it has been reported that re-accumulation of cholesterol in the LE/LY was observed, which could indicate a post-treatment up-regulation of cholesterol upon treatment [107]. This means that treatment using HP-β-CD has to be mediated by a sustained dosage by continuous administration of HP-β-CD by multiple/repeating doses [107]. This clearly states the drug delivery issue of CDs in accordance to the high doses needed and the continuous therapeutic dose treatment of NPC.
CD-based PRs become therefore useful as an efficient carrier of CDs, as multiple units of CDs can be threaded onto the polymer/axle. Likewise applying a long-time circulation property could improve a more persistent treatment and delivery of CDs to NPC affected cells.
The group of Thompson recently published the construction of HP-β-CD/pluronic PRs. HP-β-CD was chosen over β-CD due to the higher water solubility of HP-β-CD (650 mg·mL^{-1}) as opposed to native β-CD (18 mg·mL^{-1}) which also is reported to be

parenterally nephrotoxic. The study of Harada *et al.* showed how the dimensions of cavity of CDs has a significant influence on the overall threading []. Harada *et al.* showed that α-CDs are easily threaded onto PEG while β-CD are not threaded. β-CD is on the other hand preferably threaded on PPG. This is exemplified in the preceding polyrotaxane assemblies. The coverage of the PPG has been verified by 2D-NOESY NMR experiment where a spatial correlation between the methyl group of PPG as structural backbone of the CDs [106]. Various derivatives of CDs have likewise been threaded on pluoronic polymers.

4.2 Threading/inclusion complex formation of CDs

Usually the inclusion complex formation is conducted in a polar solvent, by which the CDs will be soluble while the guest molecule will be less soluble. Using this setup, the solvent can be used to drive the inclusion complex formation – based on the principles of the hydrophobic effect - as the cavity would act as hydrophobic pocket where the hydrophobic guest molecule can reside. Together with the entropic release of the high energetic restricted water molecules residing inside the cavity, these aspects are some of the most important effects influencing the dynamic of the inclusion complex formation.
Normally in CD-based PRs formation, the entropy will be disfavored due to the loss of conformational flexibility of the polymer. As the CDs likewise become more ordered with only longitudinal – and rotational movement, this will contribute to an entropic disfavor. The enthalpy contribution are mainly dominated by the hydrophobic effect of the inclusion complex formation as well as the solvent relaxation upon threading [105]. According to the recent papers within Thompsons group, threading conducted in apolar solvents have led to higher threading efficiencies of CDs. The rationale for the higher threading efficiencies would be that multiple CDs would tend to form aligned channels/tubings in a hydrophobic environment, by which the pluoronic polymer is easily threaded []. When entering the aligned arrangement of cavities, the pluoronic polymers is more easily directed through the alignment of multiple CDs resulting in a higher loading/threading.

4.3 *In vivo* bio-distributions studies of CD/pluoronic PRs

A study conducted in the group of Thompson showed the synthesis of HP-β-CD/pluronic PRs with trinitrobenzene as endcapping group [106], and various pluoronic polymers was threaded using HP-β-CDs. The threading was conducted in hexane which afforded promising threading efficiencies. The PRs were tested *in vitro* at a buffered pH of 5.5 and 7.4, displaying prolonged stability. The synthesized PRs were likewise tested *in vitro* on npc2$^{-/-}$ fibroblast cell line and showed a remarkable reduction of aberrant un-esterified cholesterol according to filipin staining, which is commonly used for the quantification of cholesterol (Figure 4.3). The mechanism of mobilization and corresponding uptake of the cholesterol remain unknown.

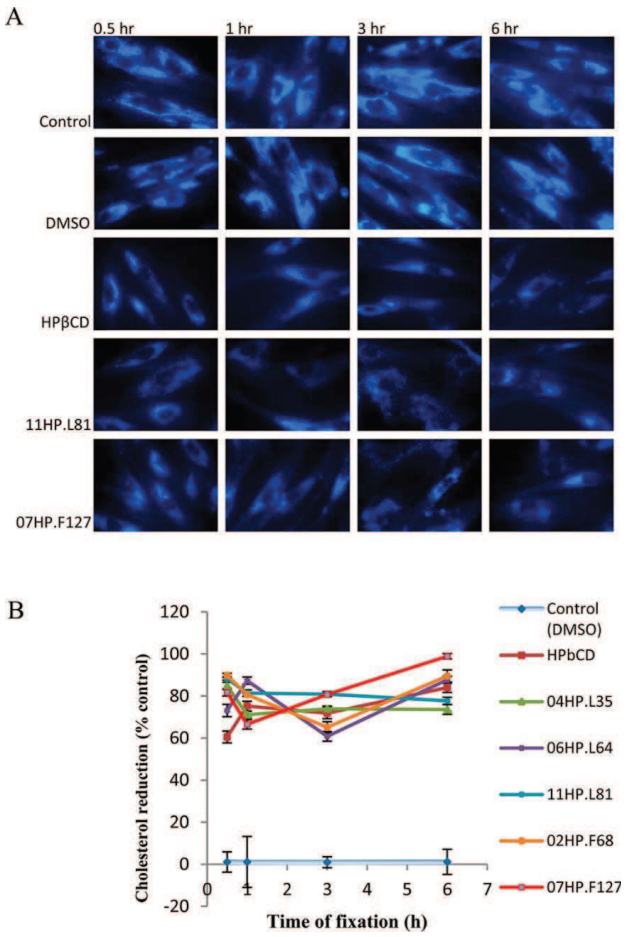

Figure 4.3: *In vitro* evaluation of cholesterol-uptake by CD/pluoronic based PRs. A) The filipin stain of npc2$^{-/-}$ fibroblasts treated with CD/pluoronic based PRs (entry 11HP.L81 and 07.HPF127) and HP-β-CD as a function of time. When compared to the control, the intensity of stain is significantly lowered, indicating that the amount of cholesterol have decerased. B) direct quantification of the effect the CD/pluoronic based PRs to lower the amount cholesterol.

4.4 CD/pluoronic PRs as contrast agents

HP-β-CD/ pluoronic PRs have likewise found use as MRI contrast agent for blood pool imaging. PRs conjugated with GD^{3+} chelates (T1 paramagnetic relaxation enhancement) would provide the property of enhancing the relaxation rate of T1 of coordinated H_2O-molecules. As highlighted in the study in Thompson group, the attractable features of using PRs as contrast agents contrary to clinical approved contrast agents in current use, would be prolonged circulation times as well as higher Gd^{3+} loading per molecule. Moreover, other nanomaterials used as contrast agents, suffer from poor renal filtration as well as hepatobiliary uptake and *in vivo* accumulation. Additionally, the use of acyclic chelates can cause leakage of GD by which these chelates are referred as being kinetically labile. Leakage of Gd from the contrast agent can lead to nephrogenic systemic fibrosis.

As stated, a polyrotaxane scaffold-based contrast agent will offer the benefit of higher Gd-loading - as multiple Gd chelates can be appended per polymer - and prolonged circulation time according to the flexible rod-like structure of PRs []. Several studies have indicated that the morphology has an influence on the macrophage uptake, i.e. spherical nanoparticles have proved to be taken up by macrophages and HeLa cells at higher rate than rod-like nanoparticles [].

The study concerning HP-β-CD/pluoronic PRs as MRI contrast agents was based on the Pluoronic F127 polymer with a 46% HP-β-CD threading efficiency and cholesterol as endcapping groups. The macrocyclic chelation unit of 1,4,7,10 tetraazacyclododecane-1,4,7-triacetic acid (DO3A) was further introduced in a post-modification strategy of the PRs. The hydroxy shell of the HP-β-CD of the PR was first functionalized with 1,8-diamino-3,6-dioxooctane (EDA) via a CDI activation followed by nucleophilic addition of *p*-thioisocyanate-benzyl-DO3A. 14 units of DO3A were appended to the CD/pluoronic PRs and loaded with 14 Gd^{3+} ions and this construct was characterized in terms of a standardized relaxation of H_2O per Gd concentration (r1). The MRI properties is depicted in figure **??**.
A proportional tendency of increasing relaxitivity with increasing concentration of Gd was observed for both T1 - as well as T2 relaxation. In accordance to the higher loading of Gd per PR, the relaxation rate of the bound H_2O was observed to be faster than the corresponding DO3A-HP-β-CD monomer. This was further supported by the *in vivo* performance. Enhanced contrast was observed of the cardiovascular system (blood pool) for prolonged time with subsequently clearance. These findings were promising as no persistent *in vivo* accumulation of the PRs was observed.

This was further substantiated in the follow up structure-property relationship study of the class of HP-β-CD/pluoronic PRs with cholesterol as endcaps. The aim of this study was to analyze the *in vivo* distribution, pharmacokinetics, clearance and the interaction with the protein corona with common proteins found in the blood plasma [108].
This study indicated that a tendency between the threading efficiency of the PRs and the overall *in vivo* performance. The corresponding PRs made from the L35 and L81 pluoronic polymers possessed the highest threading efficiencies but also exhibited longest circulation time in BALB/c mice [108]. The overall observed trend was a fast kinetic phase along with a biphasic clearance [108]. In both cases, it was reasoned that the flexible rod-like morphology was determining the outcome of the *in vivo* clearance. As the PPG-segment of L35 and L81 constitute the main part of these pluoronic polymers, high threading efficiencies make the PRs of L35 and L81 adopt a rod-like structure [108].
In terms of the bio-distribution, the highly threaded PRs showed preferentially uptake in the liver while less PRs were accumulating in the lungs. The blood compatibility of PRs was likewise evaluated. No evident kidney toxicity nor liver damage or signs of hemolysis were observed. As expected, the interaction of PRs with the protein corona was mainly constituted by lipoproteins which was in accordance to the design of PRs with cholesterol endcaps. As part of the design in the above-mentioned PR for MRI contrast enhancement, the choice of cholesterol as endcapping group was based on the choice of a drug delivery tag. As cholesterol is transported by several lipoproteins to the LE, the concentration of the PR could hopefully be enhanced at the LE/LY site [108]. The relaxitivity of this

family of PRs with cholesterol was likewise characterized and compared to DOTA chelated Gd (DOTAREM). In comparison to the previously developed PRs with TNTS endcaps, the cholesterol endcapped PRs showed similar relaxitivities, which was concluded to be in the range of 2-4 fold higher than the monomeric DOTAREM [108].

4.5 Problem statement

Having the positron emitting ^{64}Cu cyclotron disposable at the Heavesy laboratory at the Center of Nuclear Technologies, Technical University of Denmark, the ^{64}Cu-chelated PRs could be synthesized. A collaboration was therefore established between the group of Professor Thompson and DTU Chemistry. To enable a more sensitive imaging of the CD/Pluoronic-based PRs *in vivo*, and obtain improved information of the bio-distribution, CD/Pluoronic-based PRs able of chelating ^{64}Cu would have to be synthesized.

4.6 Design and theoretical deliberation of PET HP-β-CD/pluoronic PRs

With the well-established and documented use of HP-β-CD/pluoronic PRs as contrast agents within the MRI modality, PET imaging would offer a higher sensitivity and potentially more clearly elucidation of the *in vivo* performance and biodistribution of tissues with low accumulation of PRs. One issue that remains an open question would be whether PRs are able to cross the blood brain barrier? This question could potentially be addressed by the development of PRs for ^{64}Cu chelation.
In order to correlate the already achieved MRI imaging of CD/pluoronic based PRs with the PET-imaging the construct of the PRs for PET imaging should not deviate too far from the CD/pluoronic based PRs core-structure used in the MRI imaging study. In accordance with the previous studies of the cholesterol endcapped HP-β-CD/pluoronic PRs, the PRs of L35 and L81 showed the longest circulation times. It was therefore decided to base the PRs on the pluoronic polymers of L35 and L81. CD-based PRs generally possess poor solubility hypothesized by the conformational orientation of the CDs that provide hydrogen bonding in-between the repeating units of CDs. This has the effect that the pluoronic polymer and threaded CDs have a confined/restricted interaction with the solvent through hydrogen bonding [105]. In order to improve the solubility of this class/-type of PRs for PET imaging, the threading experiments were conducted using a mixture of HP-β-CD and the commercially available Captisol. Captisol is a CD derivative with randomly ether-modified butyl sodium sulfonates which by the polar sulfonates enhance solubility compared to the native CD []. The average degree of modification of sulfonates is stated to be approximately 6.6.
In terms of applying functionalities of PRs two strategies are often used. The most commonly way is post-modification of the hydroxyl shell of CDs. This is determined by the hydroxy-group chemistry. This method usually lacks control as the modification takes place randomly. Improved control can be achieved by threading functionalized CD derivatives. Various mono-functionalized CD-derivatives are achievable from the mono-tosylated β-CD. The mono-tosylated β-CD can then easily be exchanged with i.e. azide that offer the feasible click chemistry of the Cu catalyzed azide alkyne cycloaddition (CuAAC) with

a corresponding alkyne.
Based on the previous designs, the employed linkage was based on carbamates. The carbamates are hypothesized to undergo hydrolysis by enzymatic cleavage and was proven to be stable at pH of 5.5 and 7.4 corresponding to pH levels found in the blood and LE/LY.

A secondary objective of this project was to develop a PR-based contrast agent for dual modality imaging. Besides introducing the DOTA moiety for chelation it would be interesting to see if an aryl-TMS moiety could be appended/grafted to PRs as a precursor for radioiodination. Gd chelation combined with the radioactive isotopes of iodine would offer a dual imaging modality. Inspired of the post-modifications strategies of dextran-polymers using CD derivatives [109], it was envisioned that the aryl-TMS could be grafted onto the CD-PRs through the ring-opening of the corresponding (*p*-TMS)-phenyl glycidyl ether (keeping in mind that β-elimination could be a potentially side-reaction) or through click chemistry having threaded N_3-B-CD followed by a subsequent CuAAC with *p*-ethynylphenyltrimethylsilane. The triazole would potentially induce an inductive effect on the activation of the *p*-ethynylphenyltrimethylsilane according to the three nitrogen atoms constituting the ring. It was hypothesized that the mesomeric effect would be dominating and thus provide the activation of the aryl-TMS to undergo electrophilic aromatic *ipso*-substitution with the iodonium ion.

4.7 Synthesis of the CD/pluoronic based polyrotaxanes

The pluronic polymers of L81 **4.1** and L35 **4.2** was first functionalized at the end terminals with the tris(2-aminoethyl)amine (TAEA) using a CDI mediated activation of the terminal hydroxyl groups. Prior to the reaction, the pluoronic polymers was azeotropic concentrated *in vacuo* using toluene. The pluoronic polymers was then pre-activated using CDI in CH_3CN followed by the addition of tris(2-aminoethyl)amine (TAEA). TAEA modification of L81 **4.3** was afforded in a low yield of 13%. but repetition of the TAEA modification afforded the TAEA modified L81 pluoronics polymer **4.3** in 79%. The TAEA modification of L35 **4.4** was synthesized in 62% yield (Scheme 4.1)

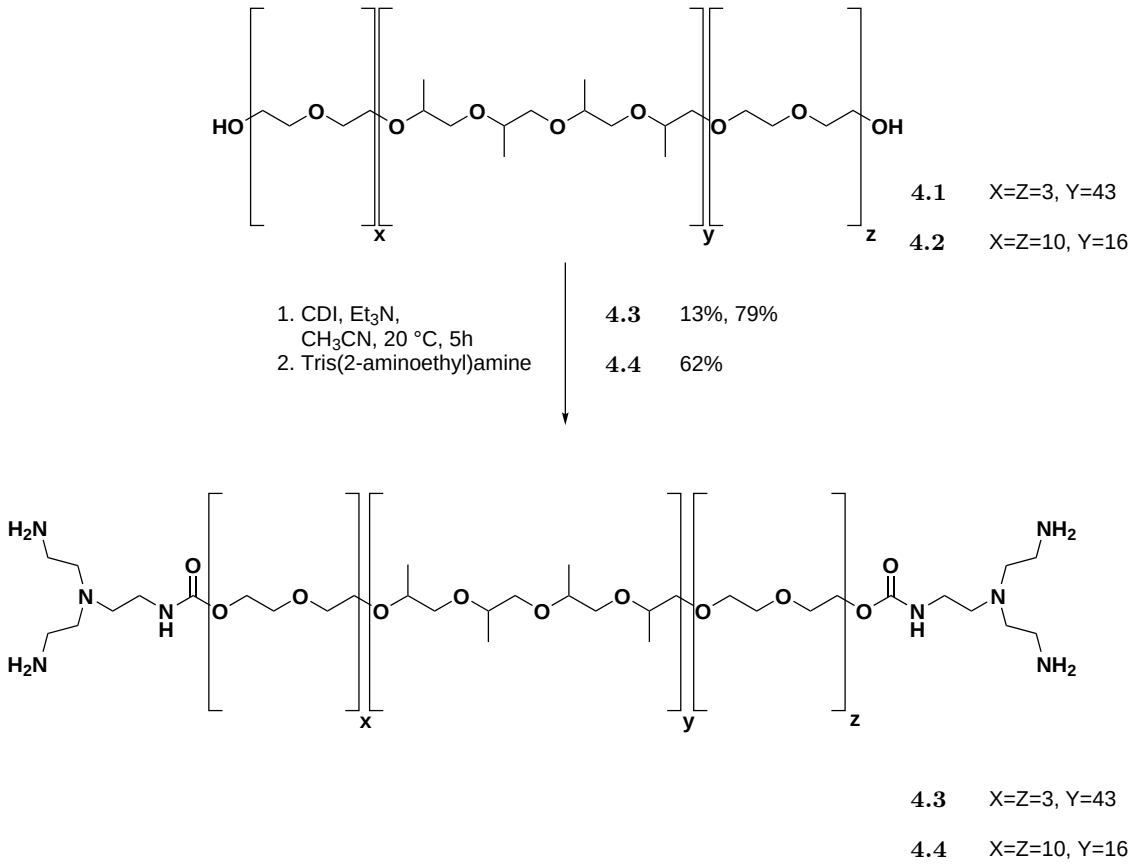

Scheme 4.1: TAEA modification of the pluoronic polymers of **4.1** and and **4.2** respectively.

The polymers of **4.3** and **4.4** was then threaded using a CD feed ratio of 70/30 of HP-β-CD/captisol, respectively. The total CD amount used was based on the theoretical amount of threaded PPGs units of the respective pluoronic polymers. As an estimate, it was assumed that β-CDs cover the PPG-segment with an average coverage of 2 PPG/CD. This will give a maximum of threaded CDs possible of 8 and 21 CDs for L35 **4.2** and L81 **4.2**, respectively. Before threading, **4.3** and **4.4** were vigorously suspended in hexane overnight. HP-β-CD and captisol was added as fine-grinded mixed solid to the hexane solutions of **4.4** or **4.3**, respectively. Bath and probe sonication were then conducted as sonication has proven to improve the threading efficiencies in previous studies []. Sonication is reasoned to disrupt any micelle formation that is believed to be the state of supramolecular assembly above the level of the aggregation concentration []. The threading reaction was then conducted for 72 h. The solvent was then changed from hexane to CH_2Cl_2 and the formed pseudorotaxanes was then endcapped using cholesteryl chloroformate and Et_3N. Subsequent dialysis and lyophillization afforded the threaded L35 and L81 HP-β-CD/Captisol PRs, **4.5** and **4.6** respectively (Scheme 4.2).

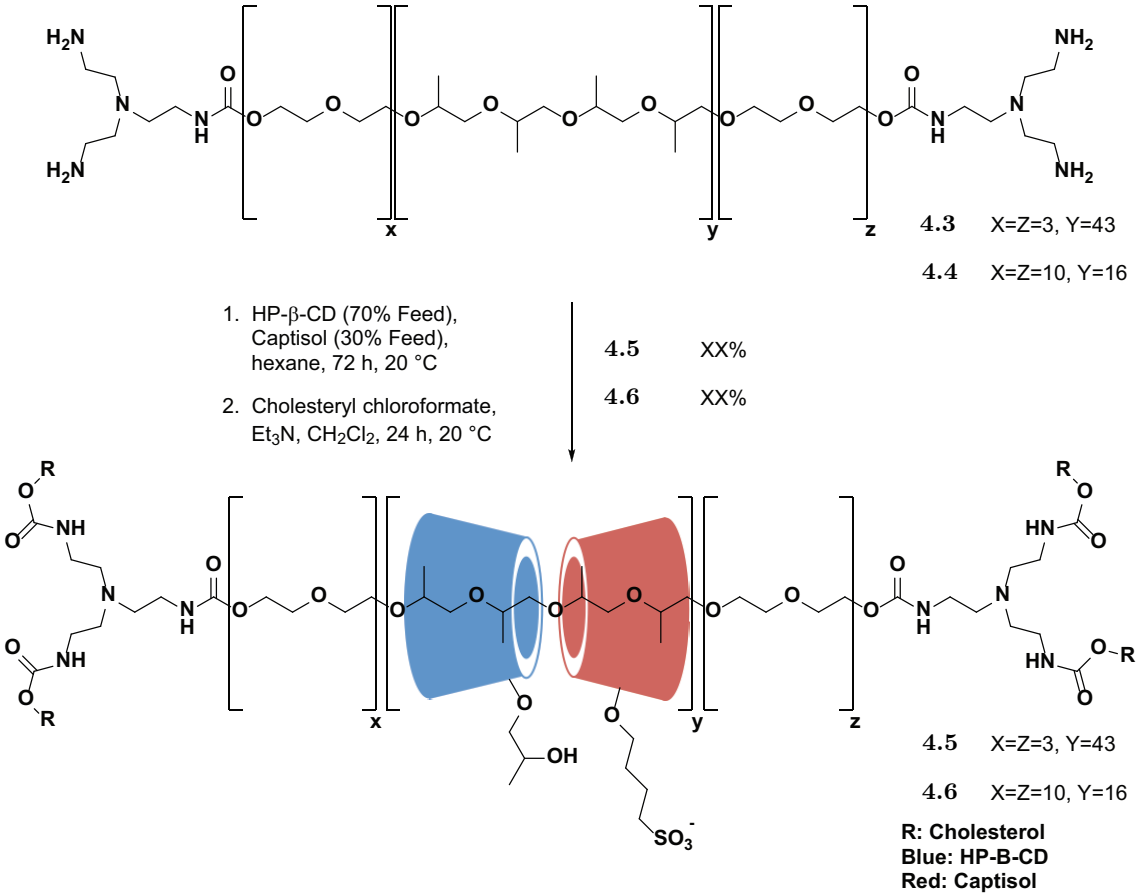

Scheme 4.2: The threading and formation of CD/Pluoronic-based PRs of **4.5** and **4.6**, respectively

Other CD feed ratios of 50/30/20 and 65/30/5 of HP-β-CD/Captisol/N_3-β-CD were threaded respectively. According to previous studies, 6-monodeoxy-6-monoazido-β-CD (N_3-β-CD, **4.7**) has been successfully threaded onto pluoronics []. N_3-β-CD was synthesized according to literature (Scheme 4.3). 6-*O*-mono-tosyl-β-CD (TsO-β-CD, **4.8**) was first synthesized from the inclusion complex of native β-CD **4.9** and TsCl followed by deprotonation using concentrated NaOH. This afforded **4.8** as the mono-tosylated main compound (Scheme 4.3). Recrystallization afforded the pure monotosylated **4.8**. The tosyl group was exchanged with the azide using NaN_3 in DMF at 70 °C. This afforded the 6-monodeoxy-6-monoazido-β-CD (N3-β-CD) (Scheme 4.3).

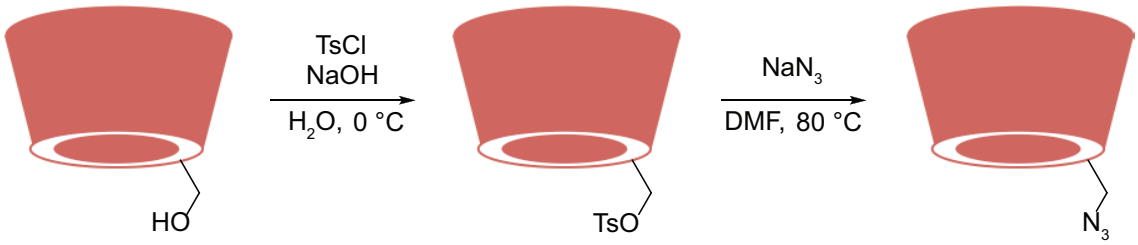

4.10 **4.9** **4.8**

Scheme 4.3: The synthesis of **4.7** via the monotosylated CD-derivative **4.8**.

The threading efficiencies was roughly estimated based on ^{1}H-NMR. By comparing the integral of CH_3-group resonance of the PPG to the integral of the anomeric protons of the threaded CDs, the threading efficiency can be estimated accordingly to the theoretical threading efficiency, defined previously. The ratio of HP-B-CD/captisol was determined by comparing the signal of the butyl-linker to the number anomeric protons representing the number of total CDs. The difference between the number of CDs and the number of captisol will determine the number of HP-β-CDs or HP-β-CD + N_3-β-CD. The first threading experiment **4.5** conducted of **4.3** was considered questionable according to the NMR analysis. This was reasoned as the number of β-CDs exceeded the number theoretical β-CDs possible. It was concluded that the threading was incomplete or impure with the presence of free CDs. Re-dialysis of **4.5** gave no further improvement of the purity by which it was concluded that **4.5** was low threaded. Repeating the threading of **4.3** afforded gave expected threading efficiencies. **4.4** was successfully threaded with a threading efficiency of the threading efficiencies of **4.6** and **4.5** are in accordance with previously reported. The estimated masses calculated are accordingly to the previously measured GPC measurements of similar constructs []. The PRs of **4.6** and **4.5** was then post-modified using 1,8-diamino-3,6-dioxooctane (EDA) and CDI in dry DMSO (Scheme 4.4). The polyrotaxane of **4.6** and **4.5** were respectively pre-activated for 24 h with CDI and Et_3N in DMSO prior to the addition of EDA. In order to ensure that no crosslinking occurred, excess of EDA and CDI were used according to procedure. This afforded the amino-functionalized PRs **4.11** and **4.10** Attempt to lower the equiv. used of EDA and CDI was tried but was not concluded successful as the DMSO used had a high water content (bubble formation during addition of CDI).
DOTA was appended to **4.11** and **4.10** in freshly distilled DMSO by the nucleophilic addition of DOTA-NCS, respectively (Scheme 4.4). The grafting of DOTA was designed with the aim of one DOTA unit per CD for **4.11** and two DOTA units per CD for **4.10**. This afforded of what to be believed at the DOTA appended PRs **4.13** and **4.12**, respectively.

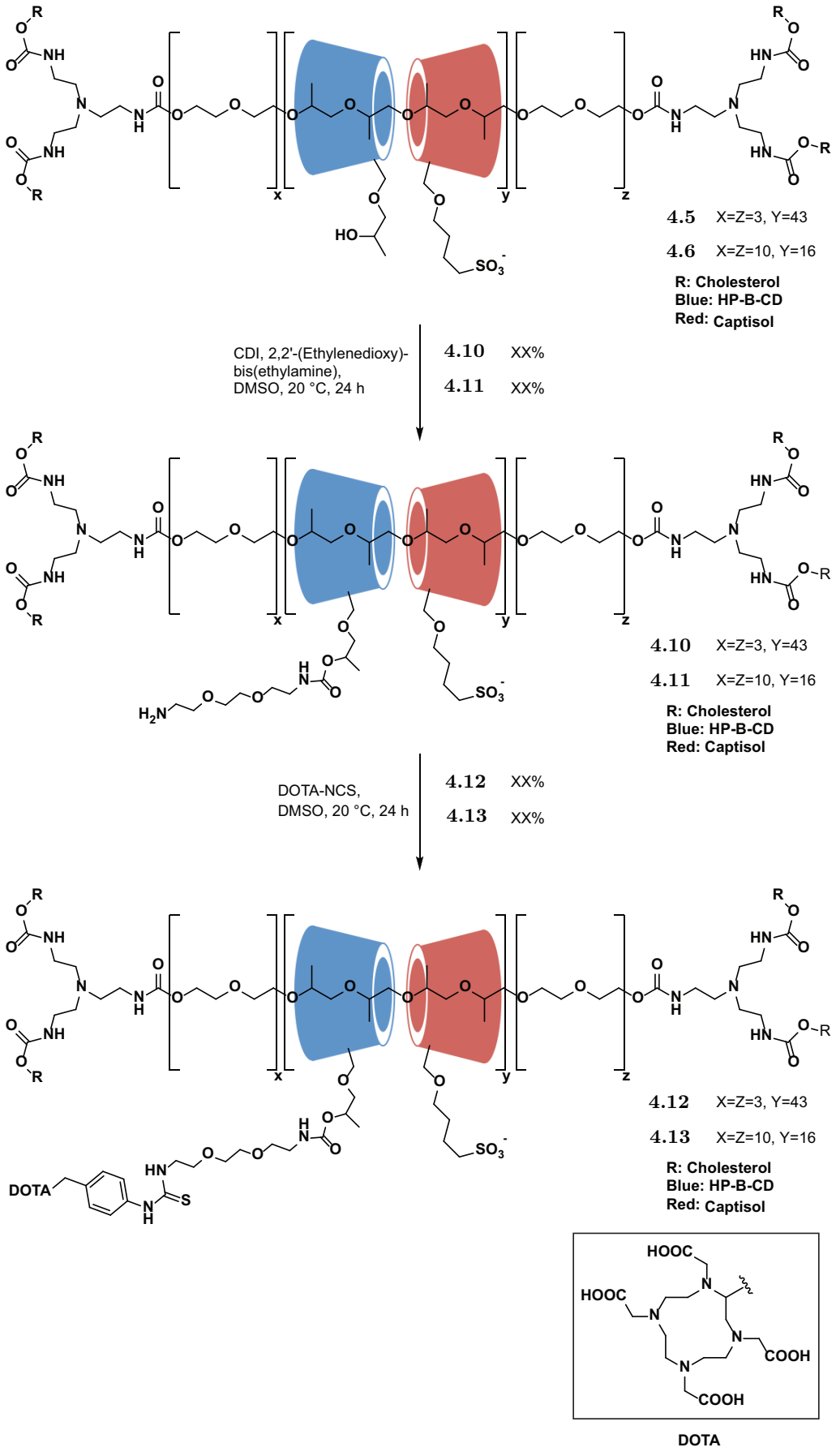

Scheme 4.4: The EDA post-modification of **4.5** and **4.6** and grafting of DOTA-NCS.

4.8 Discussion

At the moment, the successful grafting of DOTA is currently under investigation. The presence of DOTA is questionable as it is hardly detectable by ^{1}H-NMR as the resonance signals are not significant enough compared to the remaining backbone of **4.13** and **4.12**. HSQC-NMR analysis of **4.12** was conducted in order to verify the presence of the aromatic resonances of the benzylic moiety. No correlation was detected for **4.12**, unfortunately. Despite these ^{1}H-NMR analysis, **4.12** was successfully Gd-loaded to a Gd content of 9% wt, which on the other hand could verify the presence of the DOTA-moiety. Supporting analysis in needed to ensure the presence of the DOTA moiety.

Grafting experiments of the aryl TMS moieties of **2.4**, **2.1** and **4.14** are still on-going. The precursors of **2.4** and **2.1** were synthesized according to the procedures developed in chapter **??**. The epoxide of **4.14** was conducted by *O*-alkylation of **2.4** using epichlorohydrin and K_2CO_3 (Scheme not shown). The grafting of **2.4** was mediated using CDI in DMSO on **4.10** while the grafting of **2.1** was mediated using the activated ester made from EDC·HCl. The basic ring-opening of **4.14** was attempted by treating **4.15** with NaOH prior to the addition of **4.14**.

All TMS-aryl grafting has been carried out but was not conclusive as these experiments were conducted and the end of the time-frame of this project. The TMS-aryl grafting is still currently on-going.

4.9 Conclusion

PRs of based on the construct illustrated in Scheme 4.4 were synthesized. The presence of the DOTA moiety was questionable according to NMR analysis. Before loading with the PET-isotope of ^{64}Cu, improved structural characterization would be needed.

Regioselective iodination of peptides and proteins

5

Small synthetic receptor binding peptides are today favored over proteins and antibodies as peptide-based radiopharmaceuticals in the field of tumor-targeting and receptor-imaging [110]. This tendency is due to the availability of small peptides possessing a wide range of biological activities, unique receptor-recognition and the ease of gaining information from these systems [110]. Moreover, small peptides possess smaller size, easier preparation, and are in general a simplification of its corresponding complex proteins and antibodies. A number of natural occurring peptides functioning as hormones, neurotransmitters etc. are displaying a higher affinity than antibody fragments [111,112]. Due to the fact that tumor cells also possess receptors that are unique to the type of cancer and are over-expressed at the surface of the cells, this has led to the *in vivo* imaging and use of numerous bioactive peptides with high affinity for these receptors [110]. Labeling of peptides with specific binding to over-expressed receptors allow the visualization of tumor lesions by different imaging modalities or even provide the option of using these peptides as therapeutic radiopharmaceutical agents [110, 112].

Small peptides also possess attractive pharmacokinetics such as uptake at target site, and rapid clearance from not-target related tissues. Moreover, they are feasible in chemical modification and radiolabeling [110]. With solid phase peptide synthesis (SPPS), peptides are easily affordable and the corresponding labeling has developed into a strongly evolving area [].

As molecular recognition is confined to a certain region of the sequence, most peptides can be extended in sequence or modified for radiolabeling without alteration of the receptor binding site nor the biological activity (chemical flexibility) [111]. Examples of these type of peptides are Glucagon-like peptide-1, bombesin **5.1**, somatostatin **5.2** and analogs like octreotide **5.3** (**??**) [113]. The current use of receptor binding peptides in clinical research (**??**) is depicted in Figure 5.1.

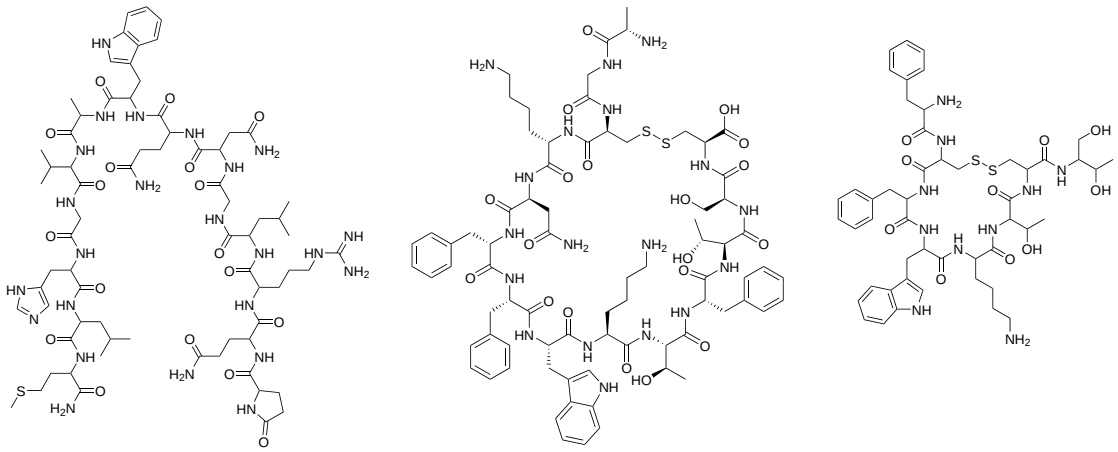

5.1
Bombesin

5.2
Somatostatin

5.3
Octreotide

(b) Structure of receptor binding peptides.

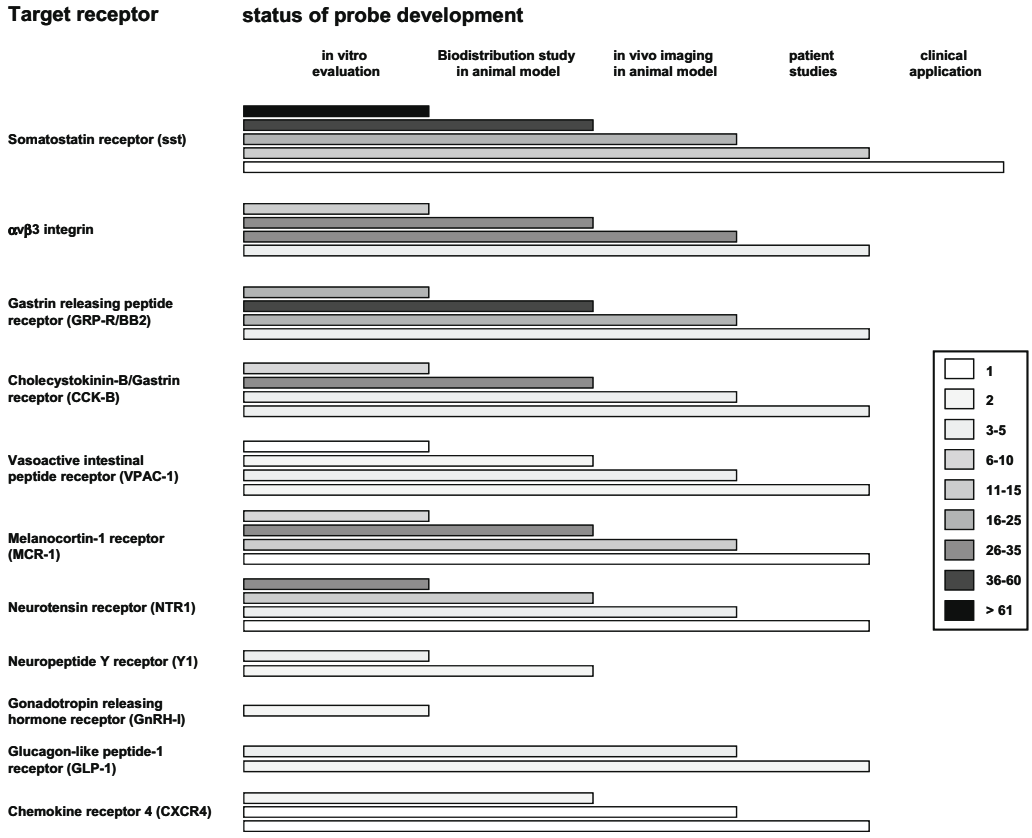

(d) Different types of receptor binding peptides and the current state in clinical research measured by the number of publications. The grey scale in the box indicates the number of studies published for the given receptor binding peptide [113].

Figure 5.1: Examples of receptor binding peptides.

Beside the application of *in vivo* imaging, radiolabeling of peptides and proteins are likewise central in radioimmunoassays (RIAs). RIAs are considered as being the current workhorse in the accurate *in vitro* screening of antibodies (at pico mol level). Within

RIA, the competitive binding between a radiolabeled antigen (known concentration) and the corresponding non-radioactive (cold) antigen (unknown concentration) to an antibody (known concentration), is used to determine the degree of binding and the unknown concentration of the antigen (Figure 5.2). From the observed ratios of bound labeled antigen-antibody complex, the unknown concentration of the unlabeled antigen can be determined from a calibration curve (Figure 5.2) [114]. RIA accounts for being the most used application, but in terms of measuring binding constants or substrate affinity, the principle of RIA can be applied elsewhere such as nonimmune specific binding reagents like thyroxine binding globulin, transcortin, cell-membrane and cytosol receptors [114].

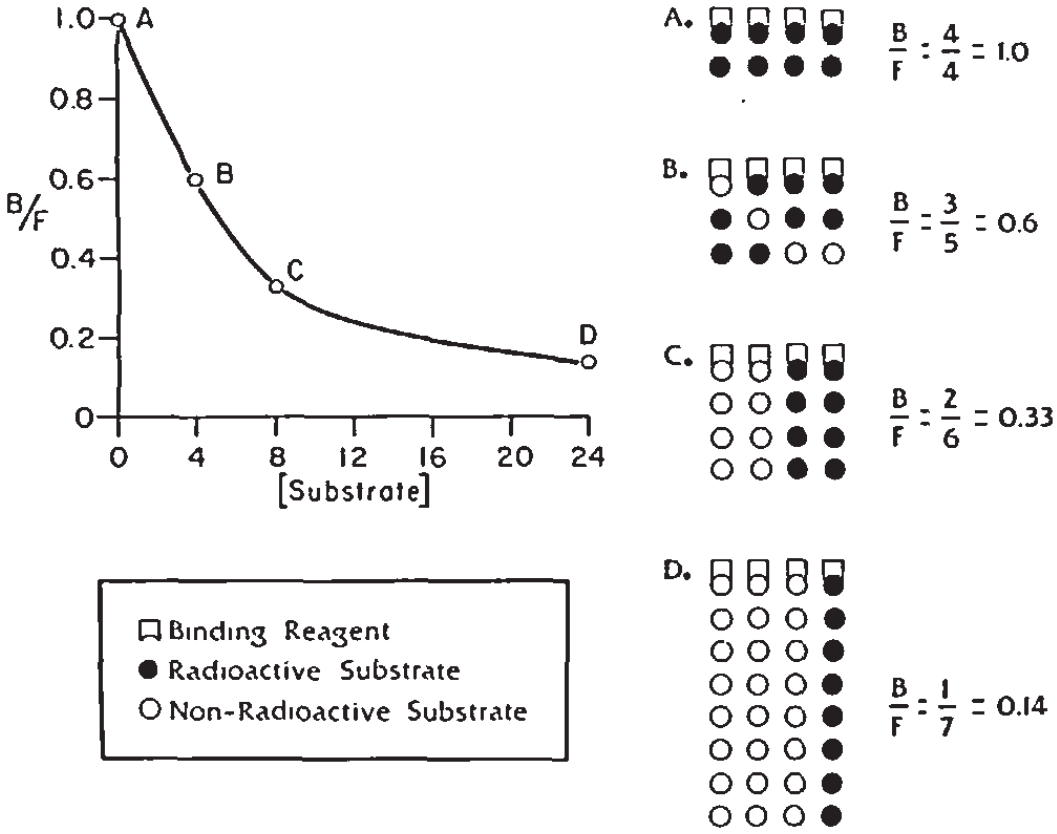

Figure 5.2: The principle of RIA. A calibration curve is established from the different ratios of bound and not bound ligand [114]. In situation A, the receptor (the peptide) is fully saturated with the radiolabeled antigen (radioactive substrate). Situation B, C and D illustrate the increasing addition of the unlabeled antigen (non-radioactive substrate) and the competitive binding to the receptor. From these binding-studies, the ratio of bound vs. free (B/F) can be measured and correlated to the known amount of unlabeled antingen (non radioactive substrate).

The unique properties of the above-mentioned applications of *in vivo* imaging and RIA, have stated the requirement of the labeling of peptides []. The regioselectivity of the labeling of peptides is rarely addressed in literature. Regioselective radiolabeling of peptides is

preferable as the number of sites for labeling are limited compared to the number of sites in the radiolabeling of proteins [111]. Likewise, with the high potency of receptor binding peptides and low tissue occurrence of corresponding receptors, the specific activity of the receptor binding peptide is crucial [111]. As highlighted by Okarvi: "an ideal labeling procedure is one in which the receptor binding properties and biological activity of the peptide remains unaffected and the peptide remains active throughout the imaging" [110]. Additionally, non-specific labeling can influence the conclusive outcome of the RIA, as the labeling of the antigen can lead to a mixture of different isomers. While the intended isomer displays the intended binding, other isomers may display (dramatically) different binding constants as a consequence of labeling near the binding site []. This scenario was highlighted in the work of Sharma *et al.*, where Chloramine T radioiodination of an α-melanotropin hormone led to complete loss of biological activity, while radioiodination of an adrenocorticotropin hormone resulted in misleading results in a radio receptor binding assay [115]. It has likewise been specified that the labeling of endogenous peptides has to be in tight structural and stereochemical accordance in order not to alter or lose potency or selectivity towards a given receptor subgroup [115]. This was substantiated by the labeling of the opoid peptide analog [D-Pen^2,D-Pen^5]enkephalin (**5.4**, DPDPE) (Figure 5.3); labeling DPDPE at the Tyr residue resulted in a 10-100-fold loss of potency while Phe-labeling improved the selectivity towards the receptor without decreasing the potency [115].

The most common way to radiolabel peptides is by synthetic post-modification; either by direct labeling of the peptide/protein or by the introduction of prosthetic group that has been pre-labeled. Examples of prosthetic groups are bifunctional chelating agents able to chelate metals of interest or a moiety with the radioactive species covalently attached []. As an example, site-specific bio-conjugation during SPPS and introducing the prosthetic group of a **[^{19}F]**-*p*-fluorobenzaldehyde via oxime or hydrazone ligation have been reported [116, 117].

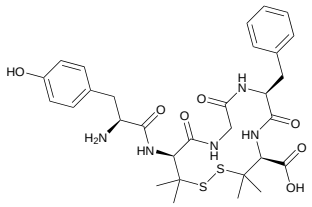

5.4
[D-Pen^{2,5}]-Enkephalin

Figure 5.3: Structure of DPDPE **5.4**.

Receptor binding peptides have been labeled with various isotopes. The most common ones are ^{111}In, ^{99m}Tc, ^{18}F, ^{64}Cu, ^{68}Ga and ^{123}I [110, 113]. One of the most used and attractive isotopes for peptide and protein labeling is iodide []. *In vitro* radioiodination of peptides and proteins has been favored over the corresponding labeling methods due to feasibility and easier labeling with proteins, higher specific activities and advantageous detection of e.g. gamma irradiation [118]. The scope of this study deals with the site specific iodination of peptides.

5.1 Iodination by electrophilic aromatic substitution

Iodination is commonly conducted by electrophilic aromatic substitution. Since the commercial available radioactive iodine is usually NaI, the iodide will have to undergo oxida-

tion. The appealing advantages by electrophile aromatic iodination are the simplicity and accessibility.
The iodination by electrophilic aromatic substitution is not without challenge, as other aromatic amino acids can undergo electrophilic aromatic iodination like Phe, Tyr, Trp and His. Tyrosine is according to its activation/nucleophilicity most prone to undergo iodination. Iodination of Trp is possible because of the electron rich indole. However, oxidation of Trp have likewise been reported [119]. Histidine likewise undergoes iodination in the presence of iodonium ions while Phe display the lowest reactivity of the aromatic amino acids [].

As the key-step/challenge in iodination of peptides remains the formation of the iodonium ion, the following sections describe the most common ways to generate iodonium ions *in situ* as well as examples of prosthetics groups used in radioiodination of peptides and methods to achieve iodination of Phe-residues and other aromatic amino acids.

5.2 Iodination by iodine monochloride

Iodination using ICl was developed by McFarlane as a consequence of low radiochemical yields using molecular iodine I_2 as the radioactive source, since radioactive I_2 suffer from the fact of being a carrier method [120]. The radioactive ICl was made by isotope exchange of ICl with radioactive NaI. Due to the electron-density on chloride, ICl undergoes electrophilic aromatic iodination on activated ring systems but electrophilic addition is also reported for double bonds [121]. The method of McFarlane was considered as more efficient and easier to handle (less hazardous) than the previous radioiodination using the highly energetic KI method developed by Yalow and Berson for the iodination of insulin [122]. Though, ICl still remained a carrier method since dilution with non-radioactive iodine monochloride was needed resulting in low specific activities [118].

5.3 Iodination by Chloramine T

One of the most well-known and established methods was developed by Hunter and colleagues, also referred to as the Chloramine T method [118, 123, 124]. The method consists of *in situ* generation of ICl by the oxidation of radioactive NaI using *N*-chloro-*p*-toluenesulfonamide (Chloramine T) (Scheme 5.1) and remains as the most cited method [118]. This approach has been applied to several peptides and proteins []. The chloramine T method is attractive as the source of radioactive iodide formed is under carrier-free conditions. Though a limitation of using chloramine T is the oxidation, which can lead to oxidation of side-groups of certain amino acids e.g. the oxidation of methionine to methionine sulfoxide or sulfone [125]. Trp is likewise prone to undergo oxidation under acidic conditions [119]. The oxidative damage of proteins has led to the development of solid-supported Chloramine T by which oxidative damage during iodination should be limited.

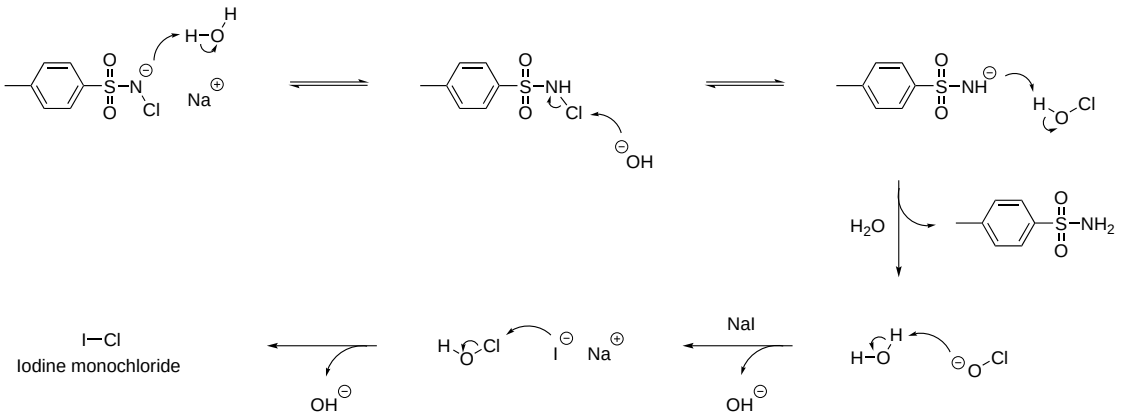

Scheme 5.1: Proposed mechanism for the *in situ* formation of ICl by the chloramine T oxidation of NaI [].

5.4 Iodination by Iodogen

To keep undesired oxidation at a minimum the use of 1,3,4,6-tetrachloro-3α,6α-diphenyl glycoluril (**5.5**, iodogen), was proposed (Figure 5.4) [125,126]. Due to its hydrophobic nature, iodogen is water-insoluble and will be deposited at the walls of the vial. The reaction is similar to the chloramine T oxidation but is taking place at the site of the local deposit of **5.5** reducing the risk of performing oxidative damages to the peptide/protein [126, 127].

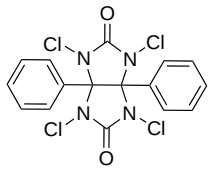

5.5
Iodogen

Figure 5.4: Structure of iodogen **5.5**.

5.5 Iodination by use of prosthetic groups

As alternative to the *in situ* oxidation and corresponding electrophilic aromatic iodination, prelabeled aromatic prosthetic moieties have been developed [128–134]. The bio-conjugation of the aromatic prosthetic group is based on the nucleophilic substitution of the *N*-hydroxysuccinimidyl ester part of the radioiodinated aromatic prosthetic group. This method therefore relies on nucleophilic functional groups e.g. the ϵ-amino group of Lys residues or the N-terminus of the peptide/protein.

The first prosthetic group developed was the Bolton-Hunter reagent, the *N*-succinimidyl 3-(4-hydroxy 3-iodo-phenyl)propionate **5.6** (Figure 5.5) [128]. Other similar constructs **5.7**-**5.10** have been developed diverging from the core-structure of an iodinated phenol in order to enhance the *in vivo* stability towards deiodination by deiodinases. *In vivo* instability is an observed trend for Tyr-iodinated-peptides explained by the action of deiodinases found e.g. in the thyroid. Zalutsky and colleagues have developed several prosthetic groups that have been applied in the bio-conjugation of peptides (Figure 5.5) [129–134]. Examples of prosthetic moieties that have been developed is based on limiting the structural recognition by deiodinases (Figure 5.5). Moreover, the activated ester of tetrafluorophenyl-5-iodo-4-

pentenoate **5.11** has been used as a prosthetic group (Figure 5.5) [135].

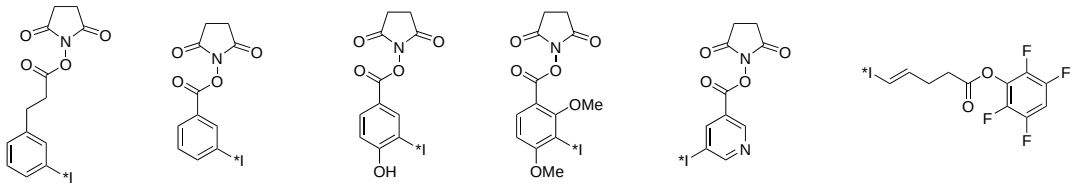

5.6 **5.7** **5.8** **5.9** **5.10** **5.11**

Figure 5.5: Various prosthetic groups that have been prelabeled with radioactive iodide prior to the post-modification of peptides. The post-modification is based on the not site-specific conjugation to a peptide via Lys residues or the N-terminus [].

In addition, the structural resemblance of the iodinated aromatic group has been studied in a structure-property/activity relationship [136]. This study tested the deiodinating activity of enzymes from the thyroid and liver microsomes towards analogs of iodinated tyrosine. Interestingly, 3-iodo-L-Tyr underwent almost full deiodination while analogs of D-iodo-tyrosine, α-methyl-DL-iodotyrosines and, 3,5-diiodo-4-hydroxyphenyl-DL-lactic acid were reported to be stable against deiodination. It was inferred from this assay that the enzymatic site seemed to be dependent on carboxyl, amino and phenol groups to exert the deiodination [136].

5.6 Miscellaneous techniques for Phe iodination

The low *in vivo* stability of peptides/proteins labeled at the Tyr residue, has led to the iodination of other amino acids like Phe. The labeling of Phe has been based on the strategy of directing the iodination (regioselectivity) using an in-direct functional group as placeholder (precursor) - that is part of the peptide/protein and will be equivalent to the radioiodinated peptide upon iodination. As an example, Escher illustrated the iodination of *p*-amino-phenylalanine by the Sandmeyer reaction; diazotiation followed the Cu-mediated insertion of the iodide [137]. The main limitation of the reaction is the relatively low radiochemical yield of 1-2% under carrier free conditions [137]. The presence of a crown ether enhanced yields to approximately 25% [115].
In the study of Wilson *et al.*, Ac-Phe(4-TMS)-OMe **5.12** was developed using TMS as directing group in the iodination (Scheme 5.2) [138]. Iodination was conducted using $AgBF_4$ and I_2 and the need for the activating effect of silyl substitution was demonstrated by the unsuccessful iodination of Ac-Phe-OMe [138]. A limited scope of sensitive substrates (methyl- and ethyl esters) was tested in this study [138]. Nevertheless, the selectivity of **5.12** as part of a peptide sequence with multiple aromatic amino acids was not evaluated, **5.12** was only tested as part of *N*-formyl-Phe(4-TMS)-Gly-OEt dipeptide [138].

Wilbur *et al.* published the enantiomerselective formation of Boc-Phe(4-Sn$(Bu)_3$)-tetrafluorophenyl ester **5.13** (Scheme 5.2) and the corresponding iodination [139]. This derivative was pre-

pared in order to conduct radioiodination of **5.13** prior to the following peptide synthesis. The stannyl derivative of **5.13** was designed for a Merrifield approach to SPPS using the Boc/Bn protecting group strategy [139]. Iodination was conduction under carrier conditions using a mixture of radioactive NaI and nonradioactive NaI together with *N*-chlorosuccinimide.
The development of the stannyl derivative **5.13** was reasoned the milder radioiodination conditions used for organostannyl compounds, which proved to be compatible with the activated tetrafluorophenyl ester of **5.13** [139]. The iodination conditions used in the iodination of **5.12** was believed according to Wilbur *et al.* not to be applicable to **5.13** due to the presence of an activated ester like **5.13**.

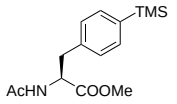

5.12

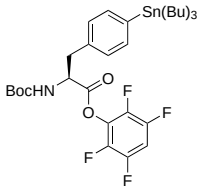

5.13

Scheme 5.2: Structures for the **5.12** and **5.13** [138, 139].

To the knowledge of the author, no other in-direct/temporary placeholder-system - as exemplified above – has been combined with other amino-acids like for instance tyrosine.

5.7 Problem statement

In order to provide an improved labeling of peptides, group-members of Mads Clausen have previously been working on using a TMS-group as a placeholder for the iodination [62]. As described in section 2.2, aryl-TMS groups undergo *ipso*-substitution and it was envisioned that the TMS-group can be used as a precursor to direct the desired iodination of peptides as also illustrated before [138]. This will allow regioselective iodinations and potentially afford more precise and conclusive RIA studies and ensure that the labeling does not takes place at the active site responsible for the biological receptor activity. Beside these attractive features, the labeling will remain direct compared to the introduction of a prosthetic group.

Previous results include synthesis of Boc-(4-TMS)Phe-OBn [140]. To evaluate the selectivity, the corresponding dipeptides of Phe (**5.15**), His (**5.16**), Tyr (**5.17**) and Trp (**5.18**) were synthesized, respectively. Iodination by thallation $Tl(OOCCF_3)_3$ indicated predominantly *ipso*-substitution of the TMS of (4-TMS)Phe with no observed iodination of the corresponding His and Phe moieties of dipeptides **5.19** and **5.20**, respectively (Table 5.1). The dipeptide of Tyr however did not display any selectivity, as products corresponding to mono-, di- and tri-iodination were observed when $Tl(OOCCF_3)_3$ (2 equiv.) and NaI (4 equiv.) were used in an excess. Lowering the amount of $Tl(OOCCF_3)_3$ (0.5 equiv.) and NaI (1 equiv.) indicated that the TMS was substituted prior to the iodination of the Tyr

occurred in **5.21** (Table 5.1). Iodination of the dipeptide of Trp **5.22** was not successful as it was inferred that oxidation of Trp under acidic conditions occurred (Table 5.1) [140].

Table 5.1: Selectivity in the iodination reaction of Phe(4-TMS)

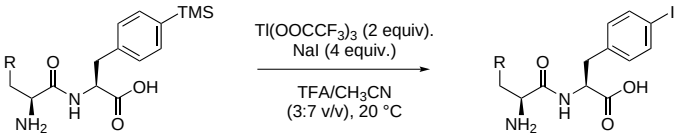

5.15 - **5.18** **5.19** - **5.22**

Dipeptide	**5.15**	**5.16**	**5.17**	**5.18**
R				
Iodinated dipeptide	**5.19**	**5.20**	**5.21**	**5.22**
Selectivity	+	+	(+)[1]	-

[1] Selectivity was observed when 0.5 equiv. $Tl(OOCCF_3)_3$ and 1. equiv NaI was used.

From these findings with predominant selectivity for the *ipso*-substitution of the TMS-group in the iodination reactions of **5.15** and **5.16**, it was deduced that improved selectivity can be achieved from the corresponding Tyr(3-TMS). With the increased nucleophilicity of the phenol of Tyr and placing the TMS in the reactive *ortho*-position to the hydroxy-group, it was predicted that this electronic effect could improve the desired selectivity. Despite the low *in vivo* stability of Tyr-iodinated peptides, iodinated Tyr peptides/proteins will still find use in the *in vitro* screening of RIA. As previously mentioned, enhanced *in vivo* stability can be achieved by certain changes in the design of the amino-acid construct e.g. 1) *N*-alkylation of the amide bond, 2) using the corresponding D-isomer and 3) employing peptoids [110]. Given that a Tyr(3-TMS) can be synthesized, selectivity over His, Phe, Trp and Tyr will have to be tested. Likewise, a corresponding Fmoc-(3-TMS)Tyr(*t*Bu)-OH derivative is a necessity to obtain so that this derived iodination strategy is applicable for Fmoc-based SPPS. With the excellent radiochemical yield and purity achieved for the iodination of **2.2** using $Tl(OOCCF_3)_3$ under carrier free conditions, it was hypothesized that high specific activities can be obtained in radioiodination of peptides with this method.

5.8 Retrosynthetic analysis for the synthesis of the TMS derived Tyrosine

Several strategies were devised within this project to install the TMS unit within a limited number of steps starting from the commercial available H-L-Tyr(3-I)-OH **5.23** and Boc-L-Tyr(*t*-Bu)-OMe **5.24**.

One comprehensive strategy to install the TMS by metal halogen exchange, (Scheme 5.3) would first involve iodination of **5.24** followed by reduction of the methyl ester that will afford the intermediate of the amino alcohol of **5.25**. Additional protecting group manipulations and with the cancellation of the acidity-issue of the α-hydrogen will allow metal halogen exchange of the iodide by which the TMS can be introduced. Reduction of the carboxylic acid of **5.23** and protecting group manipulations will likewise afford the amino alcohol of **5.25**. In both cases, several steps upon the introduction of the TMS will be needed, as the reduced amino alcohol first will need to undergo oxidation to the corresponding carboxylic acid. Following the oxidation, will be exchange of protecting groups that will be compatible with the Fmoc based-strategy of peptide synthesis. Another limitation - beside the number of steps - of this strategy could potentially be the compatibility, selectivity and orthogonality of the protecting groups involved in this strategy. This synthetic strategy was discarded according to the number of step involved to get the TMS substituted Tyr derivative **5.26**.

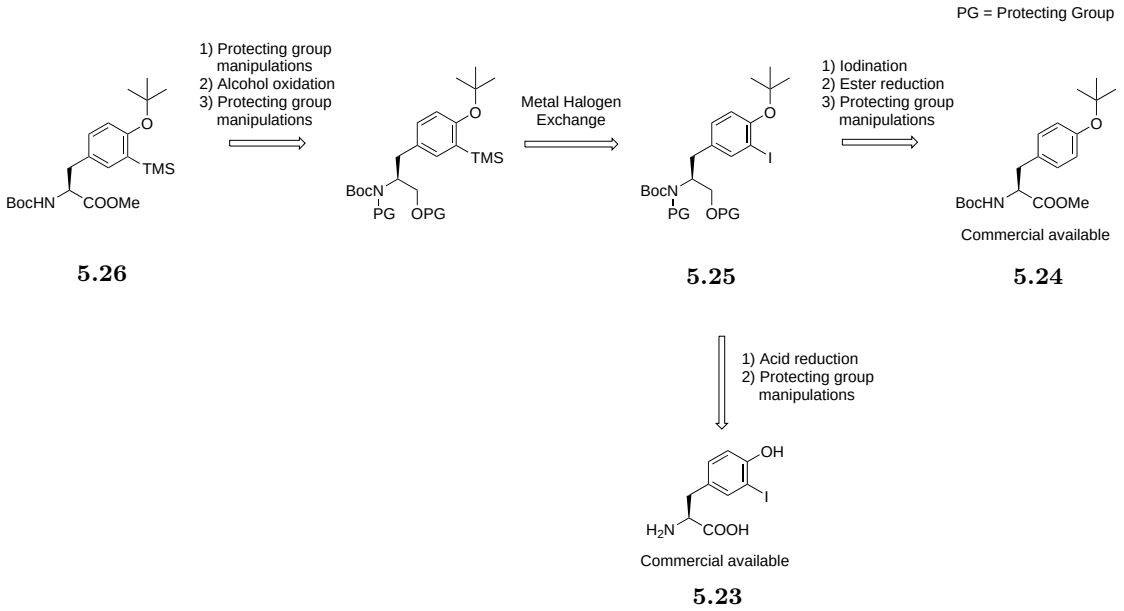

Scheme 5.3: Retrosynthetic analysis based on the formation of the protected iodinated amino Tyr alcohol **5.25** for metal halogen exchange.

An elegant and shortened/more direct synthetic strategy that will afford the TMS-substituted Tyr derivative of **5.27**, from **5.23**, is via a reverse-Brook rearrangement of the TMS protected phenol of **5.30** (Scheme 5.4). Another option would be to perform metal halogen exchange of **5.28** to afford **5.26** (Scheme 5.5). Both strategies will rely on the metal halogen exchange of the iodide at -78 °C to be faster than the competitive α-hydrogen abstraction or NH abstraction of the Boc-carbamate. The latter could be avoided by the formation of $N(Boc)_2$ protection of the α-amino group or *in situ* protection of the α-NH-carbamate. The subsequent deprotection of the $N(Boc)_2$ has though been reported to be challenging due to observed epimerization, which is hypothesized to be in accordance with the increased acidity of the α-hydrogen [141]. This favors the strategy of *in situ* protection of the α-amino-NH-carbamate e.g. silyl protection.

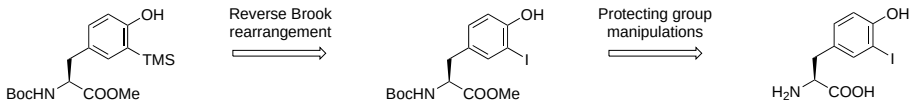

5.27 **5.30** **5.23**

Scheme 5.4: The retrosynthetic analysis for the TMS derived Tyr-derivative **5.27** starting from the commercially available **5.23**.

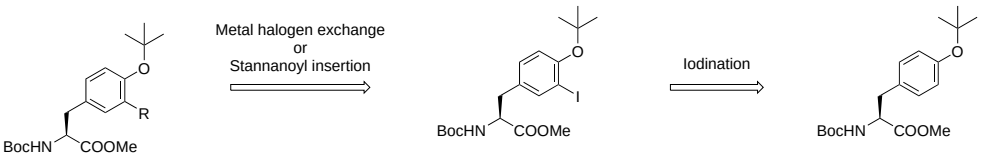

5.26 R = $Si(Me)_3$

5.29 R = $Sn(Bu)_3$

5.28 **5.24**

Scheme 5.5: The retrosynthetic analysis for the TMS derived Tyr-derivative **5.26** starting from the commercially available **5.24**.

Whether the metal halogen exchange or reverse Brook-rearrangement were achievable directly on Tyr was tested on **5.28** and **5.30** (Scheme 5.6 and Scheme 5.7). The mono-iodinated tyrosine **5.28** was assembled from the commercial available **5.24** which underwent mono-iodination using ICl in CH_2Cl_2 affording **5.28** (Scheme 5.6). Applying 2 equiv. of TMSCl followed by the addition of 2 equiv. *n*-BuLi at -78 °C only provided a mixture of **5.28** and the corresponding deiodinated derivative **5.24**, thus no TMS insertion was observed. Compound **5.30** was synthesized from **5.23** in a one-pot fashion by first forming the methyl ester using $SOCl_2$ in CH_3OH followed by the Boc-protection of the amine using Boc_2O in dioxane according to literature (Scheme 5.7) [142]. The formation of the TMS ether of **5.30** was successfully achieved by using 2. equiv. TMSCl and Et_3N in dry THF. Applying *n*-BuLi at -78 °C gave no signs of the rearranged product **5.27**, only deiodination was observed according to LC-MS analysis.

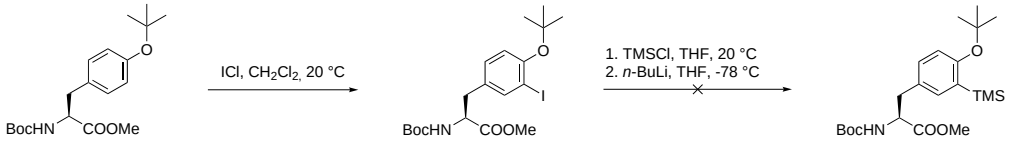

5.24 **5.28** **5.26**

Scheme 5.6: Iodination and metal halogen exchange of **5.24**.

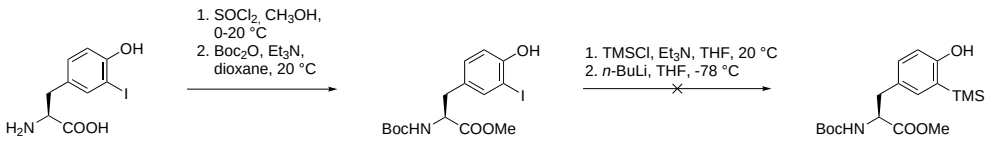

5.23 **5.30** **5.27**

Scheme 5.7: Reverse-Brook rearrangement of **5.30**.

Another alternative that will allow insertion of a placeholder would be to perform a cross-coupling reaction at the already introduced iodide of **5.28**. Despite the previous negative experience with the Pd-mediated TMS insertion (2.5.2), and despite the toxicity of organo-stannanes, they are more readily introduced by Pd-chemistry and more established in modern chemistry as they are used in numerous examples of the Stille coupling and as precursors in radio-iodinations. It was suspected that $Sn(CH_3)$- would display the same β-cationic effect and undergo *ipso*-substitution in an electrophilic aromatic iodination. Preliminary experiments indicated that the tributylstannane derivative of **5.28** could be synthesized. This was not further pursued as the synthesis of the TMS-substituted Tyr derivative via the Negishi-coupling was conducted concurrently, as described in the following sections.

.

5.9 Synthesis of amino acids using β-iodo-alanine derivatives

Jackson and co-workers reported the use of organozinc reagents based on Boc-β-iodo-Ala-OBn **5.31** to synthesize various analogs of Phe-derivatives via the Negishi-coupling [143,144]. Jackson and co-workers likewise indicated that the homoenolate of the organozinc reagent remained stable and did not undergo epimerization [143]. The enantiomeric control was further substantiated by the formation of the Mosher-ester of the formed phenylalanine derivatives which supported that the Negishi-coupling gave the phenylalanine derivative in an enantiomerically pure fashion [143]. The yields reported were moderate [144]. This led to further optimization and screening in search of the proper catalyst/ligand system and likewise the tolerance/scope of functional groups (Scheme 5.8). This led to the use of Pd_2dba_3 and SPhos **5.32** in DMF by which the yields of the cross coupled product using **5.33** were improved [145]. Beside the catalytic system, the improved Negishi reaction was also reasoned to be due to improved zinc-insertion [145].

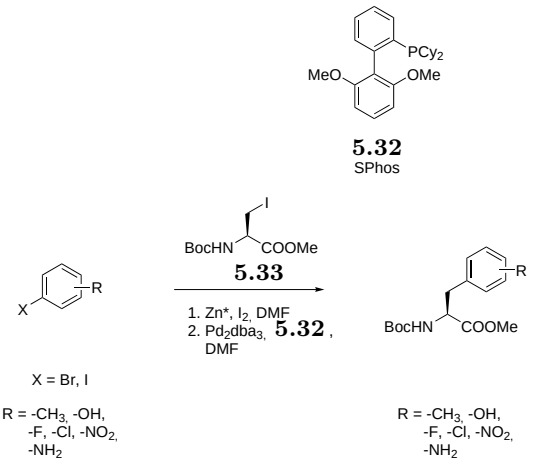

Scheme 5.8: Optimized conditions for the Negishi-Coupling of Boc-β-iodo-Ala-OMe and various aryl-iodides/bromides using Pd_2dba_3 and Sphos **5.32** [145].

The strategy of Jackson was applied to afford the Boc-Phe(4-TMS)-OBn derivative **5.14** conducted by previous members of the group of Mads Clausen (Scheme 5.9). The TMS derived phenylalanine was assembled from the corresponding 4-bromo-1-TMS-benzene **5.34**, though yields were not high (best achievable yield, 58%). The highest yield was achieved from 4-iodo-1-TMS-benzene **5.35** (69% yield).

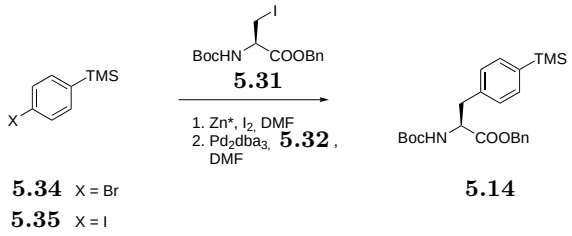

Scheme 5.9: The synthesis of **5.14** by Negishi coupling.

5.10 Synthesis of a TMS-derived tyrosine derivative by Negishi coupling

Concurrently to the previous mentioned direct strategies involved in this project, the target molecule of **5.26** was pursued by the Negishi-coupling. The building block 1-*tert*-butoxy-2-TMS-4-bromobenzene **5.36** was made in the group of Mads Clausen (Scheme 5.10). 2,4-Dibromophenol **5.37** was first *tert*-butyl *O*-alkylated to **5.38** followed by regioselective metal halogen exchange in the 2-position to afford building block **5.36**.

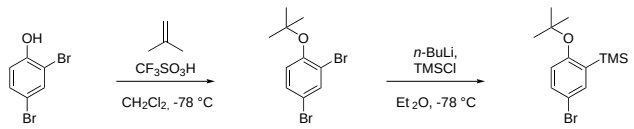

5.37 **5.38** **5.36**

Scheme 5.10: The synthesis of building block **5.36**.

The choice of *tert*-butyl as protecting group was based on the compatibility with the Fmoc-based SPPS strategy and since it is the most common protecting group of tyrosine. However this strategy could potentially come to the limitation within a Fmoc-based strategy, as side-group protection and cleavage from beads/resin usually require harsh acidic conditions which could lead to proto-desilylation of the TMS-group. This could imply that the radioiodination will have to be carried out on the resin or that the fully protected peptide will have to be cleaved from the resin in order to undergo subsequent iodination in solution. The cleavage of the fully protected peptide can be achieved by applying extreme acid-labile - or base sensitive linkers like the Cl-trityl linker (cleavage: hexafluoroisopropanol/CH_2Cl_2 (1:4 v/v) [146]), xanthenyl linker appended to 4-methylbenzhydrylamine resin (cleavage: 1% TFA/CH_2Cl_2 [147]), SASRIN linker resin (cleavage: 0.5%-1% TFA/CH_2Cl_2 or Hexafluoroisopropanol/CH_2Cl_2 (1:4 v/v) [148]), or the base labile HMBA linker (cleavage: 0.1 M NaOH [140, 149, 150]) would have to be applied. Cleavage from the resin will enable the option of conducting the radioiodination on the fully protected peptide in solution followed by deprotection of side-groups in a post-treatment fashion with e.g. TFA upon iodination. In order to display the situation where a given peptide, synthesized using a Fmoc-based strategy and cleaved from a resin, the *tert*-butyl was chosen as protecting group for the phenol of the TMS substituted Tyr derivative.

In order to get an personal impression of the Negishi-coupling and its sensitivity, experience was obtained by the formation of the Boc-Phe-OMe from **5.33** and iodobenzene. The organozinc reagent of **5.33** was made from activated Zn dust and together with iodobenzene, Pd_2dba_3 and SPhos in DMF, Boc-Phe-OMe was afforded in moderate yields according to LC-MS analysis.

For the intended Negishi cross-coupling between **5.36** and **5.33** (Path A), the organozinc reagent of **5.33** was formed from activated Zn dust (<10 μm) followed by mixing with SPhos, Pd_2dba_3 and **5.36**. This afforded product **5.26** in low yields (23%, Scheme 5.11). The low reactivity was reasoned the use of the aryl-bromide **5.36**, which was in accordance with similar results reported in the group [140].

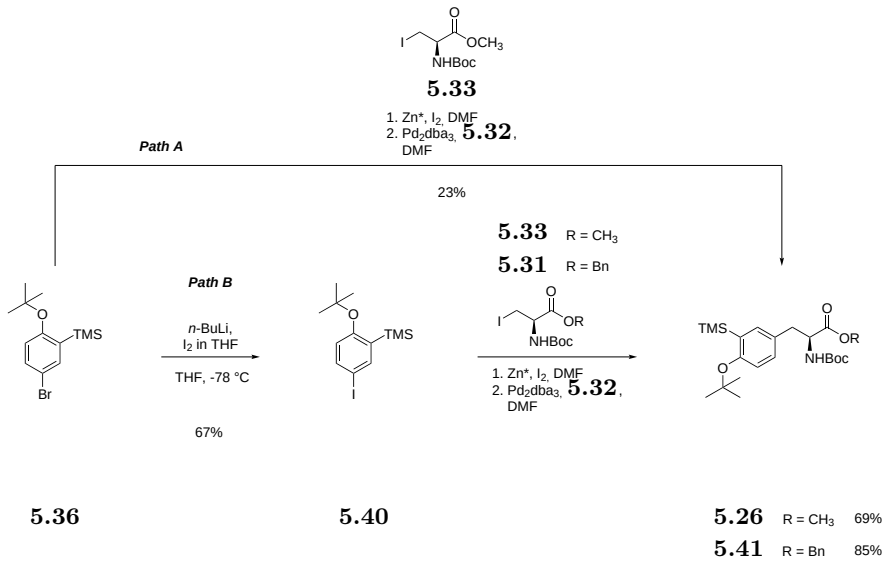

Scheme 5.11: The synthesis of metal halogen exchanged building block **5.40** and the corresponding Negishi synthesis. Note that the asterisk of the Zn refer to that Zn underwent activation in 0.1 M HCl prior to use.

The group of Buchwald reported the Cu-catalyzed halogen exchange of aryl halides also referred to as an aromatic Finkelstein type reaction [151]. The Cu-catalyzed halide exchange rely on the equilibrium between the aryl halide and a second halide salt in which the position of the equilibrium – among other parameters - is influenced by the solubility of the given halide salt [151]. Applying the conditions of CuI (5 mol%), rac-*trans-N,N'*-dimethyl-1,2 cyclohexanediamine **5.39** (10 mol %) and NaI (2 equiv.) in refluxing dioxane to **5.36** gave what was a presumed mixture of the bromide **5.36** and the iodide **5.40** in an approximately ratio of 1:1 ratio by LC-MS analysis (Scheme 5.12).

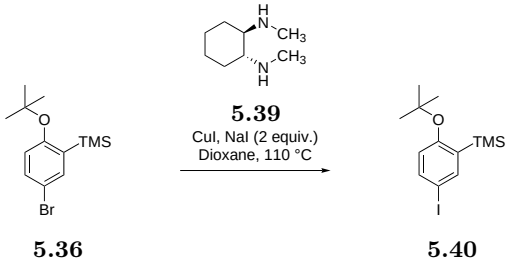

Scheme 5.12: The Cu-catalyzed halogen exchange of **5.36**.

Due to the expected difficulty isolating the aryl-iodide of **5.40** from the corresponding bromide **5.36** it was concluded that the crude mixture of the bromide and the iodide would have to be applied further on in the Negishi cross-coupling. Concurrently to the aromatic Finkelstein reaction developed by Buchwald, the bromide was successfully exchanged with iodide using *n*-BuLi followed by the addition of I_2 in THF. This afforded the iodo-substituted aryl derivative **5.40** in 67% yield (Path B, Scheme 5.11).
Exchanging the halide from the bromide to the iodide of **5.40** had a significant impact of

tripling the yield of the Negishi-coupling by the formation of **5.26** (69%) and **5.41** (85%) (Scheme 5.11).

The next step was the chemoselective Boc-deprotection of the α-amino-group without compromising the *tert*-butyl nor the aryl TMS. To elucidate the acid liability of the different groups and to see if Boc-group could be selectively removed in TFA, the stability in various ratios of TFA and Et_3SiH in CH_2Cl_2 were tested. Unfortunately no selectivity was observed for the Boc-group could be achieved.

Deprotection of *N*-Boc protected amines in the presence of the *t*-Bu-phenol ether has been reported according to literature using mild conditions of TMSOTf and 2,6-lutidine [152]. Alternatively, $AlCl_3$ has likewise been reported as a mild method for Boc-deprotection [153]. TMSOTf and 2,6-lutidine in CH_2Cl_2 exclusively removed the Boc-group in quantitative yields (Scheme 5.13) affording the amine of **5.42** and **5.43** respectively.

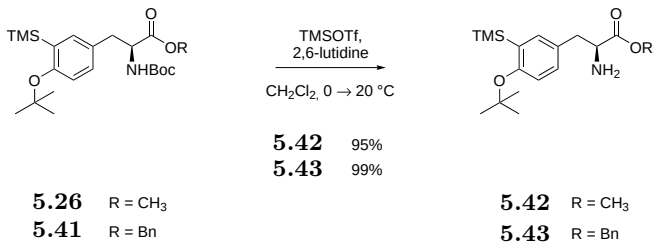

Scheme 5.13: Boc deprotection of **5.42** and **5.43** using TMSOTf and 2,6-lutidine.

The successful Boc-deprotection allowed the transformation of **5.42** into the Fmoc-protected **5.44** using Fmoc-OSu and Et_3N in CH_2Cl_2 in 75% yield (Scheme 5.14). The ester of **5.44** was hydrolyzed using Na_2CO_3 in H_2O/CH_3CN according to literature [154]. The conditions was reported to be compatible with the Fmoc-group where common hydrolytic conditions using strong bases like hydroxides are reported to lead to the (partial) loss of the Fmoc-group [154].[1] It was likewise reported that the stereochemistry was not affected during the hydrolysis [154]. The carboxylic acid **5.45** was isolated in 73% yield (Scheme 5.14), though ^{1}H-NMR surprisingly indicated an impure product.

[1]In the previous study of Phe(4-TMS), the Bn-ester was successfully removed in the presence of Fmoc using hydrogenolysis, despite that Fmoc likewise have been reported to undergo hydrogenolysis in a mixture of CH_3OH and CH_3CN [155]. As an alternative strategy, Fmoc-protection of **5.43** followed by hydrogenolysis was envisioned to potentially afford **5.45**.

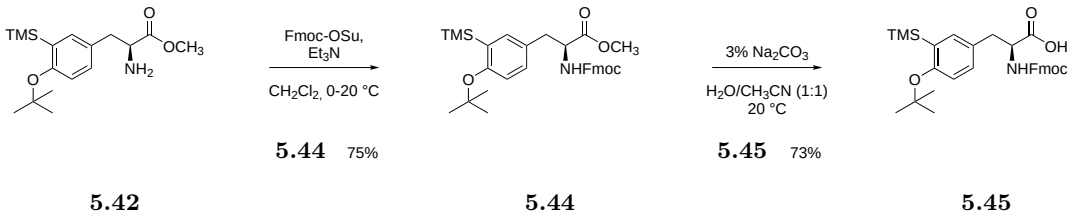

5.42 **5.44** **5.45**

Scheme 5.14: The synthesis of Fmoc-(3-TMS)Tyr(*t*-Bu)-OH **5.45** from **5.42**.

5.11 Formation of dipeptides

In order to achieve proof-of-concept, and evaluate the iodination of Tyr(3-TMS) against the amino acids most prone to undergo iodination, dipeptides with His, Phe, Tyr and Trp, were constructed. Using the corresponding Z-protected amino acids will afford the dipeptides with the C - and N termini available upon hydrogenation. In order to ensure similar reactivity in the iodination, Z-Tyr(*t*-Bu)-OH was chosen.
Prior to the dipeptide formation, the enantiomeric purity of **5.43** was evaluated by conjugation to the chiral derivatizing agent Marfey's reagent [156, 157]. The conjugate of dinitrobenzene-Ala-amide was made of **5.43** in acetone at 40 °C. It was assessed that even though the carboxylic acid of **5.43** is not available for hydrogen bonding with the amide of Ala, that the conjugate would be rigid enough that it would allow for separation by chromatographic systems. LC-MS analysis of the crude reaction mixture of the coupling only afford one peak which could indicate that **5.43** is one isomer.

The dipeptides of Phe(3-TMS), mentioned in section 5.7, was synthesized using standard EDC·HCl coupling and DMAP in CH_2Cl_2. Same conditions was applied for the assembly of Z-Phe-(3-TMS)Tyr(*t*-Bu)-OBn **5.46**. These conditions gave the desired dipeptide **5.46** in a 76% yield. Disappointingly, ^{1}H-NMR, revealed what seems to be a double pattern of resonances indicating the potential formation of diasteromers of **5.46** (Figure 5.6). The stereochemical outcome in terms of epimerization during the the peptide bond formation was not evaluated in the previous study of Phe(3-TMS). The choice of using EDC·HCl as the coupling reagent could be questioned due to the potential risk of epimerization via the oxazolone formation and due to the risk of forming the *N*-acylurea side-product that will have the effect of lowering the yield of the peptide coupling.
Inferred from the finding of the potential formation of diastereomers using EDC·HCl in the synthesis of **5.46**, the strategy for the formation of the remaining dipeptides of **5.47**, **5.48** and **5.49** was changed to the use of benzotriazol-1-yl-oxytripyrrolidinophosphonium hexafluorophosphate (PyBOP) as coupling reagent. PyBOP has been found superior as a coupling reagent to suppress epimerization and was designed for peptide synthesis [158, 159]. *N*-Ethyl-morpholine (NEM) was chosen as base, based on its lower basicity and similar nucleophilicity compared to Et_3N [160]. The increased nucleophilicity is reasoned that the ring nitrogen of NEM is less hindered. It has likewise been reported that NEM was found superior compared to the standard bases of Et_3N, $(i\text{-Pr})_2EtN$ and *N*-methyl-morpholine in terms of suppressing epimerization [160].

The reaction conditions for the dipeptide synthesis are summarized in Table 5.2. Using PyBOP and NEM afforded the dipeptides in acceptable yields. Dry column vacuum chromatography purification of Z-His-(3-TMS)-Tyr(*t*-Bu)-OBn **5.49** was unsuccessful by which **5.49** was purified by PREP-HPLC explaining the low yield. ^{1}H-NMR of the dipeptides indicated the formation of the single diastereomer for **5.47**, **5.48** and **5.49**.

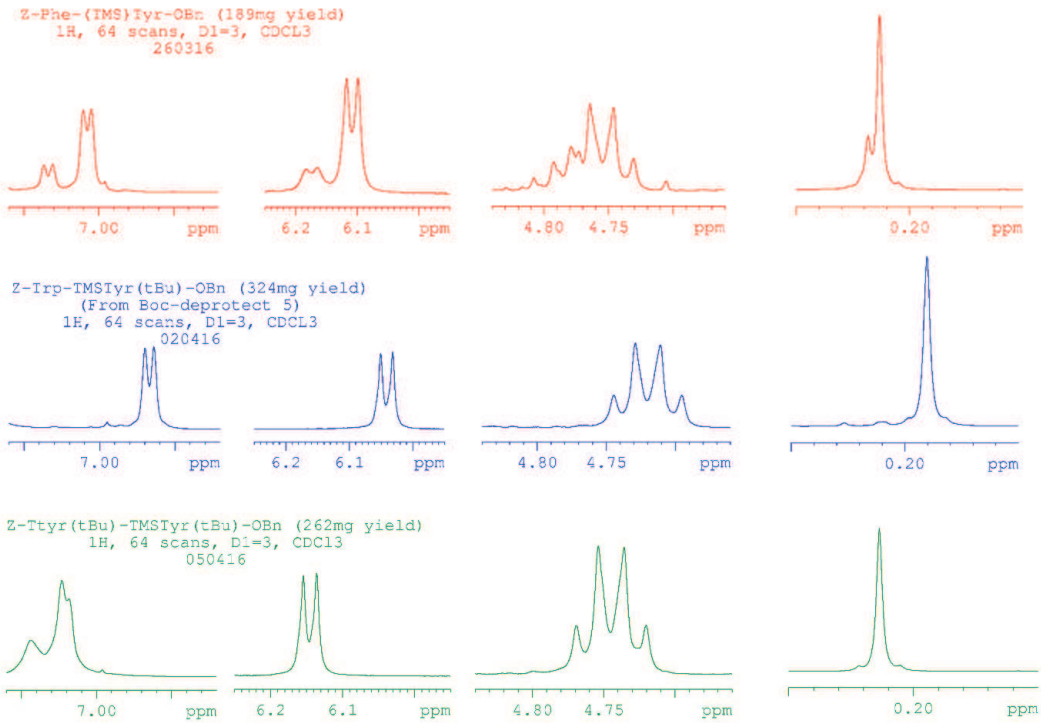

Figure 5.6: Selected ^{1}H-NMR resonances of the synthesized dipeptides of **5.46** (red), **5.48** (blue) and **5.47** (green) indicating the presence of diastereomers of **5.46**.

5.12 Hydrogenolysis of dipeptides

What seemed on the drawing board to be a promising step – the hydrogenolysis of the benzyl-ester and concurrently removal of the Cbz of **5.46**-**5.49** – turned out to be challenging. This strategy was based on the similar approach conducted for Phe(4-TMS). Standard hydrogenolysis conditions using Pd/C in CH_3OH or EtOH, disappointingly led to what was believed to be the reductive aminated product of the methylated or ethylated *N*-terminus, respectively. This has previously been reported and it was speculated to be due to the formation of formaldehylde or acetaldehyde during hydrogenolysis, respectively [161]. Due to the formation of this side product, the solvent was changed to EtOAc or THF. Unfortunately, beside the formation of the linear dipeptides **5.50**-**5.53**, a significant amount of the corresponding cyclized diketopiperazine side-product **5.54**-

Table 5.2: Peptide couplings of **5.43**.

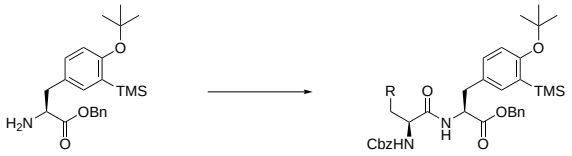

5.43 **5.46** - **5.49**

Entry	Amino acid	Coupling Reagent	Base	solvent	(R)	Yield[1]
1	Z-Phe-OH	EDC·HCl[2]	DMAP[2]	CH_2Cl_2		**5.46** (76%)
2	Z-Tyr(*t*-Bu)-OH	PyBOP[3]	NEM[3]	DMF		**5.47** (76%)
3	Z-Trp-OH	PyBOP[3]	NEM[3]	DMF		**5.48** (78%)
4	Z-His-OH	PyBOP[3]	NEM[3]	DMF		**5.49** (36%)[4]

[1] Isolated by dry column vacuum chromatography unless otherwise stated.
[2] 2 equiv. EDC·HCl & 2.1 equiv. DMAP at 20 °C
[3] 1.2 equiv. PyBOP & 6 equiv. NEM at 20 °C
[4] Isolated by Preparative HPLC

5.57 was formed concurrently. The formation of the diketopiperazine side-product was more pronounced in EtOAc than in THF, why the final hydrogenation was conducted in THF. The formation of the diketopiperazine side-product lowered the yields dramatically (Table 5.3). the up-scale hydrogenolysis of **5.49** was unsuccessful and was not further pursued in this project due to time-frame of this project.

It was hypothesized that the formation of diketopiperazine could be explained by the hydrogenolysis of Cbz of the α-amino group taking place prior to the hydrogenolysis of the Bn-ester. With the liberation of the α-amino group, cyclization by nucleophilic substitution at the C-terminus optionally speculated to be mediated by coordination of Pd, could take place. On the other hand, the liberation of the corresponding benzylate could be questioned due to its poor leaving group ability.

The hydrogenolysis was likewise sluggish, which was presumed to be due to catalyst pollution by the α-amino group of the N-terminal. The coordination of amino-groups to Pd is commonly known and have even led to the chemoselectivity in hydrogenations when using a Pd/C-ethylenediamine complex [162].

Hydrogenolysis of the Phe-dipeptide **5.46** revealed, what was indicated by ^{1}H-NMR, that the dipeptide was a mixture of diastereomers. Dry column vacuum chromatography using H_2O/CH_3CN as gradient allowed separation of the diasteromers. Disappointingly, ^{1}H-NMR revealed that the diastereomers remained mixtures.

Table 5.3: Hydrogenolysis of dipeptides **5.46-5.49**

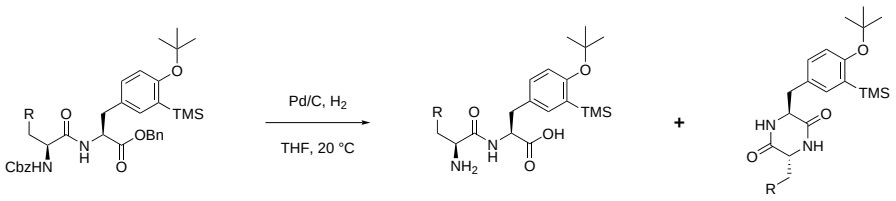

5.46 - **5.49** **5.50** - **5.53** **5.54** - **5.57**

Entry	side-chain R	yield (linear) (%)	yield (cyclic) (%)
1		**5.50** (44%)[1]	**5.54** (7%)
2		**5.51** (32%)	**5.55** (34%)
3		**5.52** (47%)	**5.56** (29%)
4		**5.53** (-)[2]	**5.57** (-)[2]

[1] The other diastereomer of **5.50** was isolated in 27% yield.
[2] Not available, hydrogenolysis of **5.49** was unsuccessful.

5.13 Iodination of dipeptides

The iodination of the linear dipeptides **5.50-5.52** were performed by thallation using $Tl(OOCCF_3)$ and NaI. Iodination by thallation was chosen since oxidative methods like lactoperoxidase and chloramine T has been reported to led to oxidation of Trp in acidic conditions [**?**]. Previous thallation-results of H-Trp-Phe(4-TMS)-OH **5.18** indicated that thallation was not successful using $Tl(OOCCF_3)_3$ (2. equiv) and NaI (4. equiv.) in a mixture of TFA/CH_3CN (3:7 v/v). Based on this, thallation of **5.52** was envisioned to be feasible by lowering the amount of TFA.

With the acid-liability stability test of **5.26** in TFA/Et_3SiH/CH_2Cl_2, the iodination reaction was tested on **5.26** and the diketopiperazines of **5.55** and **5.56** by varying the amount of TFA (0.1%, 1% and 10% TFA in CH_3CN respectively). Applying 2 equiv. of $Tl(OOCCF_3)_3$ and 4 equiv. of NaI in CH_3CN to **5.26** indicated the formation of the *ipso*-substituted iodide. The iodination reaction proceeded with the concurrently Boc-deprotection in correlation to the amount of TFA.
In case of the cyclized dipeptides of **5.55** and **5.56**, iodination took place using 2 equiv. of $Tl(OOCCF_3)_3$ and 4 equiv. of NaI in CH_3CN. The presence of TFA seemed to affect the degree of iodination. Iodination of **5.56** led to formation of multiple side-products stating the difficulty of conducting iodination in the presence of the indole under slight acidic conditions [119].

Iodination of the linear peptides was tested by varying the amount of $Tl(OOCCF_3)_3$ and NaI and evaluating the necessity of TFA. Iodinating the linear dipeptide of **5.50** using 2 equiv. of $Tl(OOCCF_3)_3$ and 4 equiv. of NaI in CH_3CN gave a mixture of the *ipso*-iodinated product **5.58** and the starting material **5.50**. Using a mixture of 0.1% TFA/CH_3CN increased the formation of the iodinated product **5.58**, though the iodination did not go to completion. At this point, it seemed clear that the iodination by thallation of the above-mentioned iodinations were sluggish compared to the previously experience of using $Tl(OOCCF_3)_3$ on **2.2**. The sluggish behavior was reasoned to be due to the presence of TFA as part of the solvent. The amount of TFA was therefore increased to 10% and iodination of **5.50** using 1 equiv. of $Tl(OOCCF_3)_3$ and 2 equiv. of NaI afforded the iodinated product of **5.58** exclusively, clearly exhibiting the desired selectivity for the *ipso*-substitution of the TMS-group (Figure 5.7).

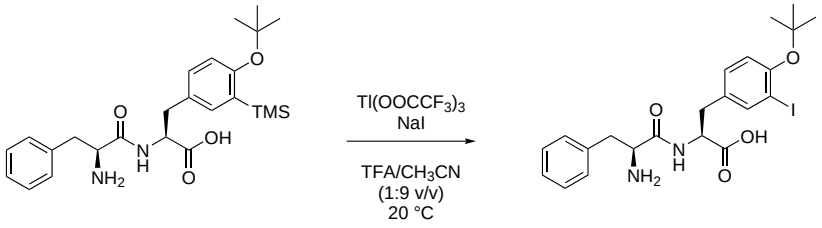

5.50 **5.58**

(b) Iodination of **5.50** using 1 equiv. of $Tl(OOCCF_3)_3$ and 2 equiv. of NaI in 10% TFA/CH_3CN

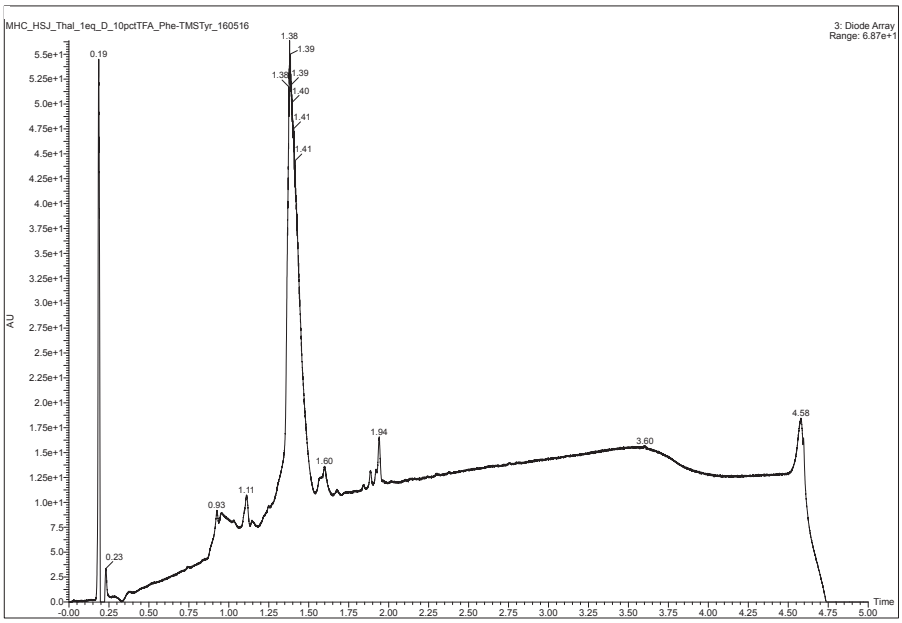

(d) UV-chromatogram of reaction mixture. The peak eluting at 1.39 min has a m/z of 511.01 correspondig to the $[M+H]^+$ adduct of **5.58**.

Figure 5.7: Reaction & LC-MS analysis of the iodination of **5.50** in 10% TFA/CH_3CN.

Iodination of the Tyr-dipeptide **5.51** (**??**) was of interest taking the iodination of the Tyr-(4-TMS)Phe dipeptide **5.17** into account where selectivity was difficult to achieve. Lack of reactivity was seen when **5.51** was treated with $Tl(OOCCF_3)_3$ (2 equiv.) and NaI (4 equiv.) in CH_3CN or 0.1% TFA/CH_3CN. Applying the similar conditions of $Tl(OOCCF_3)_3$ (1 equiv) and NaI (2 equiv.) in 10% TFA/CH_3CN formed the *ipso*-iodinated product **5.59** in a clean fashion with traces of what was expected to be the di-iodinated dipeptide with one *tert*-butyl missing was observed (m/z = 652.90, peak eluting at 1.49 min, **??**) (Figure 5.8).

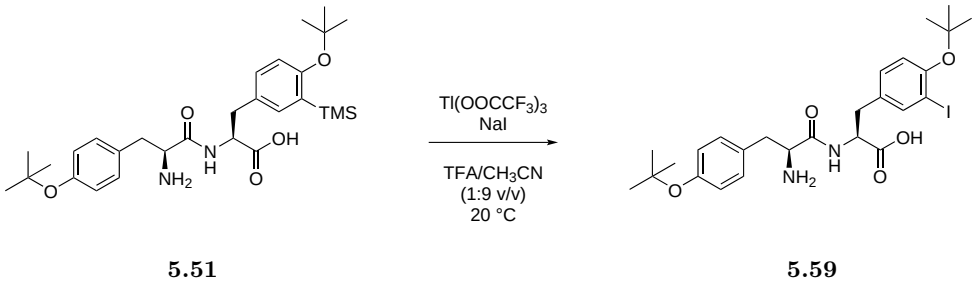

5.51 **5.59**

(b) Iodination of **5.51** using 1 equiv. of $Tl(OOCCF_3)_3$ and 2 equiv. of NaI in 10% TFA/CH_3CN

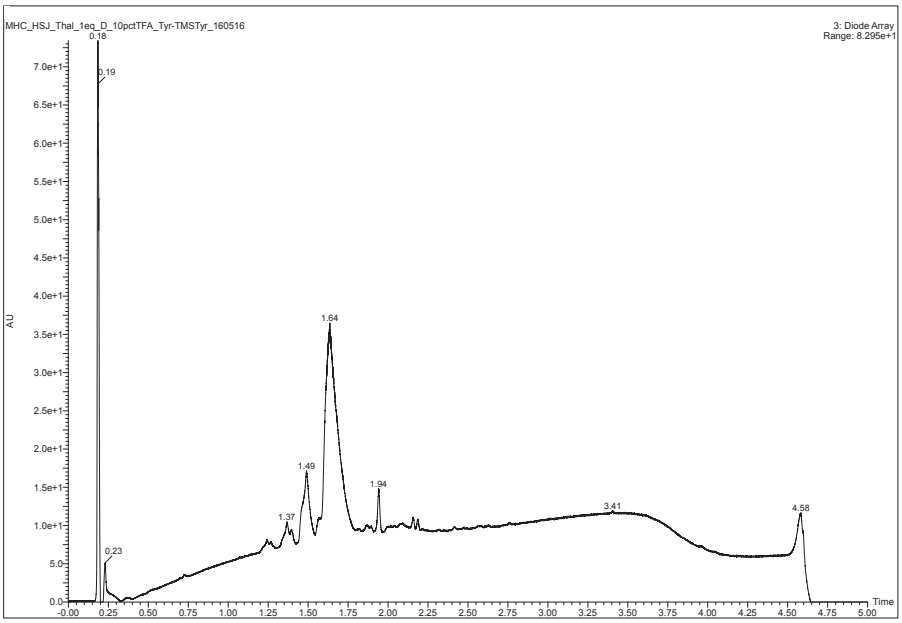

(d) UV-chromatogram of reaction mixture. The peak eluting at 1.64 min min has a m/z of 583.11 correspondig to the $[M+H]^+$ adduct of **5.59**.

Figure 5.8: Iodination of **5.51** in 10% TFA/CH_3CN.

Lastly, the iodination of the Trp-dipeptide **5.52** was tested (**??**). Iodination using $Tl(OOCCF_3)_3$ (2 equiv.) and NaI (4 equiv.) in CH_3CN did not give any iodination, neither did iodination conducted in 0.1% TFA/CH_3CN. Thallation using $Tl(OOCCF_3)_3$ (1 equiv.) and NaI (2 equiv.) in 10% TFA/CH_3CN (Figure 5.9) afforded the iodinated product **5.60** with the formation of several side-products (figure **??**). The iodination of **5.52** was considered promising as a first step towards the selective iodination in the presence of Trp, despite the formation of several side-products. It is evident that further optimization is needed.

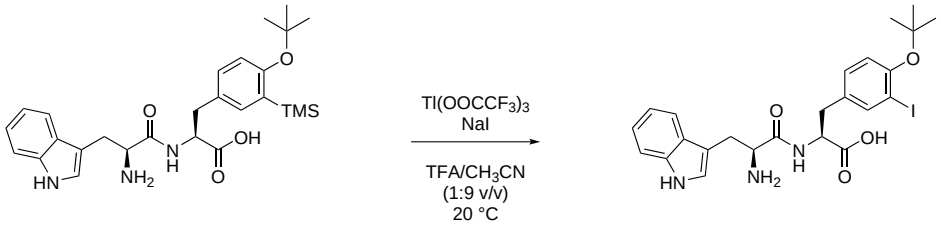

5.52 **5.60**

(b) Iodination of **5.52** using 1 equiv. of $Tl(OOCCF_3)_3$ and 2 equiv. of NaI in 10% TFA/CH_3CN.

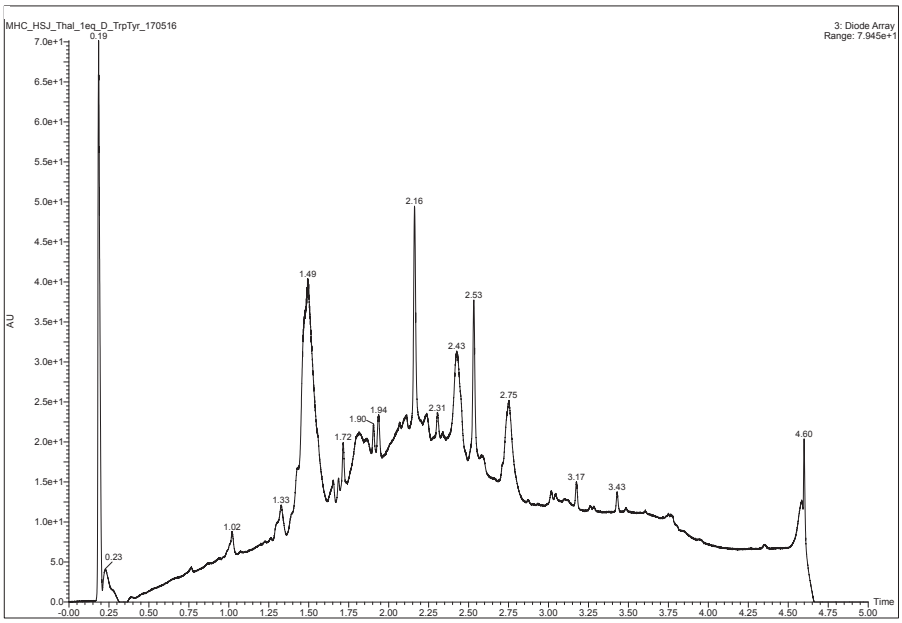

(d) UV-chromatogram of reaction mixture. The peak eluting at 1.49 min min has a m/z of 550.05 correspondig to the $[M+H]^+$ adduct of **5.60**.

Figure 5.9: Iodination of **5.52** in 10% TFA/CH_3CN.

To summarize - Applying 1 equiv. of $Tl(OOCCF_3)_3$ and 2 equiv. of NaI in 10% TFA/CH_3CN gave successful iodinations of all three dipeptides tested.

5.14 Discussion

Despite the successful synthesis and iodination of the TMS substituted Tyr derivatives, evaluated in the context of the dipeptides of **5.50**, **5.51** and **5.52**, there is still room for improvements and questions to be addressed. The construction of **5.26** and **5.41** was conducted by the Negishi-Coupling which compared to the previous-mentioned strategies was attractive in number of steps and yields. With the yield in the range of 69-85% using the building block **5.40**, the Negishi coupling proved to be promising for the assembly of **5.26** and **5.41**. Applying the Negishi-coupling provide the attractable option/flexibility, that the D-isomer can be assembled in a similar fashion from the commercially available

D-isomer of **5.31** or **5.33**, respectively. This could be attractive as the D-isomer when entering into a peptide sequence, could enhance the *in vivo*-stability as reported [110]. The Negishi-coupling has likewise been reported using Fmoc-β-iodo-Ala-OMe [163]. The *N,N*-Boc-methyl β-iodo-alanine methyl ester **5.61** is likewise hypothesized to be reachable within a few number of steps (Scheme 5.15). This provides another building block for the Negishi-coupling, which will give the methyl substituted α-amino group which likewise could enhance the stability against proteolysis. These examples demonstrate and state the chemical flexibility in the Negishi-coupling allowing different protecting groups and starting materials in the synthesis of synthetic amino acids.

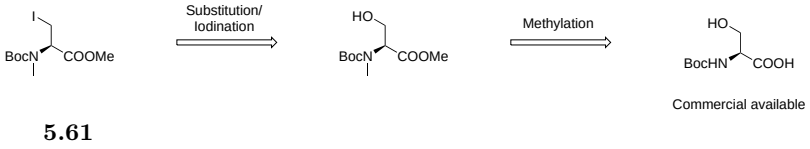

5.61

Scheme 5.15: Retrosynthetic analysis for the synthesis of the methylated Negishi building block **5.61**.

Despite the formation of the diastereomer of Marfey's reagent of **5.43**, the stereochemically outcome of the peptide bond formation of **5.50** and **5.51** seemed not conclusive as ^{1}H-NMR indicated mixtures of diastereomers. Further experiments and analysis are needed of the linear peptides of **5.50** and **5.51** to confirm the stereochemistry, optionally supported by the synthesis of the corresponding D-isomer.
In regard to the synthesis of the dipeptides – though that the dipeptides were designed in order to evaluate the proof of selectivity in the iodination reaction, and since the dipeptides are most likely not going to find use elsewhere - the significant formation of the α-*N*-alkylation as well as the cyclized diketopiperazines during the hydrogenolysis reaction imply that another approach would have been preferable. Modifications to the applied strategy, could be the use of orthogonal protecting groups of the α-amino group and C-terminus, as well as carrying out the deprotections step-wise. One orthogonal combination that could have been advantageous, would be to mask the α-amino group as the Boc carbamate while the C-terminus remains as the benzyl ester. Hydrogenation of the benzyl ester followed by Boc deprotection using TMSOTf and 2,6-lutidine will potentially lead to the linear dipeptide with less probability of forming the diketopiperazine. Another possibility that potentially could suppress the formation of diketopiperazine would be to synthesize the tri-peptide with a Gly or Ala residue inbetween, **5.43** and the His, Phe, Tyr, or Trp, respectively. Cyclization of the corresponding tri-peptides is less likely because this occurs by formation of a 9-membered ring compared to the 6-membered of the diketopiperazine.

The iodination reactions by thallation seemed promising, though optimization could have been interesting in order to improve the selectivity. In order to improve the selectivity of iodination and the difficulty of the iodination of the Trp-dipeptide **5.52**, Boc-protection of the indole could potentially result in deactivation of the indole, by which the selectivity of the iodination could be improved towards the *ipso*-substitution of the TMS. In regard

to the difficulties in the purification of **5.49** and the loss during hydrogenolysis, the strategy of using Z-His-OH without any protecting groups of the imidazole was a risky choice. Using His, with the τ-N protected as the Trt or Boc could likewise lower the nucleophilicity of the imidazole ring, which in terms of the synthesis and the iodination would have become beneficial. The failure of the hydrogenation of the His-dipeptide **5.49** remains an open question. The hydrogenolysis was reported successfully for Z-His-Phe(4-TMS)-OBn in the previous study in the Mads Clausen group.
Despite that the iodination of the hydrogenated **5.49** was not tested in this study, (4-TMS)Phe was reported to displayed clear selectivity over the imidazole of His in the iodination of **5.16**. Based on this result, it was envisioned that the iodination of **5.53** would exhibit selectivity towards the *ipso*-substitution of the TMS-group of Tyr. This assumption will still have to be tested and analyzed.

5.15 Future perspectives

Short term future perspectives of this study will first of all be to evaluate the selectivity in the iodination reaction of **5.53**. Likewise, the iodination reaction on a Boc-protected indole of Trp has to be tested. This will conclusively demonstrate the scope of using TMS substituted Tyr for iodination.
Moreover, the compatibility with SPPS will have to be addressed. Questions like: Would it be possible to iodinate on the resin? It is possible to cleave the desired (protected) peptide from an acid-labile resin without proto-desilylation? Will iodination by thallation be feasible subsequent to cleavage of the peptide in its protected form? Finally testing the iodination in a system like the labeling of Leu-enkephalin or somatostatin **5.2** would state the application of using the TMS-group as a placeholder to direct iodinations reactions of peptides to be regioselective.

Long-term future perspectives; having established the use of the TMS as directing-group with the synthesis of the TMS-derivatives of Phe and Tyr, it would be interesting to develop the TMS derivatives of His and Trp. Installing the TMS group in the 2-position of the indole of Trp could potentially provide selectivity in electrophilic aromatic iodinations according to the β-cationic effect, also observed in vinylic-TMS systems. *ipso*-Iodination of a TMS positioned in the 2-position of indole-derivatives have been reported [164, 165]. Employing the TMS group at the indole is hypothesized to favor iodination without oxidation of the indole to the oxindole and subsequent cleavage of the peptide linkage.

5.16 Conclusion

TMS-substituted Tyr derivatives **5.26** and **5.41** were successfully synthesized in good yields via the corresponding Negishi cross-coupling of **5.40** and the methyl Boc-β-iodoalanine esters **5.33** or **5.31**, respectively. The Boc-group was chemoselectively removed using TMSOTf and 2,6-lutidine which allowed the transformation of **5.42** to **5.45** which is useful in the Fmoc-based strategy. The dipeptides of **5.46**, **5.47**, **5.48** and **5.49**

were likewise constructed from **5.43** and the Z-protected amino acids. Hydrogenolysis of the Cbz-protected α-amino group and the benzyl ester caused serious difficulties as reductive *N*-alkylation and diketopiperazine formation were observed, depending on the solvent used. The stereochemistry of the Phe-dipeptide **5.50** and Tyr-dipeptide **5.51** seemed questionable as, ^{1}H-NMR indicated what was believed to be mixtures of diastereomers. Based on these observations, the stereochemical control has to be substantiated by further analysis.
Iodination via thallation of the Phe and Tyr dipeptides of **5.50** and **5.51** displayed clear selectivity for the *ipso*-substitution, while iodination of Trp-dipeptide **5.52** occurred but with the formation of several side-products.
Proof-of-concept for the use of TMS substituted Tyr to direct the iodination was demonstrated for **5.50**, **5.51** and **5.52**. Further optimization will be needed in the iodination of **5.52**.

Experimental 6

6'-*O*-TBDPS-sucrose (**1.10**). Sucrose **1.3** (10 g, 29.2 mmol) was suspended in pyridine (100 mL) and DMAP (0.36 g, 2.92 mmol) was added. The reaction mixture was left stirred for 1 h. TBDPSCl (4.65 mL, 17.5 mmol) was added and the reaction mixture was heated to 70 °C for 3 h. TBDPSCl (4.65 mL, 17.5 mmol) was again added to the reaction mixture at 20 °C and the reaction mixture was left stirred overnight. Pyridine was removed *in vacuo* and the residue was purified by dry column vacuum chromatography (EtOH in EtOAc[1] with 2% increments) affording **1.10** as an amorphous solid.

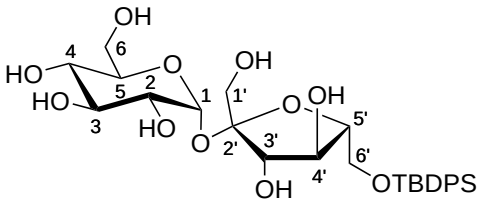

yield = (6.8 g, 40%)

m.p.: 174°C.

$[\alpha]_D^{20}$ = +38° (c 1.00, MeOH)

^{1}**H-NMR** (400 MHz, MeOD-d4): δ = 7.77-7.67 (m, 4H, *o*-H_{Ar}), 7.46-7.35 (m, 6H, *m*-H_{Ar}+*p*-H_{Ar}), 5.44 (d, $J_{1\rightarrow2}$ = 3.9 Hz, 1H, H^1), 4.13-4.01 (m, 2H, $H^{3'}$+$H^{4'}$), 3.99-3.84 (m, 3H, $H^{5'}$+$H^{6'}$), 3.79-3.72 (m, 1H, H^5), 3.68-3.50 (m, 5H, H^3+H^6+$H^{1'}$), 3.35-3.25 (m, 2H, H^2+H^4), 1.04 (s, 9H, (C$\underline{H_3}$)$_3$C-Si).

^{13}**C-NMR** (100 MHz, MeOD-d4): δ = 136.8 (2C, *o*-C_{Ar}), 136.8 (2C, *o*-C_{Ar}), 134.6 (*i*-C_{Ar}), 134.5 (*i*-C_{Ar}), 130.8 (2C, *p*-C_{Ar}), 128.8 (2C, *m*-C_{Ar}), 128.8 (2C, *m*-C_{Ar}), 105.6 ($C^{2'}$), 93.0 (C^1), 83.7 ($C^{5'}$), 79.0 ($C^{3'}$), 76.2 ($C^{4'}$), 74.9 (C^3), 73.9 (C^5), 73.2 (C^2), 71.4 (C^4), 66.5 ($C^{6'}$), 64.3 ($C^{1'}$), 62.4 (C^6), 27.3 (3C, ($\underline{C}H_3$)$_3$C-Si), 20.0 ((CH$_3$)$_3\underline{C}$-Si).

HR-MS. Calculated adducts: $[M+H_2O]^+$=598.2440, $[M+Na]^+$=603.2232, $[M+K]^+$= 619.1971. Observed adducts: $[M+H_2O]^+$=598.2675, $[M+Na]^+$=603.2226, $[M+K]^+$=619.1952.

ATR-FTIR (cm^{-1}): 3285.79, 2930.17, 2857.74, 1470.26, 1428.36, 1390.34, 1111.82, 507.18, 1067.96, 1043.53, 994.46, 930.50, 701.83, 805.57.

[1] FiXme Fatal: Dette er en fejl, Tjek TLC nÃ¥r du er tilbage

Hepta-isobutyric-6'-*O*-TBDPS-sucrose (**1.24**).

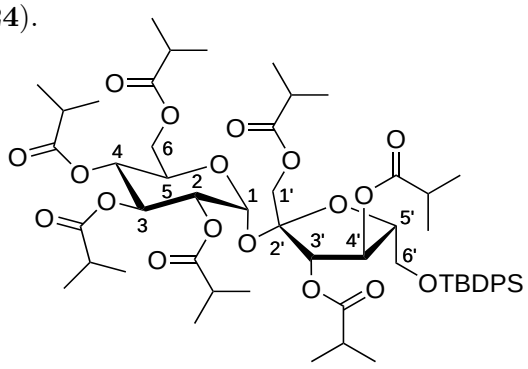

1.10 (2.00 g, 3.44 mmol) was dissolved in pyridine (40 mL) and DMAP (0.114 g, 0.924 mmol) was added. To the reaction mixture was added isobutyric anhydride (11.4 mL, 66.7 mmol) and the reaction mixture was left stirred at 20 °C overnight. TLC analysis was used to follow the the reaction. Upon reaction completion, the reaction mixture was concentrated *in vacuo* and Et_2O (200 mL) was added followed by extraction with saturated aq. $NaHCO_3$ solution (5x200 mL). The organic phase was subsequently collected and concentrated *in vacuo*. The crude residue was purified by dry column vacuum chromatography (EtOAc in heptane with 2% increments) yielding **1.24** as a transparent oily texture.

yield = (2.97 g, 80%).

$[\boldsymbol{\alpha}]_{\boldsymbol{D}}^{\mathbf{20}}$ = +37° (c 1.00, EtOH)

^{1}**H-NMR** (400 MHz, DMSO-d6): δ= 7.64-7.56 (m, 4H, *o*-H_{Ar}), 7.50-7.37 (m, 6H, *m*-H_{Ar}+*p*-H_{Ar}), 5.62 (d, $J_{1\rightarrow2}$ = 3.7 Hz, 1H, H^1), 5.49-5.46 (m, 2H, $H^{3'}$+$H^{4'}$), 5.35 (t, $J_{3\rightarrow2}$ = $J_{3\rightarrow4}$ = 10.0 Hz, 1H, H^3), 5.04 (t, $J_{4\rightarrow3}$ = $J_{4\rightarrow5}$ = 10.0 Hz, 1H, H^4), 4.86 (dd, $J_{2\rightarrow3}$ = 10.6 Hz, $J_{2\rightarrow1}$ = 3.6 Hz, 1H, H^2), 4.24 (ddd,$J_{5\rightarrow4}$ = 10.3 Hz, $J_{5\rightarrow6a}$ = 4.4 Hz, $J_{5\rightarrow6b}$ = 1.8 Hz, 1H, H^5), 4.20-4.02 (m, 4H, $H^{1'}$+$H^{5'}$+H^{6a}), 3.90 (dd, J = 13 $Hz_{6b\rightarrow6a}$, J = 1.8 $Hz_{6b\rightarrow5}$, 1H, H^{6b}), 3.86-3.75 (m, 2H, $H^{6'}$), 2.62-2.52 (m, 3H, $(CH_3)_2C\underline{H}$-), 2.48-2.32 (m, 4H, $(CH_3)_2C\underline{H}$-), 1.16-1.08 (m, 12H, $(C\underline{H_3})_2$CH-), 1.07-0.94 (m, 39H, $(C\underline{H_3})_2$CH- + $(C\underline{H_3})_3$C-Si).

^{13}**C-NMR** (100 MHz, DMSO-d6): δ = 175.6 ($(CH_3)_2$CH-$\underline{C}$(O)-O-), 175.3 ($(CH_3)_2$CH-$\underline{C}$(O)-O-), 175.2 ($(CH_3)_2$CH-$\underline{C}$(O)-O-), 175.0 (3C, $(CH_3)_2$CH-$\underline{C}$(O)-O-), 174.6 ($(CH_3)_2$CH-$\underline{C}$(O)-O-), 135.0 (4C, *o*-C_{Ar}), 132.4 (*i*-C_{Ar}), 132.3 (*i*-C_{Ar}), 130.0 (2C, *p*-C_{Ar}), 127.9 (4C, *m*-C_{Ar}), 102.4 ($C^{2'}$), 89.1 (C^1), 80.0 ($C^{5'}$), 75.3 ($C^{4'}$), 73.5 ($C^{3'}$), 69.2 (C^3), 69.1 (C^2), 68.1 (C^5), 67.1 (C^4), 63.8 ($C^{6'}$), 63.3 ($C^{1'}$), 61.2 (C^6), 33.3-32.9 (7C, $(CH_3)_2\underline{C}$H-), 30.7 ($(CH_3)_3\underline{C}$-Si), 26.4 (3C,($\underline{C}H_3)_3$C-Si), 19.0-18.0 (14C, ($\underline{C}H_3)_2$CH-)).

HR-MS. Calculated adducts: $[M+H_2O]^+$=1088.5376, $[M+Na]^+$=1093.5163, $[M+K]^+$=1109.4902. Observed adducts, $[M+H_2O]^+$=1088.5609, $[M+Na]^+$=1093.5175, $[M+K]^+$=1109.4892.

ATR-FTIR (cm^{-1}): 3285.44, 2973.83, 2934.80, 2877.85, 1741.41, 1470.12, 1388.47, 1247.91, 1186.65, 1139.69, 1111.82, 1071.63, 1030.51, 823.65, 742.56, 504.26, 702.23.

Hepta-2,3,4,6,1',3',4'-*O*-isobutyryl-sucrose (**1.25**). Hepta-isobutyryl-6'-*O*-TBDPS-sucrose **1.24** (1.032 g, 0.95 mmol) was solubilized under inert atmosphere in dry THF (20 mL). To the stirred reaction mixture was added acetic acid (0.082 mL, 1.43 mmol) followed by the drop-wise addition of a 1.0 M TBAF solution in THF (1.2 mL, 1.2 mmol). The reaction mixture was left stirred at 20 °C overnight. The reaction was followed by TLC. Upon reaction completion, the reaction mixture was directly purified by dry column vacuum chromatography (EtOAc in heptane with 4% increments). This afforded the deprotected product **1.25** as a transparent oily texture.

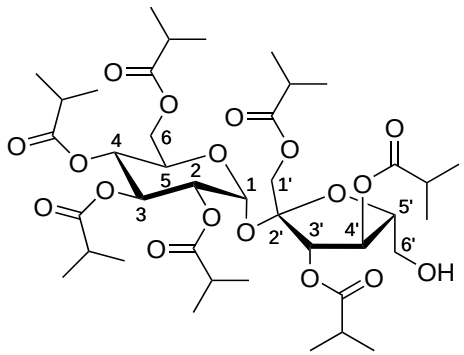

yield = (0.768 g, 97%).

$[\alpha]_D^{20}$ = +47° (c 1.00, EtOH)

^{1}**H-NMR** (400 MHz, DMSO-d6): δ= 5.67 (d, $J_{1\rightarrow2}$ = 3.7 Hz, 1H, H^1), 5.47 (d, $J_{3'\rightarrow4'}$ = 7.5 Hz, 1H, $H^{3'}$), 5.40 (t, $J_{3\rightarrow2} = J_{3\rightarrow4}$ = 9.9 Hz, 1H, H^3), 5.34 (t, $J_{4'\rightarrow3'} = J_{4'\rightarrow5'}$ = 7.5 Hz, 1H, $H^{4'}$), 5.11 (t, $J_{4\rightarrow3} = J_{4\rightarrow5}$ = 9.9 Hz, 1H, H^4), 4.96 (t, J = 5.5 Hz, 1H, -CH_2-O-$\underline{H}$), 4.91 (dd, $J_{2\rightarrow3}$ = 10.4 Hz, $J_{2\rightarrow1}$ = 3.6 Hz, 1H, H^2), 4.34 (ddd, $J_{5\rightarrow4}$ = 10.4 Hz, $J_{5\rightarrow6a}$ = 4.4 Hz, $J_{5\rightarrow6b}$ = 1.8 Hz, 1H, H^5), 4.21 (dd, $J_{6a\rightarrow6b}$ = 13.0 Hz, $J_{6a\rightarrow5}$ = 4.4 Hz, 1H, H^{6a}), 4.12-4.00 (m, 4H, $H^{1'}$+$H^{5'}$+H^{6b}), 3.60 (m, 2H, $H^{6'}$), 2.66-2.34 (m, 7H (DMSO overlap), $(CH_3)_2C\underline{H}$-), 1.21-0.95 (m, 42 H, $C\underline{H_3})_2$CH-).

^{13}**C-NMR** (100 MHz, DMSO-d6): δ= 175.8 ($(CH_3)_2$CH-$\underline{C}$(O)-O-), 175.4 ($(CH_3)_2$CH-$\underline{C}$(O)-O-), 175.3 ($(CH_3)_2$CH-$\underline{C}$(O)-O-), 175.0 (3C, $(CH_3)_2$CH-$\underline{C}$(O)-O-), 174.6 ($(CH_3)_2$CH-$\underline{C}$(O)-O-), 102.2 ($C^{2'}$), 89.1 (C^1), 80.8 ($C^{5'}$), 75.2 ($C^{3'}$), 73.7 ($C^{4'}$), 69.3 (C^3), 69.2 (C^2), 68.0 (C^5), 67.3 (C^4), 63.3 ($C^{1'}$), 61.5 ($C^{6'}$), 61.4 (C^6), 33.3-32.9 (7C, $(CH_3)_2\underline{C}$H-), 19.0-18.0 (14C, $(\underline{C}H_3)_2$CH-).

HR-MS. Calculated adducts: $[M+H_2O]^+$=850.4193, $[M+Na]^+$=855.3985, $[M+K]^+$=871.3724. Observed adducts: $[M+H_2O]^+$=850.4449, $[M+Na]^+$=855.3999, $[M+K]^+$=871.3738.

ATR-FTIR (cm^{-1}): 3531.46, 2974.80, 2939.02, 2878.48, 1739.30, 1470.09, 1388.51, 1344.51, 1247.10, 1186.51, 1142.42, 1077.10, 1048.73, 1005.66, 748.36.

6'-*O*-(5-((*R*)-1,2-dithiolan-3-yl)pentanoyl)-hepta-2,3,4,6,1',3',4'-*O*-isobutyryl-sucrose) (**1.26**). 1',2,3,3',4 ,4',6-hepta-*O*-isobutyryl-sucrose **1.25** (0.543 g, 0.64 mmol) was dissolved in dry DMF (10 mL) under inert atmosphere. In another flask under inert atmosphere, (5-(*R*)-(+)-1,2-dithiolan-3-yl)-pentanoic acid (0.206 g, 0.96 mmol), DMAP (0.246 g, 1.91 mmol) and EDC·HCl (0.190 g, 0.96 mmol) were dissolved in dry DMF (10 mL) and stirred for 15 min. The mixture, containing the activated ester was subsequently transferred to the reaction mixture of **1.25**. The reaction mixture was left stirred at 20 ° for reaction. The reaction was followed by TLC. After 24 h a new mixture of activated ester: (5-(*R*)-(+)-1,2-dithiolan-3-yl)-pentanoic acid (0.0706 g, 0.32 mmol), DMAP (0.080 g, 0.64 mmol) and EDC·HCl (0.065 g, 0.32 mmol) dissolved in dry DMF (10 mL) under inert atmosphere was added to the reaction mixture. At the point of reaction completion, the reaction mixture was concentrated *in vacuo* followed by addition of Et_2O (100 mL) and phase extraction with water (3x100 mL). The organic phase was collected and purified by dry column vacuum chromatography (EtOAc in heptane with 4% increment per fraction) affording **1.26** as a yellowish oily texture.

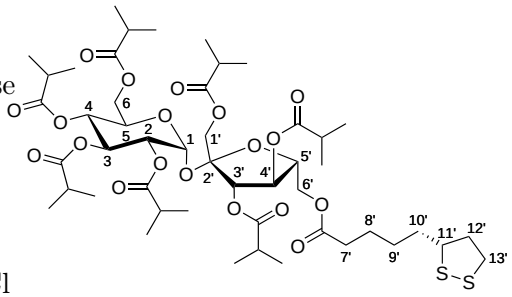

yield = (0.558 g, 86%)

$[\boldsymbol{\alpha}]_{\boldsymbol{D}}^{\mathbf{20}}$ = +55° (c 1.00, EtOH)

^{1}**H-NMR** (400 MHz, DMSO-d6): δ= 5.64 (d, $J_{1\rightarrow2}$ = 3.7 Hz, 1H, H^1), 5.52 (d, $J_{3'\rightarrow4'}$ = 7.5 Hz, 1H, $H^{3'}$), 5.34-5.43 (m, 2H, H^3+$H^{4'}$), 5.10 (t, $J_{4\rightarrow3}$ = $J_{4\rightarrow5}$ = 9.9 Hz, 1H, H^4), 4.91 (dd, $J_{2\rightarrow3}$ = 10.4 Hz, $J_{2\rightarrow1}$ = 3.7 Hz, 1H, H^2), 4.40-4.16 (m, 5H, H^5+H^{6a}+$H^{5'}$+$H^{3'}$+$H^{6'}$), 4.14-4.03 (m, 3H, H^{6b}+$H^{1'}$), 3.59 (dq, J = 8.5 Hz, 6.2 Hz, 1H, $H^{11'}$), [2] 3.14 (m, 2H, $H^{13'}$), 2.66-2.44 (m, 6H, $(CH_3)_2C\underline{H}$-), 2.44-2.36 (m, 2H, $H^{12a'}$+$(CH_3)_2C\underline{H}$-)), 2.33 (t, $J_{7'\rightarrow8'}$ = 7.3 Hz, 2H, $H^{7'}$), 1.86 (dq, $J_{12b'\rightarrow12a'}$ = 13.4 Hz, J = 6.4 Hz, 1H, $H^{12b'}$), [3] 1.72-1.48 (m, 4H, $H^{8'}$+$H^{10a'}$+$H^{10b'}$), 1.38 (m, 2H, $H^{9'}$), 1.18-0.96 (m, 42H, $C\underline{H_3})_2$CH-).

^{13}**C-NMR**: δ 175.8 ($(CH_3)_2$CH-$\underline{C}$(O)-O-), 175.4 ($(CH_3)_2$CH-$\underline{C}$(O)-O-), 175.2 ($(CH_3)_2$CH-$\underline{C}$(O)-O-), 175.0 (2C, $(CH_3)_2$CH-$\underline{C}$(O)-O-), 174.9 ($(CH_3)_2$CH-$\underline{C}$(O)-O-), 174.5 ($(CH_3)_2$CH-$\underline{C}$(O)-O-), 172.4 (1,2-dithiolan-3-yl-$(CH_2)_4$-$\underline{C}$(O)-O-), 102.4 ($C^{2'}$), 89.3 (C^1), 77.5 ($C^{5'}$), 74.8 ($C^{3'}$), 73.5 (C'), 69.2 (C'), 69.2 (C^2), 68.2 (C^5), 67.3 (C^4), 63.3 ($C^{1'}$), 63.2 ($C^{6'}$), 61.4 (C^6), 56.0 ($C^{11'}$), 40.0 ($C^{12'}$, DMSO overlap), 38.1 ($C^{13'}$), 34.1 ($C^{10'}$), 33.3-33.0 (8C, $C^{7'}$+$(CH_3)_2\underline{C}$H-), 28.1 ($C^{9'}$), 24.1 ($C^{8'}$), 19.0-18.0 (14C, ($\underline{C}H_3)_2$CH-).

HR-MS. Calculated adducts: $[M+H_2O]^+$ = 1038.4522, $[M+Na]^+$ = 1043.4314, $[M+K]^+$ = 1059.4054. Observed adducts: $[M+H_2O]^+$ = 1039.4844, $[M+Na]^+$ = 1043.4355, $[M+K]^+$= 1059.4136.

ATR-FTIR (cm^{-1}): 2974.16, 2936.72, 2877.68, 1738.20, 1469.77, 1388.11, 1344.85, 1246.17,

[2] FiXme Fatal: ikke assignet koblingskonstanter
[3] FiXme Fatal: ikke assignet koblingskonstanter

1185.60, 1140.82, 1074.25, 1028.24, 963.11, 916.58, 849.06, 748.51, 476.19.

***p*-TMS-phenol** (**2.4**). *p*-Bromophenol **2.3** (2.37 g, 13.3 mmol) was solubilized in dry THF (150 mL) under an argon atmosphere and cooled to -78 °C. *n*-BuLi (1.6 M, 25 mL, 40.0 mmol) was added drop-wise to the reaction mixture at -78 °C. 15 min upon addition, the reaction mixture was removed from the cooling bath and allowed to reach 20 °C for 2 h leading to a white cloudy suspension. The reaction mixture was re-cooled to -78 °C and TMSCl (5.12 mL, 40.0 mmol) was then added to the reaction mixture which was left in the cooling bath and allowed to reach 20 °C overnight. The reaction was quenched by addition of sat. NH_4Cl (40 mL). H_2O (50 mL) was added and the mixture was then extracted using EtOAc (3x100 mL). The organic phases were combined, dried (Na_2SO_4) and concentrated *in vacuo* followed by purification by dry column vacuum chromatography (1% EtOAc/heptane linear increments). The product **2.4** was further refined by sublimation at 50 °C.

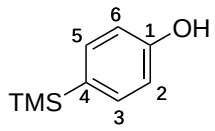

yield = (1.74 g, 78%).

m.p.: 74.3 °C.

^{1}**H-NMR** (400 MHz, $CDCl_3$) δ: 7.41 (d, $J_{m\rightarrow o}$ = 8.5 Hz, 2H, *m*-H_{Ar}), 6.84 (d, $J_{o\rightarrow m}$ = 8.5 Hz, 2H, *o*-H_{Ar}), 4.85 (s, 1H, *p*-TMS-Ph-O-$\underline{H}$), 0.24 (s, 9H, (C$\underline{H_3}$)$_3$-Si).

^{13}**C-NMR** (100 MHz, $CDCl_3$) δ: 156.3 (C^1), 135.1 (2C, C^3+C^5), 131.8 (C^4), 115.0 (2C, C^2+C^6), -0.8 (3C, ($\underline{C}H_3$)$_3$-Si).

LC-MS: Calculated adducts $[M-H]^-$: 165.07. Observed adducts: $[M-H]^-$: 165.07.

ATR-FTIR (cm^{-1}): 3174.58, 2952.11, 2774.57, 2695.51, 2636.61, 1892.45, 1597.19, 1582.07, 1501.04, 1419.11, 1358.65, 1249.24, 1231.76, 1179.69, 1105.29, 837.99, 813.08, 752.72, 709.83, 649.42, 514.15.

All observed spectral shifts are in agreement with literature [] [29].

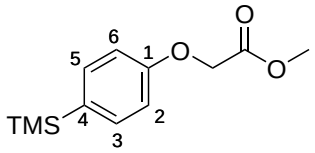

Methyl 2-(*p*-TMS-phenoxy)acetate (**2.5**). *p*-TMS-phenol **2.4** (0.170 g, 1.0 mmol) was dissolved in acetone (25 mL). Methyl bromoacetate (0.15 mL, 1.5 mmol) was added together with K_2CO_3 (0.215 gm, 1.5 mmol) and the reaction mixture was refluxed for 4 h and left stirred at 20 °C overnight. The reaction mixture was filtered and concentrated *in vacuo*. The residue was dissolved in EtOAc (10 mL) and washed with H_2O (2x10 mL). The organic phase was then dried (Na_2SO_4) and concentrated *in vacuo* yielding **2.5** as off-white crystals. The product was verified by GC-MS.
yield = (0.230 g, 90%).
m.p.: 40.4 °C.

^{1}**H-NMR** (400 MHz, $CDCl_3$) δ: 7.45 (d, $J_{m\rightarrow o}$ = 8.6 Hz, 2H, *m*-H_{Ar}), 6.90 (d, $J_{o\rightarrow m}$ = 8.6 Hz, 2H, *o*-H_{Ar}), 4.64 (s, 2H, -O-C$\underline{H_2}$-C(O)-O-CH_3), 3.81 (s, 3H, -O-CH_2-C(O)-O-C$\underline{H_3}$), 0.24 (s, 9H, (C$\underline{H_3}$)$_3$-Si).

^{13}**C-NMR** (100 MHz, $CDCl_3$) δ: 169.6 (-O-CH_2-$\underline{C}$(O)-O-CH_3), 158.4 (C^1), 135.0 (2C, C^3+C^5), 133.0 (C^4), 114.2 (2C, C^2+C^6), 65.2 (-O-$\underline{C}H_2$-C(O)-O-CH_3), 52.4 (-O-CH_2-C(O)-O-$\underline{C}H_3$), -0.84 (3C, ($\underline{C}H_3$)$_3$-Si)).

HR-MS. Calculated adducts: $[M+H]^+$ = 239.1098, $[M+Na]^+$: 261.0917. Observed adducts: $[M+H]^+$: 239.1107, $[M+Na]^+$: 261.0929.

ATR-FTIR (cm^{-1}): 3059.10, 3020.63, 2952.30, 2895.22, 2847.71, 1898.93, 1765.52, 1747.78, 1589.95, 1498.62, 1446.76, 1433.79, 1383.75, 1294.24, 1222.89, 1179.77, 1110.98, 1072.28, 976.20, 834.44, 818.09, 754.60, 701.77, 604.42, 546.78, 510.23.

Conditions inspired from [] [30].

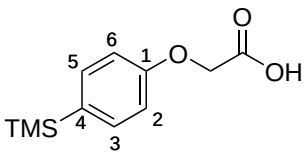

2-(p-TMS-phenoxy)acetic acid (**2.1**). The ester **2.5** (0.105 g, 0.345 mmol) was solubilized in CH_3OH (0.3 mL) at 20 °C. KOH in CH_3OH (4.95 M, 0.3 mL, 1.5 mmol) was added to the stirred solution of **2.5** leading to precipitation of a white solid. The reaction mixture was stirred for 1 h at 20 °C. The reaction was quenched by diluting with H_2O (2 mL). The reaction mixture was washed with Et_2O (2x10 mL) followed by acidification to pH 2 (using 0.1 M HCl). The reaction mixture was extracted with Et_2O (2x10 mL) and the combined Et_2O-fractions were concentrated *in vacuo*. The crude residue was recrystallized using a mixture of CH_3OH (8 mL) and H_2O (5 mL) that was concentrated *in vacuo* upon cooling (left above waterbath in rotary-evaporator with slow rotation) leading to the intended product **2.1** as white crystals. The flask was upon recrystallization left in the fridge overnight to assure full recrystallization. The suspension was filtered and the white crystals were dried *in vacuo* affording **2.1**.

yield = (0.075 g, 77%).

m.p.: 89.3 - 92°C

^{1}**H-NMR** (400 MHz, $CDCl_3$) δ: 9.45 (s (broad), 1H, -O-CH_2-C(O)-O$\underline{H}$), 7.47 (d, $J_{m\rightarrow o}$ = 8.5 Hz, 2H, *m*-H_{Ar}), 6.92 (d, $J_{o\rightarrow m}$ = 8.5 Hz, 2H, *o*-H_{Ar}), 4.70 (s, 2H, -O-C$\underline{H_2}$-C(O)-OH), 0.25 (s, 9H, (C$\underline{H_3}$)$_3$-Si)).

^{13}**C-NMR** (100 MHz, $CDCl_3$) δ: 174.1 (-O-CH_2-$\underline{C}$(O)-OH), 158.1 (C^1), 135.1 (2C, C^3+C^5), 133.4 (C^4), 114.2 (2C, C^2+C^6), 64.7 (-O-$\underline{C}H_2$-C(O)-OH), -0.86 (3C, ($\underline{C}H_3$)$_3$-Si)).

HR-MS. Calculated adducts: $[M\text{-}H]^-$ = 223.08. Observed adducts: $[M\text{-}H]^-$: 223.13.

ATR-FTIR (cm^{-1}): 3020.18, 2953.90, 2898.17, 2786.33, 2579.03, 1745.72, 1708.35, 1590.43, 1562.12, 1503.03, 1427.48, 1268.56, 1232.63, 1188.50, 1109.8, 1083.38, 917.34, 832.51, 804.25, 750.80, 704.36, 646.21, 604,02, 521.14.

Conditions inspired from [] [31]

6'-*O*-(2-(*p*-TMS-phenoxy)acetyl)-1',2,3,3',4,4',6-hepta-*O*-isobutyryl-sucrose (**2.2**). To a solution of 1',2,3,3',4,4',6-hepta-*O*-isobutyryl-sucrose **1.25** (0.334 g, 0.4[4] mmol) in dry DMF (9 mL) under inert atmosphere, was added a solution of **2.1** (0.143 g, 0.61 mmol), DMAP (0.146 g, 1.2 mmol) and EDC·HCl (0.111 g, 0.57 mmol) in dry DMF (15 mL) which had been premixed for 15-30 min. The reaction mixture was left stirred for reaction at 20 °C. The reaction was followed by TLC (2:3 EtOAc/heptane). Freshly made mixtures of the activated ester prepared as described above were added to the reaction mixture after 24 h and 48 h respectively. [24 h: **2.1** (0.049 g, 0.21 mmol), DMAP (0.051 g, 0.41 mmol), and EDC·HCl (0.039 g, 0.20 mmol) in dry DMF (10 mL). 48 h: **2.1** (0.080 g, 0.34 mmol), DMAP (0.051 g, 0.41 mmol), and EDC·HCl (0.063 g, 0.32 mmol) in dry DMF (10 mL)]. Upon reaction completion, the reaction mixture was concentrated *in vacuo* and Et_2O (40 mL) was added. The organic phase was washed with H_2O (2x40 mL), dried (Na_2SO_4) and purified by dry column vacuum chromatography (4% EtOAc/heptane linear increments) yielding compound **2.2** as a transparent oil.

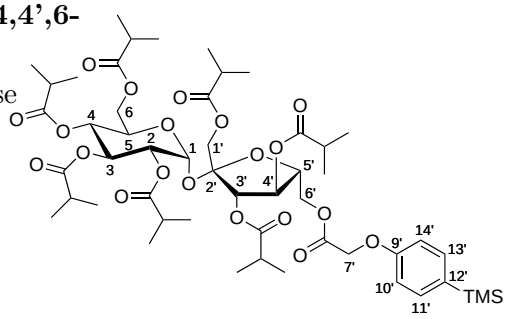

yield = (0.339 g, 82%).

$[\alpha]_D^{20}$ = +34° (c 1.00, EtOH)

^{1}**H-NMR** (400 MHz, DMSO-d6) δ: 7.41 (d, $J_{m\rightarrow o}$ = 8.6 Hz, 2H, *m*-H_{Ar}), 6.9 (d, $J_{o\rightarrow m}$ = 8.6 Hz, 2H, *o*-H_{Ar}), 5.68 (d, $J_{1\rightarrow 2}$ = 3.6 Hz, 1H, H^1), 5.55 (d, $J_{3'\rightarrow 4'}$ = 7.8 Hz, 1H, $H^{3'}$), 5.46-5.36 (m, 2H, H^3+$H^{4'}$), 5.10 (t, $J_{4\rightarrow 3} = J_{4\rightarrow 5}$ = 10.0 Hz 1H, $H^{4'}$), 4.94 (dd, $J_{2\rightarrow 3}$ = 10.3 Hz, $J_{2\rightarrow 1}$ = 3.6 Hz, 1H, H^2), 4.81 (s, 2H, -O-C$\underline{H_2}$-C(O)-O-), 4.45-4.30 (m, 4H, H^5, $H^{5'}$, $H^{6'}$), 4.22 (dd, $J_{6a\rightarrow 6b}$ = 12.7 Hz, $J_{6a\rightarrow 5}$ = 4.2 Hz, 1H, H^{6a}), 4.09 (m, 3H, H^{6b}+$H^{1'}$), 2.64-2.34 (m (overlap with DMSO), 7H, $(CH_3)_2C\underline{H}$-), 1.19-0.95 (m, 42H, $(C\underline{H_3})_2$CH-), 0.20 (s, 9H, $(C\underline{H_3})_3$-Si)).

^{13}**C-NMR** (100 MHz, DMSO-d6) δ: 175.8 ($(CH_3)_2$CH-$\underline{C}$(O)-O-), 175.6 ($(CH_3)_2$CH-$\underline{C}$(O)-O-), 175.3 ($(CH_3)_2$CH-$\underline{C}$(O)-O-), 175.0 (3C, $(CH_3)_2$CH-$\underline{C}$(O)-O-), 174.6 ($(CH_3)_2$CH-$\underline{C}$(O)-O-), 168.5 (*p*-TMS-Ph-O-CH_2-$\underline{C}$(O)-O-), 158.3 ($C^{9'}$), 134.6 (2C, $C^{11'}$+$C^{13'}$), 131.4 ($C^{12'}$) , 114.0 (2C, $C^{10'}$+$C^{14'}$), 102.3 ($C^{2'}$), 89.2 (C^1), 77.3 ($C^{5'}$), 74.7 ($C^{3'}$), 73.1 ($C^{4'}$), 69.3 (C^3), 69.2 (C^2), 68.2 (C^5), 67.2 (C^4), 64.2 (*p*-TMS-Ph-O-$\underline{C}H_2$-C(O)-O-), 63.5 (2C, $C^{1'}$+$C^{6'}$), 61.3 (C^6), 33.3-32.9 (7C, $(CH_3)_2\underline{C}$H-), 18.8-18.3 (13C, $(\underline{C}H_3)_2$CH-), 18.1 ($(\underline{C}H_3)_2$CH-), -0.9 (3C, $(\underline{C}H_3)_3$-Si)).

HR-MS. Calculated adducts: $[M+H_2O]^+$ = 1056.4956, $[M+Na]^+$ = 1061.4748. Observed adducts: $[M+H_2O]^+$ = 1056.5190 , $[M+Na]^+$ = 1061.4740.

ATR-FTIR (cm^{-1}): 2974.30, 2878.08, 1739.64, 1593.31, 1469.88, 1388.33, 1246.93, 1183.12, 1142.00, 1112.25, 1074.62, 1027.52, 839.59, 754.43.

[4] FiXme Fatal: X

Methyl 2-(p-iodo-phenoxy)acetate (**2.6**).

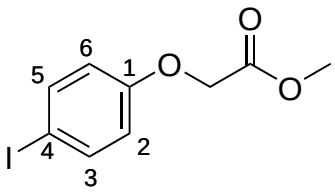

Synthesis of 2.6 using $Tl(OOCCF_3)_3$ and NaI.
The ester of **2.5** (0.107 g, 0.45 mmol) was dissolved in TFA/CH_3CN (7 mL, 3:7 v/v). A stock solution of $Tl(OOCCF_3)_3$ in TFA/CH_3CN (184 mM, 3:7 v/v), was prepared from which an aliquot of $Tl(OOCCF_3)_3$ (4.4 mL, 0.81 mmol) was added to the reaction mixture. The reaction mixture turned slightly red and was left stirred at 20 °C. After 40 min, NaI (0.237 g, 1.58 mmol) was added to the reaction mixture resulting in a dark black/red solution. After 5 min, the reaction was quenched using aq. sat. Na_2CO_3 (20 mL). The solution turned slightly orange with a precipitate. The solution was extracted using EtOAc (3x10 mL) and the organic phases were combined, washed with $Na_2S_2O_3$ (10 mL, 10% w/w), dried (Na_2SO_4) and concentrated *in vacuo*. The crude product was re-suspended in $CDCl_3$ and filtered. The filtrate was analyzed by ^{1}H-NMR and corresponded to the intended product **2.6**. Purity by ^{1}H-NMR, 90%.

Synthesis of 2.6 using ICl.
The ester of **2.5** (0.057 g, 0.24 mmol) was dissolved in dry CH_2Cl_2 (1 mL) and cooled to 0 °C. A stock solution of ICl in dry CH_2Cl_2 (1.54 M, 0.25 g·mL dry CH_2Cl_2) was prepared from which ICl (0.022 mL, 0.034 mmol) was added to the reaction mixture at 0 °C. The reaction mixture was left stirred for 3 h at 0 °C. After 3 h, the reaction was quenched using aq. $Na_2S_2O_3$ (2 mL, 10% w/w). The organic phase was collected and the H_2O phase was further washed using EtOAc (3x3 mL). The organic phases were combined, dried (Na_2SO_4) and concentrated *in vacuo*. The residue was then purified by dry column vacuum chromatography (4% EtOAc/heptane increments) yielding methyl 2-(*p*-iodo-phenoxy)acetate **2.6**. **yield** = (0.048 g, 77%). [32]. [5]

Synthesis of 2.6 using NIS and TMSOTf.
The ester of **2.5** (0.063 g, 0.27 mmol) and NIS (0.077 g, 0.35 mmol) were suspended in dry CH_2Cl_2 (1 mL). TMSOTf (0.01 mL, 0.055 mmol) was added and the reaction mixture was left stirred at 20 °C. After approx. 20 h, the reaction mixture had turned dark red and more homogenous. The reaction was followed by TLC analysis (EtOAc/heptane, 2:3 v/v). Upon reaction completion, the reaction was quenched using aq. $Na_2S_2O_3$ (2 mL, 10% w/w) and extracted using EtOAc (3x3 mL). The organic phases were combined, dried (Na_2SO_4) and purified by dry column vacuum chromatography (4% EtOAc/heptane linear increments) yielding **2.6**. **yield** = (0.057 g, 82%). [6]

[5] FiXme Fatal: MHC-HSJ-49 040314
[6] FiXme Fatal: MHC-HSJ-48

Synthesis of 2.6 using CAT and NaI.
The ester of **2.5** (0.101 g, 0.42 mmol), CAT (0.240 g, 0.85 mmol) and NaI (0.174 g, 1.16 mmol) were suspended in DMF (2 mL) and stirred for 1 h min at 20 °C (solution turned orange). After 1 h, the reaction mixture was diluted with H_2O and dilute HCl (5% w/w) was added. The mixture was extracted using EtOAc (2x10 mL) and the H_2O phase was further washed with EtOAc (2x10 mL). The organic phases were combined and washed with aq. $Na_2S_2O_3$ (2 x 15 mL, 10% w/w), H_2O (2x15 mL) and sat. brine (15 mL). The organic phase was dried (Na_2SO_2) and the residue was purified by dry column vacuum chromatography (4% EtOAc/heptane linear increments). The purification afforded methyl 2-(p-iodo-phenoxy)-acetate **2.6**. **yield** = (0.084 g, 70%). MHC-HSJ-39. Conditions inspired from [] [7] [33].

Analysis data of 2.6.
m.p.: 67.8 - 70.2°C
^{1}**H-NMR** (400 MHz, $CDCl_3$) δ: 7.57 (d, $J_{m\rightarrow o}$ = 9.0 Hz, 2H, m-H_{Ar}), 6.67 (d, $J_{o\rightarrow m}$ = 9.0 Hz, 2H, o-H_{Ar}), 4.60 (s, 2H, -O-C$\underline{H_2}$-C(O)-O-CH_3), 3.80 (s, 3H, -O-CH_2-C(O)-O-C$\underline{H_3}$).

^{13}**C-NMR** (100 MHz, $CDCl_3$) δ: 169.1 (-O-CH_2-$\underline{C}$(O)-O-CH_3), 157.8 (C^1), 138.5 (2C, C^3+C^5), 117.1 (2C C^2+C^6), 84.3 (C^4), 65.4 (-O-$\underline{C}H_2$-C(O)-O-CH_3), 52.5 (-O-CH_2-C(O)-O-$\underline{C}H_3$).

HR-MS. Calculated adducts. $[M+H]^+$: 292.9669, $[M+Na]^+$: 314.9489. Observed adducts: $[M+H]^+$: 292.9670, $[M+Na]^+$: 314.9494.

ATR-FTIR (cm^{-1}): 3504.51, 3081.41, 3062.84, 3034.40, 3006.62, 2947.07, 2923.58, 2853.45, 1757.27, 1583.21, 1567.55, 1484.10, 1435.82, 1394.37, 1282.07, 1241.99, 1209.64, 1173.24, 1082.27, 1060.00, 1000.55, 971.95, 914.30, 834.80, 810.24, 713.94, 597.46, 510.84.

[7] FiXme Fatal: kilde skal indsÃ¦ttes

6'-*O*-(2-(*p*-iodo-phenoxy)acetyl)-1',2,3,3',4,4',6-hepta-*O*-isobutyryl-sucrose, (**2.7**).

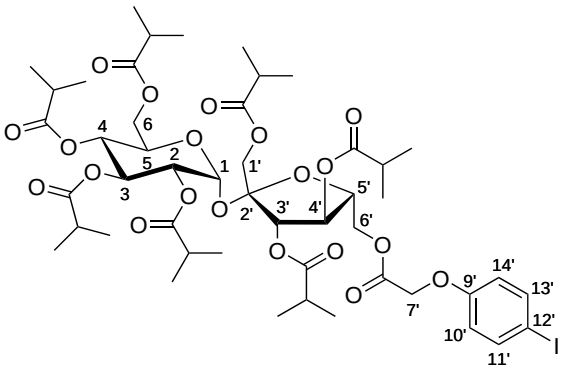

Synthesis of 2.7 using $Tl(OOCCF_3)_3$ and NaI.
The TMS precursor **2.2** (0.030 g, 0.029 mmol) was dissolved in TFA/CH_3CN (0.46 mL, 3:7 v/v) at 20 °C. $Tl(OOCCF_3)_3$ (0.289 mL, 0.062 mmol) was added from a $Tl(OOCCF_3)_3$ in TFA/CH_3CN stock solution (215 mM, 3:7 v/v) and the reaction mixture was left stirred at 20 °C for reaction for 30 min. NaI (0.022 g, 0.147 mmol) was added after 30 min by which the reaction mixture turned deep red/black. After another 5 min, the reaction was quenched by addition of aq. sat. Na_2CO_3 (3 mL). The suspension was extracted using EtOAc (3x3 mL). TLC (2:3 EtOAc/heptane) of the EtOAc phase indicated full conversion. The product **2.7** was isolated as a transparent oil by dry column vacuum chromatography (4% EtOAc/heptane linear increments). **Yield = (0.029 g, 97%)**.

Conditions inspired from [34] [8]
Synthesis of 2.7 using ICl.
The TMS precursor **2.2** (0.029 g, 0.028 mmol) was dissolved in dry CH_2Cl_2 (1 mL). ICl (0.025 g, 0.15 mmol) was dissolved in dry CH_2Cl_2 (0.25 mL) and then added to the reaction mixture of **2.2** at 0 °C. TLC analysis (EtOAc/heptane 2:3 v/v) indicated full completion after 2 h at 0 °C. The reaction was quenched by addition of aq. $Na_2S_2O_3$ (2 mL, 10% w/w). The mixture was extracted using EtOAc (3x3 mL). The organic phases were combined, dried (Na_2SO_4) and concentrated *in vacuo* yielding the product **2.7** as a transparent oil. **Yield = (0.028 g, 93%).**

Conditions inspired from [32]. [9]
Synthesis of 2.7 using NIS and TMSOTf.
The TMS precursor **2.2** (0.028 g, 0.027 mmol) and NIS (0.010 g, 0.045 mmol) were dissolved in dry CH_2Cl_2 (1 mL). A stock solution of TMSOTf in CH_2Cl_2 (691 mM, TMSOTf/CH_2Cl_2 - 1:7 v/v) was prepared, from which TMSOTf (0.015 mL, 0.010 mmol) was added to the reaction mixture. The reaction was left stirred at 20 °C. TLC analysis (EtOAc/heptane 2:3 v/v) conducted after 2 h indicated full completion. The reaction was quenched by addition of aq. $Na_2S_2O_3$ (2 mL, 10% w/w). The product was extracted using EtOAc (3x3 mL). The organic phases were combined, dried (Na_2SO_4) and concentrated

[8] FiXme Fatal: MHC-HSJ-52.
[9] FiXme Fatal: MHC-HSJ-51

in vacuo yielding the product **2.7** as a transparent oil. **yield = (0.024 g, 81%** [10]**).** [11]

Analysis data of 2.7.

$[\alpha]_D^{20}$ = [12]° [13]

^{1}**H-NMR** (400 MHz, DMSO-d6) δ: 7.58 (d, $J_{m\to o}$ = 9.0 Hz, 2H, m-H$_{Ar}$), 6.78 (d, $J_{o\to m}$ = 9.0 Hz, 2H, o-H$_{Ar}$), 5.67 (d, $J_{1\to 2}$ = 3.6 Hz, 1H, H^1), 5.54 (d, $J_{3'\to 4'}$ = 7.5 Hz, 1H, H$^{3'}$), 5.43-5.35 (m, 2H, H^3+H$^{4'}$), 5.10 (t, $J_{4\to 3}$ = $J_{4\to 5}$ = 10.2 Hz, 1H, H^4), 4.95 (dd, $J_{2\to 3}$ = 10.2 Hz, $J_{2\to 1}$ = 3.6 Hz, 1H, H^2), 4.80 (s, 2H, -O-C$\underline{H_2}$-C(O)-O-), 4.44-4.28 (m, 4H, H^5, H$^{5'}$, H$^{6'}$), 4.22 (dd, $J_{6a\to 6b}$ = 12.7 Hz, $J_{6a\to 5}$ = 4.2 Hz, 1H, H^{6a}), 4.09 (m, 3H, H^{6b}+H$^{1'}$), 2.65-2.35 (m, 7H (overlap with DMSO), (CH$_3$)$_2$C$\underline{H}$-), 1.18 - 0.95 (m, 42H, (C$\underline{H_3}$)$_2$CH-).

^{13}**C-NMR** (100 MHz, DMSO-d6) δ: 175.8 ((CH$_3$)$_2$CH-$\underline{C}$(O)-O-), 175.6 ((CH$_3$)$_2$CH-$\underline{C}$(O)-O-), 175.2 ((CH$_3$)$_2$CH-$\underline{C}$(O)-O-), 175.0 (2C, (CH$_3$)$_2$CH-$\underline{C}$(O)-O-), 174.9 ((CH$_3$)$_2$CH-$\underline{C}$(O)-O-), 174.6 ((CH$_3$)$_2$CH-$\underline{C}$(O)-O-), 168.3 (p-I-Ph-O-CH$_2$-$\underline{C}$(O)-O-), 157.6 (C$^{9'}$), 138.0 (2C, C$^{11'}$+C$^{13'}$), 117.3 (2C, C$^{10'}$+C$^{14'}$), 102.3 (C$^{2'}$), 89.2 (C^1), 84.0 (C$^{12'}$), 77.3 (C$^{5'}$), 74.7 (C$^{3'}$), 73.2 (C$^{4'}$), 69.3 (C^3), 69.1 (C^2), 68.2 (C^5), 67.2 (C^4), 64.5 (p-I-Ph-O-$\underline{C}$H$_2$-C(O)-O-), 63.8 (C$^{6'}$), 63.4 (C$^{1'}$), 61.3 (C^6), 33.3-33.0 (7C, (CH$_3$)$_2$$\underline{C}$H-), 18.8-18.3 (13C, ($\underline{C}H_3$)$_2$CH-), 18.1 (($\underline{C}H_3$)$_2$CH-).

HR-MS. Calculated adducts: [M+H$_2$O]$^+$= 1110.3527, [M+Na]$^+$ = 1115.3319. Observed adducts: [M+H$_2$O]$^+$ = 1110.3776, [M+Na]$^+$ = 1115.3333.

ATR-FTIR (cm^{-1}): 3470.02, 2974.30, 2937.67, 2877.84, 1860.25, 1740.03, 1699.63, 1592.28, 1486.69, 1456.79, 1388.22, 1289.06, 1238.30, 1184.04, 1145.05, 1072.93, 1027.80, 1001.50, 917.32, 816.79, 762.93, 694.72, 666.78. [14]

[10] FiXme Fatal: Dobbelttjek!
[11] FiXme Fatal: MHC-HSJ-50.
[12] FiXme Fatal: XX
[13] FiXme Fatal: (c ,)
[14] FiXme Fatal: SAMME IR-DATA fra SAIB-I ICl.

2,4-diiodo-6-TMS-phenol (**2.26**). 2,4,6-triiodo-phenol **1.37** (2 g, 4.11 mmol) was dissolved in dry THF (7 mL). Et_3N (0.75 mL, 6.06 mmol) was added together with TMSCl (0.83 mL, 6.24 mmol) to the stirred reaction mixture of **1.37** at 20 °C. A precipitate was observed. After 2 h, hexane (25 mL) was added and the suspension was filtered through celite. The filtrate was washed with H_2O (25 mL), dried (Na_2SO_4) and concentrated *in vacuo*. The residue was re-dissolved in dry THF (7 mL) and cooled to -78 °C. *s*-BuLi (1.4 M, 5.5 mL, 7.7 mmol) was added dropwise to the reaction mixture of the TMS protected phenol **1.37**. The reaction mixture was left stirred in the dry ice bath and allowed to reach 20 °C overnight. The reaction was quenched using aq. sat. NH_4Cl (5 mL) and H_2O (50 mL) was added. The organic phase was separated, dried (Na_2SO_4) and purified by dry column vacuum chromatography (using 1% EtOAc in heptane linear increments) affording **2.26** as a white solid.

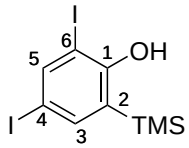

yield = (1.21 g, 72%).

m.p.: 95 - 96°C

^{1}**H-NMR** (400 MHz, $CDCl_3$) δ: 7.91 (d, $J_{5\rightarrow3}$ = 2.0 Hz, 1H, H^5), 7.51 (d, $J_{3\rightarrow5}$ = 2.0 Hz, 1H, H^3), 5.44 (s, 4,6-diiodo-2-TMS-Ph-O-*H*), 0.28 (s, 9H, (CH_3)$_3$-Si)).

^{13}**C-NMR** (100 MHz, $CDCl_3$) δ: 158.5 (C^1), 146.1 (C^5), 144.1 (C^3), 129.8 (C^2), 88.1 (C^6), 83.8 (C^4), -1.21 (3C, (CH_3)$_3$-Si).

LC-MS. Calculated adducts: $[M+H]^+$ = 417.8747, $[M+Na]^+$ = 440.8639. Observed adducts: $[M+H]^+$ = XX[15], $[M+Na]^+$ = XX[16].

ATR-FTIR (cm^{-1}): 3488.97, 2948.15, 2893.94, 1553.39, 1536.40, 1421.83, 1369.93, 1306.31, 1225.85, 1158.03, 1063.34, 839.51, 761.26, 692.83, 638.75, 620.06, 536.46.

[15] FiXme Fatal: Mangler
[16] FiXme Fatal: Mangler

Methyl 2-(2,4-diiodo-6-TMS-phenoxy)acetate (**2.27**). The phenol **2.26** (0.4 g, 0.96 mmol) was dissolved in acetone. K_2CO_3 (0.2 g, 1.44 mmol) was added to the reaction mixture followed by methyl bromoacetate (0.15 mL, 1.53 mmol). The reaction mixture was then refluxed for 3.5 h after which it was filtered. The filtrate was concentrated *in vacuo* and the residue was re-dissolved in EtOAc (30 mL). The EtOAc phase was washed with H_2O and sat. brine. The EtOAc phase was dried (Na_2SO_4) and concentrated *in vacuo* affording **2.27** as a white solid. **yield = (0.428 g, 96%).**

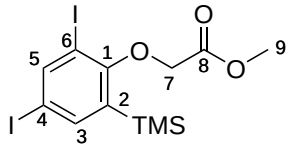

m.p.: 87 - 89°C

^{1}**H-NMR** (400 MHz, $CDCl_3$) δ: 8.11 (d, 1H, $J_{5\rightarrow3}$ = 2.1 Hz, H^5), 7.63 (d, 1H, $J_{3\rightarrow5}$ = 2.1 Hz, H^3), 4.56 (s, 2H, -O-C$\underline{H_2}$-C(O)-O-CH_3), 3.58 (s, 3H, -O-CH_2-C(O)-O-C$\underline{H_3}$), 0.28 (s, 9H, (C$\underline{H_3}$)$_3$-Si)).

^{13}**C-NMR** (100 MHz, $CDCl_3$) δ: 168.4 (C^8), 161.8 (C^1), 148.9 (C^5), 144.5 (C^3), 138.4 (C^2), 92.1 (C^6), 90.5 (C^4), 70.1 (C^7), 52.4 (C^9), -0.38 (3C, ($\underline{C}H_3$)$_3$-Si).

HR-MS. Calculated adducts: $[M+H]^+$ = 490.9031, $[M+Na]^+$ = 512.8850. Observed adducts: $[M+H]^+$ = 490.9028, $[M+Na]^+$ = 512.8850.

ATR-FTIR (cm^{-1}): 2953.00, 2918.89, 2902.46, 1760.24, 1523.54, 1434.36, 1404.47, 1245.74, 1197.71, 1061.86, 838.73, 772.49, 694.79, 641.86, 623.05.

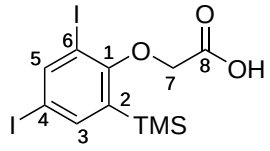

2-(2,4-diiodo-6-TMS-phenoxy)acetic acid (**2.30**). The methyl ester of **2.27** (0.667 g, 1.35 mmol) was dissolved in CH_3CN (120 mL) at 20 °C. 3% aq. w/v Na_2CO_3 solution (80 mL) was added to the reaction mixture. Phase separation was observed. More 3% aq. w/v Na_2CO_3 solution (120 mL) together with CH_3CN (40 mL). The reaction mixture was left stirred for 1 h for reaction at 20 °C which led to the formation of a precipitate. Na_2CO_3 (1 g, 9.4 mmol) was added to assure full hydrolysis of the ester. Upon the full hydrolysis, the suspension was concentrated *in vacuo* to remove as much CH_3CN as possible. The remaining suspension was subsequently washed with Et_2O (2x200 mL) to remove any residuals of **2.27**. The suspension was then carefully acidified to pH 2-3 using drop-wise addition of 0.1 M HCl. The acidified solution was rapidly extracted using Et_2O (2x200 mL), dried (Na_2SO_4) and concentrated *in vacuo* afford the acid **2.30** as a white solid.

yield = (0.580 g, 90%).

m.p.: 137 - 140°C

^{1}**H-NMR** (400 MHz, DMSO-d6) δ: 8.15 (d, $J_{5\rightarrow3}$ = 2.1 Hz, 1H, H^5), 7.59 (d, $J_{3\rightarrow5}$ = 2.1 Hz, 1H, H^3), 4.40 (s, 2H, -O-C$\underline{H_2}$-C(O)-OH), 0.24 (s, 9H, (C$\underline{H_3}$)$_3$-Si)).

^{13}**C-NMR** (100 MHz, DMSO-d6) δ: 168.9 (C^8), 161.8 (C^1), 148.1 (C^5), 143.5 (C^3), 137.4 (C^2), 93.4 (C^6), 91.0 (C^4), 70.0 (C^7), -0.69 (3C, ($\underline{C}H_3$)$_3$-Si).

HR-MS. Calculated adducts: $[M+H]^+$ = 476.8874, $[M+Na]^+$ = 498.8694. Observed adducts: $[M+H]^+$ = 476.8873, $[M+Na]^+$ = 498.8693.

ATR-FTIR (cm^{-1}): 2962.84, 2915.54, 2759.43, 2686.89, 2553.46, 1730.70, 1705.90, 1428.62, 1399.66, 1251.30, 1210.40, 1072.97, 1057.41 833.17, 771.17, 687.98, 635.34, 560.28.

6,6'-di-*O*-(2-(2,4-diiodo-6-TMS-phenoxy)acetyl)-1',2,3,3',4,4',-hexa-*O*-isobutyryl-sucrose (**2.31**).

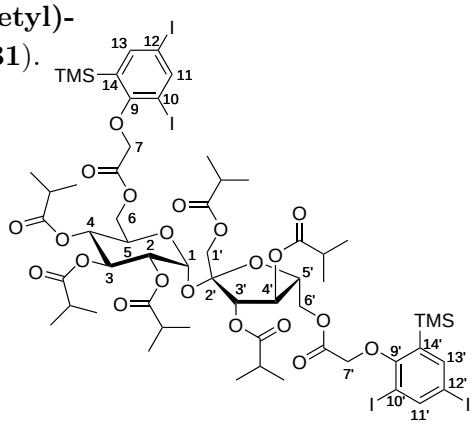

The diol of **1.34** was dissolved in dry CH_2Cl_2 (1.5 mL). The acid **2.30** (0.376 g, 0.79 mmol), EDC·HCl (0.159 g, 0.79 mmol) and DMAP (0.136 g, 1.1 mmol) were mixed in dry CH_2Cl_2 (3.2 mL) and added immediately to the solution of the diol (final concentration 68 mM). The reaction mixture was left stirred at 20 °C for reaction and followed by LC-MS analysis. Upon reaction completion (approx. 2-3 h), the reaction mixture was directly purified by dry column vacuum chromatography (using 1% linear increment of EtOAc/heptane) affording **2.31** as a white solid.

yield = (0.454 g, 83%).

m.p.: 65 - 68°C

$[\alpha]_D^{20}$ = +24° (c 1.00, EtOH)

^{1}**H-NMR** (400 MHz, $CDCL_3$) δ: 8.09 (d, $J_{11\to13} = J_{11'\to13'}$ = 2.1 Hz, 2H, H^{11}+$H^{11'}$) 7.617 (d, $J_{13\to11} = J_{13'\to11'}$ = 2.1 Hz, 1H H^{13} or $H^{13'}$) 7.614 (d, $J_{13\to11} = J_{13'\to11'}$ = 2.1 Hz, 1H H^{13} or $H^{13'}$) 5.62 (d, $J_{1\to2}$ = 3.6 Hz, 1H, H^1), 5.57 (d, $J_{3'\to4'}$ = 7.6 Hz, 1H, $H^{3'}$) 5.48 (t, $J_{3\to2} = J_{3\to4}$ = 9.9 Hz, 1H, H^3) 5.39 (t, $J_{4'\to3'} = J_{4'\to5'}$ = 7.6 Hz, 1H, $H^{4'}$) 5.14 (t, $J_{4\to3} = J_{4\to5}$ = 9.9 Hz, 1H, H^4) 4.96 (dd, $J_{2\to3}$ = 10.3 Hz, $J_{2\to1}$ = 3.6 Hz, 1H, H^2) 4.65 (s, 2H, -O-C$\underline{H_2}$-C(O)-O-) 4.58 (s, 2H, -O-C$\underline{H_2}$-C(O)-O-) 4.54 (dd, $J_{6a'\to6b'}$ = 12.0 Hz, $J_{6a'\to5'}$ = 3.9 Hz, 1H, $H^{6a'}$) 4.50-4.31 (m, 4H, H^5+$H^{6b'}$+H^6) 4.25 (dt, $J_{5'\to4'}$ = 7.7 Hz, $J_{5'\to6a'} = J_{5'\to6b'}$ = 3.9 Hz, 1H, $H^{5'}$) 4.04 (d, $J_{1a'\to1b'}$ = 11.9 Hz, 1H, $H^{1'}$) 3.98 (d, $J_{1b'\to1a'}$ = 11.9 Hz, 1H, $H^{1'}$) 2.72-2.37 (m, 6H, $(CH_3)_2C\underline{H}$-) 1.31-1.03 (m, 36H, $(C\underline{H_3})_2$CH-) 0.30 (9H, $(C\underline{H_3})_3$-Si) 0.28 (9H, $(C\underline{H_3})_3$-Si).

^{13}**C-NMR** (100 MHz, $CDCL_3$) δ: 176.2 ($(CH_3)_2$CH-$\underline{C}$(O)-O), 176.0 ($(CH_3)_2$CH-$\underline{C}$(O)-O), 176.0 ($(CH_3)_2$CH-$\underline{C}$(O)-O), 175.8 ($(CH_3)_2$CH-$\underline{C}$(O)-O), 175.8 ($(CH_3)_2$CH-$\underline{C}$(O)-O), 175.2 ($(CH_3)_2$CH-$\underline{C}$(O)-O), 167.7 (2,4-diiodo-6-TMS-Ph-O-CH_2-$\underline{C}$(O)-O-), 167.5 (2,4-diiodo-6-TMS-Ph-O-CH_2-$\underline{C}$(O)-O-), 161.9 (C^9/$C^{9'}$), 161.8 (C^9/$C^{9'}$), 148.9 (C^{11}/$C^{11'}$), 148.8 (C^{11}/$C^{11'}$), 144.4 (C^{13}/$C^{13'}$), 144.3 (C^{13}/$C^{13'}$), 138.5 (C^{14}/$C^{14'}$), 138.4 (C^{14}/$C^{14'}$), 103.2 ($C^{1'}$), 92.1 (C^{10}/$C^{10'}$), 91.9 (C^{10}/$C^{10'}$), 90.5 (C^{12}/$C^{12'}$), 90.4 (C^{12}/$C^{12'}$), 89.7 (C^1), 78.4 ($C^{5'}$), 74.8 ($C^{3'}$), 74.0 ($C^{4'}$), 69.9 (2C, 2,4-diiodo-6-TMS-Ph-O-$\underline{C}H_2$-C(O)-O-)), 69.8 (C^2), 69.4 (C^3), 68.8 (C^5), 67.6 (C^4), 65.1 ($C^{6'}$), 63.4 ($C^{1'}$), 62.5 (C^6), 34.1-33.8 (6C, $(CH_3)_2\underline{C}$H-), 19.3-18.8 (12C, $(\underline{C}H_3)_2$CH-), -0.3 (3C, $(\underline{C}H_3)_3$-Si), -0.3 (3C, $(\underline{C}H_3)_3$-Si).

HR-MS. Calculated adducts: $[M+H_2O]^+$ = 1696.1171, $[M+Na]^+$ = 1701.0958. Observed adducts: $[M+H_2O]^+$ = 1696.1417, $[M+Na]^+$ = 1701.0958.

ATR-FTIR (cm^{-1}): 2972.69, 2876.53, 1741.03, 1469.02, 1407.33, 1388.03, 1247.70, 1184.43, 1142.48, 1070.97, 839.48, 750.97.

Concluding remarks 7

This thesis has described the development of five diagnostic tools that are applicable within different fields of diagnostics and theranostics. In the Nanoguide project, a nanoparticle based fiducial marker for image-guided radiotherapy was developed based on AuNPs and the gelation matrix of SAIB (SAIB/EtOH/PLA (75:20:5 vol%)). The fiducial marker was injectable through 25 G hypodermic needles. The scientific challenge was the surface-engineering of the AuNPs to ensure full dispersion (homogenous distribution) within the hydrophobic environment of the SAIB gel. Polymeric coatings like PEG_{5000}-SH and $PNIPAM_{3500}$-SH was tested together with a dithiolane-functionalized SAIB derivative **1.26** that was synthesized in four steps from sucrose. The choice of coating was decisive for the homogeneity of the SAIB-formulation. Coating of AuNPs using **1.26** was unsuccessful. Highest loading and best achievable homogeneity was obtained when $PNIPAM_{3500}$-SH coated AuNPs was applied (30 mg PNIPAM-coated AuNPs mL^{-1}) in the formulation. The SAIB formulation containing PNIPAM coated AuNPs was tested *in vivo* as a fiducial marker in mice and a canine dog, displaying contrast in the range of 1200 HU which decreased to 800 HU over 8 weeks indicating potentially aggregation of AuNPs within the SAIB formulation. The observed inhomogeneity of the formulation led to the development of the hexa-iodinated derivative of SAIB **1.33**.

A tissue marker for surgical guidance of non-palpable tumors in breast cancer was also developed based on the fiducial marker of **1.33** and the synthesis of **[^{125}I]-2.7**. An aryl-TMS precursor of SAIB **2.2** was synthesized in 4 steps from sucrose that underwent radioiodination under carrier free conditions using $Tl(OOCCF_3)_3$ and NaI. The radiochemical yield was 83% with a radiochemical purity of 95%. The formulation of **1.33** and **[^{125}I]-2.7** was tested *in vivo* as a potential tissue marker in mice and was dosimetric evaluated for application in humans. A **[^{125}I]**-biodistribution study indicated an limited uptake *in vivo* in the thyroid gland of 3.5% ID·g^{-1} after seven days in mice. The dosimetric analysis calculated for human patients indicated that vital organs and tissues would not be considerably affected by the radiation dose from the gel deposit nor from uptake as indicated in the biodistribution.
A more suitable aryl-TMS precursor **2.31** was synthesized that upon the radio-iodination would be identical to **1.33** that was approved by the Danish Health Authority for use as medical device in patients. The radioiodination and *in vivo* study of **2.31** are currently on-going.

A small library of iodide-based contrast agents for remote loading in liposomes was synthesized for blood pool imaging. The amino functionalized contrast agents of **3.10** and **3.15** were remote loaded into liposomes where only **3.15** was successfully loaded with an encapsulation efficiency of 85%. An *in vivo* study indicated that the amount loaded of

3.15 did not correspond to sufficient contrast to be visible in blood pool imaging. It was concluded that the gradient established across bilayer membrane was not sufficient to load the amount needed to achieve a proper contrast.

During the stay in the group of David Thompson, the CD/pluronic-based PRs of **4.13** and **4.12** was synthesized. The presence of the DOTA moiety was questionable according to NMR analysis. Further structural characterization is undertaken before the chelation of ^{64}Cu and *in vivo* study. Lastly, a TMS substituted tyrosine derivatives of **5.26** and **5.41** was developed for the site-specific iodination of peptides and proteins. These derivatives were synthesized in yields of 69% and 85% respectively from the Negishi coupling of the corresponding building blocks of **5.40** and **5.33** or **5.31** respectively. Compound **5.41** was transformed into the corresponding dipeptides of **5.50**, **5.51** and **5.52** that were used to evaluate the selectivity in the iodination reaction. Iodination was performed by Tl(OOCCF$_3$) and NaI which showed *ipso*-iodination of the TMS moiety in the dipeptides of **5.50** and **5.51**. The iodination of **5.52** also indicated the *ipso*-iodination of the TMS-group, though further optimization is needed in order to perform the iodination in a more clean fashion. The first steps towards the regioselective iodination of peptide and proteins using a TMS-group as placeholder has been demonstrated from this study.

Bibliography

[1] R. Baskar, K. A. Lee, R. Yeo, and K.-W. Yeoh, "Cancer and radiation therapy: current advances and future directions," Int J Med Sci, vol. 9, no. 3, pp. 193–199, 2012.

[2] D. Verellen, M. De Ridder, N. Linthout, K. Tournel, G. Soete, and G. Storme, "Innovations in image-guided radiotherapy," Nature Reviews Cancer, vol. 7, no. 12, pp. 949–960, 2007.

[3] D. J. Brenner, L. R. Hlatky, P. J. Hahnfeldt, Y. Huang, and R. K. Sachs, "The linear-quadratic model and most other common radiobiological models result in similar predictions of time-dose relationships," Radiation Research, vol. 150, no. 1, pp. 83–91, 1998. [Online]. Available: http://www.jstor.org/stable/3579648

[4] L. A. Dawson and M. B. Sharpe, "Image-guided radiotherapy: rationale, benefits, and limitations," The Lancet Oncology, vol. 7, no. 10, pp. 848 – 858, 2006. [Online]. Available: http://www.sciencedirect.com/science/article/pii/S1470204506709044

[5] D. A. Jaffray, "Image-guided radiotherapy: from current concept to future perspectives," Nature Reviews Clinical Oncology, vol. 9, no. 12, pp. 688–699, 2012.

[6] R. I. Jølck, T. Binderup, A. E. Hansen, J. B. Scherman, P. Munch af Rosenschold, A. Kjær, and T. L. Andresen, "Injectable colloidal gold in a sucrose acetate isobutyrate gelating matrix with potential use in radiation therapy," Advanced Healthcare Materials, vol. 3, no. 10, pp. 1680–1687, 2014. [Online]. Available: http://dx.doi.org/10.1002/adhm.201300668

[7] M. Imura, K. Yamazaki, H. Shirato, R. Onimaru, M. Fujino, S. Shimizu, T. Harada, S. Ogura, H. Dosaka-Akita, K. Miyasaka, and M. Nishimura, "Insertion and fixation of fiducial markers for setup and tracking of lung tumors in radiotherapy," International Journal of Radiation Oncology*Biology*Physics, vol. 63, no. 5, pp. 1442 – 1447, 2005. [Online]. Available: http://www.sciencedirect.com/science/article/pii/S0360301605007133

[8] D. J. Moseley, E. A. White, K. L. Wiltshire, T. Rosewall, M. B. Sharpe, J. H. Siewerdsen, J.-P. Bissonnette, M. Gospodarowicz, P. Warde, C. N. Catton, and D. A. Jaffray, "Comparison of localization performance with implanted fiducial markers and cone-beam computed tomography for on-line image-guided radiotherapy of the prostate," International Journal of Radiation Oncology*Biology*Physics, vol. 67, no. 3, pp. 942 – 953, 2007. [Online]. Available: http://www.sciencedirect.com/science/article/pii/S0360301606033633

[9] R. I. Jølck, J. S. Rydhög, A. N. Christensen, A. E. Hansen, L. M. Bruun, H. Schaarup-Jensen, A. S. von Wenck, B. Børresen, A. T. Kristensen, M. H. Clausen, A. Kjær, K. Conradsen, R. Larsen, P. M. af Rosenschöld, and T. L.

Andresen, "Injectable colloidal gold for use in intrafractional 2d image-guided radiation therapy," Advanced Healthcare Materials, vol. 4, no. 6, pp. 856–863, 2015. [Online]. Available: http://dx.doi.org/10.1002/adhm.201400651

[10] S. S. Korreman, T. Juhler-Nøttrup, and A. L. Boyer, "Respiratory gated beam delivery cannot facilitate margin reduction, unless combined with respiratory correlated image guidance," Radiotherapy and Oncology, vol. 86, no. 1, pp. 61 – 68, 2008. [Online]. Available: http://www.sciencedirect.com/science/article/pii/S0167814007005488

[11] S. Yousefi, B. T. Collins, C. A. Reichner, E. D. Anderson, C. Jamis-Dow, G. Gagnon, S. Malik, B. Marshall, T. Chang, and F. Banovac, "Complications of thoracic computed tomography–guided fiducial placement for the purpose of stereotactic body radiation therapy," Clinical Lung Cancer, vol. 8, no. 4, pp. 252 – 256, 2007. [Online]. Available: http://www.sciencedirect.com/science/article/pii/S1525730411705150

[12] N. Kothary, J. J. Heit, J. D. Louie, W. T. Kuo, B. W. L. Jr, A. Koong, D. T. Chang, D. Hovsepian, D. Y. Sze, and L. V. Hofmann, "Safety and efficacy of percutaneous fiducial marker implantation for image-guided radiation therapy," Journal of Vascular and Interventional Radiology, vol. 20, no. 2, pp. 235 – 239, 2009. [Online]. Available: http://www.sciencedirect.com/science/article/pii/S105104430800883X

[13] N. Bhagat, N. Fidelman, J. C. Durack, J. Collins, R. L. Gordon, J. M. LaBerge, and R. K. Kerlan, "Complications associated with the percutaneous insertion of fiducial markers in the thorax," CardioVascular and Interventional Radiology, vol. 33, no. 6, pp. 1186–1191, 2010. [Online]. Available: http://dx.doi.org/10.1007/s00270-010-9949-0

[14] J. Hong, N. Eclov, Y. Yu, A. Rao, S. Dieterich, Q.-T. Le, M. Diehn, D. Sze, J. Billy Loo, N. Kothary, and P. Maxim, "Migration of implanted markers for image-guided lung tumor stereotactic ablative radiotherapy," Journal of Applied Clinical Medical Physics, vol. 14, no. 2, 2013.

[15] X.-D. Zhang, M.-L. Guo, H.-Y. Wu, Y.-M. Sun, Y.-Q. Ding, X. Feng, and L.-A. Zhang, "Irradiation stability and cytotoxicity of gold nanoparticles for radiotherapy," Int J Nanomedicine, vol. 4, pp. 165–73, 2009.

[16] W. Eck, A. I. Nicholson, H. Zentgraf, W. Semmler, and S. Bartling, "Anti-cd4-targeted gold nanoparticles induce specific contrast enhancement of peripheral lymph nodes in x-ray computed tomography of live mice," Nano Letters, vol. 10, no. 7, pp. 2318–2322, 2010, pMID: 20496900. [Online]. Available: http://dx.doi.org/10.1021/nl101019s

[17] J. F. Hainfeld, D. N. Slatkin, T. M. Focella, and H. M. Smilowitz, "Gold nanoparticles: a new x-ray contrast agent," The British Journal of Radiology, vol. 79, no. 939, pp. 248–253, 2006, pMID: 16498039. [Online]. Available: http://dx.doi.org/10.1259/bjr/13169882

[18] D. Xi, S. Dong, X. Meng, Q. Lu, L. Meng, and J. Ye, "Gold nanoparticles as computerized tomography (ct) contrast agents," RSC Adv., vol. 2, pp. 12 515–12 524, 2012. [Online]. Available: http://dx.doi.org/10.1039/C2RA21263C

[19] D. Kim, S. Park, J. H. Lee, Y. Y. Jeong, and S. Jon, "Antibiofouling polymer-coated gold nanoparticles as a contrast agent for in vivo x-ray computed tomography imaging," Journal of the American Chemical Society, vol. 129, no. 24, pp. 7661–7665, 2007, pMID: 17530850. [Online]. Available: http://dx.doi.org/10.1021/ja071471p

[20] Y. Lu, Y. Yu, and X. Tang, "Sucrose acetate isobutyrate as an in situ forming system for sustained risperidone release," Journal of Pharmaceutical Sciences, vol. 96, no. 12, pp. 3252–3262, 2007. [Online]. Available: http://dx.doi.org/10.1002/jps.21091

[21] J. Siepmann and N. A. Peppas, "Higuchi equation: Derivation, applications, use and misuse," International Journal of Pharmaceutics, vol. 418, no. 1, pp. 6 – 12, 2011, mathematical modeling of drug delivery systems:Fifty years after Takeru Higuchi's models. [Online]. Available: http://www.sciencedirect.com/science/article/pii/S0378517311002687

[22] F. Tasselli, Non-solvent Induced Phase Separation Process (NIPS) for Membrane Preparation. Berlin, Heidelberg: Springer Berlin Heidelberg, 2015, pp. 1–3.

[23] J. Turkevich, P. C. Stevenson, and J. Hillier, "A study of the nucleation and growth processes in the synthesis of colloidal gold," Discuss. Faraday Soc., vol. 11, pp. 55–75, 1951. [Online]. Available: http://dx.doi.org/10.1039/DF9511100055

[24] G. Frens, "Controlled nucleation for the regulation of the particle size in monodisperse gold suspensions," Nature, vol. 241, no. 105, pp. 20–22, 1973.

[25] S. Jarosz and M. Mach, "Regio- and stereoselective transformations of sucrose at the terminal positions," European Journal of Organic Chemistry, vol. 2002, no. 5, pp. 769–780, 2002. [Online]. Available: http://dx.doi.org/10.1002/1099-0690(200203)2002:5<769::AID-EJOC769>3.0.CO;2-F

[26] Y. Queneau, S. Jarosz, B. Lewandowski, and J. Fitremann, "Sucrose chemistry and applications of sucrochemicals," ser. Advances in Carbohydrate Chemistry and Biochemistry, D. Horton, Ed. Academic Press, 2007, vol. 61, pp. 217 – 292. [Online]. Available: http://www.sciencedirect.com/science/article/pii/S0065231807610051

[27] H. Karl, C. K. Lee, and R. Khan, "Synthesis and reactions of tert-butyldiphenylsilyl ethers of sucrose," Carbohydrate Research, vol. 101, no. 1, pp. 31 – 38, 1982. [Online]. Available: http://www.sciencedirect.com/science/article/pii/S0008621500807922

[28] I. R. Vlahov, P. I. Vlahova, and R. J. Linhardt, "Regioselective synthesis of sucrose monoesters as surfactants," Journal of carbohydrate chemistry, vol. 16, no. 1, pp. 1–10, 1997.

[29] ——, "Regioselective synthesis of sucrose monoesters as surfactants," Journal of Carbohydrate Chemistry, vol. 16, no. 1, pp. 1–10, 1997. [Online]. Available: http://www.tandfonline.com/doi/abs/10.1080/07328309708006506

[30] A. Sofian, C. K. Lee, and A. Linden, "Regioselective sulfonylation of 6,1?,6?-tri-o-tritylsucrose through dibutylstannylation: synthesis of 4?-o-sulfonyl derivatives of sucrose," Carbohydrate Research, vol. 337, no. 24, pp. 2377 – 2381, 2002. [Online]. Available: http://www.sciencedirect.com/science/article/pii/S0008621502003476

[31] B. C. Mei, E. Oh, K. Susumu, D. Farrell, T. J. Mountziaris, and H. Mattoussi, "Effects of ligand coordination number and surface curvature on the stability of gold nanoparticles in aqueous solutions," Langmuir, vol. 25, no. 18, pp. 10 604–10 611, 2009, pMID: 19588955. [Online]. Available: http://dx.doi.org/10.1021/la901423z

[32] A. A. Volkert, V. Subramaniam, M. R. Ivanov, A. M. Goodman, and A. J. Haes, "Salt-mediated self-assembly of thioctic acid on gold nanoparticles," ACS Nano, vol. 5, no. 6, pp. 4570–4580, 2011, pMID: 21524135. [Online]. Available: http://dx.doi.org/10.1021/nn200276a

[33] M. Lista, D. Z. Liu, and P. Mulvaney, "Phase transfer of noble metal nanoparticles to organic solvents," Langmuir, vol. 30, no. 8, pp. 1932–1938, 2014, pMID: 24479856. [Online]. Available: http://dx.doi.org/10.1021/la404569h

[34] S. J. Hurst, A. K. R. Lytton-Jean, and C. A. Mirkin, "Maximizing dna loading on a range of gold nanoparticle sizes," Analytical Chemistry, vol. 78, no. 24, pp. 8313–8318, 2006, pMID: 17165821. [Online]. Available: http://dx.doi.org/10.1021/ac0613582

[35] H. D. Hill, J. E. Millstone, M. J. Banholzer, and C. A. Mirkin, "The role radius of curvature plays in thiolated oligonucleotide loading on gold nanoparticles," ACS Nano, vol. 3, no. 2, pp. 418–424, 2009, pMID: 19236080. [Online]. Available: http://dx.doi.org/10.1021/nn800726e

[36] K. B. Cederquist and C. D. Keating, "Curvature effects in dna:au nanoparticle conjugates," ACS Nano, vol. 3, no. 2, pp. 256–260, 2009, pMID: 19236058. [Online]. Available: http://dx.doi.org/10.1021/nn9000726

[37] C. Xu, G. A. Tung, and S. Sun, "Size and concentration effect of gold nanoparticles on x-ray attenuation as measured on computed tomography," Chemistry of Materials, vol. 20, no. 13, pp. 4167–4169, 2008, pMID: 19079760. [Online]. Available: http://dx.doi.org/10.1021/cm8008418

[38] Z. Wang, L. Wu, and W. Cai, "Size-tunable synthesis of monodisperse water-soluble gold nanoparticles with high x-ray attenuation," Chemistry – A European Journal, vol. 16, no. 5, pp. 1459–1463, 2010. [Online]. Available: http://dx.doi.org/10.1002/chem.200902463

[39] T. L. Andresen, R. I. Jølck, and M. Albrechtsen, "Gel formulations for guiding radiotherapy," Patent WO2 014 187 962 (A1), 11 27, 2014.

[40] J. Scherman Rydhög, R. Irming Jølck, T. L. Andresen, and P. Munck af Rosenschöld, "Quantification and comparison of visibility and image artifacts of a new liquid fiducial marker in a lung phantom for image-guided radiation therapy," Medical Physics, vol. 42, no. 6, pp. 2818–2826, 2015. [Online]. Available: http://scitation.aip.org/content/aapm/journal/medphys/42/6/10.1118/1.4919616

[41] J. S. Rydhög, S. R. Mortensen, K. R. Larsen, P. Clementsen, R. I. Jølck, M. Josipovic, M. C. Aznar, L. Specht, T. L. Andresen, P. M. af Rosenschöld, and G. F. Persson, "Liquid fiducial marker performance during radiotherapy of locally advanced non small cell lung cancer," Radiotherapy and Oncology, vol. 121, no. 1, pp. 64 – 69, 2016. [Online]. Available: http://www.sciencedirect.com/science/article/pii/S0167814016311690

[42] N. N. Y. Janssen, J. Nijkamp, T. Alderliesten, C. E. Loo, E. J. T. Rutgers, J.-J. Sonke, and M. T. F. D. Vrancken Peeters, "Radioactive seed localization in breast cancer treatment," British Journal of Surgery, vol. 103, no. 1, pp. 70–80, 2016.

[43] M. van der Noordaa, K. Pengel, E. Groen, E. van Werkhoven, E. Rutgers, C. Loo, W. Vogel, and M. V. Peeters, "The use of radioactive iodine-125 seed localization in patients with non-palpable breast cancer: A comparison with the radioguided occult lesion localization with 99m technetium," European Journal of Surgical Oncology (EJSO), vol. 41, no. 4, pp. 553 – 558, 2015.

[44] E. L. Postma, A. J. Witkamp, M. A. van den Bosch, H. M. Verkooijen, and R. van Hillegersberg, "Localization of nonpalpable breast lesions," Expert Review of Anticancer Therapy, vol. 11, no. 8, pp. 1295–1302, 2011.

[45] L. Langhans, T. Klausen, T. Tvedskov, M.-L. Talman, P. Oturai, I. Vejborg, N. Kroman, and B. Hesse, "Preparation and administration of i-125 labeled seeds for localization of nonpalpable breast lesions," Current Radiopharmaceuticals, vol. 9, no. 2, pp. 143–149, 2016. [Online]. Available: http://www.eurekaselect.com/node/133756/article

[46] J. Rarick, B. F. Kimler, and O. Tawfik, "Comparison of margin status and lesional size between radioactive seed localized vs conventional wire localized breast lumpectomy specimens," Annals of Diagnostic Pathology, vol. 21, pp. 47–52, 2016.

[47] M. W. Barentsz, M. A. A. J. van den Bosch, W. B. Veldhuis, P. J. van Diest, R. M. Pijnappel, A. J. Witkamp, and H. M. Verkooijen, "Radioactive seed localization for non-palpable breast cancer," British Journal of Surgery, vol. 100, no. 5, pp. 582–588, 2013. [Online]. Available: http://dx.doi.org/10.1002/bjs.9068

[48] B. Pouw, I. van der Ploeg, S. Muller, R. V. Olmos, L. Janssen-Pinkse, H. Oldenburg, and M. V. Peeters, "Simultaneous use of an 125i-seed to guide tumour excision and 99mtc-nanocolloid for sentinel node biopsy in non-palpable breast-conserving surgery," European Journal of Surgical Oncology (EJSO), vol. 41, no. 1, pp. 71 – 78, 2015. [Online]. Available: http://www.sciencedirect.com/science/article/pii/S0748798314011834

[49] G. D. Dodd, K. Fry, and W. Delany, "Pre-operative localization of occult carcinoma of the breast," Management of the Patient with Cancer, pp. 88–113, 1965. [Online]. Available: www.scopus.com

[50] M. Ahmed, I. T. Rubio, J. M. Klaase, and M. Douek, "Surgical treatment of nonpalpable primary invasive and in situ breast cancer," Nat Rev Clin Oncol, vol. 12, no. 11, pp. 645–663, Nov 2015, review. [Online]. Available: http://dx.doi.org/10.1038/nrclinonc.2015.161

[51] A. Luini, S. Zurrida, V. Galimberti, and G. Paganelli, "Radioguided surgery of occult breast lesions," European Journal of Cancer, vol. 34, no. 1, pp. 204 – 205, 1998, correspondence.

[52] A. Luini, S. Zurrida, G. Paganelli, V. Galimberti, V. Sacchini, S. Monti, P. Veronesi, G. Viale, and U. Veronesi, "Comparison of radioguided excision with wire localization of occult breast lesions," British Journal of Surgery, vol. 86, no. 4, pp. 522–525, 1999. [Online]. Available: http://dx.doi.org/10.1046/j.1365-2168.1999.01078.x

[53] G. Mariani, L. Moresco, G. Viale, G. Villa, M. Bagnasco, G. Canavese, J. Buscombe, H. W. Strauss, and G. Paganelli, "Radioguided sentinel lymph node biopsy in breast cancer surgery," Journal of Nuclear Medicine, vol. 42, no. 8, pp. 1198–1215, 2001. [Online]. Available: http://jnm.snmjournals.org/content/42/8/1198.abstract

[54] C. Thind, S. Tan, S. Desmond, O. Harris, H. Ramesh, L. Chagla, A. Ray, and R. Audisio, "Snoll. sentinel node and occult (impalpable) lesion localization in breast cancer," Clinical Radiology, vol. 66, no. 9, pp. 833 – 839, 2011. [Online]. Available: http://www.sciencedirect.com/science/article/pii/S0009926011001565

[55] G. Mariani, P. Erba, G. Villa, M. Gipponi, G. Manca, G. Boni, F. Buffoni, F. Castagnola, G. Paganelli, and H. W. Strauss, "Lymphoscintigraphic and intraoperative detection of the sentinel lymph node in breast cancer patients: The nuclear medicine perspective," Journal of Surgical Oncology, vol. 85, no. 3, pp. 112–122, 2004. [Online]. Available: http://dx.doi.org/10.1002/jso.20023

[56] J. W. Jakub, R. J. Gray, A. C. Degnim, J. C. Boughey, M. Gardner, and C. E. Cox, "Current status of radioactive seed for localization of non palpable breast lesions," The American Journal of Surgery, vol. 199, no. 4, pp. 522 – 528, 2010. [Online]. Available: http://www.sciencedirect.com/science/article/pii/S0002961009005212

[57] R. J. Gray, C. Salud, K. Nguyen, E. Dauway, J. Friedland, C. Berman, E. Peltz, G. Whitehead, and C. E. Cox, "Randomized prospective evaluation of a novel technique for biopsy or lumpectomy of nonpalpable breast lesions: Radioactive seed versus wire localization," Annals of Surgical Oncology, vol. 8, no. 9, pp. 711–715, 2001. [Online]. Available: http://dx.doi.org/10.1007/s10434-001-0711-3

[58] J. W. Jakub, R. J. Gray, A. C. Degnim, J. C. Boughey, M. Gardner, and C. E. Cox, "Current status of radioactive seed for localization of non palpable breast

lesions," The American Journal of Surgery, vol. 199, no. 4, pp. 522 – 528, 2010. [Online]. Available: http://www.sciencedirect.com/science/article/pii/S0002961009005212

[59] S. H. Goudreau, J. P. Joseph, and S. J. Seiler, "Preoperative radioactive seed localization for nonpalpable breast lesions: Technique, pitfalls, and solutions," RadioGraphics, vol. 35, no. 5, pp. 1319–1334, 2015, pMID: 26274097. [Online]. Available: http://dx.doi.org/10.1148/rg.2015140293

[60] E. V. Bloomquist, N. Ajkay, S. Patil, A. E. Collett, T. G. Frazier, and A. V. Barrio, "A randomized prospective comparison of patient-assessed satisfaction and clinical outcomes with radioactive seed localization versus wire localization," The Breast Journal, vol. 22, no. 2, pp. 151–157, 2016. [Online]. Available: http://dx.doi.org/10.1111/tbj.12564

[61] J. S. Sung, V. King, C. M. Thornton, J. D. Brooks, C. W. Fry, M. El-Tamer, L. T. Dauer, E. Brogi, J. M. S. Germain, and E. A. Morris, "Safety and efficacy of radioactive seed localization with i-125 prior to lumpectomy and/or excisional biopsy," European Journal of Radiology, vol. 82, no. 9, pp. 1453 – 1457, 2013. [Online]. Available: http://www.sciencedirect.com/science/article/pii/S0720048X13002039

[62] M. H. Rønnest, F. Nissen, P. J. Pedersen, T. O. Larsen, W. Mier, and M. H. Clausen, "A mild method for regioselective labeling of aromatics with radioactive iodine," European Journal of Organic Chemistry, vol. 2013, no. 19, pp. 3970–3973, 2013. [Online]. Available: http://dx.doi.org/10.1002/ejoc.201300419

[63] T. H. Chan and I. Fleming, "Electrophilic substitution of organosilicon compounds- applications to organic synthesis," Synthesis, vol. 1979, no. 10, pp. 761–786, 1979, 761.

[64] J. Clayden, N. Greeves, S. Warren, and P. Wothers, Organic chemistry, ser. 1. Edition. Oxford university press, 2004, (ISBN) 019850346 6.

[65] A. McKillop, J. D. Hunt, M. J. Zelesko, J. S. Fowler, E. C. Taylor, G. McGillivray, and F. Kienzle, "Thallium in organic synthesis. xxii. electrophilic aromatic thallation using thallium(iii) trifluoroacetate. simple synthesis of aromatic iodides," Journal of the American Chemical Society, vol. 93, no. 19, pp. 4841–4844, 1971. [Online]. Available: http://dx.doi.org/10.1021/ja00748a029

[66] D. S. Wilbur, W. E. Stone, and K. W. Anderson, "Regiospecific incorporation of bromine and iodine into phenols using (trimethylsilyl)phenol derivatives," The Journal of Organic Chemistry, vol. 48, no. 9, pp. 1542–1544, 1983. [Online]. Available: http://dx.doi.org/10.1021/jo00157a035

[67] J. Clayden, Organolithiums: selectivity for synthesis. Elsevier, 2002, vol. 23.

[68] M. A. Reed, M. T. Chang, and V. Snieckus, "Anionic o -> alpha - and beta-vinyl carbamoyl translocation of 2-(o-carbamoyl) stilbenes," Organic Letters, vol. 6, no. 14, pp. 2297–2300, 2004, pMID: 15228263. [Online]. Available: http://dx.doi.org/10.1021/ol049740t

[69] M. P. Sibi and V. Snieckus, "The directed ortho lithiation of o-aryl carbamates. an anionic equivalent of the fries rearrangement," The Journal of Organic Chemistry, vol. 48, no. 11, pp. 1935–1937, 1983. [Online]. Available: http://dx.doi.org/10.1021/jo00159a040

[70] J. Morin, Y. Zhao, and V. Snieckus, "Reductive cleavage of aryl o-carbamates to phenols by the schwartz reagent. expedient link to the directed ortho metalation strategy," Organic Letters, vol. 15, no. 16, pp. 4102–4105, 2013, pMID: 23919281. [Online]. Available: http://dx.doi.org/10.1021/ol401547d

[71] K. W. Quasdorf, M. Riener, K. V. Petrova, and N. K. Garg, "Suzuki?miyaura coupling of aryl carbamates, carbonates, and sulfamates," Journal of the American Chemical Society, vol. 131, no. 49, pp. 17 748–17 749, 2009, pMID: 19928764. [Online]. Available: http://dx.doi.org/10.1021/ja906477r

[72] M. Kauch and D. Hoppe, "Synthesis of substituted phenols by directed ortho-lithiation of in situ n-silyl-protected o-aryl n-monoalkylcarbamates," Canadian Journal of Chemistry, vol. 79, no. 11, pp. 1736–1746, 2001. [Online]. Available: http://www.nrcresearchpress.com/doi/abs/10.1139/v01-146

[73] ——, "Synthesis of halogenated phenols by directed ortho-lithiation and ipso-iododesilylation reactions of o-aryl n-isopropylcarbamates," Synthesis, vol. 2006, no. 10, pp. 1578–1589, 2006.

[74] R. Li-Yuan Bao, R. Zhao, and L. Shi, "Progress and developments in the turbo grignard reagent i-prmgcl[middle dot]licl: a ten-year journey," Chem. Commun., vol. 51, pp. 6884–6900, 2015. [Online]. Available: http://dx.doi.org/10.1039/C4CC10194D

[75] E. Shirakawa, T. Kurahashi, H. Yoshida, and T. Hiyama, "Diphenylphosphinophenolate: a ligand for the palladium-catalysed silylation of aryl halides activating simultaneously both palladium and silicon," Chem. Commun., pp. 1895–1896, 2000. [Online]. Available: http://dx.doi.org/10.1039/B006165O

[76] B. Wang, H.-X. Sun, and Z.-H. Sun, "Lioac-catalyzed chemoselective deprotection of aryl silyl ethers under mild conditions," The Journal of Organic Chemistry, vol. 74, no. 4, pp. 1781–1784, 2009, pMID: 19146386. [Online]. Available: http://dx.doi.org/10.1021/jo802472s

[77] C.-E. Yeom, H. W. Kim, S. Y. Lee, and B. M. Kim, "Dbu-mediated mild and chemoselective deprotection of aryl silyl ethers and tandem biaryl ether formation," Synlett, vol. 2007, no. 01, pp. 0146–0150, 2007.

[78] T. Ikawa, S. Masuda, T. Nishiyama, A. Takagi, and S. Akai, "Synthesis of fluorinated aromatic compounds by one-pot benzyne generation and nucleophilic fluorination," Australian Journal of Chemistry, vol. 67, no. 3, pp. 475–480, 2014.

[79] J. G. Adamson, M. A. Blaskovich, H. Groenevelt, and G. A. Lajoie, "Simple and convenient synthesis of tert-butyl ethers of fmoc-serine, fmoc-threonine, and

fmoc-tyrosine," The Journal of Organic Chemistry, vol. 56, no. 10, pp. 3447–3449, 1991. [Online]. Available: http://dx.doi.org/10.1021/jo00010a050

[80] F. Hallouard, N. Anton, P. Choquet, A. Constantinesco, and T. Vandamme, "Iodinated blood pool contrast media for preclinical x-ray imaging applications – a review," Biomaterials, vol. 31, no. 24, pp. 6249–6268, 2010.

[81] C.-Y. Kao, E. A. Hoffman, K. C. Beck, R. V. Bellamkonda, and A. V. Annapragada, "Long-residence-time nano-scale liposomal iohexol for x-ray–based blood pool imaging," Academic Radiology, vol. 10, no. 5, pp. 475–483, 2003.

[82] M. Bettmann and T. Morris, "Recent advances in contrast agents," Radiologic clinics of North America, vol. 24, no. 3, p. 347—357, September 1986. [Online]. Available: http://europepmc.org/abstract/MED/3529226

[83] M. Bourin, P. Jolliet, and F. Ballereau, "An overview of the clinical pharmacokinetics of x-ray contrast media," Clinical Pharmacokinetics, vol. 32, no. 3, pp. 180–193, 1997.

[84] W. He, K. Ai, and L. Lu, "Nanoparticulate x-ray ct contrast agents," Science China Chemistry, vol. 58, no. 5, pp. 753–760, 2015.

[85] J. Gubernator, "Active methods of drug loading into liposomes: recent strategies for stable drug entrapment and increased in vivo activity," Expert Opinion on Drug Delivery, vol. 8, no. 5, pp. 565–580, 2011, pMID: 21492058.

[86] G. Storm and D. J. Crommelin, "Liposomes: quo vadis?" Pharmaceutical Science and Technology Today, vol. 1, no. 1, pp. 19–31, 1998.

[87] M. R. Zalutsky, M. A. Noska, and S. E. Seltzer, "Characterization of liposomes containing iodine-125-labeled radiographic contrast agents." Investigative Radiology, vol. 22, no. 2, pp. 141–147, 1987.

[88] W. Krause, J. Leike, A. Sachse, and G. Schuhmann-Giampieri, "Characterization of iopromide liposomes." Investigative Radiology, vol. 28, no. 11, pp. 1028–1032, 1993.

[89] S. E. Seltzer, "Contrast-carrying liposomes current status." Investigative Radiology, vol. 23, pp. S122–S125, 1988.

[90] S. E. Seltzer, M. A. Davis, D. F. Adams, P. M. Shulkin, W. J. Landis, and A. Havron, "Liposomes carrying diatrizoate: Characterization of biophysical properties and imaging applications." Investigative Radiology, vol. 19, no. 2, pp. 142–151, 1984.

[91] P. J. Ryan, M. A. Davis, and D. L. Melchior, "The preparation and characterization of liposomes containing x-ray contrast agents," Biochimica et Biophysica Acta (BBA) - General Subjects, vol. 756, no. 1, pp. 106–110, 1983. [Online]. Available: http://www.sciencedirect.com/science/article/pii/0304416583900296

[92] J. U. Leike, A. Sachse, and K. Rupp, "Characterization of continuously extruded iopromide-carrying liposomes for computed tomography blood pool imaging," Investigative Radiology, vol. 36, no. 6, pp. 303–308, 2001.

[93] A. Sachse, J. U. Leike, T. Schneider, S. E. Wagner, G. L. Röling, W. Krause, and M. Brandl, "Biodistribution and computed tomography blood-pool imaging properties of polyethylene glycol-coated iopromide-carrying liposomes," Investigative Radiology, vol. 32, no. 1, pp. 44–50, 1997.

[94] S. E. Seltzer, M. Blau, L. W. Herman, R. L. Hooshmand, L. A. Herman, D. F. Adams, S. R. Minchey, and A. S. Janoff, "Contrast material-carrying liposomes: biodistribution, clearance, and imaging characteristics." Radiology, vol. 194, no. 3, pp. 775–781, 1995, pMID: 7862978.

[95] J. W. Nichols and D. W. Deamer, "Net proton-hydroxyl permeability of large unilamellar liposomes measured by an acid-base titration technique," Proceedings of the National Academy of Sciences, vol. 77, no. 4, pp. 2038–2042, 1980.

[96] D. Zucker, D. Marcus, Y. Barenholz, and A. Goldblum, "Liposome drugs' loading efficiency: A working model based on loading conditions and drug's physicochemical properties," Journal of Controlled Release, vol. 139, no. 1, pp. 73–80, 2009. [Online]. Available: http://www.sciencedirect.com/science/article/pii/S0168365909003873

[97] I. V. Zhigaltsev, G. Winters, M. Srinivasulu, J. Crawford, M. Wong, L. Amankwa, D. Waterhouse, D. Masin, M. Webb, N. Harasym, L. Heller, M. B. Bally, M. A. Ciufolini, P. R. Cullis, and N. Maurer, "Development of a weak-base docetaxel derivative that can be loaded into lipid nanoparticles," Journal of Controlled Release, vol. 144, no. 3, pp. 332–340, 2010.

[98] R. Parkesh, W. Gowin, T. C. Lee, and T. Gunnlaugsson, "Synthesis and evaluation of potential ct (computer tomography) contrast agents for bone structure and microdamage analysis," Org. Biomol. Chem., vol. 4, pp. 3611–3617, 2006.

[99] D. B. Elrod, R. Partha, D. Danila, S. W. Casscells, and J. L. Conyers, "An iodinated liposomal computed tomographic contrast agent prepared from a diiodophosphatidylcholine lipid," Nanomedicine: Nanotechnology, Biology and Medicine, vol. 5, no. 1, pp. 42–45, 2009.

[100] R. Takeda, S. Y. Ryu, J. H. Park, and K. Nakanishi, "Additivity in cd amplitudes of p-phenylbenzyl ethers and p-phenylbenzoates of 2-aminosugars," Tetrahedron, vol. 46, no. 16, pp. 5533–5542, 1990. [Online]. Available: http://www.sciencedirect.com/science/article/pii/S0040402001877516

[101] A. F. Abdel-Magid, K. G. Carson, B. D. Harris, C. A. Maryanoff, and R. D. Shah, "Reductive amination of aldehydes and ketones with sodium triacetoxyborohydride. studies on direct and indirect reductive amination procedures," The Journal of Organic Chemistry, vol. 61, no. 11, pp. 3849–3862, 1996, pMID: 11667239. [Online]. Available: http://dx.doi.org/10.1021/jo960057x

[102] J. Henriksen and A. T.L., ""personal communications"."

[103] V. Wintgens, T. T. Nielsen, K. L. Larsen, and C. Amiel, "Size-controlled nanoassemblies based on cyclodextrin-modified dextrans," Macromolecular Bioscience, vol. 11, no. 9, pp. 1254–1263, 2011.

[104] J. Szejtli, "Past, present and futute of cyclodextrin research," Pure and Applied Chemistry, vol. 76, no. 10, pp. 1825–1845, 2004.

[105] S. Loethen, J. Kim, and D. H. Thompson, "Biomedical applications of cyclodextrin based polyrotaxanes," Polymer Reviews, vol. 47, no. 3, pp. 383–418, 2007.

[106] Y. A. Mondjinou, L. A. McCauliff, A. Kulkarni, L. Paul, S.-H. Hyun, Z. Zhang, Z. Wu, M. Wirth, J. Storch, and D. H. Thompson, "Synthesis of 2-hydroxypropyl-?-cyclodextrin/pluronic-based polyrotaxanes via heterogeneous reaction as potential niemann-pick type c therapeutics," Biomacromolecules, vol. 14, no. 12, pp. 4189–4197, 2013.

[107] C. J. Collins, L. A. McCauliff, S.-H. Hyun, Z. Zhang, L. N. Paul, A. Kulkarni, K. Zick, M. Wirth, J. Storch, and D. H. Thompson, "Synthesis, characterization, and evaluation of pluronic-based ?-cyclodextrin polyrotaxanes for mobilization of accumulated cholesterol from niemann-pick type c fibroblasts," Biochemistry, vol. 52, no. 19, pp. 3242–3253, 2013, pMID: 23560535.

[108] C. J. Collins, Y. Mondjinou, B. Loren, S. Torregrosa-Allen, C. J. Simmons, B. D. Elzey, N. Ayat, Z.-R. Lu, and D. Thompson, "Influence of molecular structure on the in vivo performance of flexible rod polyrotaxanes," Biomacromolecules, vol. 17, no. 9, pp. 2777–2786, 2016, pMID: 27387820.

[109] T. T. Nielsen, V. Wintgens, C. Amiel, R. Wimmer, and K. L. Larsen, "Facile synthesis of ?-cyclodextrin-dextran polymers by "click" chemistry," Biomacromolecules, vol. 11, no. 7, pp. 1710–1715, 2010, pMID: 20553039.

[110] S. Okarvi, "Peptide-based radiopharmaceuticals: Future tools for diagnostic imaging of cancers and other diseases," Medicinal Research Reviews, vol. 24, no. 3, pp. 357–397, 2004.

[111] A. J. Fischman, J. W. Babich, and H. W. Strauss, "A ticket to ride: Peptide radiopharmaceuticals," Journal of Nuclear Medicine, vol. 34, no. 12, pp. 2253–2263, 1993.

[112] D. Blok, R. I. J. Feitsma, P. Vermeij, and E. J. K. Pauwels, "Peptide radiopharmaceuticals in nuclear medicine," European Journal of Nuclear Medicine, vol. 26, no. 11, pp. 1511–1519, 1999.

[113] M. Schottelius and H.-J. Wester, "Molecular imaging targeting peptide receptors," Methods, vol. 48, no. 2, pp. 161 – 177, 2009, molecular Imaging.

[114] S. J. Goldsmith, "Radioimmunoassay: Review of basic principles," Seminars in Nuclear Medicine, vol. 5, no. 2, pp. 125–152, 2017/02/05 1975. [Online]. Available: http://dx.doi.org/10.1016/S0001-2998(75)80028-6

[115] S. D. Sharma, G. Toth, and V. J. Hruby, "A simple general method for (radio)iodination of a phenylalanine residue in peptides: preparation of [cyclic][d-pen2,4'-125i-phe4,d-pen5]enkephalin, a peptide with extraordinary selectivity for .delta.-opioid receptors," The Journal of Organic Chemistry, vol. 56, no. 16, pp. 4981–4983, 1991.

[116] A. Dirksen and P. E. Dawson, "Rapid oxime and hydrazone ligations with aromatic aldehydes for biomolecular labeling," Bioconjugate Chemistry, vol. 19, no. 12, pp. 2543–2548, 2008, pMID: 19053314.

[117] M. Glaser, M. Morrison, M. Solbakken, J. Arukwe, H. Karlsen, U. Wiggen, S. Champion, G. M. Kindberg, and A. Cuthbertson, "Radiosynthesis and biodistribution of cyclic rgd peptides conjugated with novel [18f]fluorinated aldehyde-containing prosthetic groups," Bioconjugate Chemistry, vol. 19, no. 4, pp. 951–957, 2008, pMID: 18341272.

[118] J. Darius and D. R. RICHARDSON, "William hunter and radioiodination: revolutions in the labelling of proteins with radionuclides of iodine."

[119] N. M. Alexander, "Oxidative cleavage of tryptophanyl peptide bonds during chemical- and peroxidase-catalyzed iodinations," Journal of Biological Chemistry, vol. 249, no. 6, pp. 1946–1952, 1974.

[120] A. S. McFARLANE, "Efficient trace-labelling of proteins with iodine," Nature, vol. 182, no. 4627, pp. 53–53, Jul 1958.

[121] R. H. Seevers and R. E. Counsell, "Radioiodination techniques for small organic molecules," Chemical Reviews, vol. 82, no. 6, pp. 575–590, 1982.

[122] R. S. YALOW and S. A. BERSON, "Immunoassay of endogenous plasma insulin in man," Obesity Research, vol. 4, no. 6, pp. 583–600, 1996.

[123] W. M. HUNTER and F. C. GREENWOOD, "Preparation of iodine-131 labelled human growth hormone of high specific activity," Nature, vol. 194, no. 4827, pp. 495–496, May 1962.

[124] F. C. Greenwood, W. M. Hunter, and J. S. Glover, "The preparation of (131)i-labelled human growth hormone of high specific radioactivity," Biochem J, vol. 89, no. 1, pp. 114–123, Oct 1963, 14097352[pmid].

[125] P. R. Salacinski, C. McLean, J. E. Sykes, V. V. Clement-Jones, and P. J. Lowry, "Iodination of proteins, glycoproteins, and peptides using a solid-phase oxidizing agent, 1,3,4,6-tetrachloro-3?,6?-diphenyl glycoluril (iodogen)," Analytical Biochemistry, vol. 117, no. 1, pp. 136 – 146, 1981.

[126] P. J. Fraker and J. C. Speck, "Protein and cell membrane iodinations with a sparingly soluble chloroamide, 1,3,4,6-tetrachloro-3a,6a-diphenylglycoluril," Biochemical and Biophysical Research Communications, vol. 80, no. 4, pp. 849 – 857, 1978.

[127] W. Wood, C. Wachter, and P. Scriba, "Experiences using chloramine-t and 1, 3, 4, 6-tetrachloro-3α, 6α-diphenylglycoluril (lodogen®) for radioiodination of materials for radioimmunoassay," Clinical Chemistry and Laboratory Medicine, vol. 19, no. 10, pp. 1051–1056, 1981.

[128] A. E. Bolton and W. M. Hunter, "The labelling of proteins to high specific radioactivities by conjugation to a 125i-containing acylating agent. application to the radioimmunoassay," Biochemical Journal, vol. 133, no. 3, pp. 529–538, 1973.

[129] G. Vaidyanathan and M. R. Zalutsky, "Radioiodination of antibodies via n-succinimidyl 2,4-dimethoxy-3-(trialkylstannyl)benzoates," Bioconjugate Chemistry, vol. 1, no. 6, pp. 387–393, 1990.

[130] ——, "Protein radiohalogenation: observations on the design of n-succinimidyl ester acylation agents," Bioconjugate Chemistry, vol. 1, no. 4, pp. 269–273, 1990.

[131] S. Garg, P. K. Garg, and M. R. Zalutsky, "N-succinimidyl 5-(trialkylstannyl)-3-pyridinecarboxylates: a new class of reagents for protein radioiodination," Bioconjugate Chemistry, vol. 2, no. 1, pp. 50–56, 1991.

[132] G. Vaidyanathan, D. J. Affleck, and M. R. Zalutsky, "Radioiodination of proteins using n-succinimidyl 4-hydroxy-3-iodobenzoate," Bioconjugate Chemistry, vol. 4, no. 1, pp. 78–84, 1993, pMID: 8431515.

[133] G. Vaidyanathan and M. R. Zalutsky, "Preparation of n-succinimidyl 3-[[ast]i]iodobenzoate: an agent for the indirect radioiodination of proteins," Nat. Protocols, vol. 1, no. 2, pp. 707–713, Jul 2006.

[134] M. Pruszynski, E. Koumarianou, G. Vaidyanathan, S. Chitneni, and M. R. Zalutsky, "D-amino acid peptide residualizing agents bearing n-hydroxysuccinimido- and maleimido-functional groups and their application for trastuzumab radioiodination," Nuclear Medicine and Biology, vol. 42, no. 1, pp. 19 – 27, 2015.

[135] S. W. Hadley and D. S. Wilbur, "Evaluation of iodovinyl antibody conjugates: comparison with a p-iodobenzoyl conjugate and direct radioiodination," Bioconjugate Chemistry, vol. 1, no. 2, pp. 154–161, 1990. [Online]. Available: http://dx.doi.org/10.1021/bc00002a011

[136] P. Dumas, B. Maziere, N. Autissier, and R. Michel, "Specificite de l'iodotyrosine desiodase des microsomes thyroïdiens et hepatiques," Biochimica et Biophysica Acta (BBA) - Enzymology, vol. 293, no. 1, pp. 36 – 47, 1973. [Online]. Available: http://www.sciencedirect.com/science/article/pii/0005274473903732

[137] E. Escher, "A new method of iodine labelling of peptide hormones," Journal of Receptor Research, vol. 4, no. 1-6, pp. 331–336, 1984. [Online]. Available: http://dx.doi.org/10.3109/10799898409042559

[138] S. R. Wilson and L. A. Jacob, "Iodination of aryltrimethylsilanes. a mild approach to (iodophenyl)alanine," The Journal of Organic Chemistry, vol. 51, no. 25, pp. 4833–4836, 1986.

[139] D. S. Wilbur, D. K. Hamlin, R. R. Srivastava, and H. D. Burns, "Synthesis and radioiodination of n-boc-p-(tri-n-butylstannyl)-l-phenylalanine tetrafluorophenyl ester: Preparation of a radiolabeled phenylalanine derivative for peptide synthesis," Bioconjugate Chemistry, vol. 4, no. 6, pp. 574–580, 1993, pMID: 8305529.

[140] P. J. Pedersen and M. H. Clausen, "Modified approach to labeling of phenylalanine in peptides with ^{125}i," Unpublished Results (Draft).

[141] J. M. Padrón, G. Kokotos, T. Mart??n, T. Markidis, W. A. Gibbons, and V. S. Mart??n, "Enantiospecific synthesis of ?-amino acid semialdehydes: a key step for the synthesis of unnatural unsaturated and saturated ?-amino acids," Tetrahedron: Asymmetry, vol. 9, no. 19, pp. 3381 – 3394, 1998.

[142] J. M. Chalker, C. S. C. Wood, and B. G. Davis, "A convenient catalyst for aqueous and protein suzuki?miyaura cross-coupling," Journal of the American Chemical Society, vol. 131, no. 45, pp. 16 346–16 347, 2009, pMID: 19852502.

[143] R. F. W. Jackson, N. Wishart, A. Wood, K. James, and M. J. Wythes, "Preparation of enantiomerically pure protected 4-oxo .alpha.-amino acids and 3-aryl .alpha.-amino acids from serine," The Journal of Organic Chemistry, vol. 57, no. 12, pp. 3397–3404, 1992.

[144] C. L. Oswald, T. Carrillo-Márquez, L. Caggiano, and R. F. Jackson, "Negishi cross-coupling reactions of ?-amino acid-derived organozinc reagents and aromatic bromides," Tetrahedron, vol. 64, no. 4, pp. 681 – 687, 2008.

[145] A. J. Ross, H. L. Lang, and R. F. W. Jackson, "Much improved conditions for the negishi cross-coupling of iodoalanine derived zinc reagents with aryl halides," The Journal of Organic Chemistry, vol. 75, no. 1, pp. 245–248, 2010, pMID: 19938812.

[146] R. Bollhagen, M. Schmiedberger, K. Barlos, and E. Grell, "A new reagent for the cleavage of fully protected peptides synthesised on 2-chlorotrityl chloride resin," J. Chem. Soc., Chem. Commun., pp. 2559–2560, 1994. [Online]. Available: http://dx.doi.org/10.1039/C39940002559

[147] Y. Han, S. L. Bontems, P. Hegyes, M. C. Munson, C. A. Minor, S. A. Kates, F. Albericio, and G. Barany, "Preparation and applications of xanthenylamide (xal) handles for solid-phase synthesis of c-terminal peptide amides under particularly mild conditions1-3," The Journal of Organic Chemistry, vol. 61, no. 18, pp. 6326–6339, 1996, pMID: 11667474. [Online]. Available: http://dx.doi.org/10.1021/jo960312d

[148] M. Mergler, J. Gosteli, P. Grogg, R. Nyfeler, and R. Tanner, "Sasrin a versatile tool in peptide synthesis and solid-phase organic chemistry," CHIMIA International Journal for Chemistry, vol. 53, no. 1-2, pp. 29–34, 1999. [Online]. Available: http://www.ingentaconnect.com/content/scs/chimia/1999/00000053/F0020001/art00007

[149] E. Atherton, C. J. Logan, and R. C. Sheppard, "Peptide synthesis. part 2. procedures for solid-phase synthesis using n[small alpha]-fluorenylmethoxycarbonylamino-acids on polyamide supports. synthesis of substance p and of acyl carrier protein 65-74 decapeptide," J. Chem. Soc., Perkin Trans. 1, pp. 538–546, 1981. [Online]. Available: http://dx.doi.org/10.1039/P19810000538

[150] J. Hansen, F. Diness, and M. Meldal, "C-terminally modified peptides via cleavage of the hmba linker by o-, n- or s-nucleophiles," Org. Biomol. Chem., vol. 14, pp. 3238–3245, 2016. [Online]. Available: http://dx.doi.org/10.1039/C6OB00213G

[151] A. Klapars and S. L. Buchwald, "Copper-catalyzed halogen exchange in aryl halides:? an aromatic finkelstein reaction," Journal of the American Chemical Society, vol. 124, no. 50, pp. 14 844–14 845, 2002, pMID: 12475315.

[152] H. M. M. Bastiaans, J. L. van der Baan, and H. C. J. Ottenheijm, "Flexible and convergent total synthesis of cyclotheonamide b," The Journal of Organic Chemistry, vol. 62, no. 12, pp. 3880–3889, 1997.

[153] D. S. Bose and V. Lakshminarayana, "Lewis acid-mediated selective removal of n-tert-butoxycarbonyl protective group (t-boc)," Synthesis, vol. 1999, no. 01, pp. 66–68, 1999, 66.

[154] J. G. Adamson, M. A. Blaskovich, H. Groenevelt, and G. A. Lajoie, "Simple and convenient synthesis of tert-butyl ethers of fmoc-serine, fmoc-threonine, and fmoc-tyrosine," The Journal of Organic Chemistry, vol. 56, no. 10, pp. 3447–3449, 1991.

[155] T. Maegawa, Y. Fujiwara, T. Ikawa, H. Hisashi, Y. Monguchi, and H. Sajiki, "Novel deprotection method of fmoc group under neutral hydrogenation conditions," Amino Acids, vol. 36, no. 3, pp. 493–499, 2009. [Online]. Available: http://dx.doi.org/10.1007/s00726-008-0109-7

[156] P. Marfey, "Determination ofd-amino acids. ii. use of a bifunctional reagent, 1,5-difluoro-2,4-dinitrobenzene," Carlsberg Research Communications, vol. 49, no. 6, p. 591, 1984.

[157] R. Bhushan and H. Brückner, "Marfey's reagent for chiral amino acid analysis: A review," Amino Acids, vol. 27, no. 3, pp. 231–247, 2004.

[158] J. Coste and P. Jouin, (1H-Benzotriazol-1-yloxy)tripyrrolidino-phosphonium Hexafluorophosphate. John Wiley & Sons, Ltd, 2001.

[159] J. Coste, D. Le-Nguyen, and B. Castro, "Pybop: A new peptide coupling reagent devoid of toxic by-product," Tetrahedron Letters, vol. 31, no. 2, pp. 205 – 208, 1990.

[160] M. B. Andrus, N-Ethylmorpholine. John Wiley & Sons, Ltd, 2001.

[161] S. Lin, Z.-Q. Yang, B. H. B. Kwok, M. Koldobskiy, C. M. Crews, and S. J. Danishefsky, "Total synthesis of tmc-95a and -b via a new reaction leading to z-enamides. some preliminary findings as to sar," Journal of the American Chemical Society, vol. 126, no. 20, pp. 6347–6355, 2004, pMID: 15149232.

[162] H. Sajiki, K. Hattori, and K. Hirota, "The formation of a novel pd/c?ethylenediamine complex catalyst:? chemoselective hydrogenation without deprotection of the o-benzyl and n-cbz groups," The Journal of Organic Chemistry, vol. 63, no. 22, pp. 7990–7992, 1998.

[163] H. Shao, J. W. Lockman, and J. R. Parquette, "Coupled conformational equilibria in ?-sheet peptide?dendron conjugates," Journal of the American Chemical Society, vol. 129, no. 7, pp. 1884–1885, 2007, pMID: 17256863.

[164] M. A. Campo and R. C. Larock, "Synthesis of fluoren-9-ones by the palladium-catalyzed cyclocarbonylation of o-halobiaryls," The Journal of Organic Chemistry, vol. 67, no. 16, pp. 5616–5620, 2002, pMID: 12153259.

[165] A. Fînaru, A. Berthault, T. Besson, G. Guillaumet, and S. Berteina-Raboin, "Microwave-assisted solid-phase synthesis of 5-carboxamido-n-acetyltryptamine derivatives," Organic Letters, vol. 4, no. 16, pp. 2613–2615, 2002, pMID: 12153191.

FULL PAPER

Injectable Colloidal Gold for Use in Intrafractional 2D Image-Guided Radiation Therapy

*Rasmus I. Jølck, Jonas S. Rydhög, Anders N. Christensen, Anders E. Hansen, Linda M. Bruun, Henrik Schaarup-Jensen, Asger Stevner von Wenck, Betina Børresen, Annemarie T. Kristensen, Mads H. Clausen, Andreas Kjær, Knut Conradsen, Rasmus Larsen, Per Munck af Rosenschöld, and Thomas L. Andresen**

In the western world, approximately 50% of all cancer patients receive radiotherapy alone or in combination with surgery or chemotherapy. Image-guided radiotherapy (IGRT) has in recent years been introduced to enhance precision of the delivery of radiation dose to tumor tissue. Fiducial markers are often inserted inside the tumor to improve IGRT precision and to enable monitoring of the tumor position during radiation therapy. In the present article, a liquid fiducial tissue marker is presented, which can be injected into tumor tissue using thin and flexible needles. The liquid fiducial has high radiopacity, which allows for marker-based image guidance in 2D and 3D X-ray imaging during radiation therapy. This is achieved by surface-engineering gold nanoparticles to be highly compatible with a carbohydrate-based gelation matrix. The new fiducial marker is investigated in mice where they are highly biocompatible and stable after implantation. To investigate the clinical potential, a study is conducted in a canine cancer patient with spontaneous developed solid tumor in which the marker is successfully injected and used to align and image-guide radiation treatment of the canine patient. It is concluded that the new fiducial marker has highly interesting properties that warrant investigations in cancer patients.

1. Introduction

Nanomaterials offer unique properties that can provide society with new healthcare technologies for treatment of disease. With the increasing aging of the population in the western world, cancer incidence continues to rise creating a crucial demand for efficient and cost-effective therapies. Radiation therapy is a cost-effective treatment modality and approximately 50% of cancer patients receive radiation therapy after being diagnosed with cancer.[1] Modern radiation oncology relies on advanced, high-precision imaging techniques such as computed tomography (CT), positron emission tomography (PET), and magnetic resonance (MR) to enable the delivery of high radiation doses to defined targets.[2–4] However, tumors rarely display a fixed position during irradiation or within the treatment period

Dr. R. I. Jølck, Dr. A. E. Hansen, L. M. Bruun, Prof. T. L. Andresen
DTU Nanotech, Department of Micro-and Nanotechnology
Center for Nanomedicine and Theranostics
Technical University of Denmark
Building 345E, Ørsteds Plads,
2800 Lyngby, Denmark
E-mail: thomas.andresen@nanotech.dtu.dk

J. S. Rydhög, Dr. P. Munck af Rosenschöld
Department of Oncology
Section of Radiotherapy
3994, Rigshospitalet
Blegdamsvej 9, 2100 Copenhagen, Denmark

J. S. Rydhög, Dr. P. Munck af Rosenschöld
the Niels Bohr Institute, University of Copenhagen
Blegdamsvej 17, 2100 Copenhagen, Denmark

A. N. Christensen, Prof. K. Conradsen, Prof. R. Larsen
DTU Compute, Department of Applied Mathematics
and Computer Science
Technical University of Denmark
Building 321/324, Matematiktorvet, 2800 Lyngby, Denmark

H. Schaarup-Jensen, Prof. M. H. Clausen
DTU Chemistry
Department of Chemistry
Center for Nanomedicine and Theranostics
Technical University of Denmark
Building 207, Kemitorvet, 2800 Lyngby, Denmark

A. Stevner von Wenck, B. Børresen,
Prof. A. T. Kristensen
Department of Veterinary Clinical and Animal Sciences
Faculty of Health and Medical Sciences
University of Copenhagen
Dyrlægevej 16, 1870 Frederiksberg C, Denmark

Prof. A. Kjær
Department of Clinical Physiology
Nuclear Medicine & PET and Cluster for Molecular Imaging
Rigshospitalet and University of Copenhagen
Blegdamsvej 9, 2100 Copenhagen, Denmark

DOI: 10.1002/adhm.201400651

due to breathing motion, changes in organ filling, and tumor size.[5–7] To compensate for variations in tumor position frequent imaging (kilovoltage radiographs or fluoroscopy—also referred to as 2D X-ray imaging) during the course of treatment or image-guided radiation therapy (IGRT) is now being used in the clinic to improve radiation precision and accuracy, thereby reducing the treatment toxicity and optimizing therapeutic efficacy.[2,6,8] When the tumor position cannot be correlated with internal reference points such as the skeleton, tumor localization can be enhanced by alignment to radiographic markers implanted in or near the tumor.[9–11] Such markers can improve treatment through optimized planning, tumor positioning accuracy, and tumor tracking resulting in more precise dose delivery and enable treatment of cancers, which are presently not eligible for radiotherapy.[12,13] Tissue markers currently used in the clinic are metal-based solid implants with large physical dimensions, which require complicated insertion procedures and therefore the risk of complications. Lung tumor insertion is especially problematic, with pneumothorax (reported in 33%–68% of patients) as well as bleeding being reported as primary complications.[14–16] In order to increase the usability and patient compliance of radiographic markers, we recently described the concept of a liquid injectable fiducial marker by exploiting polyethylene glycol (PEG)-coated gold nanoparticles (AuNPs) in a nonsolvent-induced phase separation (NIPS) gelation matrix.[17] This system was found to be biocompatible and clearly visible on 3D X-ray imaging, However, due to the chemical properties of the encapsulated AuNPs only 10 mg AuNPs mL^{-1} providing approximately 200 Hounsfield units (HU) of contrast could be included, which is insufficient for 2D X-ray visualization. For gating-based radiation procedures, often exploited in for example lung cancer patients, 2D X-ray visualization is required for intrafractional real-time imaging of moving tumors.[6,18–20] Additionally, fiducial marker visualization using 2D X-ray techniques lowers the X-ray exposure level to the patients and may reduce treatment time compared to 3D X-ray-based procedures.[2] Furthermore, with the increasing focus on stereotactic radiation procedures and the clinical introduction of proton therapy, visualization of tumor position and motion becomes crucial to optimize irradiation of cancerous tissue.[21,22] Therefore, radiopaque fiducial markers continue to be in high demand and development of new marker systems is of paramount importance.

In the present work, we have investigated a novel liquid fiducial marker (nanogel) system based on sucrose acetate isobutyrate (SAIB) and uniform poly(*N*-isopropyl acrylamide) (PNIPAM)-coated AuNPs with radio-opacity adequate for 2D X-ray visualization. SAIB, a fully acylated derivative of sucrose, is a biodegradable nonpolymeric compound, which has been approved for oral consumption and is generally regarded as safe (GRAS) by the FDA. SAIB mixtures with ethanol (EtOH) behaves as Newtonian liquids and have a low viscosity (50–200 mPa s) suited for injection using thin hypodermic needles.[23–25] Upon hydration, an amorphous (gel-like) solid is formed, which efficiently encapsulate high concentrations (>100 mg Au mL^{-1}) of PNIPAM-coated AuNPs providing contrast levels sufficient for visualization in 2D X-ray imaging techniques such as fluoroscopy and ExacTrac imaging (Brainlab AG, Feldkirchen, Germany). The developed nanogel has been characterized in vitro and the in vivo stability and visibility was evaluated in immunocompetent mice over a period of 8 weeks. Proof-of-concept in a clinical canine cancer patient with a spontaneous growing tumor was additionally established and the developed nanogel with PNIPAM-coated AuNPs was applied in IGRT in a canine cancer patient where marker visibility, stability, and marker migration were evaluated over time during the course of radiotherapy. The developed nanogel fulfills the requirements for use in guidance of radiation therapy as it is easy to inject, remains stable over the full time course of radiation treatment (6 weeks), shows no sign of migration, and is the first liquid fiducial marker to enable visualization using both 2D and 3D X-ray-based imaging techniques.

2. Results and Discussion

Visualization of fiducial markers in 2D X-ray imaging requires high electron density within the nanogel to possess efficient X-ray attenuation/radio-opacity, which can be achieved by doping the injectable gel with colloid AuNPs. We recently exploited the use of PEG-coated AuNPs but due to the high hydrophilicity of the PEG-coated AuNPs only 10 mg AuNPs mL^{-1} could be included in the liquid marker, which was insufficient for 2D X-ray visibility. Higher AuNP-concentrations resulted in a significant burst release due to the higher preference of the hydrophilic PEG-coated AuNPs for the surrounding aqueous phase.[17]

2.1. Engineering AuNPs for Enhanced Nanogel Compatibility

In order to increase the concentration of AuNPs and enhance the compatibility of the AuNPs with the hydrophobic SAIB-based gelation matrix, two different strategies were investigated: i) Masking the AuNPs by chemisorption of a dithiolane SAIB derivate ($(SH)_2$-SAIB) (**5**) (see Section 2.1.1, and Supporting Information) and ii) using commercially available thiol-functionalized PNIPAM with a molecular weight of 3.500 Da (SH-$PNIPAM_{3.500}$). Both strategies resulted in hydrophobic AuNPs, which was anticipated to reduce the previously observed AuNP burst release from the nanogels. Hence, we hypothesized that realization of one or both of these strategies should enable formulation of nanogels with higher concentrations of AuNPs resulting in higher X-ray contrast levels.

2.1.1. Synthesis of SAIB-Based Capping Agent for AuNP Functionalization

The dithiolane-functionalized SAIB derivate **5** was prepared as outlined in Scheme S1 (Supporting Information) starting from sucrose (**1**). Mono silyl protection of the 6′-OH position of the fructofuranose unit was achieved using *tert*-butyl(chloro)diphenylsilane (TBDPS-Cl) and 4-dimethylaminopyridine (DMAP) yielding 6′-O-TBDPS-sucrose (**2**).[26] The remaining hydroxyl groups were isobutyrylated using isobutyric anhydride and DMAP resulting hepta-isobutyryl-6′-O-TBDPS-sucrose (**3**). Initial attempts of deprotection of the TBDPS group using

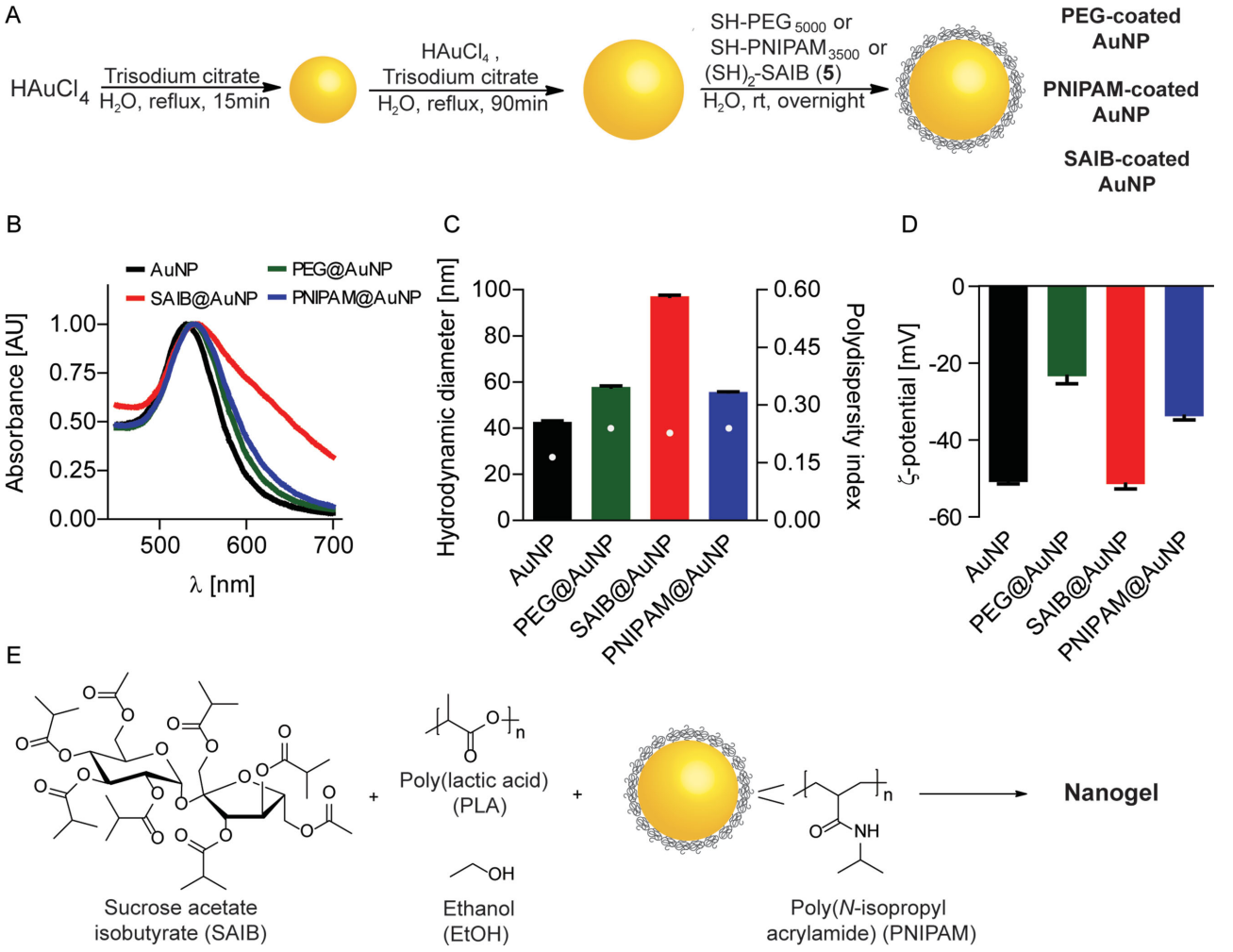

Figure 1. A) Synthesis protocol for obtaining PEG-, PNIPAM, and SAIB-coated AuNPs based on a three steep seeding protocol using chloroauric acid as Au^{3+} source and trisodium citrate as reductant and stabilizer; B) UV–vis characterization of PEG-, PNIPAM-, and SAIB-coated AuNPs in aqueous solution; C) DLS characterization of PEG-, PNIPAM-, and SAIB-coated AuNPs in aqueous solution; and D) ζ-potential characterization of PEG-, PNIPAM-, and SAIB-coated AuNPs in aqueous solution. E) Nanogel composition and preparation procedure.

tetra-n-butylammonium fluoride (TBAF) indicated a high degree of isobutyryl migration; fortunately, this could be suppressed by addition of acetic acid leading to hepta-isobutyryl-sucrose (**4**). Finally, the dithiolane moiety was introduced by *N*-(3-dimethylaminopropyl)-*N′*-ethylcarbodiimide (EDC) activation of lipoic acid in the presence of DMAP yielding the dithiolane-functionalized SAIB derivate **5** (a detailed description of synthesis and compound characterization is available as Supporting Information).

2.1.2. AuNP Synthesis, Functionalization, and Characterization

Citrate-stabilized AuNPs were synthesized using a seeding procedure as previously described resulting in uniform electrostatic-stabilized AuNPs with a diameter of approximately 40 nm.[17] Subsequently, chemisorption of SH-PEG_{5000}, SH-$PNIPAM_{3500}$ or $(SH)_2$-SAIB (**5**) to the citrate-stabilized AuNPs was conducted in aqueous solution in order to increase the colloid compatibility with SAIB-based gels (**Figure 1**A). Increasing the compatibility of the AuNPs with the SAIB-matrix includes increasing the hydrophobicity of the particles. However, a delicate balance exists where the hydrophobicity of the particles is increased without compromising their stability in aqueous solution during synthesis. As evident from the UV–vis (Figure 1B) and dynamic light scattering (DLS) (Figure 1C) analysis, AuNP coating with PEG and PNIPAM was successful. Only a slight increase in the surface plasmon resonance was observed, which is expected due to the microenvironmental changes on the surface of the particles. Additionally, DLS confirmed the presence of the two polymers at the colloid interface since an increase of 15.1 and 12.9 nm was observed for the PEG-coated and PNIPAM-coated AuNPs, respectively. However, chemisorption of $(SH)_2$-SAIB (**5**) to the surface of the electrostatic-stabilized AuNPs caused considerably aggregation due to the poor aqueous solubility of the formed particles, even under the very diluted conditions used. The aggregates formed from SAIB-coated AuNPs were isolated but redispersion in organic solvents such as absolute ethanol was not possible; thus, this class of particles was not investigated further. Synthesis and

subsequently coating of AuNPs with $(SH)_2$-SAIB (**5**) in pure organic solvent using the Burst–Shiffin method may be feasible, but this was not attempted due to the small size of particles formed by this method (<10 nm) and the fact that non-biocompatible solvents such as toluene and toxic phase-transfer agents have to be used, which could limit their use in biological settings.[27]

Additionally, handling of PNIPAM-coated AuNPs was found to be superior compared to PEG-coated AuNPs as these could be lyophilized and stored for prolonged time as an air stabile nanopowder, which readily dispersed into MQ-H_2O and a wide range of protic- and aprotic organic solvents including anhydrous ethanol without causing any changes to particle morphology (Figure S1, Supporting Information). This enabled easy up-concentration, storage, and nanogel formulation compared to the previous described method where AuNPs were transferred into anhydrous EtOH by centrifugation prior to use.

2.2. Contrast Evaluation for 2D X-Ray Visualization of Nanogel in Humans

In order to evaluate the required concentration of AuNPs within the nanogel for visibility on 2D X-rays images in humans, a simulation of 2D digitally reconstructed radiographs (DRRs) was performed based on clinical 3D CT-data for a patient diagnosed with lung cancer. A lung tumor model was chosen as this region is considered as a worst-case scenario due to the high concentration of bone structure in the thoracic region. A simulated nanogel (500 µL) was digitally placed inside the lung tumor of the patient and the specified HU contrast level was varied from 500 to 2000 HU with increments steps of 500 HU on the 3D CT-data. 2D DRRs were created for all angles entering perpendicular around the patient in steps of 5° using a ray-tracing algorithm[28,29] resulting in 72 simulated projections for each contrast level (**Figure 2**). The center position of the DRRs was chosen to be in the center of the simulated nanogel placed centrally within the lung tumor of the patient. On the resulting DRRs, the visibility for each contrast level was evaluated by a contrast-to-noise ratio (CNR) approach, where a region of interest (ROI) for one projection and contrast level was contoured to define the nanogel and then transferred to all other projections. The mean intensity (M_m) and standard deviation (σ_m) of ROIs were calculated and compared to the mean

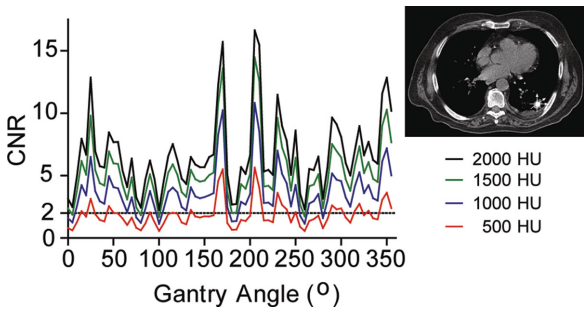

Figure 2. Contrast to noise (CNR) level versus angle of entrance for a simulated nanogel (500 µL) with various contrast levels (500–2000 HU) placed digitally inside a lung tumor.

(M_b) and standard deviation (σ_b) from a ROI on a DRR with no simulated nanogel present according to a CNR evaluation (Equation (1)).

$$\mathrm{CNR} = \frac{|M_m - M_b|}{\sqrt{\sigma_m^2 - \sigma_b^2}} \quad (1)$$

The CNR level can be considered a quantitative measurement of the visibility of the object measured compared to the background contrast from the surroundings. Generally, high CNR translate to increased visibility of the marker. We considered the simulated nanogel visible in the 2D DRR if CNR > 2. This value corresponds to a significance level of 0.05 obtained from a two-tailed *t*-test with a large number of degrees-of-freedom.[30] As evident from Figure 2, some angles requires a higher X-ray contrast level of the nanogel in order to obtain a CNR > 2 as these penetrates bone structure prior to reaching the nanogel. Other angles are more easily accessible and thereby result in lower background contrast, thus making the nanogel more visible on the 2D DRRs. Based on the lung cancer patient projection simulation on the DRRs, it was evident that the contrast level required for CNR > 2 in 95% of all perpendicular angles was approximately 1000 HU (spherical nanogel with a total volume of 500 µL) corresponding to a nanogel with approximately 30 mg AuNPs mL^{-1}. A comparison of the 2D X-ray contrast level from PNIPAM-coated AuNPs (10, 30, 60, and 90 mg mL^{-1}) and clinically used solid fiducial markers is provided in Figure S2, Supporting Information.

2.3. In Vitro Evaluation of Nanogel Performance

In vitro release kinetics of encapsulated PEG-coated and PNIPAM-coated AuNPs in SAIB nanogels doped with polylactic acid (PLA) with the composition SAIB/EtOH/PLA (75:20:5) + 30 mg AuNPs mL^{-1} were examined by placing small droplets (200 µL) of nanogels into MQ-H_2O at physiological temperature. Small aliquots of MQ-H_2O were removed at specific time intervals and replaced with fresh MQ-H_2O to mimic the sink effect in vivo. The amount of released AuNPs was determined by UV–vis spectroscopy using a standard curve of individual synthesized and coated AuNPs with a known concentration (Figure S3, Supporting Information). Injection of nanogel into aqueous solution causes an efflux of EtOH from the nanogel into the aqueous compartment. Efflux of EtOH results in rapid increase in gel viscosity,[24] but may also induce a burst release of encapsulated AuNPs.[24] Indeed, a rapid burst release of PEG-coated AuNPs from nanogels composed of SAIB/EtOH/PLA (75:20:5) + 30 mg PEG-coated AuNPs mL^{-1} was observed. In contrast, the use of PNIPAM-coated AuNPs resulted in highly stable nanogels with no (<1%) AuNP release over time in vitro despite the high AuNP concentration in the gel (Figure S3, Supporting Information). Concentrations as high as 100 mg PNIPAM-coated AuNPs mL^{-1} were evaluated without induced burst release of encapsulated PNIPAM-coated AuNPs (data not shown). The enhanced compatibility of the PNIPAM-coated AuNPs with the SAIB matrix compared to the PEG-coated counterpart can be explained by the enhanced hydrophobicity and potential hydrogen bonding interactions between

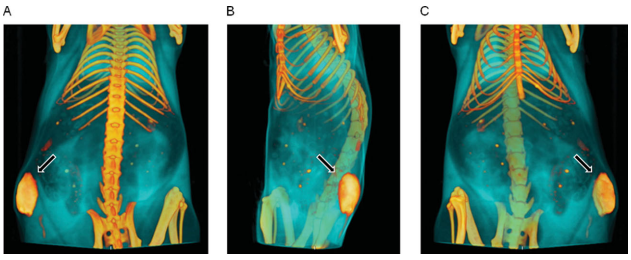

Figure 3. Representative 3D reconstruction from micro-CT images of mouse. Nanogel composed of SAIB/EtOH/PLA (75:20:5) + 30 mg PNIPAM-coated AuNPs mL^{-1} administered subcutaneously to immunocompetent mice at the upper left flank. Nanogel visualized from different angles.

the PNIPAM-coating polymers and the polyester backbone of SAIB. The positive in vitro stability results and known target AuNP concentration for 2D X-ray visibility encouraged us to further evaluate the nanogels composed of SAIB/EtOH/PLA (75:20:5) + 30 mg PNIPAM-coated AuNPs mL^{-1} in vivo using immunocompetent mice.

2.4. In Vivo Evaluation of Nanogel Performance

2.4.1. Evaluation of Nanogel in Immunocompetent Healthy NMRI-Mice

Nanogels (200 µL) composed of SAIB/EtOH/PLA (75:20:5) + 30 mg PNIPAM-coated AuNPs mL^{-1} were injected subcutaneously in immunocompetent NMRI-mice ($n = 5$) at the upper left flank using a 25G needle under general anesthesia. The nanogel was visualized using micro-CT imaging over a period of 8 weeks (images acquired directly after injection and again after 24, 48 h, 1, 2, 4, and 8 weeks) using a dedicated small-animal scanner (**Figure 3**). Based on the recorded micro-CT images, the nanogel X-ray contrast level, degradation rate, and homogeneity were evaluated as a function of time (**Figure 4**). No significant changes in the nanogel volume were observed after the initial EtOH efflux phase, which caused approximately 20% reduction of nanogel volume in good correlation with the known EtOH content of the nanogel prior to injection. The nanogel doped with 30 mg PNIPAM-coated AuNPs mL^{-1} provided a mean X-ray contrast level in the range of 1200 HU, which is sufficient for 2D X-ray visualization as previously described. A reduction of the mean contrast level of the nanogel was observed over time possible due to some AuNP leakage or aggregation of particles within the nanogel. Figure 4B clearly displays the increased maximum contrast level within the nanogel during the first week following intra-gel AuNP aggregation resulting in very high contrast levels (>15.000 HU) (Figure S4, Supporting Information). The homogeneity of the nanogel in terms of PNIPAM-coated AuNP distribution within the gel matrix was analyzed further by investigating each voxel of the micro-CT images as illustrated in Figure 4C. As evident from the cumulative histograms for a representative mouse, the PNIPAM-coated AuNPs were found to gradually aggregate within the nanogel as previously observed for PEG-coated AuNPs within the same gel matrix.[17] In fact, no significant difference was found in the variance of the PEG-coated and PNIPAM-coated AuNPs within the nanogels as analyzed by the Wilcoxon rank-sum test ($p = 0.0734$).[31] The inhomogeneous PNIPAM-coated AuNPs distribution within the nanogel could be visualized in the mice due to the high resolution and small slice thickness ($0.092 \times 0.092 \times 0.092$ mm^3) of the micro-CT scanner. The aggregation phenomenon of the PNIPAM-coated AuNPs within the nanogel has no clinical impact as human clinical scanners operate with significant larger slice thickness (2–3 mm) and lower resolution (1×1 mm^2) causing the AuNP microstructure aggregation to be below the resolution of recorded images.

2.4.2. Evaluation of Nanogel in a Canine Cancer Patient with Spontaneously Developed Solid Tumor

In order to fully validate the concept of liquid injectable fiducial markers for IGRT, the nanogel was evaluated in a canine cancer patient suffering from spontaneously developed malignant solid tumor (mast cell tumor). Solid tumors often show an increased interstitial fluid pressure (IFP) possibly due to vessel abnormalities, fibrosis, and contraction of the interstitial matrix mediated by stromal fibroblasts.[32,33] Increased IFP may serve as an obstacle for intratumoral injection of the developed nanogel as the available intracellular space for marker assembly post-injection is limited and the increased IFP may repel the nanogel into adjacent areas. Additionally, migration of the nanogel over time may compromise the accuracy of fiducial

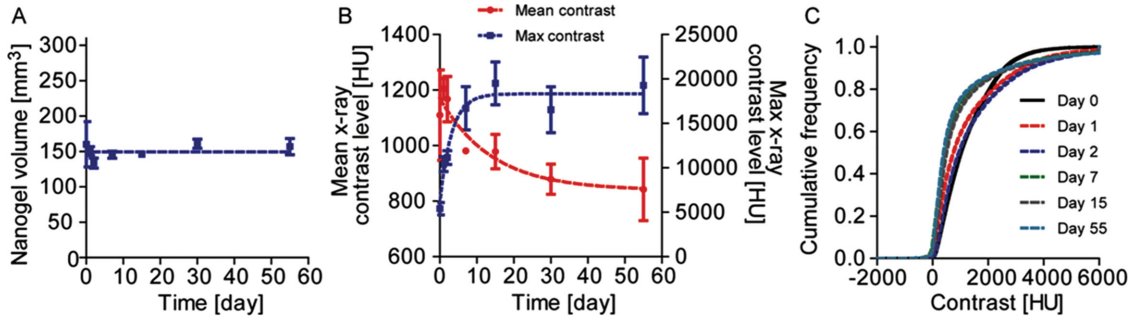

Figure 4. In vivo characteristics of nanogel composed of SAIB/EtOH/PLA (75:20:5) + 30 mg PNIPAM-coated AuNPs mL^{-1} administered subcutaneously to immunocompetent mice at the upper left flank. A) Nanogel degradation over a period of 8 weeks (mean ± SEM, $n = 5$); B) Mean (left axis) and maximum (right axis) X-ray contrast level of nanogel over a period of 8 weeks (mean ± SEM, $n = 5$) and C) Accumulated histogram of nanogel contrast level within each pixel from a representative mouse over a period of 30 d.

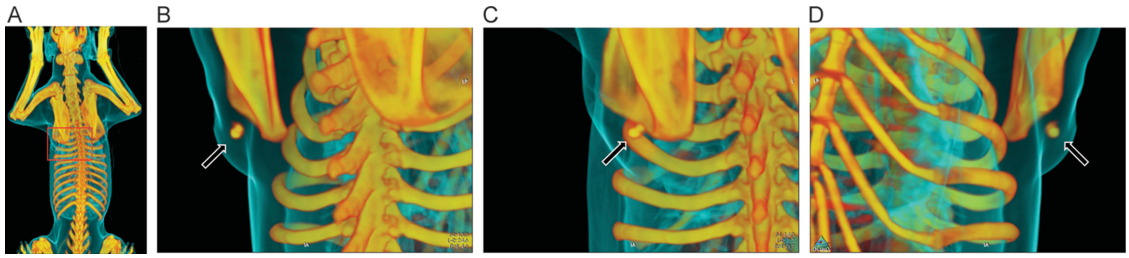

Figure 5. 3D reconstruction based on CT images of canine patient with injected nanogel. Nanogel composed of SAIB/EtOH/PLA (75:20:5) + 30 mg PNIPAM-coated AuNPs mL^{-1} administered intratumorally into a canine suffering from an intermediate-grade subcutaneous mast cell tumor (maximum distance ($x \times y \times z$); $1.82 \times 5.81 \times 5.32$ cm^3, CT volume; 31.64 cm^3) adherent to the underlying soft tissue located over the dorsal aspect of the left shoulder blade. A) Full-body scan of the canine. Area of interest indicated with a red box. B–D) Nanogel visualized from different angles.

marker-based IGRT and potentially result in misguidance of the external radiation beam, which, in turn, leads to poor tumor coverage and increased radiation to healthy adjacent tissue.[16,34] Such obstacles are not encountered for subcutaneous injections of the nanogel as evaluated in immunocompetent NMRI-mice, hence the canine cancer patient with a spontaneously developed solid tumor (mast cell tumor) served as a clinical animal model with high translational value for evaluating the clinical potential of the developed nanogel.

A companion dog (Male, Rhodesian Ridgeback, 10 years, body weight 38 kg) diagnosed with a subcutaneous mast cell tumor (maximum distance ($x \times y \times z$); $1.82 \times 5.81 \times 5.32$ cm^3, CT volume; 31.64 cm^3) adherent to the underlying soft tissue located over the dorsal aspect of the left shoulder blade was given an intratumoral injection of nanogel (300 µL) composed of SAIB/EtOH/PLA (75:20:5) + 30 mg PNIPAM-coated AuNPs mL^{-1} under general anesthesia (**Figure 5**) prior to radiation therapy. Approximately 24 h after the injection of the nanogel, a diagnostic planning CT-scan of the tumor/nanogel region was performed and the therapeutic regimen consisting of four fractions of 6 Gy radiation therapy planned accordingly. Radiation therapy was delivered over 16 d on a clinical linear accelerator equipped with on-board imaging (OBI) capabilities (3D cone beam CT (CBCT) and 2D X-ray imaging).

Prior to each fraction of radiotherapy, CBCT (**Figure 6**) images and 2D X-ray imaging (Figure S5, Supporting Information) were acquired and used for positioning based on nanogel and tumor. Radiation therapy was delivered according to the nanogel position. The size (**Table 1**) and stability of the nanogel in terms of migration and deformation were evaluated based on the recorded CBCT images (Figure 6) by manually contouring the nanogel using 300 HU as a lower threshold. The nanogel size remained constant over the time of treatment with no change in overall volume was observed. The small variations observed in Table 1 are a consequence of motion artifacts from respiratory movement on the recorded CBCT images. Additionally, image analysis revealed that the nanogel retained its 3D shape and was found to be immobilized/associated with the tumor as no migration of the nanogel was observed during the course of radiation therapy despite the canine patient exercising and resting on the tumor inducing mechanical stress on the nanogel. Finally, exposure to four fractions of 6 Gy each was not found to alter the nanogel morphology as evaluated based on the CBCT images. The nanogel was well tolerated and no clinical side effects were observed throughout the study.

3. Conclusion

A novel nanogel composition based on PNIPAM-coated AuNPs formulated in a mixture of SAIB/EtOH/PLA (70:20:5) has been developed. PNIPAM-coated AuNPs were found to be highly compatible with the hydrophobic SAIB-based gel matrix facilitating encapsulation of high concentration of colloidal gold, which enables 2D X-ray visualization of the nanogel. This was confirmed by a simulation of 2D DRRs of a patient suffering from lung cancer. The developed nanogel is the first injectable fiducial marker that can be visualized in 2D X-ray imaging thereby enabling intra- and interfractional IGRT by referencing the nanogel position. The nanogel performance was evaluated

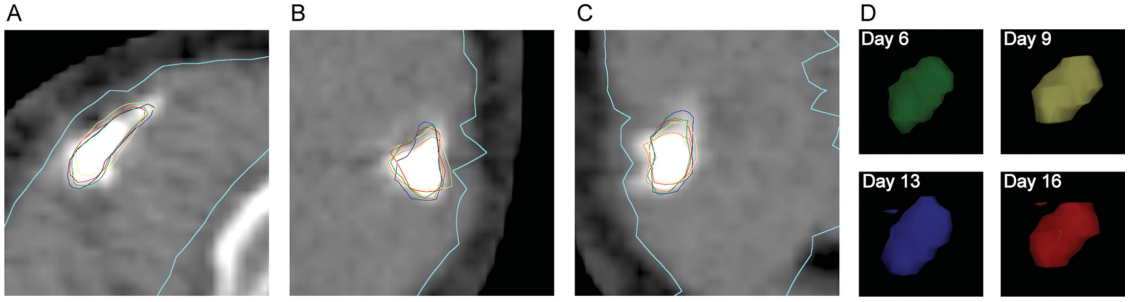

Figure 6. Nanogel composed of SAIB/EtOH/PLA (75:20:5) + 30 mg PNIPAM-coated AuNPs mL^{-1} administered intratumorally into a canine mast cell tumor visualized by CBCT imaging. A) Transversal plane (day 0); B) frontal plane (day 0); C) sagittal plane (day 0). Contours in A–C represent the nanogel on day 6 (green), day 9 (yellow), day 13 (blue), and day 16 (red). The light blue contour represents the gross tumor volume. D) 3D renderings of all the four surfaces represent the nanogel from each day of treatment.

Table 1. Nanogel volume following intratumoral injection in a canine model.

Day #	Nanogel volume [cm^3]
0	0.20
6	0.18
9	0.21
13	0.22
16	0.19

in vivo in immunocompetent mice by subcutaneous injection. Excellent visibility of the nanogel by micro-CT imaging was observed with a mean contrast level of 1200 HU after injection. Over time, the PNIPAM-coated AuNPs were found to form microaggregates within the gel matrix as confirmed by image analysis of the high-resolution micro-CT images. This phenomenon was found to have no clinical impact due to the larger slice thickness of human clinical scanners and lower resolution compared to small animal micro-CT scanners.

The concept of an injectable fiducial marker for use in IGRT was finally validated in a canine cancer patient with a large spontaneous solid tumor. The canine patient provides translational understanding and allowed us to evaluate the clinical potential of the nanogel. The nanogel displayed high image contrast on both conventional CT and CBCT images and could additionally be identified by 2D X-ray imaging, thus providing sufficient radiographic properties for visualization with all the imaging modalities associated with modern linear accelerators. Furthermore, the nanogel retained its size and 3D structure within the tumor microenvironment and no migration of the nanogel was observed within the time period for the radiotherapy treatment procedure. The developed nanogel was utilized to align the canine patient prior to external beam radiation therapy, was found to be unaffected by the deposited radiation dose within the tumor, and no side effects were observed in neither the murine nor the clinically relevant canine model. However, it should be noted that AuNPs are currently not approved for human use and the knowledge about the potential short- and long-term toxicological effects after AuNP exposure is still limited.[36]

The developed nanogel presented in this article is the first liquid fiducial marker, which can be inserted using thin and flexible needles and with a high enough contrast to make it visible in 2D X-ray imaging, which is an important feature for use in IGRT. Furthermore, active pharmaceutical ingredients may be included in the nanogel formulation to improve the therapeutic benefit for the patient, and the AuNPs may enhance the effect of the radiation therapy if the gel is injected directly into tumors.[37,38] In conclusion, the nanogel may provide both human and veterinary radiation oncologists with a new tool for improving planning, alignment, and tumor tracking in radiotherapy and could improve treatment outcome by providing a more precise delivery of the radiation dose to tumors.

4. Experimental Section

Materials: Tetrachloroauric acid trihydrate was purchased from Wako Chemicals GmbH (Neuss, Germany) and MeO-PEG_{5000}-SH was purchased from Rapp Polymere (Tuebingen, Germany). SH-PNIPAM (M_w = 3500Da, PDI = 1.24) was purchased from Polymer Source Inc. (Dorval, Canada). All other chemicals including SAIB, PLA (M_w = 10–18 kDa), trisodium citrate dihydrate, Au-standard for inductively coupled plasma atomic emission spectroscopy (ICP-AES) (1000 mg L^{-1}), hydrochloride acid and nitric acid were purchased from Sigma–Aldrich (Schnelldorf, Germany). All chemicals were used as received from the manufacturer.

*Synthesis of $(SH)_2$-SAIB (**5**)*: $(SH)_2$-SAIB (**5**) was synthesized over four steps starting from sucrose (**1**) in an overall yield of 27%. Full synthetic procedure including chemical characterization (^1H NMR, ^{13}C NMR, HRMS, and FTIR) is available in the Supporting Information.

AuNP Synthesis and Characterization: AuNPs were synthesized as previously described using a two-step seeding procedure resulting in citrate-stabilized AuNPs with an average diameter of 40 nm.[17] The citrate-stabilized AuNPs were subsequently coated with either SH-PEG_{5000}, SH-$PNIPAM_{3500}$, or $(SH)_2$-SAIB (**5**) using eight molecules per nm^2 surface area. Chemisorption of coating materials was in all cases conducted overnight at RT after which the volume was reduced to approximately 15 mL by centrifugation (9.500 RPM, 15 min). The PEG-coated AuNPs, PNIPAM-coated AuNPs, and SAIB-coated AuNPs colloid solutions were washed with MQ-H_2O (3 × 15 mL) and the finally up-concentrated to approximately 75 mg Au mL^{-1} as determined by ICP-MS using an ICP-MS Au standard (1000 mg L^{-1}) as reference. Colloid solutions (citrate-stabilized AuNPs, PEG-, PNIPAM-, and SAIB-coated AuNPs) were furthermore characterized by UV–vis spectrometry, DLS, and ζ-potential measured. PNIPAM-coated AuNPs were finally characterized by TEM (Figure S2, Supporting Information).

Nanogel Formulation: SAIB (1.75 g, 90 w/w% in EtOH) and PLA (105 mg) were mixed and homogenized by a ball homogenizer (frequency 30 s^{-1}, 30 min) to give a clear homogenous solution. Lyophilized PNIPAM-coated AuNPs (63 mg) was weighed off and redispersed into anhydrous EtOH (310 µL) by extensive vortexing and added to the SAIB/PLA mixture to give a final nanogel forming matrix composed of SAIB/EtOH/PLA (75:20:5) with 3.0 w/w% (30 mg mL^{-1}) PNIPAM-coated AuNPs. Formed nanogels were stored at RT and used within 4 h from preparation with vortexing prior to use. Nanogels with PEG-coated AuNPs were prepared as described elsewhere.[17]

*In Vitro Release of PNIPAM- and PEG-*Coated *AuNPs from Nanogel*: Nanogels composed of SAIB/EtOH/PLA (75:20:5) with 3.0 w/w% (30.0 mg mL^{-1}) of either PEG- or PNIPAM-coated AuNPs were prepared as described above. Nanogels (200 µL) were added to glass vials containing MQ-H_2O (10.0 mL, 37 °C) and aliquots (1.0 mL) were removed as a function of time and replaced with an equal amount of MQ-H_2O. The release profile from both nanogels was measured by correlating the UV–vis absorbance of the individual AuNPs with a standard curve based on Au-standards of known concentration (5.0–50.0 µg mL^{-1}).

Simulation of CNR in Lung Cancer Patient: 2D DRRs were performed based on clinical 3D CT-data for a patient diagnosed with lung cancer. 2D DRRs were created using the drrCode ray-tracing algorithm available online (https://code.google.com/p/drrsuite/downloads/list). 2D DRRs were created using a source to detector distance of 150 cm and a detector size of 768 × 1024 pixels (identical to a clinical settings). For conversion from HU to attenuation coefficient, a μ_ρ for water was used assuming monochromatic photons of 120 kV. ROI contouring and CNR calculations for the simulated projections were performed in MATLAB (The MathWorks Inc., Natick, MA, USA) using an in-house-developed simulation and analysis tool.

Animal Models (Mice): Immunocompetent 7-week-old female NMRI mice (n = 5) were given a subcutaneous injection (200 µL) of SAIB/EtOH/PLA (75:20:5) + 30 mg mL^{-1} PNIPAM-coated AuNPs using a 25 G needle in the upper left flank of the anesthetized mice. The animals were given free access to food and water and micro-CT scans were recorded over a period of 8 weeks (24, 48 h, 1, 2, 4, and 8 weeks) using a dedicated small-animal MicroCAT II system (Siemens Medical Solutions, Malvern, PA, USA). Micro-CT images were recorded using the following settings; tube voltage of 67 kVp, tube current of 500 µA, 360 rotation steps, an exposure time of 400 ms, and a voxel size of 0.092 × 0.092 × 0.092 mm^3. The animal experiments were approved by the Animal Research Committee of the Danish Ministry of Justice.

Canine: A privately owned companion dog (Male, Rhodesian Ridgeback, 10 years, bodyweight 38 kg) suffering from a spontaneously developed subcutaneous mast cell tumor (maximum distance ($x \times y \times z$); 1.82 × 5.81 × 5.32 cm^3, CT volume; 31.64 cm^3) adherent to the underlying soft tissue located over the dorsal aspect of the left shoulder blade was used as a clinical relevant model. In conjunction with the standard diagnostic procedures, nanogel (300 µL) was manually injected centrally in the tumor using a 23 G needle and 1 mL syringe. Approximately 24 h after the injection of the nanogel, a diagnostic CT scan (Biograph 40, Siemens Medical Solutions, Erlangen, Germany) of the tumor region was performed with the dog under general anesthesia using the following acquisition parameters; 120 kV, 150 mAs, pixel size 0.977 × 0.977 × 1.00 mm^3). As part of the therapeutic procedure radiation therapy was planned according to the tumor histology and imaging characteristic, and a therapeutic regimen consisting of four fractions of 6 Gy radiation treatments was chosen. Radiation therapy was delivered by a linear accelerator (Novalis TX, Varian Medical Systems, Palo Alto, CA, USA) with on-board imaging capabilities (Cone Beam CT and 2D X-ray imaging) and orthogonal ExacTrac radiography (Brainlab AG, Feldkirchen, Germany). No side effects were observed throughout the study. The canine cancer patient study was approved by the Ethics and Administrative Committee at the Department of Veterinary Clinical and Animal Sciences, Faculty of Health and Medical Sciences, University of Copenhagen, Denmark.

Analysis of Nanogel Homogeneity: The nanogels were delineated by hand using ITK-SNAP.[35] All data analyses were done in MATLAB (The MathWorks Inc., Natick, MA, USA) using in-house- developed software. Based on the voxel values in the gels mean and max values, as well as cumulative histograms were calculated. The cumulative histograms were used for homogeneity evaluation, as changes in the AuNP distribution are reflected in the voxels values and thus the histograms.

Supporting Information

Supporting Information is available from the Wiley Online Library or from the author.

Acknowledgements

This work has been funded by the Technical University of Denmark (DTU), the Niels Bohr Institute, the Danish Council for Strategic Research (Nanoguide, application no. 0603-00442B), and the Novo Foundation.

Received: October 17, 2014
Revised: December 3, 2014
Published online: January 21, 2015

[1] R. Baskar, K. A. Lee, R. Yeo, K. Yeoh, *Int. J. Med. Sci.* **2012**, *9*, 193.
[2] L. A. Dawson, M. B. Sharpe, *Lancet Oncol.* **2006**, *7*, 848.
[3] J. Bussink, J. H. A. M. Kaanders, W. T. A. van der Graaf, W. J. G. Oyen, *Nat. Rev. Clin. Oncol.* **2011**, *8*, 233.
[4] D. Verellen, R. M. De, N. Linthout, K. Tournel, G. Soete, G. Storme, *Nat. Rev. Cancer* **2007**, *7*, 949.
[5] K. M. Langen, D. T. Jones, *Int. J. Radiat. Oncol. Biol. Phys.* **2001**, *50*, 265.
[6] H. Shirato, Y. Seppenwoolde, K. Kitamura, R. Onimura, S. Shimizu, *Semin. Radiat. Oncol.* **2004**, *14*, 10.
[7] P. Giraud, E. Yorke, S. Jiang, L. Simon, K. Rosenzweig, G. Mageras, *Cancer Radiother.* **2006**, *10*, 269.
[8] M. Falk, P. M. af Rosenschold, P. Keall, H. Cattell, B. C. Cho, P. Poulsen, S. Povzner, A. Sawant, J. Zimmerman, S. Korreman, *Radiother. Oncol.* **2010**, *94*, 218.
[9] D. P. Harley, W. S. Krimsky, S. Sarkar, D. Highfield, C. Aygun, B. Gurses, *Ann. Thorac. Surg.* **2010**, *89*, 368.
[10] M. Imura, K. Yamazaki, H. Shirato, R. Onimaru, M. Fujino, S. Shimizu, T. Harada, S. Ogura, H. Dosaka-Akita, K. Miyasaka, M. Nishimura, *Int. J. Radiat. Oncol. Biol. Phys.* **2005**, *63*, 1442.
[11] D. J. Moseley, E. A. White, K. L. Wiltshire, T. Rosewall, M. B. Sharpe, J. H. Siewerdsen, J. Bissonnette, M. Gospodarowicz, P. Warde, C. N. Catton, D. A. Jaffray, *Int. J. Radiat. Oncol. Biol. Phys.* **2007**, *67*, 942.
[12] I. Gauthier, J. Carrier, D. Beliveau-Nadeau, B. Fortin, D. Taussky, *Int. J. Radiat. Oncol. Biol. Phys.* **2009**, *74*, 1128.
[13] R. Khosa, S. Nangia, K. S. Chufal, D. Ghosh, R. Kaul, L. Sharma, *J. Cancer Res. Ther.* **2010**, *6*, 172.
[14] S. Yousefi, B. T. Collins, C. A. Reichner, E. D. Anderson, C. Jamis-Dow, G. Gagnon, S. Malik, B. Marshall, T. Chang, F. Banovac, *Clin. Lung Cancer* **2007**, *8*, 252.
[15] N. Kothary, J. J. Heit, J. D. Louie, W. T. Kuo, B. W. J. Loo, A. Koong, D. T. Chang, D. Hovsepian, D. Y. Sze, L. V. Hofmann, *J. Vasc. Interv. Radiol.* **2009**, *20*, 235.
[16] N. Bhagat, N. Fidelman, J. C. Durack, J. Collins, R. L. Gordon, J. M. LaBerge, R. K. J. Kerlan, *Cardiovasc. Interv. Radiol.* **2010**, *33*, 1186.
[17] R. I. Jølck, T. Binderup, A. E. Hansen, J. B. Scherman, P. M. af Rosenschold, A. Kjær, T. L. Andresen, *Adv. Healthcare Mater.* **2014**, *3*, 1680.
[18] H. Shirato, K. Suzuki, G. C. Sharp, K. Fujita, R. Onimaru, M. Fujino, N. Kato, Y. Osaka, R. Kinoshita, H. Taguchi, S. Onodera, K. Miyasaka, *Int. J. Radiat. Oncol. Biol. Phys.* **2006**, *64*, 1229.
[19] T. Juhler-Nottrup, S. S. Korreman, A. N. Pedersen, G. F. Persson, L. R. Aarup, H. Nystrom, M. Olsen, N. Tarnavski, L. Specht, *Acta Oncol.* **2008**, *47*, 1406.
[20] S. S. Korreman, T. Juhler-Nottrup, G. F. Persson, P. A. Navrsted, M. Enmark, H. Nystrom, L. Specht, *Acta Oncol.* **2008**, *47*, 1390.
[21] M. L. Taylor, T. Kron, R. D. Franich, *Acta Oncol.* **2011**, *50*, 483.
[22] C. Rubio, O. Hernando, R. Morera, T. Leroy, S. E. Lartigau, *Rep. Pract. Oncol. Radiother.* **2013**, *18*, 387.
[23] Y. Lu, H. He, Y. Cui, X. Tang, *Yao Xue Xue Bao.* **2007**, *42*, 445.
[24] Y. Lu, Y. Yu, X. Tang, *J. Pharm. Sci.* **2007**, *96*, 3252.
[25] X. Lin, S. Yang, J. Gou, M. Zhao, Y. Zhang, N. Qi, H. He, C. Cai, X. Tang, P. Guo, *J. Mater. Sci.: Mater. Med.* **2012**, *23*, 443.
[26] M. M. Andrade, M. T. Barros, *Tetrahedron* **2004**, *60*, 9235.
[27] M. Brust, M. Walker, D. Bethell, D. J. Schiffrin, R. Whyman, *Chem. Commun.* **1994**, *7*, 801.
[28] F. Jacobs, E. Sundermann, B. De Sutter, M. Christiaens, I. Lemahieu, *J .Comput. Inf. Technol.* **1998**, *6*, 89.
[29] R. L. Siddon, *Phys. Med. Biol.* **1985**, *30*, 817.
[30] Y. Chen, J. J. O'Connell, C. J. Ko, R. R. Mayer, A. Belard, J. E. McDonough, *Phys. Med. Biol.* **2012**, *57*, 155.
[31] F. Wilcoxon, *J. Econ. Entomol.* **1946**, *39*, 269.
[32] C. Heldin, K. Rubin, K. Pietras, A. Oestman, *Nat. Rev. Cancer* **2004**, *4*, 806.
[33] P. Vaupel, *Semin. Radiat. Oncol.* **2004**, *14*, 198.
[34] J. C. Hong, N. C. W. Eclov, Y. Yu, A. K. Rao, S. Dieterich, Q. Le, M. Diehn, D. Y. Sze, B. W. Loo Jr., N. Kothary, P. G. Maxim, *J. Appl. Clin. Med. Phys.* **2013**, *14*, 4046.
[35] P. A. Yushkevich, J. Piven, H. C. Hazlett, R. G. Smith, S. Ho, J. C. Gee, G. Gerig, *Neuroimage* **2006**, *31*, 1116.
[36] A. Gerber, M. Bundschuh, D. Klingelhofer, D. A. Groneberg, *J. Occup. Med. Toxicol.* **2013**, *8*, 32.
[37] X. Zhang, D. Wu, X. Shen, J. Chen, Y. Sun, P. Liu, X. Liang, *Biomaterials* **2012**, *33*, 6408.
[38] X. Zhang, J. Chen, Z. Luo, D. Wu, X. Shen, S. Song, Y. Sun, P. Liu, J. Zhao, S. Huo, S. Fan, F. Fan, X. Liang, J. Xie, *Adv. Healthcare Mater.* **2014**, *3*, 133.

ADVANCED HEALTHCARE MATERIALS

Supporting Information

for *Adv. Healthcare Mater.*, DOI: 10.1002/adhm.201400651

Injectable Colloidal Gold for Use in Intrafractional 2D Image-Guided Radiation Therapy

*Rasmus I. Jølck, Jonas S. Rydhög, Anders N. Christensen, Anders E. Hansen, Linda M. Bruun, Henrik Schaarup-Jensen, Asger Stevner von Wenck, Betina Børresen, Annemarie T. Kristensen, Mads H. Clausen, Andreas Kjær, Knut Conradsen, Rasmus Larsen, Per Munck af Rosenschöld, and Thomas L. Andresen**

Supporting Information

Injectable Colloidal Gold for use in Intrafractional 2D Image Guided Radiation Therapy

*Rasmus I. Jølck, Jonas S. Rydhög, Anders N. Christensen, Anders E. Hansen, Linda M. Bruun, Henrik Schaarup-Jensen, Asger Stevner von Wenck, Betina Børresen, Annemarie T. Kristensen, Mads H. Clausen, Andreas Kjær, Knut Conradsen, Rasmus Larsen, Per Munck af Rosenschöld and Thomas L. Andresen**

Dr. R. I. Jølck, Dr. A. E. Hansen, L. M. Bruun and Prof. T. L. Andresen.
DTU Nanotech, Department of Micro-and Nanotechnology, Center for Nanomedicine and Theranostics, Technical University of Denmark, Building 345E, Ørsteds Plads, 2800 Lyngby, Denmark.
E-mail: thomas.andresen@nanotech.dtu.dk

J. S. Rydhög, Dr. P. Munck af Rosenschöld
Department of Oncology, Section of Radiotherapy, 3994, Rigshospitalet, Blegdamsvej 9, 2100 Copenhagen, Denmark and the Niels Bohr Institute, University of Copenhagen, Blegdamsvej 17, 2100 Copenhagen, Denmark.

A. N. Christensen, Prof. K. Conradsen and Prof. R. Larsen.
DTU Compute, Department of Applied Mathematics and Computer Science, Technical University of Denmark, Building 321/324, Matematiktorvet, 2800 Lyngby, Denmark.

H. Schaarup-Jensen and Prof. M. H. Clausen.
DTU Chemistry, Department of Chemistry, Center for Nanomedicine and Theranostics, Technical University of Denmark, Building 207, Kemitorvet, 2800 Lyngby, Denmark.

Prof. A. Kjær
Department of Clinical Physiology, Nuclear Medicine & PET and Cluster for Molecular Imaging, Rigshospitalet and University of Copenhagen, Blegdamsvej 9, 2100 Copenhagen, Denmark.

Prof. A. T. Kristensen, A. Stevner von Wenck and B. Børresen
Department of Veterinary Clinical and Animal Sciences, Faculty of Health and Medical Sciences, University of Copenhagen, Dyrlægevej 16, 1870 Frederiksberg C, Denmark.

1. Synthetic Procedure to $(SH)_2$-SAIB and Product Characterization

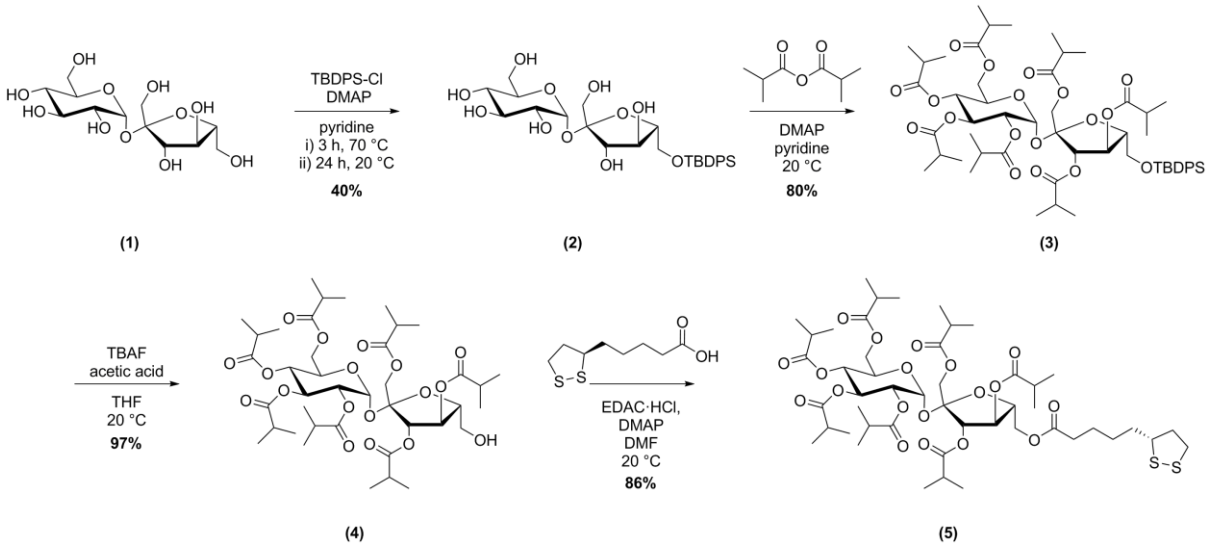

Scheme S1. Synthesis scheme for obtaining $(SH)_2$-SAIB (**5**) over four synthetic steps starting from sucrose (**1**) resulting in $(SH)_2$-SAIB (**5**) in an overall yield of 27%.

General Information

Nuclear Magnetic Resonance (NMR) was conducted on a Bruker Ascend^{TM} 400 MHz - operating at 401.3 MHz for ^{1}H and 100.62 MHz for ^{13}C - with a 5 mm H – Broadband Dual Channel z-gradient Prodigy cryoprobe instrumentation. All spectrums were measured at 298 K and the spectrums recorded were calibrated according to the solvent residues. Thin Layer Chromatography (TLC) analysis was conducted by use of TLC Silica gel 60 F_{254} aluminum sheets, Merck KGaA, 64271 Darmstadt, Germany. As developing agent a mixture (Cemol-dip) consisting of 9 g cerium sulfate, 47 g ammonium molybdate, 849 mL H_2O and 94 mL of sulfuric acid was applied on the TLC plate followed by heat treatment. For dry column purification, a silica gel 60 (0.015-0.040 mm) from Merck KGaA, 64271 Darmstadt, Germany was used. High Resolution Mass spectroscopy (HR-MS) was conducted on a Bruker Daltronics maXis 3G QTOF-MS fitted with a Dionex Ultimate 3000 UHPLC instrumentation. Attenuated Total Reflection Fourier Transformation Inferred radiation (ATR-FTIR) analysis was conducted on a Bruker Alpha platinum ATR instrumentation with a single reflection diamond ATR module. Melting point was measured with a Stuart SMP 30 instrumentation. Sucrose (99.5%, 57-50-1), 4-(dimethylamino)pyridine (DMAP, puriss, 1122-58-3), isobutyric anhydride (97%, 97-72-3), (*R*)-(+)-1,2-dithiolane-pentanoic acid (97%, 1200-22-2), *N*-(3-dimethylaminopropyl)-*N'*-ethylcarbodiimide hydrochloride (EDAC·HCl, 98%, 25952-53-8) and tetra-*n*-butylammoniumfluoride (TBAF, 1.0 M, 429-41-4) in THF were purchased from Sigma Aldrich (Steinheim, Germany) and used as received. *tert*-Butyl(chloro)diphenylsilane (TBDPS-Cl, 98%, 58479-61-1) was purchased from ABCR (Karlsruhe, Germany).

(2R,3R,4S,5S,6R)-2-(((2S,3S,4S,5R)-5-(((tert-Butyldiphenylsilyl)oxy)methyl)-3,4-dihydroxy-2-(hydroxymethyl)tetrahydrofuran-2-yl)oxy)-6-(hydroxymethyl)tetrahydro-2H-pyran-3,4,5-triol **(2)**. To a suspension of sucrose (**1**) (10 g, 29.2 mmol) in pyridine (100 mL) was added DMAP (0.36 g, 2.92 mmol). The reaction mixture was stirred at room temperature for 1 h followed by addition of TBDPS-Cl (4.65 mL, 17.5 mmol) and heated to 70 ^{0}C for 3 h. Another portion of TBDPS-Cl (4.65 mL, 17.5 mmol) was added to the reaction mixture at room temperature and then left stirred overnight. The reaction was followed by TLC. Pyridine was then removed *in vacuo* and the crude compound was purified by dry column vacuum chromatography (EtOH in EtOAc with 2% increments). Yield: 6.8 g amorphous solid; 40%.

Mp: 174 °C. ^{1}H-NMR (400 MHz, MeOD): δ = 1.04 (s, 9H), 3.25-3.35 (m, 2H), 3.50-3.68 (m, 5H), 3.72-3.79 (m, 1H), 3.84-3.99 (m, 3H), 4.01-4.13 (m, 2H), 5.44 (d, *J*=3.9 Hz, 1H), 7.35-7.46 (m, 6H), 7.67-7.77 (m, 4H). ^{13}C-NMR (100 MHz, MeOD): δ = 20.0, 27.3 (3C), 62.4, 64.3, 66.5, 71.4, 73.2, 73.9, 74.9, 76.2, 79.0, 83.7, 93.0, 105.6, 128.8 (2C), 128.8 (2C), 130.8 (2C), 134.5, 134.6, 136.8 (2C), 136.8 (2C); HR-MS. Calculated adducts: [M+H$^+$] = 581.2413, [M+Na$^+$] = 603.2232, [M+K$^+$] = 619.1971. Observed adducts, [M+H_2O] = 598.2675, [M+Na$^+$] = 603.2226, [M+K$^+$] = 619.1952. ATR-FTIR (cm^{-1}): 507.18, 701.83, 805.57, 930.50, 994.46, 1043.53, 1067.96, 1111.82, 1390.34, 1428.36, 1470.26, 2857.74, 2930.17, 3285.79.

(2R,3R,4S,5R,6R)-2-(((2S,3S,4R,5R)-5-(((tert-Butyldiphenylsilyl)oxy)methyl)-3,4-bis(isobutyryloxy)-2-((isobutyryloxy)methyl)tetrahydrofuran-2-yl)oxy)-6-((isobutyryloxy)methyl-)tetrahydro-2H-pyran-3,4,5-triyl tris(2-methylpropanoate) **(3)**. 6'-O-TBDPS-sucrose (**2)** (2.00 g, 3.44 mmol) was dissolved into pyridine (40 mL) together with DMAP (0.114 g, 0.924 mmol). Isobutyric anhydride (11.4 mL, 66.7 mmol) was added and the reaction mixture was stirred at room temperature overnight. The reaction was followed by TLC. At the point of reaction completion, the reaction mixture was concentrated *in vacuo* and diethyl ether (200 mL) was added followed by extraction with saturated aqueous sodium bicarbonate solution (5×200 mL). The organic phase was subsequently collected and concentrated *in vacuo*. The crude product was purified by dry column purification (EtOAc in heptane with 2% increments). Yield = 2.97 g transparent oily texture; 80%.^{1}H-NMR (400 MHz, DMSO): δ = 0.94-1.07 (m, 39H), 1.08-1.16 (m, 12H), 2.32-2.48 (m, 4H), 2.52-2.62 (m, 3H), 3.75-3.86 (m, 2H), 3.90 (dd, *J* = 13 Hz, 2 Hz, 1H), 4.02-4.20 (m, 4H), 4.24 (ddd, *J* = 10.3 Hz, 4.4 Hz, 1.8 Hz, 1H), 4.86 (dd, *J* = 10.6 Hz, 3.6 Hz, 1H), 5.04 (t, *J* = 10.0 Hz, 1H), 5.35 (t, *J* = 10.0 Hz, 1H); 5.46-5.49 (m, 2H); 5.62 (d, *J* = 3.7 Hz, 1H), 7.37-7.50 (m, 6H), 7.56-7.64 (m, 4H).^{13}C-NMR (100 MHz, DMSO): δ = 18.0-19.0 (14C), 26.4 (3C), 30.7, 32.9-33.3 (7C), 61.2, 63.3, 63.8, 67.1, 68.1, 69.1, 69.2, 73.5, 75.3, 80.0, 89.1, 102.4, 127.9 (4C), 130.0 (2C), 132.3, 132.4, 135.0 (4C), 174.6, 175.0 (3C), 175.2, 175.3, 175.6,. HR-MS. Calculated adducts: [M+H$^+$] = 1071.5343, [M+Na$^+$] = 1093.5163, [M+K$^+$] = 1109.4902. Observed adducts, [M+H_2O] = 1088.5609, [M+Na$^+$] = 1093.5175, [M+K$^+$] = 1109.4892. ATR-FTIR (cm^{-1}): 504.26, 702.23, 742.56, 823.65, 1030.51, 1071.63, 1111.82, 1139.69, 1186.65, 1247.91, 1388.47, 1470.12, 1741.41, 2877.85, 2934.80, 2973.83, 3285.44.

(2R,3R,4S,5R,6R)-2-(((2S,3S,4R,5R)-5-(hydroxymethyl)-3,4-bis(isobutyryloxy)-2-(iso-butyryloxy)methyl)tetrahydrofuran-2-yl)oxy)-6-((isobutyryloxy)methyl)tetrahydro-2H-pyran-3,4,5-triyl tris(2-methylpropanoate) **(4)**.

Hepta-isobutyryl-6'-O-TBDPS-sucrose (**3)** (1.032 g, 0.95 mmol) was dissolved in dry THF (20 mL) under inert atmosphere. Acetic acid (0.082 mL, 1.43 mmol) was added to the stirred mixture followed by the addition of a 1.0 M TBAF solution in THF (1.2 mL, 1.2 mmol). The reaction mixture was stirred at room temperature overnight. The reaction was followed by TLC. The reaction mixture was directly purified by dry column purification (EtOAc in heptane with 4% increments). Yield: 0.768 g transparent oily texture; 97%. ^{1}H-NMR (400 MHz, DMSO): δ = 0.95-1.21 (m, 42 H), 2.34-2.66 (m, 7H (DMSO overlap)), 3.60 (m, 2H), 4.00-4.12 (m, 4H), 4.21 (dd, *J* = 13.0 Hz, 4.4 Hz, 1H), 4.34 (ddd, *J* = 10.4 Hz, 4.5 Hz, 1.8 Hz, 1H), 4.91 (dd, *J* = 10.4, 3.6 Hz, 1H), 4.96 (t, *J* = 5.5 Hz, 1H), 5.11 (t, *J* = 9.9 Hz, 1H), 5.34 (t, *J* = 7.5 Hz, 1H), 5.40 (t, *J* = 9.9 Hz, 1H), 5.47 (d, *J* = 7.5 Hz, 1H), 5.67 (d, *J* = 3.5 Hz, 1H). ^{13}C-NMR (100 MHz, DMSO): δ = 18.0-19.0 (14C), 32.9-33.3 (7C), 61.4, 61.5, 63.3, 67.3, 68.0, 69.2, 69.3, 73.7, 75.2, 80.8, 89.1, 102.2, 174.6, 175.0 (3C), 175.3, 175.4, 175.8. HR-MS. Calculated adducts: [M+H$^+$] = 833.4165, [M+Na$^+$] = 855.3985, [M+K$^+$] = 871.3724. Observed adducts: [M+H_2O] = 850.4449, [M+Na$^+$] = 855.3999, [M+K$^+$] = 871.3738. ATR-

FTIR (cm^{-1}): 748.36, 1005.66, 1048.73, 1077.10, 1142.42, 1186.51, 1247.10, 1344.51, 1388.51, 1470.09, 1739.30, 2878.48, 2939.02, 2974.80, 3531.46.

*(2R,3R,4S,5R,6R)-2-(((2S,3S,4R,5R)-5-(((5-((R)-1,2-dithiolan-3-yl)pentanoyl)oxy)methyl)-3,4-bis(isobutyryloxy)-2-((isobutyryloxy)methyl)tetrahydrofuran-2-yl)oxy)-6-((isobutyryloxy)-methyl)tetrahydro-2H-pyran-3,4,5-triyl tris(2-methylpropanoate) (***5***).*
Hepta-isobutyryl-sucrose (**4)** (0.543 g, 0.64 mmol) was dissolved in dry DMF (10 mL) under inert atmosphere. In another flask under inert atmosphere, (*R*)-(+)-1,2-Dithiolane-pentanoic acid (0.206 g, 0.96 mmol), DMAP (0.246 g, 1.91 mmol) and EDAC·HCl (0.190 g, 0.96 mmol) were dissolved in dry DMF (10 mL) and stirred for 15 min. The mixture, containing the activated ester was subsequently transferred to the reaction mixture of hepta-isobutyryl-sucrose (**4).** The reaction mixture was left stirred at room temperature for reaction. The reaction was followed by TLC. After 24 h a new mixture of activated ester: (*R*)-(+)-1,2-Dithiolane-pentanoic acid (0.0706 g, 0.32 mmol), DMAP (0.080 g, 0.64 mmol) and EDAC·HCl (0.065 g, 0.32 mmol) dissolved in dry DMF (10 mL) under inert atmosphere was added to the reaction mixture. At the point of reaction completion, the reaction mixture was concentrated *in vacuo* followed by addition of diethyl ether (100 mL) and phase extraction with water (3×100 mL). The organic phase was collected and finally purified by dry column purification (EtOAc in heptane with 4% increment per fraction). Yield: 0.558 g yellowish oily texture; 86%. ^{1}H-NMR (400 MHz, DMSO): δ = 0.96-1.18 (m, 42H), 1.38 (m, 2H), 1.48-1.72 (m, 4H), 1.86 (dq, *J* = 13.4 Hz, 6.4 Hz, 1H), 2.33 (t, *J* = 7.3 Hz, 2H), 2.36-2.44 (m, 2H), 2.44-2.66 (m, 6H), 3.14 (m, 2H), 3.59 (dq, *J* = 8.5 Hz, 6.2 Hz, 1H), 4.03-4.14 (m, 3H), 4.16-4.40 (m, 5H), 4.91 (dd, *J* = 10.4 Hz, 3.6 Hz, 1H), 5.10 (t, *J* = 9.9 Hz, 1H), 5.34-5.43 (m, 2H), 5.52 (d, *J* = 7.5 Hz, 1H); 5.64 (d, *J* = 3.5 Hz, 1H). ^{13}C-NMR (100 MHz, DMSO): δ = 18.0-19.0 (14C), 24.1, 28.1, 33.0-33.3 (8C), 34.1, 38.1, 40.0 (DMSO overlap), 56.0, 61.4, 63.2, 63.3, 67.3, 68.2, 69.2, 69.2, 73.5, 74.8, 77.5, 89.3, 102.4, 172.4, 174.5, 174.9, 175.0 (2C), 175.2, 175.4, 175.8. HR-MS. Calculated adducts: $[M+H^+]$ = 1021.4495, $[M+Na^+]$ = 1043.4314, $[M+K^+]$ = 1059.4054. Observed adducts, $[M+H_2O]$ = 1039.4844, $[M+Na^+]$ = 1043.4355, $[M+K^+]$ = 1059.4136. ATR-FTIR (cm^{-1}): 476.19, 748.51, 849.06, 916.58, 963.11, 1028.24, 1074.25, 1140.82, 1185.60, 1246.17, 1344.85, 1388.11, 1469.77, 1738.20, 2877.68, 2936.72, 2974.16.

2. AuNP Characterization and Handling

General considerations
The synthesized AuNPs were diluted with MQ-H_2O (Au-seeds ×4), citrate stabilized AuNPs (×4) and PNIPAM-coated AuNPs (×4000) prior to UV-vis, DLS and ζ-potential measurements.

UV-vis Measurements
The UV-vis absorption spectra of the synthesized AuNPs were measured using a Unicam Helios α Uni 9423 UV-vis spectrophotometer by scanning the UV-range from 450-900 nm. UV-vis absorption spectra of hydrosols were measured using disposable PS cuvettes whereas organosols were measured in quarts cuvettes of identical dimensions (1.0 cm × 1.0 cm). The apparent solvent was used in the reference cell for the individual measurements and blanks were run prior to AuNP analysis.

Dynamic Light Scattering Measurements
The hydrodynamic diameter and polydispersity of the synthesized AuNPs were determined using a Zeta PALS Analyzer (Brookhaven Instruments, NY, USA). Data was fitted using built-in software to calculate the hydrodynamic size of the AuNP-colloids.

ζ-potential Measurements

The ζ-potential was measured in the same sample as the DLS analysis using a Zeta PALS Analyzer (Brookhaven Instruments, NY, USA) with a pre-conditioned electrode with 10 sub-runs while observing a fitting model residual less than 0.04.

ICP-MS Measurements

The Au-concentration of the purified and up-concentrated PEG- and PNIPAM-coated AuNPs stock solutions were determined by ICP-MS using a Thermo Scientific iCAPQ ICP-MS (MA, USA) using the following settings; RF Power: 1550 W, Plasma Gas Flow: 14L min^{-1}, Nebulizer Gas Flow: 0.945L min^{-1}, Dwell Time: 0.01 s, Sweeps: 300, Replicates: 3, Delay Time: 60 s, Wash Time: 60 s. PNIPAM-coated AuNPs (20.0 µL) was digested using fresh prepared aqua regia (400 µL) and the total volume adjusted to 6.00 mL with MQ-H_2O (5580 µL) (× 300 dilution). The ×300 dilution solution (5 µL) was further diluted with HNO_3 (4995 µL, 1% + 0.5 ppb Ir as internal standard) to give a final dilution factor of ×300.000. A standard curve covering the concentration range of 62.5 ppb ─ 500 ppb in HNO_3 (1% + 0.5 ppb Ir as internal standard) was prepared using an Au-standard for ICP-MS (1000 mg L^{-1}). The intensity of ^{197}Au (m/z = 196.9666) was measured and the concentration of coated AuNPs was determined based on the corresponding standard curve.

Lyophilization and Stability of PNIPAM-coated AuNPs

The PNIPAM-coated AuNPs stock solution (64 mg Au mL^{-1}) was diluted to 1.0- 2.5- and 5.0 mg Au mL^{-1} with MQ-H_2O in glass vials. The samples were snap frozen by submerging the samples into liquid nitrogen and lyophilized overnight ($p < 6.0 \times 10^{-2}$ mbar) to give an air stable black nanopowder which was stored in the dark at 5 °C until further use. The lyophilized PNIPAM-coated AuNPs readily re-dispersed in MQ-H_2O to form the apparent PNIPAM-coated AuNPs hydrosol with no change in particle morphology based on UV-vis spectroscopy and DLS analysis. Additionally, the lyophilized PNIPAM-coated AuNP nanopowder also readily re-dispersed in various protic- and aprotic organic solvents to form stable PNIPAM-coated AuNP organosols (**Figure S1**).

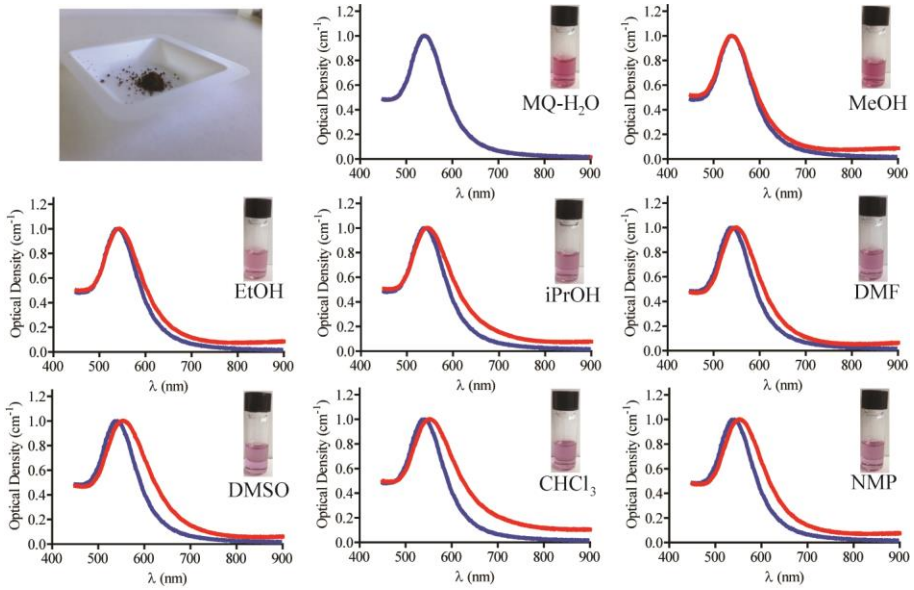

Figure S1. UV-vis spectroscopy analysis of the re-dispersibility of the air stable black nanopowder of PNIPAM-coated AuNPs obtained by lyophilization in MQ-H_2O and various protic- and aprotic polar organic solvents covering the relative polarity scale from 0.259 (chloroform) to 1.000 (MQ-H_2O). An apparent red-shift of the surface plasmon resonance peak is observed following re-dispersion in organic solvent due to the change in refractive index of the solvent.

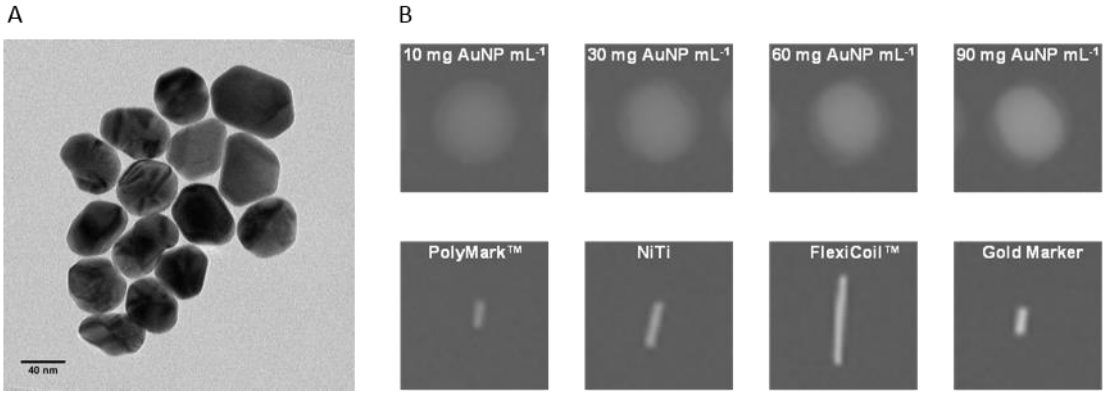

Figure S2. A) Characterization of PNIPAM-coated AuNP by TEM; B) Comparison of the obtained contrast level in 2D x-ray imaging of AuNPs containing nanogels (10- 30-, 60- and 90 mg AuNP mL^{-1}) and solid fiducial markers used in the clinic. Markers visualized in a 10 cm solid water phantom using the following settings; 80 kVp, 80 mA, 80 ms.

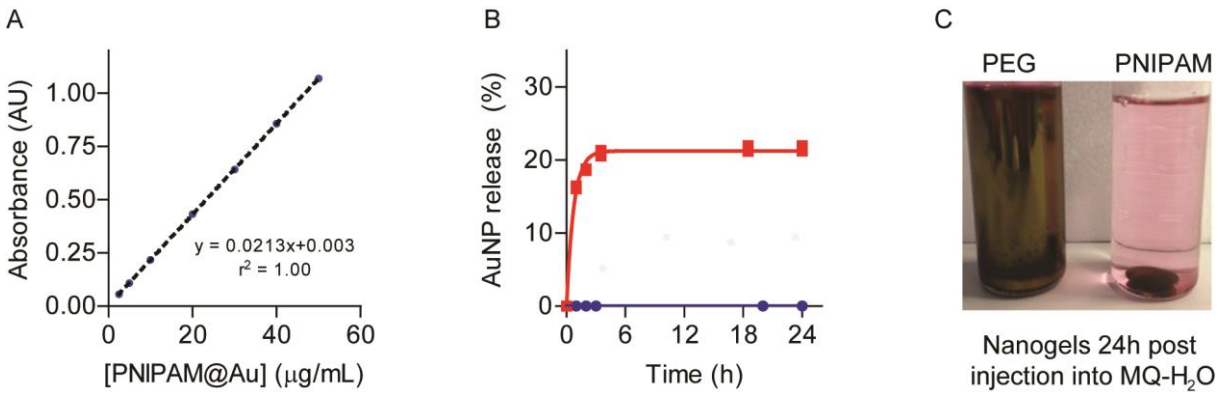

Figure S3. A) Standard curve of UV-absorbance at λ = 537 nm as a function of PNIPAM-coated AuNP concentration in MQ-H_2O (r^2 = 1.00); B) In vitro release kinetics from SAIB/EtOH/PLA (75:20:5) with either 30 mg mL^{-1} PEG-coated AuNPs or PNIPAM-coated AuNPs in MQ-H_2O at 37 °C. Each point represents the mean ± SEM (n = 3). C) Representative image of nanogels containing either PEG-coated or PNIPAM-coated AuNPs after 24 h incubation in MQ-H_2O.

3. X-ray Visualization of Nanogel in Mice/Canine

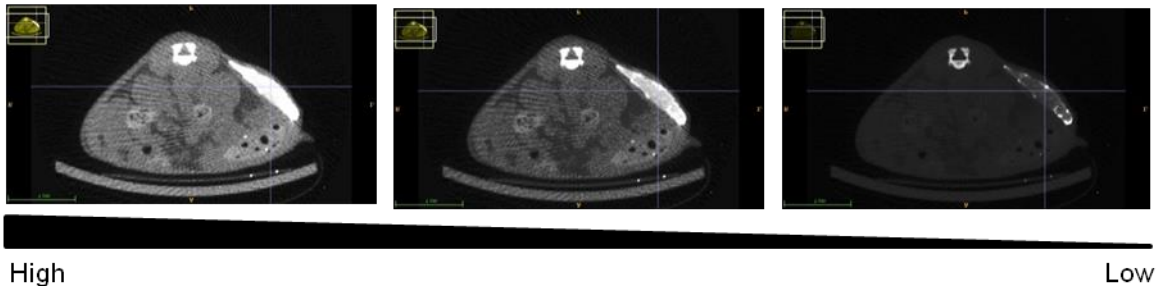

Figure S4. Visualization of nanogel composed of SAIB/EtOH/PLA (75:20:5) + 30 mg PNIPAM-coated AuNPs mL^{-1} administered subcutanously injection in immunocompetent mice. Aggregation of PNIPAM-coated AuNPs within the gel matrix visualized by reduction of the contrast level on the micro-CT image.

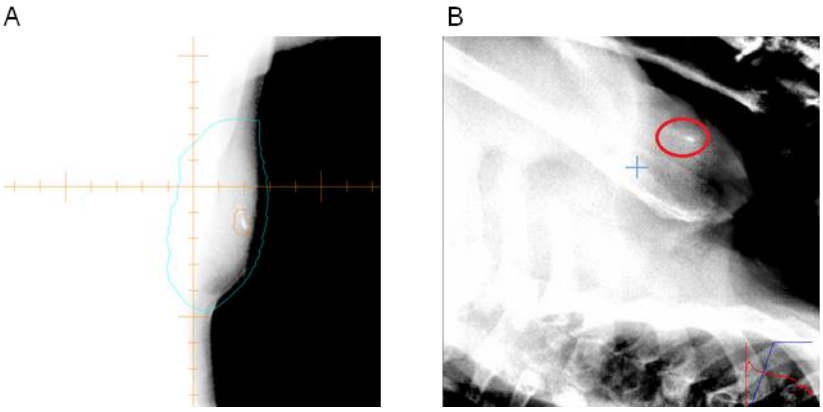

Figure S5. Nanogel composed of SAIB/EtOH/PLA (75:20:5) + 30mg PNIPAM-coated AuNPs mL^{-1} administered intratumorally into canine suffering from a solid subcutaneous mast cell tumor (maximum distance (x × y × z); 1.82 cm × 5.81 cm × 5.32 cm, CT volume; 31.64 cm^3) adherent to the underlying soft tissue located over the dorsal aspect of the left shoulder blade. A) OBI 2D x-ray imaging of nanogel and B) ExacTrac imaging of nanogel. Both images recorded prior to the first fraction of radiation therapy 6 days after injection.